DEVELOPMENT OF A FINITE VOLUME FRAMEWORK FOR CONVECTIVE-RADIATIVE FLOWS ON UNSTRUCTURED GRIDS

A thesis submitted in partial fulfillment of the requirements for the degree of

DOCTOR OF PHILOSOPHY

By

Mukul Parmananda

(Roll Number: 136103019)

to the

DEPARTMENT OF MECHANICAL ENGINEERING
INDIAN INSTITUTE OF TECHNOLOGY GUWAHATI

August 2018

CERTIFICATE

It is certified that the work contained in the thesis entitled **"Development of a finite volume framework for convective-radiative flows on unstructured grids"**, by **Mukul Parmananda** has been carried out under my supervision and that this work has not been submitted elsewhere for a degree.

(Amaresh Dalal)

August 2018

Associate Professor

Department of Mechanical Engineering

Indian Institute of Technology Guwahati

Dedicated to My Aagi

Smt. Tara Parmananda

and My Parents

Shri. Mohan Parmananda

Smt. Madhuri Parmananda

Acknowledgements

I am grateful to all the people who were a part of my journey during my doctoral study at Indian Institute of Technology, Guwahati. Without their kind personal and professional support it would have been impossible for me to present the thesis to the existing estate.

Firstly, I would like to express my sincere gratitude to my supervisor Prof. Amaresh Dalal for giving me the opportunity to work with him. His constant guidance, motivation, and encouragement have helped me to successfully complete my thesis work. I am thankful to him for providing me the best of research facilities, a healthy and competitive work environment and personal workspace to carry out my research work. I shall remain obliged to him for devoting his knowledge and valuable time to this work. It is also because of his collaborative nature that I had the opportunity to work with Prof. Ganesh Natarajan (IIT-Guwahati), Shri. Venkata PPK (BARC) and Prof. Pradeep Kumar (IIT-Mandi). I am thankful to all of them as they have contributed immensely to this work. I feel fortunate and privileged to have the opportunity to work and learn from them.
I would also like to express my sincere gratitude and humble respect to my doctoral committee members: Prof. Anoop K. Dass, Prof. Ganesh Natarajan and Prof. R. K. Upadhyay for their suggestions and insightful comments on my work. My special thanks goes to the faculty members of the Department of Mechanical Engineering from whom I learned the basics of fluid and thermal engineering. Especially, the advanced course on CFD taught by Prof. Arnab Kumar De was very helpful for me in learning how to write CFD codes which helped in pursuing my research. In addition to this, I would also like to acknowledge the partial funding provided by DAE-BRNS, Government of India and ICHMT for providing a grant to attend an international conference.

These acknowledgments would not be complete without mentioning my research lab colleagues Vinod, Saurabh, Preetirekha, Subrat, Shiva and all the present and passed out M.Tech. students of our Anupravaha Laboratory. It was really a great pleasure working with all of them and I thank all of them for their support. Special thanks goes to my seniors Dr. Pitambar Randive, Dr. Sathisha H. M. and Dr. Jai Manik for helping me in various aspects of my work. I would also like to thank Mr. Salman Khan and Mr. Rama Krishnan for working with me.

Apart from having a large workgroup I was privileged to enjoy the company of my friends with whom I had a great time off the lab. The campus of IIT-Guwahati has provided me many opportunities to explore myself. Badminton, cycling, swimming, trekking were some of the activities which helped me in keeping a fit mind and body. In the process, I made many friends with whom I had some unforgettable times. I am thankful to my badminton teammates Hemanshul, Shyam Singh, Shyam Trivedi,

Subrat, Basant, Uttam, Anand, Vinod, Panky, Kishor, Siddesh, Rajendra, Shatru, Arun with whom I had a great time on the court. Special thanks to Shyam, the time we spent on trekking, cycling and several Spardha wins will always be memorable. I am also thankful to Mrs. Swapnali Bora and Dr. Anamika Barua for offering a home-like environment. Several dinner parties organized at your place and Diwali Mela celebration will always be remembered. Special thanks to Pankaj Sing for cooking delicious meals. Apart from them, I am thankful to my friends Kush, Ashish and Manpreet for taking care of my family while I was away. Special thanks to Anshul Garg who is like an elder brother to me and Mrs. Aditi Garg for taking care of me during my sickness. Special thanks to Dr. Syed Humayun Basha for his constant support and motivation for doing better work. The late night chats and biryani treats will always be remembered. I would also like to thank Ms. Flavia Miranda, for helping me improve my work. Special thanks to Pitambar Randive, Vinod Pandey and Hemanshul Garg, they were the people I looked forward to in times of any need both personally and professionally.

Finally, I would like to say that this work would not have been possible without the blessings of the Almighty and the constant support of my family members. Especially my parents, for whom I think whatever I do will be less compared to the support, good wishes and blessings they have bestowed upon me. Thanks will be a very small word for acknowledging them. I express my gratitude to Mr. Ravi Parmananda, Mrs. Varsha Parmananda, Abhishek, Shantanu and Maithily for their love and continuous support.

Mukul Parmananda

ABSTRACT

Several experimental and numerical studies have been carried out on the interaction of laminar and turbulent natural convection in conjunction with thermal radiation owing to its immense applications in atmospheric and geophysical research. Most of the studies have been realized in enclosures to model various industrial applications. These applications include the design of nuclear reactor cooling systems, furnace, burners, buildings for safe evacuation in case of fires and combustion. Majority of the applications listed above are significantly influenced by thermal radiation and compressibility effects. Computation of accurate numerical simulations in such scenario could be of great practical importance and remains a challenge.

In general, an incompressible flow solver based on constant density advection, zero velocity divergence, and the Boussinesq approximation is a preferred choice for solving these class of problems. However, the use of Boussinesq assumption becomes ambiguous for problems encompassing large temperature difference radiative-convective heat transfer. The use of this approximation is limited to small density variations i.e. a relative temperature difference must be less than 10 %. This issue can be circumvented by the use of a non-Boussinesq flow solver which employs the low-Mach number formulation in regimes where Mach number is sufficiently small ($Ma < 0.3$) typical for buoyancy-driven flows. The present doctoral thesis focuses on the development of a generic three-dimensional numerical solver using a pressure-based approach. The solver employs a low-Mach approximation to compute combined natural convection coupled with thermal radiative heat transfer both in laminar and turbulent regimes.

The initial advancement in the proposed solver is the development of a pure radiative heat transfer model based on the finite volume method in a collocated grid framework. Subsequently, a variable density flow solver based on low-Mach number formulation is devised for simulating large temperature difference (non-Boussinesq) convection. The development is further extended by coupling the flow and radiative heat transfer solver which is then employed to simulate laminar buoyancy-induced convection with surface and gas radiation in enclosures. Lastly, the k-ε turbulence

model based on Favre-averaged Navier-Stokes equations is implemented to compute non-Boussinesq turbulent radiative-convective flows. The description of the solver is followed by extensive validation for two and three-dimensional problems on the hybrid unstructured grid.

The pure radiative heat transfer solver is validated for simulating surface to surface and grey-gas radiation in absorbing, emitting and scattering medium for scenarios pertaining to combustion chambers. The laminar low-Mach number solver is validated against benchmark works for natural convection flows inside an enclosure at large temperature difference with variable thermo-physical properties. Furthermore, the convection coupled with thermal radiation solver is validated against the two- and three-dimensional problems available in the literature. Finally, the low-Mach number framework for turbulent flows is validated against experimental and numerical benchmark problems. The validation study is followed by demonstrating the need for non-Boussinesq low-Mach number solver by showing the invalidity of the incompressible model for convective-radiative flows.

Investigations are performed to check the validity of Boussinesq approximation which is typically used in the radiative-convective flows. The investigations are targeted at quantifying the deviations in the results when the Boussinesq approximation is violated. This study demonstrates the failure of Boussinesq approximation for large temperature difference natural convection (high Gay-Lussac number) where it is observed that the presence of surface and gas radiation aggravates the problem. Interestingly, the Boussinesq approximation also does not hold true in small temperature difference natural convection particularly when radiative heat transfer is dominant (small Planck number). Furthermore, the results from the present non-Boussinesq low-Mach number solver for scenarios involving combined convection and radiation at large temperature difference with significant radiation are verified by performing comparisons against the results obtained using a compressible model of OpenFOAM. The verification of low-Mach number solver is followed by presenting three different algorithms based on a low-Mach number formulation for coupling the flow and radiative heat transfer.

The three algorithms compute the coupled governing equations in a segregated manner using the conservative form of momentum equations in conjunction with a variable coefficient pressure Poisson equation. The first algorithm (Algorithm A) uses conservation of mass and energy equation to compute density and temperature. The Algorithm B calculates temperature while the Algorithm C computes density from the equation of state. Furthermore, a conservative form of the continuity and energy equation is solved to obtain density and temperature for Algorithms B and C respectively. The energy and mass conservation errors arising due to the use of Algorithms B and C are derived concerning various non-dimensional parameters governing the flow and heat transfer. Impact of these errors has been found signif-

icant as established from several investigations over a range of Rayleigh, Prandtl, and Planck numbers. The role of balancing of the pressure and buoyancy terms is also emphasized for robust calculation of large density variation flows. Having demonstrated the importance of low-Mach number model and the robustness of different algorithms for quasi-incompressible flows the numerical framework is applied to simulate application problems.

The first study involves the influence of partitions on buoyancy induced convection with thermal radiation in a differentially heated cubical enclosure typical of industrial furnace and high rise buildings. Four distinct arrangements of partitions from the top-bottom and front-back walls are examined by adopting a symmetric (inline) and asymmetric (offset) configuration of partitions for higher heat transfer rates (Nusselt number). Irreversibilities associated with conduction, convection, and radiation heat transfer with viscous dissipation are studied to investigate the role of partitioning walls in overall volumetric entropy production. This study aims to optimize the thermal design (higher heat transfer rates with minimum entropy production) among all partition configurations. The offset configuration with front-back partitions exhibits highest heat transfer rates with minimum total entropy generation. The offset design of partitions could be a preferred choice from a building design and heat transfer point of view.

Next study discusses the buoyancy-driven turbulent natural convection with and without the influence of thermal radiation in a differentially heated square cavity at large temperature difference. The impact of surface and gas radiation on overall flow dynamics and heat transfer is discussed by performing comparisons with a classic natural convection case at $Ra = 10^{10}$. The results from the present study reveal that the inclusion of surface and gas radiation leads to asymmetry in the flow and heat transfer. Furthermore, the convection currents intensify, and the magnitude and extent of the turbulence effects primarily increase with the consideration of thermal radiation in the simulation. This study also quantifies the deviations between the proposed variable density low-Mach number model and popularly used incompressible model based on Reynolds averaged governing equations. Finally, the thesis concludes with a summary of the main findings and recommendations for future work.

Contents

List of Figures

List of Tables

Nomenclature

English Symbols

Symbol	Definition
c_p	specific heat at constant pressure
$c_\mu, c_{\varepsilon 1}, c_{\varepsilon 2}, c_{\varepsilon 3}, c_{\varepsilon 4}$	turbulence model constants
$\hat{\mathbf{e}}_\mathbf{y}$	unit vector along y direction
Fr	Froude number ($\frac{U^2}{g_0 l}$)
$\mathbf{g}$	acceleration due to gravity
Ga	Gay-Lussac number ($\beta_T(T_{hot} - T_{cold})$)
H	height of the square enclosure
I	radiation intensity
I_b	radiation intensity for a perfectly black body ($\frac{\sigma_b T^4}{\pi}$)
k	turbulent kinetic energy
$\hat{\mathbf{n}}$	unit normal vector
Nu_c	convective Nusselt number ($\frac{q_c H}{\kappa \Delta T}$)
Nu_r	radiative Nusselt number ($\frac{q_r H}{\kappa \Delta T}$)
p	pressure
$\bar{P}$	thermodynamic pressure
Pe	Peclet number ($Pe = \frac{\rho_0 c_{p0} U l}{\kappa_0}$)
Pl	Planck number ($\frac{k_0}{4\sigma_b T^3 H}$)
Pr	Prandtl Number ($\frac{\nu}{\alpha}$)
Pr_t	turbulent Prandtl Number
$\mathbf{q_r}$	heat flux due to radiation
$\mathbf{r}$	position vector
R	universal gas constant
Ra	Rayleigh Number ($\frac{2\epsilon g H^3}{\nu \alpha}$)
$\mathbf{s}$	direction vector
T	temperature
T_o	bulk mean temperature $\frac{(T_{hot}+T_{cold})}{2}$
X, Y, Z	Cartesian co-ordinates in dimensionless form
x_p	normal distance to the wall from the nearest cell center
y^+	non-dimensional wall distance ($\frac{u_\tau x_p}{\nu}$)
u_i	velocity vector with index notation i refer to Cartesian components
u_i''	fluctuating velocity vector
U, V, W	non-dimensional velocity components

Greek Symbols

Symbol	Definition
α	thermal diffusivity
β	extinction coefficients $(\kappa_a + \sigma_s)$
β_T	thermal expansion coefficients
ϵ	Boussinesq parameter $(\frac{T_{hot}-T_{cold}}{2T_0})$
ε	turbulent dissipation rate
ε_w	emissivity of the wall
γ	specific heat ratio
κ	thermal conductivity
κ_a	absorption coefficient
Υ	volume of the enclosure
μ	dynamic viscosity
μ_t	turbulent viscosity
ν	kinematic viscosity
ρ	density
σ_b	Stefan-Boltzmann constant
$\sigma_k, \sigma_\varepsilon$	turbulent Prandtl numbers of k and ε
σ_s	scattering coefficient
τ	optical thickness (βH)
Ω	solid angle
Φ	scattering phase function

Subscripts

Symbol	Definition
bf	total number of faces in boundaries
c	convection
$cold$	cold wall
hot	hot wall
f	value at a face of a cell
i, j	index notations refers Cartesian components
m	discrete direction of intensity
N	value of cell centroid of neighbor cell
NC	total number of cells
o	reference state
P	value of cell centroid of owner cell
r	radiation

Superscripts

Symbol	Definition
$n, n+1$	time levels
*	intermediate time level between n and $n+1$
$-$	Reynolds averaging
$\sim$	Favre averaging

Abbreviations

Symbol	Definition
CDS	central difference scheme
DOM	discrete ordinate method
FVM	finite volume method
LMN	low-Mach number
LIS	library of iterative solver
RTE	radiative transfer equation

Chapter 1

Introduction and Literature Review

Experimental and numerical studies on coupled flow and heat transfer are vital owing to its immense applicability in engineering, atmospheric and geophysical research. The majority of engineering heat transfer applications are governed by conduction, convection, and radiation. On distinguishing the three modes of heat transfer it is realized that heat transfer by conduction transpires by the transfer of energy through the atomic lattice via internal rotational, translational, and vibrational motion of the molecules. The energy transfer by diffusion and bulk motion of the fluids is accountable for heat transfer by convection due to kinetic energy transfer. In this context, the convection currents can be self-induced, forced induced by the application of external mechanical device and combination of both. The self-induced convection also termed as natural convection is driven by buoyancy forces in presence of gravity. On the other hand, forced convection is effected by applying an external flow field or due to the pressure difference. Similarly, a mixed convection scenario includes a combination of buoyancy and pressure forces. From the industrial point of view making the most of buoyancy induced heat transfer is preferable owing to its cheap expense in carrying out the process (self induced flow).

The radiative heat transfer is among the most commonly experienced modes of heat transfer. The key stimulus to the radiative heat transfer is the electromagnetic

waves. The electromagnetic waves vary with wavelength and in the spectrum of wavelength between 0.1 μm to 100 μm are responsible for inducing temperature difference and hence termed as thermal radiations. Among the three modes of heat transfer; conduction and convection signify a linear dependence on the temperature difference whereas radiative heat transfer rates are proportional to the fourth power of difference in absolute temperatures. Hence, the radiative heat transfer becomes significant in high-temperature industrial applications. As already mentioned that natural convective heating/cooling are preferable for industrial problems, however in scenarios involving large temperature difference and high heat flux the role of thermal radiation cannot be neglected. The interaction of laminar and turbulent natural convection with thermal radiation can be observed in many industrial applications like the design of nuclear reactor cooling systems, combustion chambers, boilers, furnace design, glass forming, industrial and building fires etc. While few experimental investigations have been carried out to understand the complex flow and heat transfer characteristics in such scenario, computation of accurate numerical simulations remains a challenge.

The complexities involved in the numerical analysis of radiative heat transfer vary as per the nature of the medium. The medium can either participate i.e. absorb, emit and scatter radiation or does not participate. Radiative heat transfer in non-participating medium is also known as the surface to surface radiation. It is relatively easy to analyze via view factors. However, high temperature industrial flow problems like combustion require handling carbon monoxide, soot, oxides of nitrogen and sulfur as byproducts. The accurate prediction of these pollutants demands the exact calculation of radiative heat transfer in participating media keeping into account the effects of absorption, emission, and scattering. As radiant energy is convected in all directions the directional dependence needs to be distinctly considered as intensity in a given direction remains unaffected by the intensity in other direction. In addition, the participating medium also depends upon the wavelength of the incoming radiation; hence the solution to radiative transfer equation (RTE) requires the consideration of all directions as well as wavelength. Furthermore, it is preferable to solve the RTE for radiation intensity rather than temperature in order to reduce the nonlinearity of the equation. It can be seen that the dependent variable for radiation is intensity (I), which depends on six independent variables like space, direction, and wavelength. By making a gray medium assumption, the wavelength

dependency can be neglected to reduces the complexity. Keeping into consideration the wide applicability and the complexity involved in the numerical simulation of coupled flow and heat transfer process, the primary focus of the present thesis is on the development and application of numerical models for such scenario. In this context, the basic terminology used in radiative heat transfer (Incropera et al. [1]), introduction to numerical models for radiation (Modest [2]) and a comprehensive literature review have been presented in the following section.

1.1 Introduction to the Fundamental Radiation Terminology

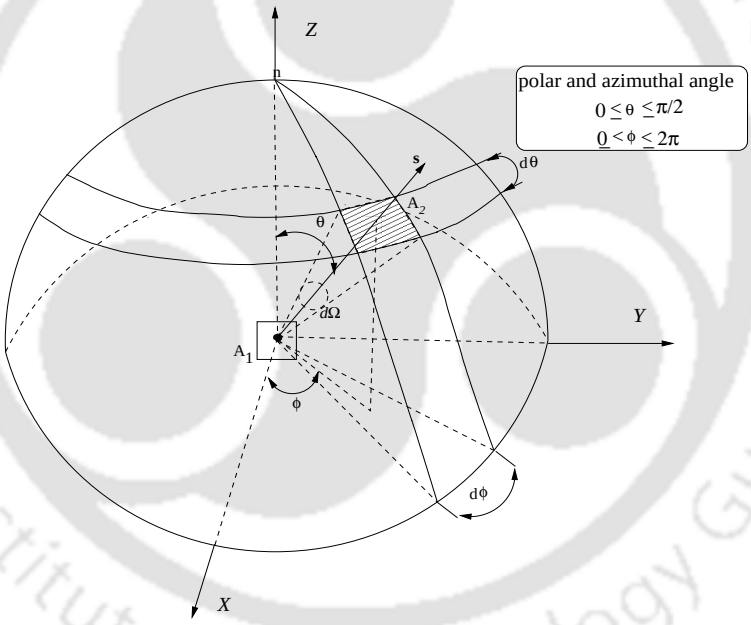

Figure 1.1: Radiation emission from a surface of area A_1 along the direction **s**

1.1.1 Solid angle

Figure 1.1 represents the emission of radiant energy from a surface of area A_1 along the direction **s**. The direction **s** is represented in terms of ϕ (azimuthal) and θ (zenith) angles. The elemental area dA_2 on the surface of hemisphere of radius r is

equal to $\mathrm{r}^2 \sin\theta \ \mathrm{d}\phi \ d\theta$. The solid angle subtended by this elemental area $\mathrm{d}A_2$ when viewed from a point on $\mathrm{d}A_1$ is given by

$$\mathrm{d}\Omega = \frac{\mathrm{dA}_2}{r^2} = \frac{(\mathrm{r}\ \mathrm{d}\theta) \times (\mathrm{r}\sin\theta\ \mathrm{d}\phi)}{r^2} \tag{1.1}$$

$$\mathrm{d}\Omega = \sin\theta\ \mathrm{d}\theta\ \mathrm{d}\phi \tag{1.2}$$

1.1.2 Emissive power

The radiative heat flux or emissive power depends on temperature, wavelength, and direction of the emitted radiation. The directional, spectral (wavelength dependent) emissive power is the rate at which radiation is emitted from a surface in the (θ, ϕ) direction per unit solid angle, wavelength $d\lambda$, and surface area.

$$E_\lambda(\lambda, \theta, \phi) = \frac{\mathrm{d}q}{dA_1\ \mathrm{d}\Omega\ \mathrm{d}\lambda} \tag{1.3}$$

1.1.3 Total hemispherical emissive power

It is the rate at which energy is emitted per unit area at all wavelengths and directions.

$$E = \int_0^\infty \int_{\phi=0}^{2\pi} \int_{\theta=0}^{\pi/2} E(\lambda, \theta, \phi)\ \sin\theta\ \mathrm{d}\theta\ \mathrm{d}\phi\ \mathrm{d}\lambda \tag{1.4}$$

1.1.4 Intensity

The intensity is the rate at which radiant energy is emitted at the wavelength λ in the (θ, ϕ) direction, per unit area of the emitting surface normal to this direction, solid angle, and wavelength interval $\mathrm{d}\lambda$. Since the area used to define the intensity is the component of $\mathrm{d}A_1$ perpendicular to the direction of radiation it is equal to $\mathrm{d}A_1 \cos\theta$.

$$I_\lambda(\lambda, \theta, \phi) = \frac{\mathrm{d}q}{dA_1\ \cos\theta\ \mathrm{d}\Omega\ \mathrm{d}\lambda} \tag{1.5}$$

From Eqs. 1.3 - 1.5 it can be seen that the directional spectral emissive power and intensity are related by "Lambert cosine law".

$$E_\lambda(\lambda, \theta, \phi) = I_\lambda(\lambda, \theta, \phi) \cos\theta \tag{1.6}$$

Hence total hemispherical emissive power and total hemispherical intensity can be defined as

$$E = \int_0^\infty \int_{\phi=0}^{2\pi} \int_{\theta=0}^{\pi/2} I(\lambda, \theta, \phi)\ \cos\theta\ \sin\theta\ \mathrm{d}\theta\ \mathrm{d}\phi\ \mathrm{d}\lambda \tag{1.7}$$

$$I = \int_0^\infty \int_{\phi=0}^{2\pi} \int_{\theta=0}^{\pi/2} I(\lambda, \theta, \phi)\ \sin\theta\ \mathrm{d}\theta\ \mathrm{d}\phi\ \mathrm{d}\lambda \tag{1.8}$$

1.1.5 Irradiation

It is related to incident radiation, i.e. the radiation originating from other surfaces by emission and reflection. The total irradiation is the rate at which radiation of wavelength λ is incident on a surface per unit area at all wavelengths and directions.

$$G = \int_0^\infty \int_{\phi=0}^{2\pi} \int_{\theta=0}^{\pi/2} I_{\lambda,i}(\lambda, \theta, \phi)\ \cos\theta\ \sin\theta\ \mathrm{d}\theta\ \mathrm{d}\phi\ \mathrm{d}\lambda \tag{1.9}$$

For a diffuse emitter, the emitting intensity is independent of direction. In this case, Eq. (1.7) can be integrated over all the directions to obtain a relation between hemispherical spectral emissive power and hemispherical spectral intensity as given below.

$$E_\lambda(\lambda) = \pi I_\lambda(\lambda) \tag{1.10}$$

1.2 Introduction to Radiative Exchange in a Participating Medium

The beam of emitted radiation from a surface attenuates and augments energy while propagating through a medium as shown in Fig. 1.2. Attenuation of energy is due to absorption by the media, out-scattering i.e, scattering away from the direction of travel. The augmentation of energy is due to emission from within the medium due

to its own temperature in addition to in-scattering of radiation from other directions $\mathbf{s}_i$ into the direction of travel $\mathbf{s}$. Changes in intensity due to absorption, emission, in-scattering, and out-scattering are modeled as below.

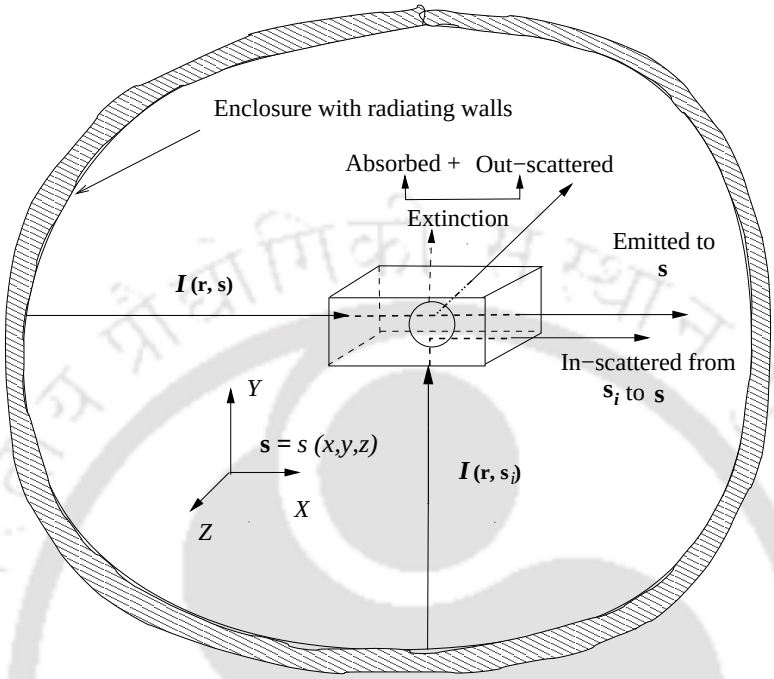

Figure 1.2: Schematics of absorption, emission, in-scattering and out-scattering of radiant energy inside the participating media.

1.2.1 Attenuation by absorption and out-scattering

The loss of the radiant energy while propagating through the medium is due to absorption and out-scattering. The absorption of radiant energy by the medium is simply converted to internal energy whereas out-scattering is basically change in direction of the radiant energy to other direction. It can also be viewed as augmentation in other direction. The attenuation due to absorption and out-scattering is expressed as,

$$\left(\frac{\mathrm{d}I(\mathbf{s})}{\mathrm{d}s}\right)_{\text{absorption}} = -\kappa_a I(\mathbf{s}) \tag{1.11}$$

$$\left(\frac{\mathrm{d}I(\mathbf{s})}{\mathrm{d}s}\right)_{\text{out-scattering}} = -\sigma_s I(\mathbf{s}) \tag{1.12}$$

where κ_a and σ_s is known as the absorption and scattering coefficient respectively. The negative sign represents the loss of intensity. The total attenuation of the radiation intensity is described in terms of extinction coefficient expressed as,

$$\beta = \kappa_a + \sigma_s \tag{1.13}$$

1.2.2 Augmentation by emission and in-scattering

The augmentation of radiant energy by emission is due to the finite temperature of the medium. The energy emitted by the medium is the product of material emissivity (emissivity equals absorptivity (κ_a) using Kirchoff's law) to the intensity of the blackbody radiation. Hence, the change in intensity of radiation due to emission is expressed as,

$$\left(\frac{\mathrm{d}I(\mathbf{s})}{\mathrm{d}s}\right)_{\text{emission}} = \kappa_a I_b \tag{1.14}$$

In-scattering is defined as the augmentation of intensity due to the contribution of scattering from all portions of the material in every direction. An integration needs to be performed over all incoming directions, as the enhancement of the intensity in the different direction is due to the contribution by all out-scattering rays. The out-scattered fraction of intensity $\mathrm{d}I$ gets in scattered in all other directions (indicated as $\mathbf{s}$) over the total solid angle of 4π. A function $\Phi(\mathbf{s}_i, \mathbf{s})$, called the scattering phase function that describes the probability that a ray from one direction ($\mathbf{s}_i$) will be scattered into a certain other direction ($\mathbf{s}$). The fraction of intensity in-scattered along the direction ($\mathbf{s}$) can be expressed as,

$$\frac{\Phi(\mathbf{s}_i, \mathbf{s})}{4\pi}\sigma_s I(\mathbf{s}_i)\mathrm{d}\Omega_i \tag{1.15}$$

The in-scattering in the direction $\mathbf{s}$ from all incoming direction $\mathbf{s}_i$ can be obtained by integrating over all solid angles as.

$$\left(\frac{\mathrm{d}I(\mathbf{s})}{\mathrm{d}s}\right)_{\text{in-scattering}} = \int_{4\pi} \frac{\Phi(\mathbf{s}_i, \mathbf{s})}{4\pi}\sigma_s \; I(\mathbf{s}_i) \; \mathrm{d}\Omega_i \tag{1.16}$$

For isotropic scattering equal amount of energy is scattered in all directions, $\Phi(\mathbf{s}_i, \mathbf{s}) = 1$

1.3 Introduction to Radiative Transfer Equation and Solution Methods

The total change of intensity due to emission, absorption and scattering for a ray travelling in the direction $\mathbf{s}$ over a length ds is given by the energy balance along the direction $\mathbf{s}$ given by

$$I(s+\mathrm{d}s,\ \mathbf{s},\ t+\mathrm{d}t) - I(s,\ \mathbf{s},\ t) = \kappa_a\ I_b(s)\mathrm{d}s - \kappa_a\ I(s,\mathbf{s})\mathrm{d}s - \sigma_s\ I(s,\mathbf{s})\mathrm{d}s$$

$$+\frac{\sigma_s}{4\pi}\int_{4\pi} I(\mathbf{s}_i)\ \Phi(\mathbf{s}_i,\mathbf{s})\ \mathrm{d}\Omega_i\ \mathrm{d}s \tag{1.17}$$

Expanding $I(s+\mathrm{d}s,\ \mathbf{s},\ t+\mathrm{d}t)$ using Taylor series expansion and truncating it up to first order, we get

$$I(s+\mathrm{d}s,\ \mathbf{s},\ t+\mathrm{d}t) = I(s,\ \mathbf{s},\ t) + \frac{\partial I}{\partial s}\ \mathrm{d}s + \frac{\partial I}{\partial t}\ \mathrm{d}t \tag{1.18}$$

Substituting it into Eq. (1.17), we get

$$I(s,\ \mathbf{s},\ t) + \frac{\partial I}{\partial s}\ \mathrm{d}s + \frac{\partial I}{\partial t}\ \mathrm{d}t - I(s,\ \mathbf{s},\ t) = \kappa_a\ I_b(s)\ \mathrm{d}s - \kappa_a\ I(s,\mathbf{s})\ \mathrm{d}s$$

$$-\sigma_s\ I(s,\mathbf{s})\ \mathrm{d}s + \frac{\sigma_s}{4\pi}\int_{4\pi} I(\mathbf{s}_i)\Phi(\mathbf{s}_i,\mathbf{s})\ \mathrm{d}\Omega_i\ \mathrm{d}s \tag{1.19}$$

which reduces to

$$\frac{\partial I}{\partial s} + \frac{\partial I}{\partial t}\frac{1}{c} = \kappa_a\ I_b(s) - \kappa_a\ I(s,\mathbf{s}) - \sigma_s\ I(s,\mathbf{s}) + \frac{\sigma_s}{4\pi}\int_{4\pi} I(\mathbf{s}_i)\Phi(\mathbf{s}_i,\mathbf{s})\ \mathrm{d}\Omega_i \tag{1.20}$$

where c is the speed of light, neglecting the second term on the left hand side of the above equation we get

$$\frac{\partial I}{\partial s} = \kappa_a I_b(s) - \beta I(s,\mathbf{s}) + \frac{\sigma_s}{4\pi}\int_{4\pi} I(\mathbf{s}_i)\ \Phi(\mathbf{s}_i,\mathbf{s})\ \mathrm{d}\Omega_i \tag{1.21}$$

where β is the extinction coefficient defined in Eq. (1.13). The above equation is the radiative transfer equation (RTE), which is a non-homogenous integro-differential equation. In the above equation, the blackbody intensity (I_b) is obtained from the

temperature field and is initially unknown. It is obtained by solving the full energy equation considering all the other modes of heat transfer. Numerical solution to RTE can be obtained by methods discussed below.

• **Spherical Harmonic Method** (**SHM**) : It is also called P_N approximation where the subscript "N" shows the term after which the spherical harmonic series is truncated. The disadvantage of this method is that the lower order approximation P_1 is imprecise whereas higher order approximations (P_5, P_7) are difficult to solve, and also beyond this the computational efforts increase immensely. The lower order approximation P_1 computes accurate results for optically thick medium (optical thickness $\tau > 2$) only. However, the results from the P_1 approximation are found to be inaccurate for optically thin medium and is unable to produce results for ($\tau = 0$) surface to surface radiation case.

• **Monte Carlo Method** (**MCM**) : It is a statistical integration method which involves usage of random numbers based on a standard probability density function to simulate radiation process. The transformation and rejection are basically the two approaches used in Monte Carlo method where radiation is expressed as a bundle of discrete energy or photons. The results obtained using MCM are considered to have accuracy close to exact solutions owing to the statistical nature of this method. However, the computational expense associated with the MCM method is extremely high as it requires sampling of a large number of photons to get stable results.

• **Discrete Ordinates Method** (**DOM**) : Similar to spherical harmonic method, DOM is also known as (S_N) approximation method. It transforms the RTE into a set of a partial differential equation to an arbitrary order of approximation "N". The discrete ordinates method is a direction wise representation of radiative intensity where the partial differential equations are solved for a set of discrete directions covering the total solid angle (4π). The equations are solved for each ordinate direction where the angular integration is replaced by performing a summation over quadrature. One of the major difficulty with DOM is to address ray-effect.

• **Finite Volume Method** (**FVM**) : In case of finite volume method the entire spatial domain is discretized into a finite number of control volumes and the entire angular domain (4π) is discretized into finite non-overlapping solid angles. The RTE

is solved by integrating the entire equation over the control volume and solid angle. This method is also called as the finite volume in space and direction. Conceptually FVM method for radiation has the same philosophy for flow and hence it is easy to solve coupled convection-radiation problems. Additionally, this method can easily handle non-orthogonal meshes which makes it applicable to engineering problems.

• **Discrete Transfer Method** (**DTM**) : It is ray tracking method where the transport equation is integrated along a series of rays emanating from boundary faces. This method is used to compute radiative heat transfer between surface without view factor calculation. The model is found to be reasonably accurate by increasing the computational grid and the number of rays traced.

• **Lattice Boltzmann Method** (**LBM**) : LBM model is based on mesoscopic modeling as opposed to conventional CFD methods which involve macroscopic models. LBM model uses particle density distribution function for fictitious particles and performs streaming and collision processes to compute radiative intensity. The use of LBM has gained popularity in the recent past owing to its ease in performing parallel computation.

Among the above mentioned methods for numerical solutions of RTE, it is further noted that FVM, DOM, and LBM are easily compatible with the traditional methods for fluid flow. In particular, FVM is more popular due to its ease of solving complex geometry, conservative nature, and algorithmic simplicity. The major challenge in the numerical computations of coupled buoyancy driven flow with radiative heat transfer for large temperature difference applications is the consideration of compressibility effects. In general, an incompressible flow solver based on constant density advection, zero velocity divergence, and the Boussinesq approximation is a preferred choice for solving these class of problems. However, the use of Boussinesq assumption becomes ambiguous for problems encompassing large temperature difference radiative-convective heat transfer. The use of this approximation is limited to small density variations i.e. a relative temperature difference must be less than 10 %. This issue can be circumvented by the use of a non-Boussinesq flow solver which employs the low-Mach number formulation in regimes where Mach number is sufficiently small ($Ma < 0.3$) typical for buoyancy-driven flows. In these flow regimes, conventional compressible solvers require preconditioning techniques whereas the

low-Mach approximation eliminates the acoustic waves from the governing equations.

The present doctoral thesis focuses on the development of a generic FVM based three-dimensional numerical solver for computing accurate solutions of combined natural convection coupled with thermal radiative heat transfer both in laminar and turbulent regimes. In this regard, an exhaustive literature survey is presented followed by detailed research objectives in the following section.

1.4 Literature Review

The main aim of the present work is to present a robust numerical framework for accurate simulation of coupled convection with thermal radiation at large temperature difference. In this regard, studies on the development of unified solver capable of simulating both large and small temperature difference thermo-buoyant (laminar and turbulent) flow coupled with radiative heat transfer are undertaken. A detailed review of the literature on numerical methods for coupled convection and thermal radiation is presented with the applicability of the convective-radiative flows in several engineering processes.

1.4.1 Numerical methods for radiative heat transfer

A major requirement in devising a numerical method for the solution of radiative transfer equation was to share the same philosophy as for solving fluid flow using body-fitted irregular meshes. Pioneering work in this regard was done by Raithby and Chui [3] who proposed FVM for solving radiative heat transfer in participating media using an explicit method. Explicit schemes for solving RTE caused a rapid decrease in convergence rate. To overcome this, Chui and Raithby [4] proposed an implicit solution scheme to accelerate the convergence scheme. Using the philosophy of control volume method for fluid flow Chai et al. [5] proposed an FVM for absorbing, emitting and an-isotropically scattering media and presented the relative ease in capturing the collimated beams. Furthermore, Chai et al. [6] presented a blocked-off technique on a Cartesian grid for (curvilinear and inclined) geometries

by using a local spatial and angular grid refinement for computing accurate results. This work was further extended by Chai et al. [7] which dealt with body-fitted grids. The results showed good agreement when compared with the previous blocked-off-region method presented in [6]. For more precise calculation of a complex geometry, Chai and Moder [8] further presented a spatial multi-block method in contrast to the single block method. In this context, the multi-blocking technique was also studied by Talukdar et al. [9] for curvilinear grids, to deal with three-dimensional radiative heat transfer problem with radiative and non-radiative equilibrium.

The errors arising due to the spatial and angular discretization were presented by several researchers [10–14]. Raithby [10] highlighted that the spatial and angular discretization caused artificial spreading and ray concentration, respectively due to the nonoverlap of the control angles with the control volume faces. In this context, the errors associated with the spatial and angular discretization was further summarized and presented by Chai and Patankar [11]. They reported that the errors reduced by grid refinement. Byun et al. [12] presented the prediction of radiative heat transfer in complex geometries. The errors associated with the Cartesian grid system in the multi-block treatment are shown, especially in the non-orthogonal walls. Tan et al. [13] studied the ray effect and false scattering for thermal radiations by comparing with four different methods (FVM, DOM, DTM, and MCM). They observed that false scattering exists in FVM and DOM but not in DTM and MCM. They highlighted the superiority of FVM over other methods. Hunter and Guo [14] presented a technique for improving the anisotropic scattering in radiative heat transfer analysis. They introduced a phase function normalization technique and applied to three-dimensional problems involving anisotropic scattering in order to reduce false scattering errors.

1.4.2 Unstructured grid FVM formulation for radiation

Most of the industrial problems involving radiative heat transfer require calculations on irregular complex geometries. Many researchers [6–9, 12] treated the irregular geometries using body-fitted, blocked-off and multi-block Cartesian grids. For a complex geometry generating a Cartesian grid (single or multi-block) is time-consuming and problem like skewness is difficult to manage.

To overcome this difficulty, Chui and Raithby [15] extended the previous work [3] for computing radiative heat transfer on non-orthogonal meshes. They presented a node based scheme with the treatment of control angle overlap at the boundaries for two-dimensional cases. Further contributing to the work of Chui and Raithby [15], Baek et al. [16] presented a three-dimensional formulation for treating non-orthogonal meshes with a capability of handling the control angle overlap. To study radiative heat transfer in participating media Murthy and Mathur [17] presented a cell-based scheme on arbitrary polyhedral, unstructured meshes. Furthermore, a pixelation technique was introduced for treating the control angle overhang. Murthy and Mathur [18] extended the previous work for treating radiative heat transfer in semi-transparent media. They presented the treatment of Fresnel boundaries keeping into account the effects of reflection and refraction.

In this context, Raithby [19] presented a radiation model to the already existing unstructured grid FVM code. They compared the FVM using unstructured grids to the DOM and found the DOM method to be inconsistent in case of anisotropic scattering and violates conservation at the walls. Based on the work of Chui and Raithby [15], Asllanaj et al. [20] presented a new FVM for unstructured triangular meshes using a cell vertex scheme. They used a modified exponential scheme and marching order map for quick convergence in case of three-dimensional grids. In this context, Gazdallah et al. [21] developed an FVM to predict three-dimensional radiative heat transfer in a participating media and eliminated the need for a particular marching order. Kim et al. [22] used FVM on an unstructured grid for approximating solutions on geometries with obstacles and reported a considerable reduction in the wiggling behavior due to the blocked-off technique. Furthermore, Kim et al. [23] introduced polygonal unstructured meshes and reported a dramatic reduction in computational time with the same level of accuracy as obtained with the baseline triangular meshes.

Capdevila et al. [24] presented a comparative study of four spatial numerical schemes for higher resolution of the radiative transfer equation on three-dimensional unstructured grids. They observed that the use of a higher order scheme lead to the reduction in spatial error, whereas the errors in the angular discretization increased. Lygidakis and Nikolos [25] presented an improved method for solving unstructured hybrid grid based radiative heat transfer solver for reducing the false scattering and

improving the accuracy. They presented a second order spatial (MUSCL) scheme for conservation laws and second-order Runge-Kutta temporal scheme for evaluating radiative fluxes.

1.4.3 Coupled natural convection with thermal radiation

Most of the earlier research on simulating combined buoyancy induced flow with radiative heat transfer was in developing appropriate radiation models consistent with the flow. Use of FVM, DOM, P_N and LBM emerged as popular models for radiation which could be easily coupled with traditional methods for flow. Several studies on the influence of optical thickness, scattering albedo and Rayleigh number on combined convection with thermal radiation were performed by many researchers [26–28] using DOM in a two and three-dimensional enclosures. Yucel et al. [26] performed a comparative study between the DOM and P_1 approximation methods whereas, Lari et al. [27] highlighted the importance of thermal radiation on flow and temperature distribution even at room temperatures. Colomer et al. [28] studied the comparison of a two-dimensional case with three-dimensional simulation in a long rectangular enclosure to signify the three-dimensionality effects due to radiation. Fusegi et al. [29] studied compartment fires considering gas/soot radiation in a three-dimensional enclosure by using P_1 approximation and a weighted sum of the grey gas model.

Due to the ease in coupling the radiation with the flow, FVM has emerged as a popular method for studying buoyancy driven flows taking into account the influence of radiative heat transfer by several researchers [30–33]. Borjini et al. [30] performed a three-dimensional simulation to show the sensitivity of inner spiraling flows to radiation whereas the peripheral spiraling flow remained insensitive to it. Kumar and Eswaran [31] studied the influence of optical thickness using a variable density model on flow and heat transfer in a cubical enclosure, further Ming and Zhang [32] demonstrated the convection radiation interaction in enclosures with and without baffles for various Grashof and conduction-radiation parameters. Darbandi and Abrar [33] signify the importance of compressible formulation at large temperature difference convection coupled with thermal radiation in a two-dimensional differentially heated cavity.

The inherent advantage of LBM in terms of its simplicity and massive parallelizabil-

ity has fascinated researchers to perform coupled convection radiation studies using LBM. Mezrhab et al. [34, 35] performed studies on convection-thermal radiation interaction in cavities with the heated cylinder and partitions. They demonstrated the significance of wall emissivity, Rayleigh number and temperature difference on flow, temperature variation and Nusselt number variation. Furthermore, researchers like [36–38] used LBM for fluid flow and radiation for predicting double-diffusive convection, natural convection and its interaction with volumetric radiation in a two-dimensional differentially heated enclosures.

1.4.4 Non-Boussinesq models for coupled convection with radiation

In spite of numerous studies on combined radiation with natural convection, the Boussinesq approximation has been widely used for accounting the density changes due to the temperature difference. However, in the presence of significant temperature differences accompanied by thermal radiative heat transfer the Boussinesq approximation does not hold good. This issue can be circumvented by the use of non-Boussinesq flow solvers based on a low-Mach approximation as described in the work of Paolucci [39] and Rehm and Baum [40]. In these flow regimes, conventional compressible solvers require preconditioning techniques as described in the works of Turkel [41] and Paillere et al. [42]. The low-Mach approximation eliminates the acoustic waves from the governing equations and splits the total pressure into a spatially varying hydrodynamic pressure and time-varying but spatially invariant thermodynamic pressure.

The use of non-Boussinesq low-Mach number formulation is mostly limited to pure convection and reacting flows with heat transfer [43–50]. Nerinckx et al. [43] presented a coupled pressure and temperature algorithm based on Mach uniformity for separating the acoustic and convective phenomena using predictor, corrector method. Najm et al. [44] presented a zero Mach number model for numerical simulation of unsteady combustion. Clifton et al. [45] presented a semi-implicit scheme for numerical simulation of compressible flows using low-Mach number method. They demonstrated the efficacy of the developed method in removing the time step requirement on acoustic waves. Nicoud [46] presented a low-Mach number approxi-

mation of Navier-Stokes equation based on finite difference method using a fourth order accurate spatial and second order accurate temporal schemes. Sewall and Tifti [47] presented a time-accurate algorithm for simulation of variable property flows at large temperature difference. However, the proposed algorithm did not use low-Mach number formulation for simulation of unsteady Poiseuille-Benard flow at large temperature difference. Mary et al. [48] proposed an algorithm for simulating unsteady compressible flows using fully compressible Navier-Stokes equations. They highlighted the capability of the developed model for simulating incompressible flows at a wide range of subsonic Mach numbers. Bouloumou et al [49] presented a low-Mach-number approximation using a three-dimensional spectral method to simulate buoyancy driven flows at large temperature difference. They highlighted the three-dimensional effects compared to Boussinesq and non-Boussinesq convection beyond $Ra = 10^5$. Kumar and Natarajan [50] presented and comparison of low-Mach number algorithms for highlighting the discrete mass conservation error for unsteady and low Prandtl non-Boussinesq natural convection. Studies using non-Boussinesq solver for coupled radiation-convection interaction are limited and have been carried out only by few researchers [31, 33, 51–53].

1.4.5 Application of coupled convection with radiative heat transfer

The contribution of radiative heat transfer is quite significant for high-temperature engineering applications. Many researchers have studied the various applications of radiative heat transfer like combined radiation and natural convection, combined transient conduction and radiation, furnace design, water sprays, the design of combustion chamber etc.

Yan and Li [54] studied the radiation heat transfer effects combined with the laminar mixed convection inside an inclined square duct. Mahapatra et al. [55] also studied the effects of mixed convection in a two-sided differentially heated square cavity with radiation. They studied the effects of various parameters on fluid flow and heat transfer inside the enclosure.

Guedri et al. [56] studied the effect of radiative heat transfer in participating me-

dia for a square enclosure with multiple baffles and finned cylinder. They observed that baffles augment the radiative heat flux which enhanced the mean medium temperature. Hostikka and McGrattan [57] presented the modeling of radiative heat transfer for water spray application. They developed an effective model for simulating time-dependent fire scenarios using the Mie theory for computing scattering and absorption attributes associated with the water droplets. Ko and Anand [58] studied the flow and radiative heat transfer in a backward facing step for steady, laminar, incompressible flow. The variation of re-attachment length was studied for distinct radiative parameters along with the variation of thermal penetration for different optical thickness and scattering albedo. Abbassi et al. [59] presented a study of radiative heat transfer in two-dimensional pyrolysis chamber and heat recuperators. They studied the effect of diffuse and grey baffles in vertical, inclined and horizontal position with the motivation of increasing gas residence time and heat transfer.

Moreover, many researchers have applied the coupled convective-radiative heat transfer studies in three-dimensional enclosures. Adams et al. [60] performed a three-dimensional numerical simulation with the experimental comparison on arrays of heat protruding source between the enclosure walls and substrate. They concluded that the wall conductance and radiation reduce the overall convective heat transfer. Brandan et al. [61] studied natural ventilation in rooms with multiple heat source. They highlighted the inaccuracy of water-based model and concluded that exclusion of radiative heat transfer leads to an inaccurate prediction of temperature distributions. Martyushev and Sheremet [62] established relations for average convection and radiation Nusselt number in a three-dimensional enclosure with a heat source located at the base of the cavity. Their study highlighted the influence of natural convection with surface radiation. Kolsi et al. [63] studied the influence of radiative heat transfer on natural convection in a three-dimensional enclosure of variable aspect ratio. They demonstrated three-dimensionality of the flow in the presence of radiation and quasi-two-dimensional flow in the absence of radiation. Lei and Patterson [64] performed a direct numerical simulation to highlight the flow development and heat transfer in a three-dimensional shallow wedge under the influence of solar radiation induced natural convection.

Two-dimensional studies in square and complex shaped enclosures with and without the presence of partitioning walls and heated cylinders were performed by many

researchers [65–73]. They established that thermal radiation reduces the buoyancy assisted flow due to the increase in bulk temperature by radiation. They also highlighted that the effect of radiation is more perceptive to partitions due to the blockage of radiation. Ren et al. [74] investigated heat and pollutant transfer in partitioned enclosures with baffles at the right wall. They demonstrated enhanced heat and mass transfer rates beyond critical values of Rayleigh numbers. Rahimi and Sabernaeemi [75] performed experimental studies on free convection with radiation from the ceiling surface of a room. They concluded that radiation is the dominant mode of heat transfer from ceiling to other surfaces.

1.4.6 Turbulence radiation interaction in enclosures

The prior work in understanding the complex flow and heat transfer associated with turbulent buoyancy-induced flows includes the experimental investigations in a differentially heated enclosure. Researchers like [76–80] presented various benchmark data for statistical validation. The initial numerical investigations involved the work of Paolucci [81] and Le. Quéré [82] who performed two-dimensional direct numerical simulations in differentially heated square enclosures for Rayleigh numbers $Ra = 10^{10}$ using finite difference and a spectral method. Their work illustrated the presence of persistent turbulence at steady state as also observed in the experiments. Furthermore, researchers [83, 84] used a two-equation turbulence $(k - \varepsilon)$ model for studying natural convection in square cavities and presented reference solutions in a standard case of $Ra = 5 \times 10^{10}$ and further compared the results provided by ten different groups. They demonstrated excellent match for velocity profiles with experiments and mentioned the improvement in the wall heat transfer by the use of low-Reynolds number model. However, the deviations from experimental results were expected to be due to the presence of potential three-dimensional effects. In this regard comparison of two-dimensional and three-dimensional direct numerical simulations were performed by [85, 86]. Their comparison highlighted a similarity between the first order statistics whereas a substantial difference was observed for the second order statistics at larger Rayleigh numbers. They mentioned that two-dimensional simulations are a cheaper alternative for capturing the general flow and heat transfer up to $Ra = 10^{10}$.

Majority of the earlier studies on turbulent natural convection were carried out

without considering the influence of thermal radiation although many engineering applications necessitate the inclusion of these effects. Studies on turbulent natural convection in enclosures with the influence of thermal radiation were initially performed by several researchers [87–95]. Mesyngier and Farouk [87] presented correlation for Nusselt number in a single/mixture of participating gases using DO and WSGG methods. They demonstrated the enhancement of heat transfer due to the presence of H_2O. Researchers [88–91] studied the influence of surface radiation in many practical scenarios involving enclosures with varying aspect ratio, building fires, liquid metal fast breeder reactor and square cavity of varying angle of inclination. They highlighted the increased turbulence and velocity at the boundary layers due to the inclusion of surface radiation and proposed correlation for the Nusselt number. Xamán et al. [92, 93] studied the asymmetric flow and heat transfer in a square enclosure with glass walls, tall cavities with varying aspect ratio and wall emissivity to derive correlations for the Nusselt number in the laminar and turbulent flow regimes. In the similar lines, the influence of coupled turbulent natural convection with surface radiation was studied by [96–99] in a differentially heated square enclosure, a rectangular enclosure with a heat source, a square cavity with a heated energy source, and inclined square cavity with a heat generating source. They demonstrated the influence of wall emissivity in intensifying the convective flows and enhancing the overall heat exchange. Shati et al. [100] studied the turbulent flow and radiative heat transfer with temperature varying properties in square and rectangular enclosures and presented empirical correlations for the Nusselt number.

It is important to note that most of the studies delineated above were carried out solving RANS with two-equation turbulence models. However, researchers [101–103] proposed wall models for large eddy simulations by admitting the influence of thermal radiative heat transfer. They used the developed LES model to study the combined convection with thermal radiation (surface and gas) in an air-filled cavity to highlight the role of surface radiation in increasing the flow and turbulence intensity. Researchers [104–107] developed a sub-grid model for radiating gases and coupled it with a DNS model to simulate turbulent flows with radiative heat transfer. The coupled DNS and the sub-grid model was used to study the transitional and turbulent buoyancy driven flows with wall and gas radiation.

The majority of the numerical investigations on understanding the turbulent natural convection flows coupled with thermal radiative heat transfer in enclosures are constrained by an incompressible assumption based on Boussinesq approximation. Studies on the influence of variable properties (density, thermal conductivity, viscosity) in a turbulent natural convection heat transfer scenario are rare and performed by few researchers [108–111]. The work of Amel et al. [111] presents the entropy generation for variable density flows in turbulent plane jets. Zamora and Kaiser [108–110] studied the radiative heat transfer effects with the influence of variable properties on turbulent buoyancy driven flows in a square and open cavities. They also performed the comparison of deviation in the results with an incompressible model.

1.5 Motivation

A rigorous analysis of the literature review in the previous section reveals that in spite of numerous studies on combined radiation with natural convection, the majority of the studies have invoked an incompressible model based on Boussinesq approximation. The use of non-Boussinesq formulation is mostly limited to pure convection and reacting flows with heat transfer [43–50]. There have been minimal studies on the importance of non-Boussinesq models for studying convective heat transfer under the influence of thermal radiation. With this motivation, a non-Boussinesq low-Mach number formulation is presented for coupled solution of both small and large temperature difference natural convection with thermal radiation. Studies have been performed to explore the importance of non-Boussinesq models, the invalidity of Boussinesq approximation and its impact on numerical results for various scenarios concerning coupled buoyancy driven convection with thermal radiation. Furthermore, three algorithms are proposed and the importance of discretely handling the pressure and buoyancy term is emphasized with a motivation to provide a robust numerical framework for convective-radiative flows.

Many researchers [28–30] have reported that the influence of thermal radiation in buoyancy-driven convection leads to significant three-dimensionality effects necessitating genuinely three-dimensional numerical studies. However, most studies in

the past involving coupled natural convection with thermal radiation in partitioned enclosures [65–73] have primarily concentrated on the two-dimensional simulation for such configurations. The influence of partitions in three-dimensional combined convective-radiative flow has never been studied. Therefore, the topic requires immediate attention and forms the basis of the present work.

From the literature survey on turbulence radiation interaction in enclosures it is revealed that the majority of the numerical investigations on understanding the turbulent buoyancy driven flow coupled with thermal radiative heat transfer in enclosures are subjected to incompressible assumption. Studies on the influence of variable properties (density, thermal conductivity, viscosity) in a turbulent natural convection heat transfer scenario are rare and are performed by few researchers like [108–111]. The limited research on variable density turbulent buoyancy driven flows particularly at large temperature difference with thermal radiative heat transfer has motivated the present study. The present work describes turbulent natural convection flows coupled with thermal radiation in differentially heated enclosures at large temperature difference considering variable temperature dependent properties.

1.6 Research Objectives

In view of these gaps in the ongoing research presented in the previous section, the objectives of the present thesis have been framed as given below.

Solver development

The present work focuses on the development of a non-Boussinesq flow solver for simulating three-dimensional coupled convective-radiative heat transfer on arbitrary polygonal meshes using the ideas of low-Mach number asymptotes. A segregated approach for solving the governing equations using a fractional step methodology on finite-volume method is considered for handling the low-Mach number formulation. The accuracy of the developed low-Mach formulation in computing combined radiative-convective flows is investigated by performing several validation studies. Further, the need for non-Boussinesq or low-Mach number formulation is examined by performing studies for coupled natural convection with thermal radiation in en-

closures over a range of Gay-Lussac, Richardson, and Planck numbers.

Implementation of robust algorithm

After presenting details of the non-Boussinesq model, three-different low-Mach number algorithms are examined for numerical computation of radiative-convective flows. The three algorithms differ in the way they use the equation of state for computing either the density, temperature or thermodynamic pressure. Furthermore, the energy and mass conservation errors arising due to the use of temperature and density update algorithms is investigated by performing studies over a range of Rayleigh, Prandtl, and Planck numbers. Investigations on the role of balancing of the pressure and buoyancy terms are also performed for robust calculations of large temperature difference thermo-buoyant convection with radiative heat transfer.

Role of partitions on radiative-convective flows in enclosure

The developed numerical model is used to study the influence of partitions on buoyancy induced convection with thermal radiation in a differentially heated cubical enclosure. Four distinct arrangements of partitions from the top-bottom and front-back walls is examined by adopting a symmetric (in-line) and asymmetric (offset) configuration of partitions. Comparative analysis of average and local Nusselt number variation at the isothermal walls with irreversibilities associated with conduction, convection, and radiation heat transfer is studied to investigate all configurations of partitions. This study aims at achieving optimum thermal design (higher heat transfer rates with minimum entropy production) among all partition configurations.

Turbulence radiation interaction in non-Boussinesq flows

The computational framework is extended for considering buoyancy-driven turbulent natural convection with and without the influence of thermal radiation in a differentially heated square cavity at large temperature difference. The impact of surface and gas radiation on overall flow dynamics and heat transfer is discussed by performing comparisons with a classic natural convection case at Rayleigh number $Ra = 10^{10}$. This study also aims at quantifying the deviations between the proposed variable density low-Mach number model and popularly used incompressible model.

1.7 Overview of the Thesis

The present work is based on the development and application of low-Mach number formulation for laminar and turbulent buoyancy induced flows coupled with radiative heat transfer.

A low-Mach number formulation for laminar and turbulent natural convection flows coupled with thermal radiation is presented in chapter 2. Furthermore, a detailed discretization of the governing equations is presented on three-dimensional unstructured polyhedral meshes using FVM.

Chapter 3 presents a detailed validation study comprising of pure radiative heat transfer in absorbing, emitting and scattering medium for various two-and three-dimensional geometries. In addition, validation studies are also presented for pure convection at large temperature difference, coupled natural convection with surface and gas radiation. Finally, validation studies on turbulent natural convection are presented using experimental and numerical benchmark data.

Chapter 4 describes the importance of non-Boussinesq models for simulation of coupled radiative-convective flows. This is achieved by highlighting the invalidity of Boussinesq approximation in such scenario.

After validating the proposed non-Boussinesq model, three-different low-Mach number algorithms are presented to examine their performance for simulating coupled convection with radiation in chapter 5. The significance of energy and mass conservation errors arising due to the use of update based algorithm is highlighted by performing investigations over a range of Rayleigh, Prandtl, and Planck numbers.

Chapter 6 describes the influence of partitions on buoyancy induced convection with thermal radiation in a differentially heated cubical enclosure. Four distinct arrangements of partitions from the top-bottom and front-back walls typically encountered in an industrial furnace and high rise buildings are studied. The results from the present work describe an offset configuration with front-back partitions as the optimum thermal design (higher heat transfer rates with minimum entropy production) among all partition configurations.

Chapter 7 presents the turbulence radiation interaction in a differentially heated cavity at large temperature difference. This study aims at presenting solutions for non-Boussinesq turbulent flows under the influence of thermal radiation at high Rayleigh number.

Finally, the work is concluded by presenting the outcomes with possible scope for future in chapter 8.

Chapter 2

Mathematical Formulation and Discretization

2.1 Introduction

The development of a variable-density flow solver for simulating (laminar and turbulent) combined radiative-convective flow and heat transfer is presented for arbitrary polygonal meshes using the ideas of low-Mach number asymptotes. A segregated approach for solving the governing equations using a fractional step methodology is presented on finite volume method. A two-equation k-ε turbulence model is employed using Favre-averaged Navier-Stokes equations for handling the turbulent flow regimes. The cell arrangement reflects a collocated framework, where the pressure-velocity decoupling is tackled using momentum interpolation due to Rhie and Chow [112]. A class of SIMPLE algorithm utilizes a face-based data structure in conjunction with a semi-implicit method following the work of Dalal et al. [113]. The numerical model for simulation of RTE on unstructured FVM is in accordance with the work of Murthy and Mathur [114]. The solver has second order spatial and temporal accuracy by employing a high-resolution scheme CUBISTA and central differencing scheme for computation of convective and diffusive fluxes respectively. A backward difference scheme is used for temporal discretization while the gradients are calculated using a modified variant of Green-Gauss.

2.2 Governing Equations

In this section, the governing equations are presented for laminar and turbulent flows coupled with thermal radiative heat transfer. The turbulent regimes are handled using the k-ε turbulence model using Favre-averaged Navier-Stokes equations. Further, the low-Mach number formulation of laminar and turbulent Favre-averaged Navier-Stokes equations are presented in detail.

2.2.1 Governing equations for laminar flow

The dimensional form of Navier-Stokes, energy, transient radiative transfer equation (TRTE) and the equation of state (EOS) are presented as below.

$$\frac{\partial \rho}{\partial t} + \frac{\partial \left(\rho u_j\right)}{\partial x_j} = 0 \tag{2.1}$$

$$\frac{\partial \left(\rho u_i\right)}{\partial t} + \frac{\partial \left(\rho u_i u_j\right)}{\partial x_j} = -\frac{\partial p}{\partial x_i} + \frac{\partial \tau_{ij}}{\partial x_j} + \rho g_i \tag{2.2}$$

$$\frac{\partial \left(\rho c_p T\right)}{\partial t} + \frac{\partial \left(\rho T c_p u_j\right)}{\partial x_j} = \frac{\partial}{\partial x_j}\left(\kappa \frac{\partial T}{\partial x_j}\right) + \frac{\partial p}{\partial t} + \frac{\partial \left(p u_j\right)}{\partial x_j} + \frac{\partial q_{rj}}{\partial x_j} \tag{2.3}$$

$$\frac{\partial I\left(\mathbf{r},\mathbf{s}\right)}{\partial t}\frac{1}{c} + \frac{\partial I\left(\mathbf{r},\mathbf{s}\right)}{\partial s} = \kappa_a I_b\left(\mathbf{r}\right) - \kappa_a I\left(\mathbf{r},\mathbf{s}\right) - \sigma_s I\left(\mathbf{r},\mathbf{s}\right) + \frac{\sigma_s}{4\pi}\int_{4\pi} I\left(\mathbf{r},\mathbf{s}_i\right)\Phi\left(\mathbf{s}_i,\mathbf{s}\right)\mathrm{d}\Omega_i \tag{2.4}$$

$$p = \rho r T \tag{2.5}$$

In the above equations κ is the thermal conductivity, κ_a and σ_s are known as the absorption and scattering coefficient and c is the speed of light. $I(\mathbf{r},\mathbf{s})$ is the intensity at any location $\mathbf{r}$ along the direction $\mathbf{s}$ and $\Phi(\mathbf{s}_i,\mathbf{s})$ is the scattering phase function. Equation (2.3) represents the energy conservation equation where the last term represents the divergence of radiative heat flux, which can be calculated as $\frac{\partial q_{rj}}{\partial x_j} = \kappa_a\left(4\pi I_b - G\right)$. I_b represents the blackbody intensity and G is the irradiation evaluated as $G = \int_{4\pi} I \mathrm{d}\Omega$. It can be seen that the evaluation of radiative heat transfer source term in the energy equation Eq. (2.3) requires calculation of intensity I which is obtained by solving Eq. (2.4). The first term in the LHS of Eq.

(2.4) represents the temporal term, this term is usually neglected for obtaining the solution to the transport equation for radiative heat transfer, as the photons propagate through the speed of light. However, several applications like the short-pulsed laser, pulsed laser in turbid media, material processing, and living tissues require the solution to transient radiative heat transfer. In the present study, the transient nature of radiative heat transfer is neglected. The first term on the RHS of Eq. (2.4) represents the augmentation of radiant energy by emission, while the second and third term represents the attenuation of energy by absorption and scattering respectively. The last term represents in-scattering. At high temperature and low pressure, most of the gases behave as ideal fluids governed by Eq. (2.5). Here, r is a gas constant defined as $r = \frac{R}{M}$, R is the universal gas constant and its value is $R = 8.31$ J.K^{-1}mol^{-1} and M is the molecular mass (kg.mol^{-1}).

2.2.2 Governing equations for turbulent flow

The turbulence modeling for compressible flows requires the consideration of density fluctuations in addition to velocity and pressure fluctuations. In this context, Favre suggested a density weighted averaging procedure unlike Reynolds averaging which simplifies the equations.

$$\widetilde{u}_i = \frac{1}{\bar{\rho}} \int_t^{t+T} \rho\left(x,\tau\right) u_i\left(x,\tau\right) d\tau \tag{2.6}$$

where $\bar{\rho}$ denotes the Reynolds averaged density. According to Favre averaging

$$\phi_i = \widetilde{\phi}_i + \phi_i'' \tag{2.7}$$

where $\widetilde{\phi}_i$ is the Favre averaged mean component and ϕ_i'' is fluctuating component. After applying the Favre averaging, the equations for mass, momentum and energy conservation reduce to

$$\frac{\partial \overline{\rho}}{\partial t} + \frac{\partial}{\partial x_j}\left(\overline{\rho}\widetilde{u}_j\right) = 0 \tag{2.8}$$

$$\frac{\partial}{\partial t}\left(\overline{\rho}\widetilde{u}_i\right) + \frac{\partial}{\partial x_j}\left(\overline{\rho}\widetilde{u}_j\widetilde{u}_i\right) = -\frac{\partial \overline{p}}{\partial x_i} + \frac{\partial}{\partial x_j}\left[\tau_{ji} - \overline{\rho u_i'' u_j''}\right] + \overline{\rho} g_i \tag{2.9}$$

$$\frac{\partial}{\partial t}\left(\overline{\rho}c_p\widetilde{T}\right)+\frac{\partial}{\partial x_j}\left(\overline{\rho}c_p\widetilde{u}_j\widetilde{T}\right)=\frac{\partial\overline{p}}{\partial t}+\frac{\partial\left(\widetilde{u}_j\overline{p}\right)}{\partial x_j}+\frac{\partial}{\partial x_j}\left(\kappa\frac{\partial\widetilde{T}}{\partial x_j}\right)$$

$$-\frac{\partial}{\partial x_j}\left(\overline{\rho c_p u_j^{''}T^{''}}\right)+\frac{\partial\overline{q_{rj}}}{\partial x_j} \tag{2.10}$$

where

$$\tau_{ij}=\mu\left(\frac{\partial\widetilde{u}_i}{\partial x_j}+\frac{\partial\widetilde{u}_j}{\partial x_i}-\frac{2}{3}\frac{\partial\widetilde{u}_k}{\partial x_k}\delta_{ij}\right) \tag{2.11}$$

Boussinesq hypothesis is used to express the Reynolds stress tensor in terms of the mean strain rate tensor while the fluctuation term in the energy equation is modelled as.

$$-\overline{\rho u_i^{''}u_j^{''}}=\mu_t\left(\frac{\partial\widetilde{u}_i}{\partial x_j}+\frac{\partial\widetilde{u}_j}{\partial x_i}-\frac{2}{3}\frac{\partial\widetilde{u}_k}{\partial x_k}\delta_{ij}\right)-\frac{2}{3}\overline{\rho}k\delta_{ij} \tag{2.12}$$

$$-\overline{\rho c_p u_j^{''}T^{''}}=-\frac{c_p\mu_t}{pr_t}\frac{\partial\widetilde{T}}{\partial x_j} \tag{2.13}$$

The equations for turbulent kinetic energy (k) and turbulent kinetic energy dissipation rate (ε) with RTE and EOS are defined as

$$\frac{\partial}{\partial t}\left(\overline{\rho}k\right)+\frac{\partial}{\partial x_j}\left(\overline{\rho}\widetilde{u}_jk\right)=\frac{\partial}{\partial x_j}\left(\left(\mu+\frac{\mu_t}{\sigma_k}\right)\frac{\partial k}{\partial x_j}\right)+P_k+G_k-\overline{\rho}\varepsilon \tag{2.14}$$

$$\frac{\partial}{\partial t}\left(\overline{\rho}\varepsilon\right)+\frac{\partial}{\partial x_j}\left(\overline{\rho}\widetilde{u}_j\varepsilon\right)=\frac{\partial}{\partial x_j}\left(\left(\mu+\frac{\mu_t}{\sigma_\varepsilon}\right)\frac{\partial\varepsilon}{\partial x_j}\right)+\left[c_{\varepsilon1}\left(P_k+c_{\varepsilon3}G_k\right)\right]\frac{\varepsilon}{k}$$

$$-c_{\varepsilon2}\overline{\rho}\frac{\varepsilon^2}{k}-c_{\varepsilon4}\overline{\rho}\varepsilon\frac{\partial\widetilde{u}_j}{\partial x_j} \tag{2.15}$$

$$\frac{\partial I\left(\mathbf{r},\mathbf{s}\right)}{\partial s}=\kappa_a\overline{I_b}\left(\mathbf{r}\right)-\kappa_aI\left(\mathbf{r},\mathbf{s}\right)-\sigma_sI\left(\mathbf{r},\mathbf{s}\right)+\frac{\sigma_s}{4\pi}\int_{4\pi}I\left(\mathbf{r},\mathbf{s}_i\right)\Phi\left(\mathbf{s}_i,\mathbf{s}\right)\mathrm{d}\Omega_i \tag{2.16}$$

$$\overline{p}=\overline{\rho}\,r\,\widetilde{T} \tag{2.17}$$

where

- $\mu_{eff} = \mu + \dfrac{\mu_t}{\sigma_\kappa}$, σ_κ is model constant (listed in Table 2.1).
- P_k is production of turbulent kinetic energy.

$$P_k = \frac{\mu_t}{\rho}\left[\left(\frac{\partial \overline{u_i}}{\partial x_j} + \frac{\partial \overline{u_j}}{\partial x_i}\right)\frac{\partial \overline{u_i}}{\partial x_j}\right] = \frac{\mu_t}{\rho}S^2 \tag{2.18}$$

  $S^2 = 2S_{ij}S_{ij}$, where S_{ij} is strain rate tensor.

- G_k is a buoyancy production of turbulent kinetic energy.

$$G_k = g\frac{\mu_t}{\overline{\rho}\sigma_T}\frac{\partial \overline{\rho}}{\partial y}$$

- $\sigma_\epsilon, C_{\epsilon 1}, C_{\epsilon 2}, C_{\epsilon 3}, C_{\epsilon 4}$ are model constants presented in Wilcox [115]. All these values are listed in Tables 2.1.

Table 2.1: Model constant used in $k-\varepsilon$ model

Model	c_μ	σ_k	σ_ϵ	$C_{\epsilon 1}$	$C_{\epsilon 2}$	$C_{\epsilon 4}$
Standard k-ε	0.09	1.0	1.3	1.44	1.92	0.33

It is important to note that the interaction between turbulence and radiation is tackled by evaluating a time-averaged radiative source term in the energy equation defined as

$$\overline{\nabla \cdot \mathbf{q}_r} = \overline{\kappa_a\left(4\pi I_b(\mathbf{s}) - \int_{4\pi} I(\mathbf{s}_i)\mathrm{d}\Omega_i\right)} = 4\pi\overline{\kappa_a I_b}(\mathbf{s}) - \int_{4\pi}\overline{\kappa_a I}(\mathbf{s}_i)\mathrm{d}\Omega_i \tag{2.19}$$

Furthermore, turbulence moments are required in order to establish a co-relation between absorption coefficient and radiative intensity $\overline{\kappa_a I_b}$. Traditional RANS based models are ineffective in evaluating the correlation thus the significance of turbulent fluctuations in radiative properties, radiative intensity, and black-body intensity are generally neglected. The calculations are based on time-averaged variables in order to accommodate the radiative heat transfer effects. For a gray medium with a constant value of absorption coefficient, the turbulence radiation interaction is evaluated as $\overline{\kappa_a I_b} = \kappa_a \frac{\overline{E_b}}{\pi}$, where

$$\overline{E_b} = \frac{1}{\delta t}\int_{\delta t}\sigma T^4 dt \tag{2.20}$$

Furthermore,

$$T(x,y,z,t) = \overline{T}(x,y,z,t) + T'(x,y,z,t),\ \overline{T'} = 0 \tag{2.21}$$

Approximating E_b by a truncated Taylor series as

$$E_b \approx E_b(\overline{T}) + T'\frac{dE_b}{d\overline{T}} + \frac{1}{2}(T')^2\frac{d^2E_b}{d\overline{T}^2} + O(T')^3 \tag{2.22}$$

Further, the time averaging of Eq. 2.22 gives,

$$\overline{E_b} \approx E_b(\overline{T}) + \frac{1}{2}\overline{(T')^2}\frac{d^2E_b}{d\overline{T}^2} = \sigma\overline{T}^4\left[1 + 6\frac{\overline{(T')^2}}{\overline{(T)^2}}\right] \tag{2.23}$$

Equation (2.23) is called the temperature self-correlation, the above equation signifies that the turbulence-radiation interaction results in enhanced emission. However, it has been previously shown by Mazumder and Modest [116] that turbulence radiation interaction is not much significant for non-reacting flows and inclusion of temperature fluctuations do not increase the radiative source by more than 10 %. Along the similar lines, the influence of turbulent fluctuations on the radiative heat transfer was neglected by Zhang et al. [101] and Ibrahim et al. [103] for studying turbulent buoyancy driven flow coupled with radiative heat transfer in a square cavity. Hence, the influence of turbulent fluctuations on radiative heat transfer is neglected in the present study.

2.3 Low-Mach Number Formulation

The low-Mach number formulation for simulation of laminar and turbulent buoyancy driven flow coupled with thermal radiative heat transfer depends upon the decoupling of acoustic and flow velocity. A detailed formulation is illustrated by following the methodology presented by Paolucci [39]. The governing equations with low-Mach number formulation are derived by considering the governing equations for laminar flows (Eqs. (2.1) - (2.4)) and turbulent flows (Eqs. (2.8) - (2.15)). These equations are non-dimensionalized by using reference values of l, l/U, p_0, c_0, T_0, and ρ_0 for length, time, pressure, velocity, temperature and density, respectively. Here, U and c_0 represent the fluid speed and speed of sound. Furthermore, U^2 and $\frac{\rho_o U^4}{\mu_o}$ are used for rescaling the turbulent kinetic energy (k) and dissipation rate (ε), respectively. The non-dimensional form of governing equations for conservation of mass, momentum, and energy for laminar flows are reduced to equations as follows.

$$\frac{\partial \rho}{\partial t} + \frac{1}{Ma}\frac{\partial (\rho u_j)}{\partial x_j} = 0 \tag{2.24}$$

$$\frac{\partial (\rho u_i)}{\partial t} + \frac{1}{Ma}\frac{\partial (\rho u_j u_i)}{\partial x_j} = -\frac{1}{\gamma Ma}\frac{\partial p}{\partial x_i} + \frac{1}{Re}\frac{\partial \tau_{ij}}{\partial x_j} + \frac{Ma}{Fr}\rho g_i \tag{2.25}$$

$$\frac{\partial (\rho\, c_p T)}{\partial t} + \frac{1}{Ma}\frac{\partial (\rho\, T\, c_p\, u_j)}{\partial x_j} = \frac{1}{Pe}\frac{\partial}{\partial x_j}\left(\kappa \frac{\partial T}{\partial x_j}\right) \tag{2.26}$$

$$+ \frac{\tau}{N\, Re\, Pr}\frac{\partial q_{rj}}{\partial x_j} + \frac{\gamma - 1}{Re}\left(\tau_{ij}\frac{\partial u_i}{\partial x_j}\right) + \frac{\gamma - 1}{\gamma}\left(\frac{\partial p}{\partial t} + \frac{1}{Ma}\frac{\partial (p u_j)}{\partial x_j}\right)$$

The radiative heat transfer source term in Eq. (2.26) is obtained by solving the RTE.

$$\frac{1}{\tau}\frac{\partial I(\mathbf{r}, \mathbf{s})}{\partial s} = (1 - \omega) I_b(\mathbf{r}) - I(\mathbf{r}, \mathbf{s}) + \frac{\omega}{4\pi}\int_{4\pi} I(\mathbf{r}, \mathbf{s}_i)\Phi(\mathbf{s}_i, \mathbf{s})\, \mathrm{d}\Omega_i \tag{2.27}$$

with the dimensionless EOS being

$$\overline{p} = \rho T \tag{2.28}$$

The non-dimensional form of the Favre-averaged continuity, momentum, and energy equations are reduced to equations as follows.

$$\frac{\partial \overline{\rho}}{\partial t} + \frac{1}{Ma}\frac{\partial}{\partial x_j}(\overline{\rho}\widetilde{u}_j) = 0 \tag{2.29}$$

$$\frac{\partial}{\partial t}(\overline{\rho}\widetilde{u}_i) + \frac{1}{Ma}\frac{\partial}{\partial x_j}(\overline{\rho}\widetilde{u}_j\widetilde{u}_i) = -\frac{1}{\gamma Ma}\frac{\partial \overline{p}}{\partial x_i} + \frac{1}{Re}\frac{\partial}{\partial x_j}\left[\tau_{ji} - \overline{\rho u_i'' u_j''}\right] + \frac{Ma}{Fr}\overline{\rho} g_i \tag{2.30}$$

$$\frac{\partial}{\partial t}\left(\overline{\rho} c_p \widetilde{T}\right) + \frac{1}{Ma}\frac{\partial}{\partial x_j}\left(\overline{\rho} c_p \widetilde{u}_j \widetilde{T}\right) = \frac{\gamma - 1}{\gamma}\left(\frac{\partial \overline{p}}{\partial t} + \frac{1}{Ma}\frac{\partial (\widetilde{u}_j \overline{p})}{\partial x_j}\right) + \frac{1}{Pe}\frac{\partial}{\partial x_j}\left(\kappa \frac{\partial \widetilde{T}}{\partial x_j}\right)$$

$$-\frac{1}{Pe}\frac{\partial}{\partial x_j}\left(\overline{\rho c_p u_j'' T''}\right) + \frac{\gamma - 1}{Re}\tau_{ij}\frac{\partial \widetilde{u}_i}{\partial x_j} + \frac{\tau}{N\ Re\ Pr}\frac{\partial q_{rj}}{\partial x_j} \tag{2.31}$$

The equations for turbulent kinetic energy (k) and turbulent kinetic energy dissipation rate (ε) are reduced to

$$\frac{\partial}{\partial t}\left(\overline{\rho}k\right)+\frac{1}{Ma}\frac{\partial}{\partial x_j}\left(\overline{\rho}\widetilde{u}_j k\right)=\frac{1}{Re}\frac{\partial}{\partial x_j}\left(\left(\mu+\frac{\mu_t}{\sigma_k}\right)\frac{\partial k}{\partial x_j}\right)+\frac{1}{Ma^2\,Re}P_k$$

$$+\frac{1}{Re\;Fr}G_k-Re\,\overline{\rho}\varepsilon \tag{2.32}$$

$$\frac{\partial}{\partial t}\left(\overline{\rho}\varepsilon\right)+\frac{1}{Ma}\frac{\partial}{\partial x_j}\left(\overline{\rho}\widetilde{u}_j\varepsilon\right)=\frac{1}{Re}\frac{\partial}{\partial x_j}\left(\left(\mu+\frac{\mu_t}{\sigma_\varepsilon}\right)\frac{\partial \varepsilon}{\partial x_j}\right)-\frac{Re}{Ma^2}c_{\varepsilon 2}\overline{\rho}\frac{\varepsilon^2}{k}$$

$$+c_{\varepsilon 1}\left[\frac{1}{Ma^2\;Re}P_k+\frac{Ma^2}{Re\;Fr}c_{\varepsilon 3}G_k\right]\frac{\varepsilon}{k}-\frac{1}{Ma}c_{\varepsilon 4}\overline{\rho}\varepsilon\frac{\partial\widetilde{u}_j}{\partial x_j} \tag{2.33}$$

Here P_k and G_k are the production of turbulent kinetic energy and buoyancy term, respectively. These terms are expressed as

$$P_k=\mu_t\left(\left(\frac{\partial\widetilde{u}_i}{\partial x_j}+\frac{\partial\widetilde{u}_j}{\partial x_i}\right)\frac{\partial\widetilde{u}_i}{\partial x_j}-\frac{2}{3}\left(\frac{\partial\widetilde{u}_l}{\partial x_l}\right)^2\right)-Ma\,Re\frac{2}{3}\overline{\rho}\,k\,\frac{\partial\widetilde{u}_l}{\partial x_l}$$

$$G_k=g\frac{\mu_t}{\overline{\rho}\sigma_T}\frac{\partial\overline{\rho}}{\partial y} \tag{2.34}$$

The Reynolds stress tensor and the turbulent heat flux are approximated using the Boussinesq hypothesis $-\overline{\rho u_i'' u_j''}=\mu_t\left(\frac{\partial\widetilde{u}_i}{\partial x_j}+\frac{\partial\widetilde{u}_j}{\partial x_i}-\frac{2}{3}\frac{\partial\widetilde{u}_k}{\partial x_k}\delta_{ij}\right)-\frac{Re}{Ma}\frac{2}{3}\rho k\delta_{ij}$ and Reynolds analogy $-\overline{\rho c_p u_j'' T''}=\frac{\mu_t c_p}{Pr_t}\frac{\partial\widetilde{T}}{\partial x_j}$, respectively. The dimensionless parameters appearing in the governing equations are

$$Ma=\frac{U}{c_0},\;Re=\frac{\rho_0 U l}{\mu_0},\;Fr=\frac{U^2}{g_0 l},\;Pe=\frac{\rho_0 c_{p0} U l}{\kappa_0},$$

$$\gamma=\frac{c_{p0}}{c_{v0}},\;N=\frac{\kappa_0\beta}{4\sigma T_0^3},\;\tau=\beta l,\beta=\kappa_a+\sigma_s,\;\omega=\frac{\sigma_s}{\beta} \tag{2.35}$$

Since the Mach number (Ma) involved for flows in enclosures are very small, Ma acts as a small parameter. Following the work of Paolucci [39], all variables are expanded in terms of Ma as given below.

$$\begin{aligned}
&u_i=Ma\left[u_i^{(0)}+Ma^2u_i^{(1)}+o\left(Ma^2\right)\right],\;T=T^{(0)}+Ma^2T^{(1)}+o\left(Ma^2\right)\\
&\rho=\rho^{(0)}+Ma^2\rho^{(1)}+o\left(Ma^2\right),\;p=p^{(0)}+Ma^2p^{(1)}+o\left(Ma^2\right)\\
&k=k^{(0)}+Ma^2k^{(1)}+o\left(Ma^2\right),\;\varepsilon=\varepsilon^{(0)}+Ma^2\varepsilon^{(1)}+o\left(Ma^2\right)\\
&I=I^{(0)}+Ma^2I^{(1)}+o\left(Ma^2\right)
\end{aligned} \tag{2.36}$$

Substituting Eq. (2.36) in Eqs. (2.24)-(2.33) results in the $O(1)$ and $O(Ma^2)$ governing conservation equations for mass, momentum, energy, RTE, EOS, and turbulent transport k-ε equations. It is seen that the leading part of the pressure is time dependent ($\frac{\partial p^{(0)}}{\partial x_i} = 0$) while the spatially varying (background) pressure $p^{(1)}(x_i, t)$ is very small in comparison to the static pressure $p^{(0)}(t)$. The total pressure can be expressed as time varying spatially invariant thermodynamic pressure $\overline{P}(t)$ and spatially varying hydrodynamic pressure $p(x_i, t)$. Furthermore, neglecting the $O(Ma^2)$ terms in the mass, energy, RTE, EOS and k-ε equations and reinstating the various scales for variables, the leading order governing equations are obtained in dimensional form expressed below.

$$\frac{\partial \rho}{\partial t} + \frac{\partial \left(\rho u_j\right)}{\partial x_j} = 0 \tag{2.37}$$

$$\frac{\partial \left(\rho u_i\right)}{\partial t} + \frac{\partial \left(\rho u_i u_j\right)}{\partial x_j} = -\frac{\partial p}{\partial x_i} + \frac{\partial \tau_{ij}}{\partial x_j} + \left(\rho - \rho_o\right) g_i \tag{2.38}$$

$$\frac{\partial \left(\rho\, c_p T\right)}{\partial t} + \frac{\partial \left(\rho\, T\, c_p\, u_j\right)}{\partial x_j} = \frac{\partial}{\partial x_j}\left(k \frac{\partial T}{\partial x_j}\right) + \frac{d\overline{P}}{dt} + \frac{\partial q_{rj}}{\partial x_j} \tag{2.39}$$

$$\frac{\partial I\left(\mathbf{r}, \mathbf{s}\right)}{\partial s} = \kappa_a I_b\left(\mathbf{r}\right) - \kappa_a I\left(\mathbf{r}, \mathbf{s}\right) - \sigma_s I\left(\mathbf{r}, \mathbf{s}\right) + \frac{\sigma_s}{4\pi} \int_{4\pi} I\left(\mathbf{r}, \mathbf{s}_i\right) \Phi\left(\mathbf{s}_i, \mathbf{s}\right) \mathrm{d}\Omega_i \tag{2.40}$$

$$\overline{P} = \rho r T \tag{2.41}$$

The governing equations for turbulent flows in dimensional form after low-Mach number formulation are expressed below.

$$\frac{\partial \overline{\rho}}{\partial t} + \frac{\partial}{\partial x_j}\left(\overline{\rho}\widetilde{u}_j\right) = 0 \tag{2.42}$$

$$\frac{\partial}{\partial t}\left(\overline{\rho}\widetilde{u}_i\right) + \frac{\partial}{\partial x_j}\left(\overline{\rho}\widetilde{u}_j\widetilde{u}_i\right) = -\frac{\partial \overline{p}}{\partial x_i} + \frac{\partial}{\partial x_j}\left[\tau_{ji} - \overline{\rho u_i'' u_j''}\right] + \overline{\rho} g_i \tag{2.43}$$

$$\frac{\partial}{\partial t}\left(\overline{\rho} c_p \widetilde{T}\right) + \frac{\partial}{\partial x_j}\left(\overline{\rho} c_p \widetilde{u}_j \widetilde{T}\right) = \frac{d\overline{P}}{dt} + \frac{\partial}{\partial x_j}\left(\kappa \frac{\partial \widetilde{T}}{\partial x_j} - \overline{\rho c_p u_j'' T''}\right) + \frac{\partial \overline{q_{rj}}}{\partial x_j} \tag{2.44}$$

$$\frac{\partial}{\partial t}\left(\overline{\rho}k\right)+\frac{\partial}{\partial x_j}\left(\overline{\rho}\widetilde{u}_j k\right)=\frac{\partial}{\partial x_j}\left(\left(\mu+\frac{\mu_t}{\sigma_k}\right)\frac{\partial k}{\partial x_j}\right)+P_k+G_k-\overline{\rho}\varepsilon \tag{2.45}$$

$$\frac{\partial}{\partial t}\left(\overline{\rho}\varepsilon\right)+\frac{\partial}{\partial x_j}\left(\overline{\rho}\widetilde{u}_j\varepsilon\right)=\frac{\partial}{\partial x_j}\left(\left(\mu+\frac{\mu_t}{\sigma_\varepsilon}\right)\frac{\partial \varepsilon}{\partial x_j}\right)+\left[c_{\varepsilon 1}\left(P_k+c_{\varepsilon 3}G_k\right)\right]\frac{\varepsilon}{k}$$

$$-c_{\varepsilon 2}\overline{\rho}\frac{\varepsilon^2}{k}-c_{\varepsilon 4}\overline{\rho}\varepsilon\frac{\partial \widetilde{u}_j}{\partial x_j} \tag{2.46}$$

$$\overline{P}=\overline{\rho}\,r\,\widetilde{T} \tag{2.47}$$

$$\frac{\partial I\left(\mathbf{r},\mathbf{s}\right)}{\partial s}=\kappa_a\overline{I_b}\left(\mathbf{r}\right)-\kappa_a I\left(\mathbf{r},\mathbf{s}\right)-\sigma_s I\left(\mathbf{r},\mathbf{s}\right)+\frac{\sigma_s}{4\pi}\int_{4\pi} I\left(\mathbf{r},\mathbf{s}_i\right)\Phi\left(\mathbf{s}_i,\mathbf{s}\right)\mathrm{d}\Omega_i \tag{2.48}$$

The dimensionless form of the governing equations for laminar and turbulent buoyancy driven flows is obtained by using suitable rescaling parameters as.

$$x_i^\star=\frac{x}{H},s^\star=\frac{s}{H},\rho^\star=\frac{\rho}{\rho_0},u_i^\star=\frac{u_i}{u_0},p^\star=\frac{p-P_0}{\rho_0 u_0^2},t^\star=\frac{tu_0}{H},\overline{P^\star}=\frac{\overline{P}}{\overline{P_0}},$$

$$\overline{P_0}=101325\text{ Pa},T^\star=\frac{T-T_c}{T_h-T_c},\rho_0=\frac{\overline{P_0}}{rT_0},I^\star=\frac{I}{I_0},I_0=\sigma T_0^4,$$

$$u_0=\sqrt{\beta g H(T_h-T_c)},k^\star=\frac{k}{u_0^2},\varepsilon^\star=\frac{\mu_0\varepsilon}{\rho_0 u_0^4},\mu^\star=\frac{\mu}{\mu_0},\kappa^\star=\frac{\kappa}{\kappa_0} \tag{2.49}$$

The non-dimensional form of the governing equations for laminar flow, RTE and EOS are presented below by dropping the superscripts for preventing overloaded symbols.

$$\frac{\partial \rho}{\partial t}+\frac{\partial\left(\rho u_j\right)}{\partial x_j}=0 \tag{2.50}$$

$$\frac{\partial\left(\rho u_i\right)}{\partial t}+\frac{\partial\left(\rho u_i u_j\right)}{\partial x_j}=-\frac{\partial p}{\partial x_i}+\sqrt{\frac{Pr}{Ra}}\frac{\partial \tau_{ij}}{\partial x_j}+\frac{1}{Ga}\left(1-\rho\right)\hat{\mathbf{e}}_\mathbf{y} \tag{2.51}$$

$$\frac{\partial(\rho T)}{\partial t}+\frac{\partial(\rho T\, u_j)}{\partial x_j}=\frac{1}{\sqrt{Ra\,Pr}}\frac{\partial}{\partial x_j}\left(\kappa\frac{\partial T}{\partial x_j}\right)+\frac{\gamma-1}{\gamma\, Ga}\frac{d\overline{P}}{dt}+\frac{1}{Pl\, Ga\sqrt{Ra\,Pr}}\frac{\partial q_r}{\partial x_j} \tag{2.52}$$

$$\overline{P}=\rho+Ga\,(\rho T) \tag{2.53}$$

$$\frac{1}{\tau}\frac{\partial I(\mathbf{r},\mathbf{s})}{\partial s}=(1-\omega)I_b(\mathbf{r})-I(\mathbf{r},\mathbf{s})+\frac{\omega}{4\pi}\int_{4\pi} I(\mathbf{r},\mathbf{s}_i)\Phi(\mathbf{s}_i,\mathbf{s})\,\mathrm{d}\Omega_i \tag{2.54}$$

The non-dimensional form of the governing equations for buoyancy driven turbulent flow is presented as

$$\frac{\partial\overline{\rho}}{\partial t}+\frac{\partial(\overline{\rho}\widetilde{u}_j)}{\partial x_j}=0 \tag{2.55}$$

$$\frac{\partial(\overline{\rho}\widetilde{u}_i)}{\partial t}+\frac{\partial(\overline{\rho}\widetilde{u}_i\widetilde{u}_j)}{\partial x_j}=-\frac{\partial\overline{p}}{\partial x_i}+\sqrt{\frac{Pr}{Ra}}\frac{\partial\tau_{ij}}{\partial x_j}-\sqrt{\frac{Pr}{Ra}}\frac{\partial}{\partial x_j}\left(\overline{\rho u_j'' u_i''}\right)+\frac{1}{Ga}(1-\overline{\rho})\,\hat{\mathbf{e}}_{\mathbf{y}} \tag{2.56}$$

$$\frac{\partial\left(\overline{\rho}\widetilde{T}\right)}{\partial t}+\frac{\partial\left(\overline{\rho}\widetilde{u}_j\widetilde{T}\right)}{\partial x_j}=\frac{1}{\sqrt{RaPr}}\frac{\partial}{\partial x_j}\left(\kappa\frac{\partial\widetilde{T}}{\partial x_j}-\overline{\rho u_j'' T''}\right)+\frac{\gamma-1}{\gamma Ga}\frac{d\overline{P}}{dt}+\frac{1}{PlGa\sqrt{RaPr}}\frac{\partial\overline{q_r}}{\partial x_j} \tag{2.57}$$

$$\frac{\partial}{\partial t}(\overline{\rho}k)+\frac{\partial}{\partial x_j}(\overline{\rho}\widetilde{u}_j k)=\sqrt{\frac{Pr}{Ra}}\frac{\partial}{\partial x_j}\left(\left(\mu+\frac{\mu_t}{\sigma_k}\right)\frac{\partial k}{\partial x_j}\right)+\sqrt{\frac{Pr}{Ra}}P_k+\sqrt{\frac{Pr}{Ra\,Ga}}G_k-\sqrt{\frac{Ra}{Pr}}\,\overline{\rho}\varepsilon \tag{2.58}$$

$$\frac{\partial}{\partial t}(\overline{\rho}\varepsilon)+\frac{\partial}{\partial x_j}(\overline{\rho}\widetilde{u}_j\varepsilon)=\sqrt{\frac{Pr}{Ra}}\frac{\partial}{\partial x_j}\left(\left(\mu+\frac{\mu_t}{\sigma_\varepsilon}\right)\frac{\partial\varepsilon}{\partial x_j}\right)-\sqrt{\frac{Ra}{Pr}}\,c_{\varepsilon 2}\overline{\rho}\frac{\varepsilon^2}{k}-c_{\varepsilon 4}\overline{\rho}\varepsilon\frac{\partial\widetilde{u}_j}{\partial x_j}+\left[c_{\varepsilon 1}\left(\sqrt{\frac{Pr}{Ra}}P_k+\sqrt{\frac{Pr}{Ra\,Ga}}\,c_{\varepsilon 3}G_k\right)\right]\frac{\varepsilon}{k} \tag{2.59}$$

The EOS is

$$\overline{P} = \overline{\rho} + Ga\,(\overline{\rho}\widetilde{T}) \tag{2.60}$$

The RTE is described as

$$\frac{1}{\tau}\frac{\partial I\,(\mathbf{r},\mathbf{s})}{\partial s} = (1-\omega)\overline{I_b}\,(\mathbf{r}) - I\,(\mathbf{r},\mathbf{s}) + \frac{\omega}{4\pi}\int\limits_{4\pi} I\,(\mathbf{r},\mathbf{s}_i)\Phi\,(\mathbf{s}_i,\mathbf{s})\,\mathrm{d}\Omega_i \tag{2.61}$$

$$-\overline{\rho u_i'' u_j''} = \mu_t\left(\frac{\partial \widetilde{u}_i}{\partial x_j} + \frac{\partial \widetilde{u}_j}{\partial x_i} - \frac{2}{3}\frac{\partial \widetilde{u}_k}{\partial x_k}\delta_{ij}\right) - \sqrt{\frac{Ra}{Pr}}\frac{2}{3}\overline{\rho}k\delta_{ij} \tag{2.62}$$

$$-\overline{\rho u_j'' T''} = \kappa_t\frac{\partial \widetilde{T}}{\partial x_j}. \tag{2.63}$$

$$P_k = \mu_t\left(\frac{\partial \widetilde{u}_i}{\partial x_j} + \frac{\partial \widetilde{u}_j}{\partial x_i}\right)\frac{\partial \widetilde{u}_i}{\partial x_j} - \frac{2}{3}\mu_t\left(\frac{\partial \widetilde{u}_l}{\partial x_l}\right)^2 - \sqrt{\frac{Ra}{Pr}}\frac{2}{3}\overline{\rho}k\frac{\partial \widetilde{u}_l}{\partial x_l} \tag{2.64}$$

$$G_k = \frac{\mu_t}{\overline{\rho}\sigma_T}\frac{\partial \overline{\rho}}{\partial y} \tag{2.65}$$

The model constants used in this study are $c_\mu = 0.09, c_{\varepsilon 1} = 1.44, c_{\varepsilon 2} = 1.92, c_{\varepsilon 3} = \tanh\left(\frac{v}{u}\right), c_{\varepsilon 4} = 0.33, \sigma_k = 1.0, \sigma_\varepsilon = 1.3$, where $\hat{\mathbf{e}}_\mathbf{y}$ is a unit vector in the y-direction and various non-dimensional parameters are described as.

$$Pr = \frac{\nu}{\alpha},\ Ra = \frac{\beta_T g \Delta T H^3}{\nu\alpha},\ Ga = \beta_T(T_h - T_c),\ Pl = \frac{\kappa}{4\sigma T_0^3 H},\ \tau = \beta H,\ \omega = \frac{\sigma_s}{\beta} \tag{2.66}$$

The buoyancy term in Eqs. (2.51), (2.56), (2.58), (2.59) does not employ a Boussinesq approximation but retains a form which requires explicit calculation of density. The calculation of density required for determining the buoyancy forces among others is obtained by solving the continuity equation (Eq. (2.55)). Notably, for the quasi-incompressible formulation described in the present work, the velocity divergence remains non-zero. As the density variations are essentially due to temperature difference and radiative heat transfer, the velocity divergence condition is obtained by rearranging energy conservation equation for laminar and turbulent flows (Eq. (2.52)), (Eq. (2.57)) respectively and using EOS (Eq. (2.53)).

$$\frac{\partial u_j}{\partial x_j} = \frac{1}{\overline{P}}\left[\frac{-1}{\gamma}\frac{d\overline{P}}{dt} + \frac{Ga}{\sqrt{Ra\,Pr}}\frac{\partial}{\partial x_j}\left(\kappa\frac{\partial T}{\partial x_j}\right) + \frac{1}{Pl\sqrt{Ra\,Pr}}\frac{\partial q_{rj}}{\partial x_j}\right] \tag{2.67}$$

$$\frac{\partial \widetilde{u}_j}{\partial x_j} = \frac{1}{\overline{P}}\left[\frac{-1}{\gamma}\frac{d\overline{P}}{dt} + \frac{Ga}{\sqrt{Ra\,Pr}}\frac{\partial}{\partial x_j}\left((\kappa+\kappa_t)\frac{\partial \widetilde{T}}{\partial x_j}\right) + \frac{1}{Pl\sqrt{Ra\,Pr}}\frac{\partial q_{rj}}{\partial x_j}\right] \tag{2.68}$$

Notably in closed enclosures, the time derivative of thermodynamic pressure, $\frac{d\overline{P}}{dt}$ appears as a source term in Eqs. (2.52) and (2.57). This term is derived from the velocity divergence condition Eq. (2.67) and Eq. (2.68) by integrating over the volume of enclosure Υ and enforcing impervious conditions at the walls of the enclosure.

$$\frac{d\overline{P}}{dt} = \frac{\gamma}{\Upsilon\sqrt{Ra\,Pr}}\left\{Ga\int_{\Upsilon}\nabla\cdot(\kappa\nabla T)\,d\Upsilon + \frac{1}{Pl}\int_{\Upsilon}\nabla\cdot\mathbf{q_r}\,d\Upsilon\right\} \tag{2.69}$$

$$\frac{d\overline{P}}{dt} = \frac{\gamma}{\Upsilon\sqrt{Ra\,Pr}}\left\{Ga\int_{\Upsilon}\nabla\cdot\left((\kappa+\kappa_t)\right)\nabla\widetilde{T}\right)d\Upsilon + \frac{1}{Pl}\int_{\Upsilon}\nabla\cdot\mathbf{q_r}\,d\Upsilon\right\} \tag{2.70}$$

The expression of thermodynamic pressure is obtained from the conservation of mass as

$$\overline{P}(t) = \frac{m_0}{\int_{\Upsilon}\frac{d\Upsilon}{1+Ga\,T}} \tag{2.71}$$

where Υ represents the volume of the entire domain and m_0 is the mass in the enclosure at time $t = t_0$.

2.4 Discretization Procedure

Now, the governing equations are discretized using the finite volume method on three-dimensional hybrid unstructured meshes. The discretization of the transport equations follows the work of Dalal et al. [113] whereas, the discretization of RTE closely resembles the work of Murthy and Mathur [114]. The governing equations

are integrated over the control volume, and the temporal term is discretized using the second order backward difference time scheme. The discretized equation of transport for general variable ϕ can be written as below.

$$V_P \frac{3(\phi)_P^{n+1} - 4(\phi)_P^n + (\phi)_P^{n-1}}{2\Delta t} + \sum_f F_f^n (\phi)_f^{n+1} - \sum_f F_{d\phi f}^{n+1} = S_\phi \tag{2.72}$$

where $\phi = \rho\mathbf{u}, \rho T, \rho k, \rho\varepsilon$ and F_f^n represents the volume flux and S_ϕ is the source term. The subscript 'P' refers to the cell where the solution is sought and 'f' corresponds to the face values. The $\sum_f$ in the convective and diffusive term corresponds to the summation over faces of cell P. The discrete terms, as well as the specific details of convective and diffusive fluxes, are described below.

2.4.1 Discretization of convection fluxes

The discretization of the convective term is defined as,

$$\int_{\mathrm{V}} \nabla \cdot (\mathbf{u}\phi)\, \mathrm{dV} = \int_S (\mathbf{u}\phi) \cdot \mathrm{d}\mathbf{S} \approx \sum_f (\phi\mathbf{u})_f \cdot \mathbf{S}_f = \sum_f F_f \phi_f \tag{2.73}$$

where $F_f = \mathbf{u}_f \cdot \mathbf{S}_f$ and $\phi = \rho,\ \rho\mathbf{u},\ \rho T,\ \rho k$ and $\rho\varepsilon$. Here, ϕ_f is the value of ϕ at the center of face f. In the present work the convective term is handled using a second order accurate high resolution scheme referred to as CUBISTA [117]. This scheme calculates the face value of the transport variable ϕ_f using the normalization of variable as,

$$\widetilde{\phi}_f = \frac{\phi_f - \phi_{\mathrm{U}}}{\phi_{\mathrm{D}} - \phi_{\mathrm{U}}} \tag{2.74}$$

where ϕ_f= $\rho, \rho\mathbf{u}, \rho T$ and subscript 'U' represents the far upwind and 'D' represents the downwind cells. The normalized variable at the faces of a cell is found using the following relation.

$$\widetilde{\phi}_f = \begin{cases} \frac{7}{4}\widetilde{\phi}_{\mathrm{c}} & 0 < \widetilde{\phi}_{\mathrm{c}} < \frac{3}{8} \\ \frac{3}{4}\widetilde{\phi}_{\mathrm{c}} + \frac{3}{8} & \frac{3}{8} \le \widetilde{\phi}_{\mathrm{c}} \le \frac{3}{4} \\ \frac{1}{4}\widetilde{\phi}_{\mathrm{c}} + \frac{3}{4} & \frac{3}{4} < \widetilde{\phi}_{\mathrm{c}} < 1 \\ \widetilde{\phi}_{\mathrm{c}} & \text{elsewhere} \end{cases}$$

The ambiguity regarding the calculation of far-upwind cell on unstructured meshes is removed using the values of known upwind cell 'C' as,

$$\widetilde{\phi}_{\mathrm{C}} = \frac{\phi_{\mathrm{C}} - \phi_{\mathrm{U}}}{\phi_{\mathrm{D}} - \phi_{\mathrm{U}}} = 1 - \frac{\phi_{\mathrm{D}} - \phi_{\mathrm{C}}}{2(\nabla\phi)_{\mathrm{C}} \cdot \hat{\mathbf{n}}_{\mathbf{f}}} \tag{2.75}$$

where $\hat{\mathbf{n}}_{\mathbf{f}}$ is the unit face normal. It is to be noted that in the present unstructured grid framework the subscripts 'P' and 'N' correspond to the owner and neighbor cells of a face which are decided by the direction of the face normal as shown in Fig. 2.1. However, the subscripts 'C' and 'D' correspond to the upwind and downwind cells which are decided by the flow direction.

2.4.2 Diffusive flux treatment

The discretization of the diffusive fluxes for variable $\Phi \left(= \frac{\phi}{\rho} \right)$ where $\phi = \rho\mathbf{u}$, ρT, ρk and $\rho\varepsilon$ is described as

$$\int_{\mathrm{V}} \nabla \cdot (\Gamma \nabla \Phi)\, \mathrm{dV} = \int_{S} (\Gamma \nabla \Phi) \cdot \mathrm{d}\mathbf{S} \approx \sum_{f} (\Gamma \nabla \Phi \cdot \mathbf{S})_f = \sum_{f} F_{d\Phi f}$$

where Γ is the diffusion coefficient for momentum and energy equations. The diffusive flux for momentum equations $\phi = \rho\mathbf{u}$ is given as.

$$\int_S \sqrt{\frac{Pr}{Ra}} \left(\vec{\bar{\tau}} \cdot \mathrm{d}\mathbf{S} \right) = \int_S \sqrt{\frac{Pr}{Ra}} \left(\mu[\nabla\mathbf{u} + (\nabla\mathbf{u})^{\mathrm{T}}] - \frac{2}{3}\,\mu\,(\nabla \cdot \mathbf{u})\,\mathrm{I} \right) \cdot \mathrm{d}\mathbf{S} \tag{2.76}$$

The RHS of Eq. (2.76) is rearranged to represent the diffusive terms in the x, y and z momentum equations as.

Diffusive term in x-momentum equation

$$\sqrt{\frac{Pr}{Ra}}\mu_f \left[\sum_f \left((\nabla u \cdot \mathbf{S}) + \left(\frac{\partial u}{\partial x} S_x + \frac{\partial v}{\partial x} S_y + \frac{\partial w}{\partial x} S_z \right) \right)_f - \frac{2}{3} \left(\frac{\partial u}{\partial x} + \frac{\partial v}{\partial y} + \frac{\partial w}{\partial z} \right)_f S_{fx} \right]$$

Diffusive term in y-momentum equation

$$\sqrt{\frac{Pr}{Ra}}\mu_f \left[\sum_f \left((\nabla v \cdot \mathbf{S}) + \left(\frac{\partial u}{\partial y} S_x + \frac{\partial v}{\partial y} S_y + \frac{\partial w}{\partial y} S_z \right) \right)_f - \frac{2}{3} \left(\frac{\partial u}{\partial x} + \frac{\partial v}{\partial y} + \frac{\partial w}{\partial z} \right)_f S_{fy} \right]$$

Diffusive term in z-momentum equation

$$\sqrt{\frac{Pr}{Ra}}\mu_f \left[\sum_f \left((\nabla w \cdot \mathbf{S}) + \left(\frac{\partial u}{\partial z}S_x + \frac{\partial v}{\partial z}S_y + \frac{\partial w}{\partial z}S_z\right)\right)_f - \frac{2}{3}\left(\frac{\partial u}{\partial x} + \frac{\partial v}{\partial y} + \frac{\partial w}{\partial z}\right)_f S_{fz}\right]$$

where $\mathbf{S}_f$ is the face area vector. In the discretization of the diffusive terms appearing in the momentum equation, only the first term is implicitly treated while the rest of the terms are treated in an explicit manner. For orthogonal grids, the surface vector and the line joining adjacent cell centers are aligned whereas, for non-orthogonal grids, they are inclined to each other. This is the basis for the non-orthogonal component of diffusive fluxes. A detailed explanation of the non-orthogonal implementation is shown in Fig. 2.1. The face "abc" is shared by two neighboring tetrahedral cells P and N. The face unit normal is represented by $\hat{\mathbf{n}}_\mathbf{f}$. Projecting the cell centers over the surface normal results in two more points P' and N'. Furthermore, the discretization of the diffusion term can be written as

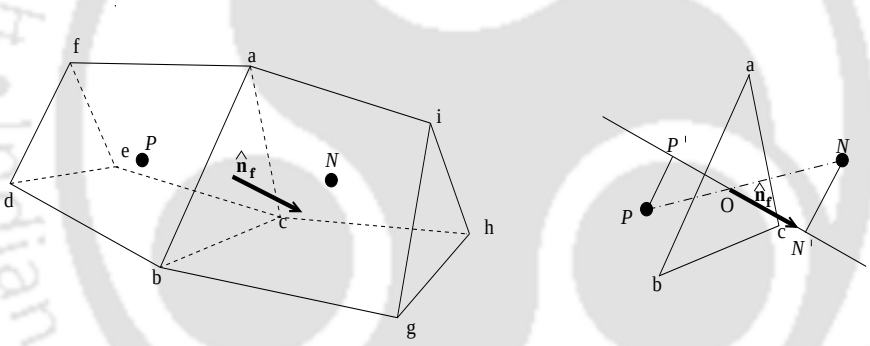

Figure 2.1: Illustration of non-orthogonality in the grids.

$$(\nabla\Phi)_f \cdot \mathbf{S}_f = A_f (\nabla\Phi)_f \cdot \hat{\mathbf{n}}_f = A_f \frac{(\Phi_{N'} - \Phi_{P'})}{\Delta n} \tag{2.77}$$

where Δn is the distance between points P' and N'. Using Taylor series expansion for $\Phi_{N'}$ and $\Phi_{P'}$ as

$$\phi_{N'} = \phi_N + \overrightarrow{\nabla\phi_N} \cdot \mathbf{NN'} \tag{2.78}$$

$$\phi_{P'} = \phi_P + \overrightarrow{\nabla\phi_P} \cdot \mathbf{PP'} \tag{2.79}$$

Further substituting Eqs. (2.78) and (2.79) in Eq. (2.77), the final equation can be written as.

$$(\nabla\Phi)_f \cdot \mathbf{S}_f = A_f \frac{(\Phi_N - \Phi_P)}{\Delta n} + \frac{(\nabla\Phi_N \cdot \mathbf{NN}' - \nabla\Phi_P \cdot \mathbf{PP}')A_f}{\Delta n} \tag{2.80}$$

The first part of Eq. (2.80) is the orthogonal component of diffusive fluxes while the second part is mainly appearing due to non-orthogonality of the grids.

2.4.3 Discretization procedure for RTE

Radiative transfer equation governs the transfer of radiant energy given by,

$$\frac{\partial I(\mathbf{r},\mathbf{s})}{\partial s} = \kappa_a I_b(\mathbf{r}) - (\kappa_a + \sigma_s) I(\mathbf{r},\mathbf{s}) + \frac{\sigma_s}{4\pi}\int_{4\pi} I(\mathbf{r},\mathbf{s}_i)\Phi(\mathbf{s},\mathbf{s}_i)\,\mathrm{d}\Omega_i \tag{2.81}$$

where $I(\mathbf{r},\mathbf{s})$ is the intensity at any location $\mathbf{r}$ along the direction $\mathbf{s}$, κ_a and σ_s represent the absorption and scattering coefficient, respectively and $\Phi(\mathbf{s}_i,\mathbf{s})$ is the scattering phase function. Since, $s = f(x,y,z)$ the L.H.S of Eq. (2.81) can be expressed as

$$\frac{\partial I}{\partial s} = \frac{\partial I}{\partial x}\frac{\partial x}{\partial s} + \frac{\partial I}{\partial y}\frac{\partial y}{\partial s} + \frac{\partial I}{\partial z}\frac{\partial z}{\partial s}$$

$$\frac{\partial I}{\partial s} = \xi\frac{\partial I}{\partial x} + \eta\frac{\partial I}{\partial y} + \mu\frac{\partial I}{\partial z}$$

$$\frac{\partial I}{\partial s} = \hat{\mathbf{s}} \cdot \nabla I \tag{2.82}$$

where $\hat{\mathbf{s}}$ is the unit vector along $\mathbf{s}$, and $\xi,\ \eta,\ \mu$ are the direction cosines in the $x,\ y,\ z$ directions, respectively, so $\hat{\mathbf{s}} = \xi\,\hat{\mathbf{i}} + \eta\,\hat{\mathbf{j}} + \mu\,\hat{\mathbf{k}}$. The RTE can be written as

$$\hat{\mathbf{s}} \cdot \nabla I = \kappa_a I_b(\mathbf{r}) - (\kappa_a + \sigma_s) I(\mathbf{r},\mathbf{s}) + \frac{\sigma_s}{4\pi}\int_{4\pi} I(\mathbf{r},\mathbf{s}_i)\Phi(\mathbf{s}_i,\mathbf{s})\,\mathrm{d}\Omega_i \tag{2.83}$$

also

$$\nabla \cdot (\hat{\mathbf{s}} I) = (\nabla \cdot \hat{\mathbf{s}}) I + \hat{\mathbf{s}} \cdot \nabla I \tag{2.84}$$

as $\hat{\mathbf{s}}$ is constant, so $\nabla \cdot \hat{\mathbf{s}} = 0$, we get

$$\nabla \cdot (\hat{\mathbf{s}} I) = \hat{\mathbf{s}} \cdot \nabla I \tag{2.85}$$

So Eq. (2.83) can be rearranged as,

$$\nabla \cdot (\mathbf{s} I) = -\beta I + S \tag{2.86}$$

where $\beta = (\kappa + \sigma_s)$ represents the extinction coefficient and S is a source term defined as

$$S = \kappa_a I_b (\mathbf{r}) + \frac{\sigma_s}{4\pi} \int_{4\pi} I (\mathbf{r}, \mathbf{s}_i) \Phi (\mathbf{s}_i, \mathbf{s}) \, \mathrm{d}\Omega_i. \tag{2.87}$$

The finite volume formulation of the radiative transfer equation Eq. (2.81) follows the unstructured grid formulation of Murthy and Mathur [114]. It requires the spatial and angular discretization of Eq. (2.81) over the control volume and control angles as shown in Fig. 2.2. For each discrete direction 'm', integrating Eq. (2.81) over the control volume and control angles results in,

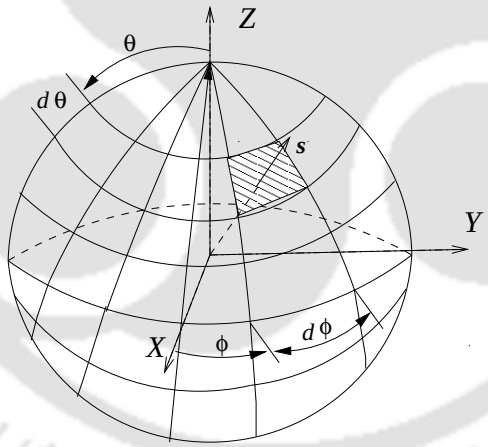

Figure 2.2: Representation of angular domain.

$$\int_{\Delta\Omega^m} \int_V \nabla \cdot (\mathbf{s} I^m) \, \mathrm{d}V \, \mathrm{d}\Omega = \int_{\Delta\Omega^m} \int_V (-\beta I^m + S^m) \, \mathrm{d}V \, \mathrm{d}\Omega \tag{2.88}$$

where I^m is the intensity in a particular direction $\mathbf{s}$. Applying Gauss divergence theorem to the above equation results in,

$$\sum_f I_f^m A_f D_f^m = (-\beta I^m + \kappa I_b + \frac{\sigma}{4\pi} \sum_{m'}^{M} I^{m'} \bar{\Phi}^{m'm} \ \Delta\Omega^{m'}) \ V \ \Delta\Omega \tag{2.89}$$

where I_b is a function of cell temperature and I^m is the intensities along the direction m for a given cell. Where, $\bar{\Phi}^{m'm}$ is the average scattering phase function, and D_f^m is the directional weight defined as,

$$D_f^m = \int_{\Delta\Omega^m} (\mathbf{s}^m \cdot \hat{\mathbf{n}}_f) \ \mathrm{d}\Omega \tag{2.90}$$

where $\mathbf{s}^m$ and $\Delta\Omega^m$ are the direction vector and solid angle respectively defined as,

$$\mathbf{s} = \sin\theta \ \sin\phi \ \hat{i} + \sin\theta \ \cos\phi \ \hat{j} + \cos\theta \ \hat{k} \tag{2.91}$$

$$\Delta\Omega^m = \int_{\Delta\phi} \int_{\Delta\theta} \sin\theta \ \mathrm{d}\theta \ \mathrm{d}\phi. \tag{2.92}$$

The final discrete form of the directional weight follows,

$$\begin{aligned} D_f^m &= \sin\phi^m \sin(0.5\Delta\phi)(\Delta\theta - \cos 2\theta^m \sin\Delta\theta) n_{fx} \\ &+ \cos\phi^m \sin(0.5\Delta\phi)(\Delta\theta - \cos 2\theta^m \sin\Delta\theta) n_{fy} \\ &+ (0.5\Delta\phi \ \sin 2\theta^m \ \sin\Delta\theta) n_{fz} \end{aligned} \tag{2.93}$$

where the LHS of Eq. (2.89) is discretized by using a hybrid scheme that is a combination of step and diamond scheme as

$$\begin{aligned} I_f^m D_f^m = \left(I_P^m \left[|D_f^m, 0| \right] - I_N^m \left[|-D_f^m, 0| \right] \right)^{n+1} + \gamma \left[D_f^m \left(\frac{V_N}{V_N + V_P} I_P^m + \frac{V_P}{V_N + V_P} I_N^m \right) \right]^n \\ - \gamma \left[I_P^m [|D_f^m, 0|] + I_N^m [|-D_f^m, 0|] \right]^n \end{aligned} \tag{2.94}$$

2.5 Pressure Gradient Calculation

In this work, in order to obtain a proper force balance between pressure and gravity, a variant of the method first proposed by Perot [118] has been adopted. In this approach, the centroidal quantities are calculated from the respective face centered values. This method has been successfully applied to calculate cell centroidal values

of pressure gradients. This approach is termed as Modified Green Gauss (MGG) and is used for the treatment of pressure and gravity terms in this work. The pressure gradient at the cell centroid is calculated as

$$\left(\frac{\partial p}{\partial x_i}\right)_P = \frac{1}{V_p}\sum_f \left(\frac{\partial p}{\partial n}\right)_f (X_{if} - X_{iP})\, A_f \tag{2.95}$$

The above gradient calculation ensures that the recovery of velocities using centroidal pressure gradients is consistent with the discretization of pressure Poisson equation which requires normal gradients of pressure at the faces of a cell.

2.6 Source Term Discretization

The source terms appearing in the momentum equations are the pressure gradient and buoyancy terms. Whereas, the time rate of change of thermodynamic pressure $\frac{d\overline{P}}{dt}$ and divergence of radiative heat flux are the source terms appearing in the energy equation.

2.6.1 Radiative heat flux

The radiative heat flux vector along a direction $\mathbf{s}$ inside a participating medium can be obtained by integrating the contribution of intensity from all solid angles

$$\mathbf{q}_r = \int_{4\pi} I\ \mathbf{s}\ \mathrm{d}\Omega \tag{2.96}$$

The heat flux vector $\mathbf{q}_r$ is expressed as the product of magnitude q_r and a direction $\mathbf{s}$. The radiative heat flux onto a surface element can be expressed in terms of the incident and outgoing intensities evaluated at the surface. For a surface whose normal is $\hat{\mathbf{n}}$, Eq. (2.96) can be expressed as

$$\hat{\mathbf{n}} \cdot q_r\mathbf{s} = \int_{4\pi} I(\mathbf{s})\ \hat{\mathbf{n}} \cdot \mathbf{s}\ \mathrm{d}\Omega \tag{2.97}$$

2.6.2 Divergence of radiative heat flux

The divergence of radiative heat flux is the volumetric heating rate that appears in the energy equation. The first term of the radiative transfer equation can be expressed as

$$\frac{1}{\beta}\nabla\cdot(\hat{\mathbf{s}}I) = -I(\mathbf{s}) + (1-\omega)I_b(\mathbf{s}) + \frac{\omega}{4\pi}\int_{4\pi} I(\mathbf{s}_i)\ \Phi(\mathbf{s}_i,\mathbf{s})\ \mathrm{d}\Omega_i \tag{2.98}$$

Integrating the above equation over all solid angles, we get

$$\frac{1}{\beta}\int_{4\pi}\nabla\cdot(\hat{\mathbf{s}}I)\mathrm{d}\Omega = \int_{4\pi}[-I(\mathbf{s}) + (1-\omega)I_b(\mathbf{s}) + \frac{\omega}{4\pi}\int_{4\pi} I(\mathbf{s}_i)\ \Phi(\mathbf{s}_i,\mathbf{s})\mathrm{d}\Omega_i]\ \mathrm{d}\Omega \tag{2.99}$$

$$\frac{1}{\beta}\nabla\cdot\int_{4\pi}(\hat{\mathbf{s}}I)\mathrm{d}\Omega = \int_{4\pi}[-I(\mathbf{s}) + (1-\omega)I_b(\mathbf{s}) + \frac{\omega}{4\pi}\int_{4\pi} I(\mathbf{s}_i)\ \Phi(\mathbf{s}_i,\mathbf{s})\mathrm{d}\Omega_i]\ \mathrm{d}\Omega \tag{2.100}$$

Since $I_b(\mathbf{s})$ is independent of direction and by using Eq. (2.96), we get

$$\frac{1}{\beta}\nabla\cdot\mathbf{q}_r = \int_{4\pi} -I(\mathbf{s})\mathrm{d}\Omega + (1-\omega)4\pi I_b(\mathbf{s}) + \frac{\omega}{4\pi}\int_{4\pi} I(\mathbf{s}_i)\int_{4\pi}\Phi(\mathbf{s}_i,\mathbf{s})\mathrm{d}\Omega_i\ \mathrm{d}\Omega \tag{2.101}$$

Now for isotropic scattering the above equation can be simplified to

$$\frac{1}{4\pi}\int_{4\pi}\Phi(\mathbf{s}_i,\mathbf{s})\mathrm{d}\Omega = 1 \tag{2.102}$$

$$\frac{1}{\beta}\nabla\cdot\mathbf{q}_r = \int_{4\pi} -I(\mathbf{s})\mathrm{d}\Omega + (1-\omega)4\pi I_b(\mathbf{s}) + \omega\int_{4\pi} I(\mathbf{s}_i)\mathrm{d}\Omega_i \tag{2.103}$$

As Ω, Ω_i are dummy variables and since the integration is performed over the entire solid angle, the first and the last term of right hand side can be brought together. Hence

$$\frac{1}{\beta}\nabla\cdot\mathbf{q}_r = (\omega-1)\int_{4\pi} I(\mathbf{s}_i)\mathrm{d}\Omega_i + (1-\omega)4\pi I_b(\mathbf{s}) \tag{2.104}$$

Where irradiation is defined as $G = \int_{4\pi} I(\mathbf{s}_i)\mathrm{d}\Omega_i$

$$\frac{1}{\beta}\nabla\cdot\mathbf{q}_r = (1-\omega)\,(4\pi I_b(\mathbf{s}) - G) \tag{2.105}$$

So finally we get

$$\nabla\cdot\mathbf{q}_r = \kappa\,(4\pi I_b(\mathbf{s}) - G) \tag{2.106}$$

Equation (2.106) signifies the conservation law of radiative energy. It relates the net heat flux in the radiative energy from the volume element to the emitted energy and the absorbed irradiation within the volume. Interestingly, scattering does not appear in the Eq. (2.106) as it only redirects the photons and does not affect the net energy content of the volume.

2.6.3 Handling of $\frac{d\overline{P}}{dt}$ term

The handling of $\frac{d\overline{P}}{dt}$ term is described below where the first term on the RHS of Eq. (2.107) is computed by performing the surface integration over the boundary faces of the enclosure while the second term is computed by performing volumetric addition over each and every cell of the enclosure. It is important to note that the treatment of the conduction and radiative heat transfer terms appearing in the RHS of Eq. (2.108) are consistent with the way they are handled in the energy equation.

$$\frac{d\overline{P}}{dt} = \frac{\gamma}{\Upsilon\sqrt{RaPr}} \left\{ Ga \int_{\Omega} \nabla \cdot (\kappa \nabla T)\, \mathrm{d}\Omega + \frac{1}{Pl} \int_{\Omega} \nabla \cdot \mathbf{q_r}\, \mathrm{d}\Omega \right\} \tag{2.107}$$

$$\frac{d\overline{P}}{dt} = \frac{\gamma}{\Upsilon\sqrt{RaPr}} \left\{ Ga \sum_{bf} (\kappa \nabla T)_f \cdot \mathbf{S}_f + \frac{1}{Pl} \sum_{NC} \nabla \cdot \mathbf{q_r}\, V_P \right\} \tag{2.108}$$

Here 'bf' represents the total faces of all boundaries and 'NC' represents the total number of control volumes in the domain.

2.7 Pressure Velocity Coupling

The momentum interpolation approach by Rhie and Chow [112] is used to avoid the pressure checkerboard problem on collocated meshes. Aforementioned is achieved by first computing the auxiliary momentum by dropping the pressure gradient and gravity terms from the momentum equations. In a fully discrete form, the auxiliary momentum equations may be written as,

$$V_P \frac{3(\rho\mathbf{u})^*_P - 4(\rho\mathbf{u})^n_P + (\rho\mathbf{u})^{n-1}_P}{2\Delta t} + \sum_f F^n_f (\rho\mathbf{u})^*_f - \sum_f F^*_{d\mathbf{u}f} = 0 \tag{2.109}$$

where $*$ quantities indicate auxiliary terms. On subtracting the auxiliary momentum equations (Eq. (2.109)) from the momentum equations (Eq. (2.72)) at $(n+1)$ level and by taking divergence we get a variable coefficient pressure Poisson equation (PPE). This equation reads,

$$\frac{2\Delta t}{3} \sum_f \left(\frac{\nabla p}{\rho} \right)_f \cdot \mathbf{S}_f = \sum_f F^*_{0f} - \sum_f F^{n+1}_f + \sum_f \frac{2\Delta t}{3Ga} \left(\frac{1-\rho_f}{\rho_f} \right) \mathbf{S}_f \cdot \hat{\mathbf{e}}_\mathbf{y} \tag{2.110}$$

Equation (2.110) represents a variable coefficient pressure Poisson equation. The first term on the RHS of Eq. (2.110) represents the auxiliary flux which is computed from auxiliary velocity ($F^*_{0f} = \mathbf{u}^*_f \cdot \mathbf{S}_f$) by solving the Navier-Stokes equation by dropping the pressure and buoyancy terms Eq. (2.109). However, the second term represents the volume flux and is obtained by using the velocity divergence condition Eq. (2.67). As already discussed for a typical incompressible flow the velocity divergence condition is invariably zero. Hence, using this criterion, the pressure equation for incompressible and low-Mach number flows are represented by Eqs. (2.111) and (2.112), respectively.

$$\frac{2\Delta t}{3}\sum_f \left(\frac{\nabla p}{\rho}\right)_f \cdot \mathbf{S}_f = \sum_f F^*_{0f} + \sum_f \frac{2\Delta t}{3Ga}\left(\frac{1-\rho_f}{\rho_f}\right)\mathbf{S}_f \cdot \hat{\mathbf{e}}_\mathbf{y} \tag{2.111}$$

$$\frac{2\Delta t}{3}\sum_f \left(\frac{\nabla p}{\rho}\right)_f \cdot \mathbf{S}_f = \sum_f {F_{0f}}^* + \sum_f \frac{2\Delta t}{3Ga}\left(\frac{1-\rho_f}{\rho_f}\right)\mathbf{S}_f \cdot \hat{\mathbf{e}}_\mathbf{y} -$$

$$\frac{1}{\overline{\overline{P}}}\left[\frac{-1}{\gamma}\frac{d\overline{P}}{dt}V_P + \frac{1}{\sqrt{RaPr}}\left\{Ga\sum_f (k\nabla T)_f \cdot \mathbf{S}_f + \frac{1}{Pl}\nabla \cdot \mathbf{q_r} V_P\right\}\right] \tag{2.112}$$

where $\left(\frac{\nabla p}{\rho}\right)_f \cdot \mathbf{S}_f$ may be evaluated in a way similar to the diffusive flux as discussed in Section. 2.4.2.

$$\left(\frac{\nabla p}{\rho}\right)_f \cdot \mathbf{S}_f = \frac{A_f}{\rho_f}\frac{(p_N - p_P)}{\Delta n} + \frac{A_f}{\rho_f}\frac{(\nabla p_N \cdot \mathbf{NN'} - \nabla p_P \cdot \mathbf{PP'})}{\Delta n} \tag{2.113}$$

The discrete PPE leads to a system of linear algebraic equations, which are efficiently solved by the Krylov solver with ILU preconditioning through Lis open source libraries [119]. After getting the pressure field, the fluxes are corrected at the faces using momentum interpolation defined as,

$$\sum_f F^{n+1}_f = \sum_f F^*_f - \frac{2\Delta t}{3}\sum_f \left(\frac{\nabla p}{\rho}\right)_f \cdot \mathbf{S}_f + \frac{2}{3}\sum_f \frac{\Delta t}{Ga}\left(\frac{1-\rho_f}{\rho_f}\right)\mathbf{S}_f \cdot \hat{\mathbf{e}}_\mathbf{y} \tag{2.114}$$

Finally, the cell centroid velocities are update as,

$$\mathbf{u}^{n+1} = \mathbf{u}^* - \frac{2}{3}\frac{\Delta t}{\rho}\frac{\partial p}{\partial x_i} + \frac{2}{3}\frac{\Delta t}{Ga}\left(\frac{1-\rho}{\rho}\right)\hat{\mathbf{e}}_\mathbf{y} \tag{2.115}$$

This fractional step approach for quasi-incompressible flows is a key feature of all three solution algorithms to be discussed in the following chapter.

2.8 Incompressible and Compressible Models

In this section, discussions on incompressible model based on Boussinesq approximation and compressible model of OpenFOAM is presented. The objective of presenting an incompressible and compressible model is to demonstrate comparison of various models for convective-radiative flows. The results obtained via compressible model of OpenFOAM also helps in validating the developed low-Mach number model.

2.8.1 Incompressible model

The incompressible model considers a constant density advection with zero velocity divergence. The buoyancy term in the momentum equation ρg_i, is approximated as $-\rho_o g_i \beta_T \Delta T$, based on a first-order Taylor-series expansion to approximate the density in terms of temperature difference [120]. Here β_T is the coefficient of thermal expansion which is taken as $\frac{1}{T_o}$ for an ideal gas. The present incompressible model is incorporated in the in-house three-dimensional solver Anupravaha and is used for solving the governing equations using both incompressible and quasi-incompressible approach. In the present work, we make use of ILU preconditioner with BiCGSTAB solver for transport equations and algebraic-multigrid-preconditioner with GMRES solver for pressure equation using Krylov subspace methods. These iterative methods have been implemented using the open-source LIS library [119].

2.8.2 Compressible approach (OpenFOAM)

In addition to the quasi-incompressible algorithms explained earlier, studies have also been performed using a compressible model. Independent validations are performed through a compressible model of OpenFOAM implemented via BuoyantSimpleFoam solver [121]. BuoyantSimpleFoam is used for solving buoyancy driven compressible flows coupled with thermal radiative heat transfer. It solves the Navier-Stokes and energy equations where the computation of the convective terms is carried out using second order linear-upwind scheme while the diffusive terms are computed using a Gauss linear scheme with non-orthogonal correction. A GAMG solver with DIC-Gauss-Seidel smoother was employed for solving the pressure equation while the Navier-Stokes and energy equations are solved using PBiCG solver with DILU

preconditioner. The radiative heat transfer was modeled using discrete ordinate method (DOM) where the intensities were solved using GAMG solver and Symm-GaussSeidel smoother.

2.9 Implementation of Boundary Conditions

In this section, the boundary conditions used in the present thesis are specified.

2.9.1 Boundary condition for Navier-Stokes and energy equation

Wall boundary condition

$$U_t = 0$$

$$U_n = 0$$

$$T = \text{specified value}$$

$$\frac{\partial p}{\partial n} = \frac{1}{Ga}(1-\rho)\,\hat{\mathbf{e}}_{\mathbf{y}}$$

Symmetry boundary condition

$$\frac{\partial U_t}{\partial n} = 0$$

$$U_n = 0$$

$$\frac{\partial T}{\partial n} = 0$$

$$\frac{\partial p}{\partial n} = 0$$

where U_t and U_n are the tangential and normal components of velocity.

2.9.2 Boundary condition for radiative heat transfer

The boundary conditions for solving the RTE are implemented by assuming the walls to be gray-diffuse. The calculation of intensity at the wall for all outgoing direction ($\mathbf{s}\cdot\hat{\mathbf{n}} < 0$) is sum of reflected and emitted intensity given as.

$$I_w = \overbrace{\frac{1-\varepsilon}{\pi}\int_{\mathbf{s}\cdot\mathbf{n}>0} I(\mathbf{s})\mathbf{s}\cdot\hat{\mathbf{n}}\mathrm{d}\Omega}^{\text{Reflection}} + \overbrace{\frac{\varepsilon\sigma T_w^4}{\pi}}^{\text{Emission}} \tag{2.116}$$

where T_w, ε is the wall temperature, and emissivity, respectively. Moreover, $1-\varepsilon$ represents the reflectivity and is multiplied with ($I_{in} = \int_{4\pi} I\ \mathbf{s}\cdot\hat{\mathbf{n}}\ \mathrm{d}\Omega, \quad (\mathbf{s}\cdot\hat{\mathbf{n}}) > 0$) the summation of intensities over all incoming directions to represent the reflected intensities.

2.9.3 Two-dimensional boundary treatment

In the present work, two-dimensional problems are solved using a three-dimensional solver by taking a unit cell in third z direction. In this case, two boundaries perpendicular to the third direction are treated as symmetry (no-flux boundaries) and the boundary conditions for intensity are implemented by treating the boundaries as mirror boundaries. For any incident ray I on the wall the reflected ray R can be calculated from vector algebra as.

$$R = I - 2(\hat{\mathbf{n}}_\mathbf{f}\cdot\mathbf{s})\hat{\mathbf{n}}_\mathbf{f} \tag{2.117}$$

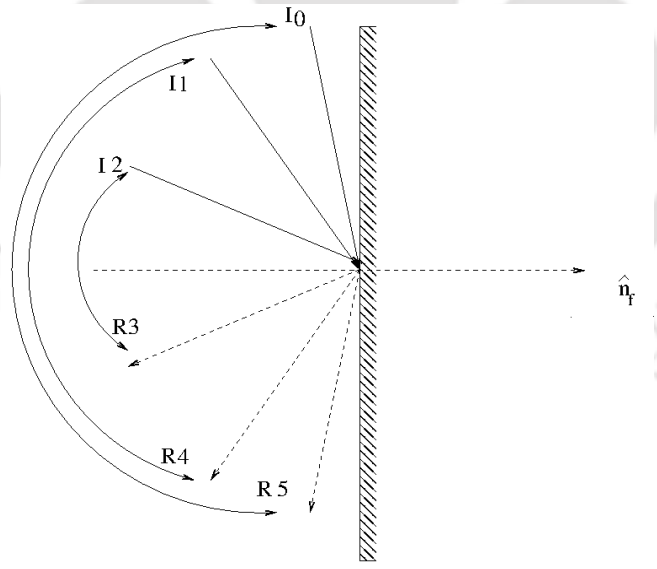

Figure 2.3: Symmetry Boundary

After finding the reflected ray for an incident ray the value of reflected ray is set equal to its corresponding incident ray. However, the above method is computationally expensive as it requires to swap through all the reflected direction to obtain the reflected ray. From the Fig. 2.3 it is see that if the total directions are varying from $0 - N_\theta$ then we can directly obtain a geometric relation between the incident and reflected ray which is shown below, this method prevents unnecessary computation.

$$\text{Reflected Ray} = N_\theta - \text{Iincident Ray} - 1 \tag{2.118}$$

The direction remains unchanged for the ϕ direction.

2.9.4 Flux specified boundary condition

This boundary condition is required for calculating the temperature at the wall for the case when both convective and radiative flux is involved. The flux specified boundary condition, q_0 is defined as:

$$q_c + q_r = q_0 \tag{2.119}$$

where q_c and q_r are the convective and radiative flux, respectively.

$$q_c = -\kappa \frac{\partial T}{\partial n}$$

$$q_r = \int_{4\pi} I(\mathbf{r}, \mathbf{s}) \mathbf{s} \cdot \hat{\mathbf{n}} \, \mathrm{d}\Omega \tag{2.120}$$

where $\hat{\mathbf{n}}$ is the unit vector normal to the surface. The final form of the equation reduces to

$$-\kappa \frac{\partial T}{\partial n} + \int_{4\pi} I(\mathbf{r}, \mathbf{s}) \mathbf{s} \cdot \hat{\mathbf{n}} \, \mathrm{d}\Omega = q_0 \tag{2.121}$$

The Equation (2.121) is solved iteratively to obtain the value for temperature.

2.10 Order of Accuracy Test

In this section, studies are performed to check the order of accuracy for the spatial and temporal schemes implemented in the developed solver. The order of accuracy

test is performed by computing discretization error which is defined as the difference between the solution of the discretized equations ϕ_k and the original partial differential equation ϕ_{exact}. Here, k refers to the mesh and time level as numerical solutions are obtained on a series of nested grids and with various values of time steps for transient problems. The spatial and temporal discretization errors are computed and compared with the theoretical order of accuracy. The discretization error are expected to decrease as $\frac{1}{r^p}$, where r is the grid refinement factor ($r = \frac{\Delta x_{coarse}}{\Delta x_{fine}}$) and p is the order of accuracy. In order to evaluate discretization errors L_2 and L_∞ norm of errors are used

$$\mathrm{L}_2 \text{ norm}_k = \left(\frac{\sum_{n=1}^{N} |\phi_{k,n} - \phi_{exact,n}|^2}{N} \right)^{1/2} \tag{2.122}$$

$$\mathrm{L}_\infty \text{ norm}_k = max|\phi_{k,n} - \phi_{exact,n}| \tag{2.123}$$

2.10.1 Discretization error for convective fluxes

In the present study, three different convective schemes are used which involves first-order upwind (FOU), a blend of first-order upwind (FOU) and central difference scheme (CDS) (Khosla-Rubin scheme with a deferred constant of 0.5), and a second-order high-resolution scheme referred to as CUBISTA [117]. The general convective-diffusive equation for a variable ϕ is defined as

$$\frac{\partial(\phi)}{\partial t} + \frac{\partial(\phi u_j)}{\partial x_j} = \frac{\partial}{\partial x_j}\left(D \frac{\partial \phi}{\partial x_j} \right) \tag{2.124}$$

In this study $D = 0$ is considered such that diffusive fluxes vanishes and only the convective fluxes are addressed. The manufactured solution for this modified equation with no diffusive contribution is defined as

$$\phi = x^3 + y^3, \qquad \text{with} \qquad u = y^2, v = -x^2 \tag{2.125}$$

To find the order of accuracy for each scheme, uniform Cartesian meshes of various grid resolutions ($\Delta x = 0.04, 0.02, 0.01, 0.005$) are chosen. The discretization error is computed on a particular mesh by initializing exact values of ϕ at the cell centroids whereas exact velocities are specified at all the face centroids. Since the convective

fluxes are calculated on the faces, the face average values of ϕ_f has been approximated by using different convective schemes. A convergence criterion of 10^{-8} has been employed in the present study. The L_∞ norms of discretization error on each grid are plotted against different grid resolutions as depicted in Fig. 2.4.

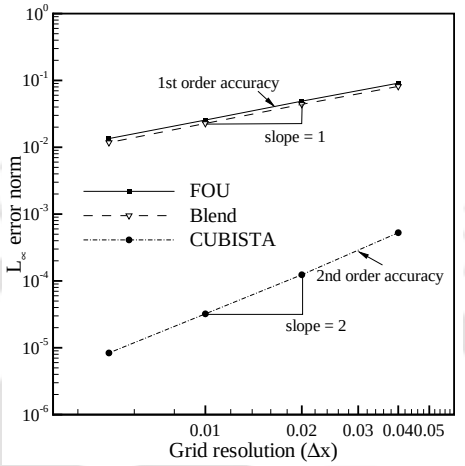

Figure 2.4: Order of accuracy test for different convective schemes.

Figure 2.4 shows the variation of discretization error with grid size for three different schemes. In all cases, the errors show a decreasing trend with grid refinement, with the slopes indicating the order of accuracy. CUBISTA scheme shows the lowest errors with the rate of decay of errors showing a slope of 2 (on the log-log scale). The Khosla-Rubin scheme which is obtained as an equi-blend of FOU and CDS schemes shows an overall first-order accuracy, evident from Fig. 2.4.

2.10.2 Discretization error for diffusive fluxes

In this section, the order of accuracy test for the discretization error of the diffusive terms is explored. The diffusive terms are discretized with a second-order central difference scheme (CDS). A general Poisson equation has been selected for the order of accuracy test of the diffusion term as shown below.

$$\nabla^2\phi = S \tag{2.126}$$

where S denotes the source term. The manufactured solution and the generated source term for Eq. 2.126 are

$$\phi = \frac{\cos(4\pi x) + \cos(4\pi y)}{4} \tag{2.127}$$

$$S = -4\pi^2[\cos(4\pi x) + \cos(4\pi y)] \tag{2.128}$$

To find the order of accuracy of the diffusive scheme, uniform hexahedral meshes with grid resolutions of $\Delta x = 0.04, 0.02, 0.01, 0.005$ are used. Figure 2.5 shows the L_∞ error norm for the diffusive scheme for each of the meshes. From the Fig. 2.5, it can be seen that the discretization error decreases at a rate of 2 which depicts a second order accuracy of the diffusion term.

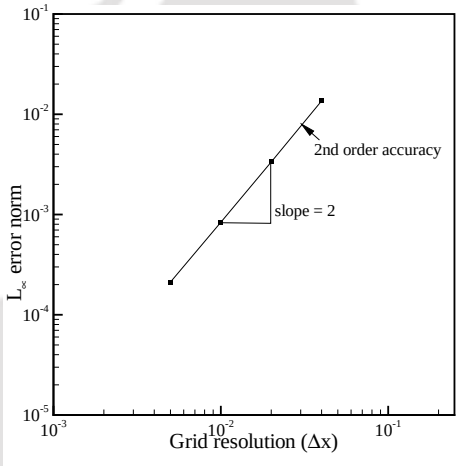

Figure 2.5: Order of accuracy for diffusive scheme.

2.10.3 Discretization error for Navier-Stokes equation

In this section, both spatial and temporal discretization errors have been computed for a Taylor-Green vortex problem. Taylor-Green vortex is an unsteady flow of a decaying vortex, which has an exact closed-form solution of the incompressible Navier-Stokes equations. A 0.5×0.5 domain has been selected for the computations. The analytical solutions for velocities (u, v) and pressure (p) are given below.

$$u = -\cos(2\pi x)\sin(2\pi y)e^{\frac{-8\pi^2 t}{Re}} \tag{2.129}$$

$$v = \sin(2\pi x)\cos(2\pi y)e^{\frac{-8\pi^2 t}{Re}} \tag{2.130}$$

$$p = \frac{-\{\cos(2\pi x) + \cos(2\pi y)\}}{4} e^{\frac{-16\pi^2 t}{Re}} \tag{2.131}$$

Dirichlet boundary conditions are specified at the boundaries by providing the exact values. The problem has been simulated for $Re = 100$ by using CUBISTA scheme for the treatment of convective fluxes, CDS for diffusive fluxes and a second order backward-difference time scheme for the discretization of the temporal term. Simulations are carried out by considering uniform hexahedral and triangulated meshes with a grid resolution of $\Delta x = 0.04,\ 0.02,\ 0.01,\ 0.005$ with $\Delta t = 5 \times 10^{-3}$ s. On similar lines using a fixed spatial resolution of Δx=0.005 simulations are carried out to evaluate the temporal discretization error by using various time step values of $\Delta t = 10^{-3}$, 5.0×10^{-4}, 2.5×10^{-4}, 1.25×10^{-4}. The numerical results obtained at $t = 1$ s are compared with the exact solutions at that particular time instant and are shown in Fig. 2.6.

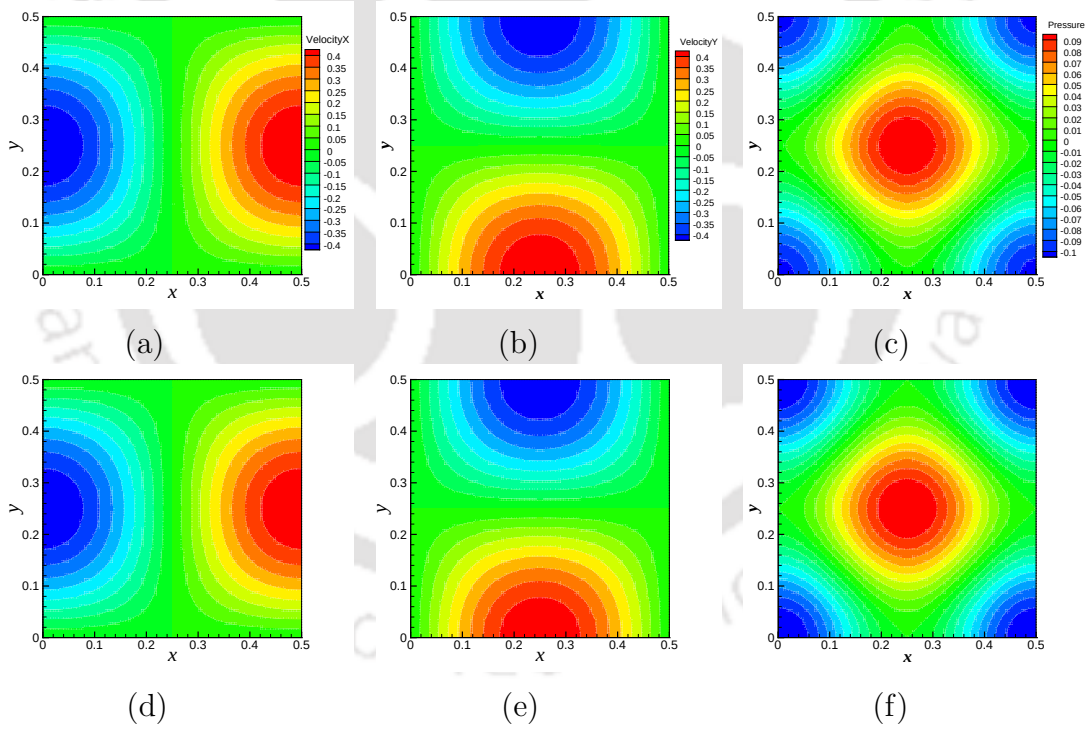

Figure 2.6: Instantaneous contours of velocity and pressure. Comparison between present simulation (a-c) with exact results (d-f) for T-G vortex problems at $t = 1$ s: (a, d) u-velocity, (b, e) v-velocity and (c, f) pressure.

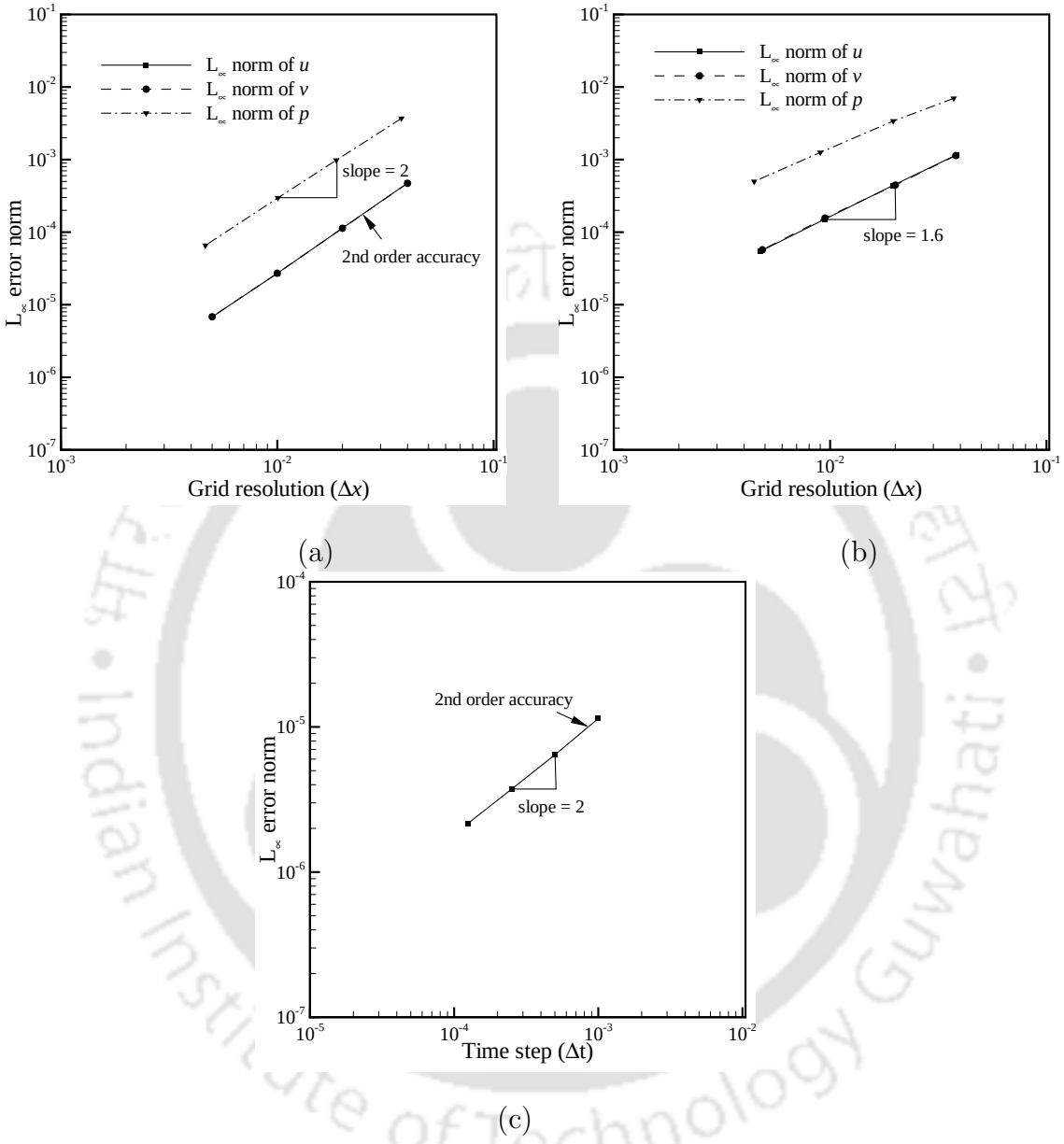

Figure 2.7: Spatial and temporal accuracy for the T-G vortex problem. (a) Spatial discretization error for uniform hexahedral meshes, (b) spatial discretization error for triangulated meshes, (c) temporal discretization error.

Numerical results are found to be in close agreement with that of the exact solutions and can be seen in Fig. 2.6. However, from the order of accuracy test as depicted in Fig. 2.7 it is seen that the spatial discretization error decreases at a rate of 2 for uniform hexahedral meshes as seen in Fig. 2.7(a). In the case of triangulated meshes, the rate of decrease of discretization error is lower than the second order (1.6) as depicted in Fig. 2.7(b). However, temporal discretization error reduces at a rate of 2 (Fig. 2.7(c)).

2.11 Closure

In this chapter, a detailed mathematical formulation for simulation of (laminar and turbulent) coupled radiative-convective flow and heat transfer is presented on unstructured FVM. A non-Boussinesq pressure based low-Mach number (LMN) formulation such as those adopted for large temperature difference convection by Paolucci [39] and extended for considering radiative heat transfer is presented. Further, a two-equation k-ε turbulence model with Favre-averaged Navier-Stokes equations are employed for handling the turbulent flow regimes. The developed computational model is nearly second order accurate (spatially and temporally) with a capability of working on any arbitrary polygonal meshes. The mathematical model shows the ability to simulate coupled convection with thermal radiation both in laminar and turbulent regimes.

Chapter 3

Validation Studies

3.1 Introduction

This chapter shows validation results of the proposed numerical model for the solution to coupled buoyancy-driven convection flows both laminar and turbulent with radiative heat transfer. Detailed validation studies are performed at every stage during the development of the solver. Firstly, the pure radiative heat transfer solver is validated for simulating surface to surface and grey-gas radiation in absorbing, emitting and scattering medium. The laminar low-Mach number solver is validated against benchmark works for natural convection flows inside an enclosure at large temperature difference. Furthermore, the convection coupled with thermal radiation solver is validated against the two- and three-dimensional problems available in the literature. Finally, the low-Mach number framework for turbulent flow is validated against experimental and numerical benchmark problems. All the test cases presented in the validation study depict an excellent agreement with the literatures.

3.2 Validation of Pure Radiation Problems

In this section pure radiative heat transfer model based on unstructured finite volume method is validated for problems with the surface to surface and gas radiation in different types of enclosure. Notably, in all the test cases the size of the spatial

and angular grids have been chosen as specified in the literature unless otherwise stated.

3.2.1 Surface to surface radiation

Surface to surface radiation problems are generally solved using surface models, in this section surface to surface radiation problems are solved using FVM by neglecting the RHS in the RTE i.e RTE does not contain any absorbing, emitting or scattering terms. Three basic problems are solved which can be found in any basic heat transfer books. Radiative heat transfer between infinite long parallel plates, between co-centric cylinders, and in a room. In all the three problems the objective is to calculate the heat flux at the walls, which is compared with the analytical results.

3.2.2 Infinitely long parallel plates

Figure 3.1 shows the grid used for the problem, the length of the plate is 20 m and the width is 1 m, the plate is made infinitely long by applying symmetry condition along the left and right boundary. The top wall is at 350 K, the bottom wall is at 300 K and the walls are assumed black. The same problem is also solved by changing the wall emissivity as 0.8 and 0.9 for the top and bottom walls respectively.

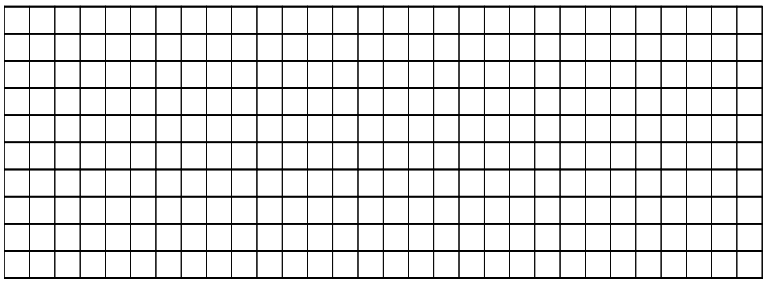

Figure 3.1: Computational domain for parallel plates

The analytical result for the heat flux at the top and bottom walls for this problem can be calculated by using the relation given below.

$$q_{12} = \frac{A\sigma\,(\,T_1^4 - T_2^4\,)}{\frac{1}{\varepsilon_1} + \frac{1}{\varepsilon_2} - 1} \tag{3.1}$$

The problem is solved by discretizing the spatial domain in 30 × 10 hexahedral grids with angular discretization of 4 × 6 in θ and ϕ direction respectively. Table 3.1 shows the wall heat flux for black walls and walls with different emissivity.

Table 3.1: Radiative heat flux at the wall between parallel plates

Temperature in K	**Wall Emissivity**	**Analytical flux**	**Numerical flux**
T_1=350.0, T_2=300.0	ϵ_1=1.0, ϵ_2=1.0	391.58 $\frac{\mathrm{W}}{\mathrm{m}^2}$	391.58 $\frac{\mathrm{W}}{\mathrm{m}^2}$
T_1=350.0, T_2=300.0	ϵ_1=0.8, ϵ_2=0.9	287.71 $\frac{\mathrm{W}}{\mathrm{m}^2}$	287.71 $\frac{\mathrm{W}}{\mathrm{m}^2}$

3.2.3 Infinitely long co-centric cylinders

Figure 3.2 shows the grid used for the problem, the length of the cocentric cylinder is 20 m and the inner and outer radius are 1 m and 2 m respectively. The cylinder is made infinitely long by applying symmetry condition along the top and bottom boundary. The outer cylinder is at 350 K and the inner cylinder is at 300 K and the walls are black, the same problem is also solved by changing the wall emissivity as 0.8 and 0.9 for the outer and inner walls respectively.

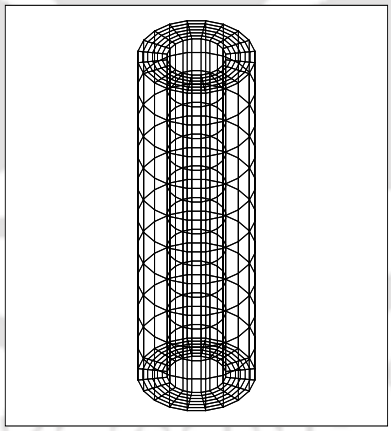

Figure 3.2: Computational domain for co-centric cylinders

The analytical result for the heat flux at the top and bottom walls for this problem can be calculated by using the relation.

$$q_{12} = \frac{A\sigma\,(\,T_1^4 - T_2^4\,)}{\frac{1}{\varepsilon_1} + \frac{1-\varepsilon_2}{\varepsilon_2}\left(\frac{r1}{r2}\right)} \tag{3.2}$$

The problem is solved by discretizing the spatial domain in 20 × 10 × 5 hexahedral grids wit angular discretization of 4 × 6 in θ and ϕ direction respectively. Table 3.2 shows the wall heat flux for black walls and walls with different emissivity.

Table 3.2: Radiative heat flux at the wall between co-centric cylinders

Temperature in K	**Wall Emissivity**	**Analytical flux**	**Numerical flux**
T_1=350.0, T_2=300.0	ϵ_1=1.0, ϵ_2=1.0	391.58 $\frac{\text{W}}{\text{m}^2}$	391.58 $\frac{\text{W}}{\text{m}^2}$
T_1=350.0, T_2=300.0	ϵ_1=0.8, ϵ_2=0.9	299.93 $\frac{\text{W}}{\text{m}^2}$	299.93 $\frac{\text{W}}{\text{m}^2}$

3.2.4 Rectangular enclosure with opening

The problem is shown in Fig. 3.3 consists of a room with all black walls. The floor of the room is at a temperature of 318 K and all the other walls including ceiling are at 298 K. There is a small window which is maintained at 283 K. The same problem is computed numerically by using 12×10×4 hexahedral grid with angular discretization of 4×20. The net heat loss by the floor is 137.39 $\frac{\text{W}}{\text{m}^2}$ calculated numerically and 137.27 $\frac{\text{W}}{\text{m}^2}$ by taking a view factor as 0.058 between the floor and window.

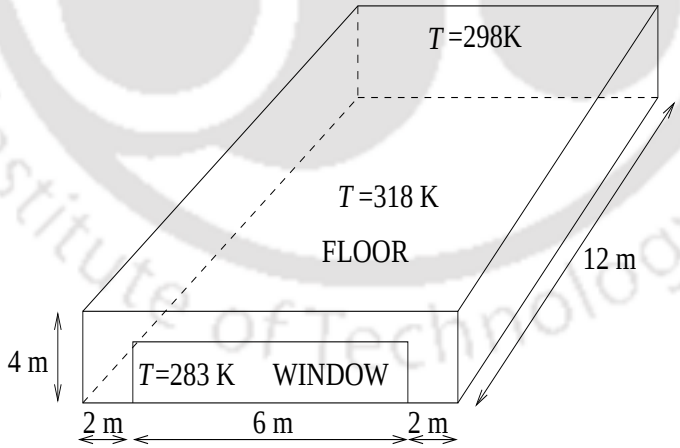

Figure 3.3: Surface radiation inside a room

From the above three problems it is seen that the present method is capable of computing surface to surface radiation.

3.2.5 Quadrilateral enclosure containing absorbing-emitting medium

The problem consists of a quadrilateral enclosure as shown in Fig. 3.4(a) filled with absorbing-emitting medium. The enclosure medium is maintained at a constant temperature T_h = 100 K while the walls are at 0 K. Three different values of absorption coefficients 0.1 m^{-1}, 1.0 m^{-1} and 10.0 m^{-1} are used in the present study while the walls of the enclosure are assumed as black. The objective is to study the non-dimensional radiative heat flux at the bottom wall. The study is carried out by employing 20×20 control volumes and 2×8 control angles as also used by Chai et al.[7].

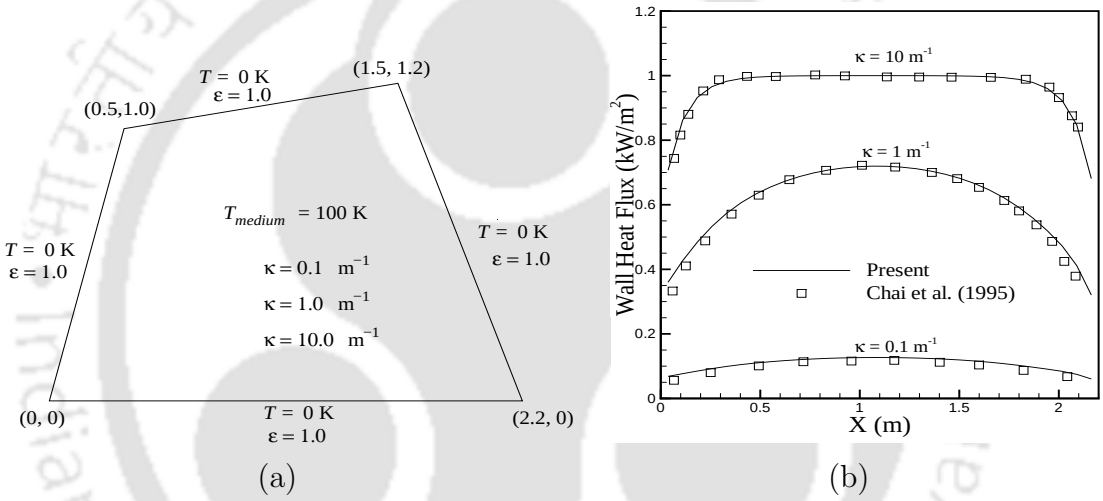

Figure 3.4: (a) Quadrilateral enclosure, (b) non-dimensional heat flux at the bottom wall for κ_a=0.1, 1.0 and 10.0

Figure 3.4(b) represents the comparison of heat fluxes at the base of the enclosure with Chai et al.[7]. From Fig. 3.4(b) an increment in wall heat flux is clearly observed with increasing absorption coefficient of the medium. For κ_a=10.0 m^{-1} the radiative heat flux is close to unity, this is primarily due to the large value of intensities incident on the wall from the neighboring hot medium. The reduction in heat fluxes near the edges is due to side cold walls. Furthermore, the reduction in absorption coefficient leads to a gradual decrease in heat flux due to the large extent of the neighboring cold walls and low self-extinction of the medium.

3.2.6 Curved enclosure containing absorbing-emitting medium

The problem consists of radiative heat transfer in an enclosure with a curved bottom wall. The top wall is at y=1.0 m, whereas the bottom wall varies as per the following relation

$$y = 0.5\,[\tanh(2 - 3x) - \tanh(2)], \quad 0 \leq x \leq 10/3 \tag{3.3}$$

Figure 3.5(a) represents the geometry of the problem where the bottom wall is black and maintained at 1000 K while the other black walls are at 0 K. The medium is kept at 0 K with a absorption coefficient of 1 m^{-1}. The objective is to calculate the heat flux at the top wall. The problem is solved numerically by using a spatial discretization of 40 $\times$ 40 grid points while the angular domain is discretized into 4 $\times$ 24 control angles in the θ and ϕ directions, respectively following the work of Chai et al.[7]. Figure 3.5 (b) represents the comparison of radiative heat flux at the top wall with the results of Chai et al.[7]. The results show good agreement with the published literature.

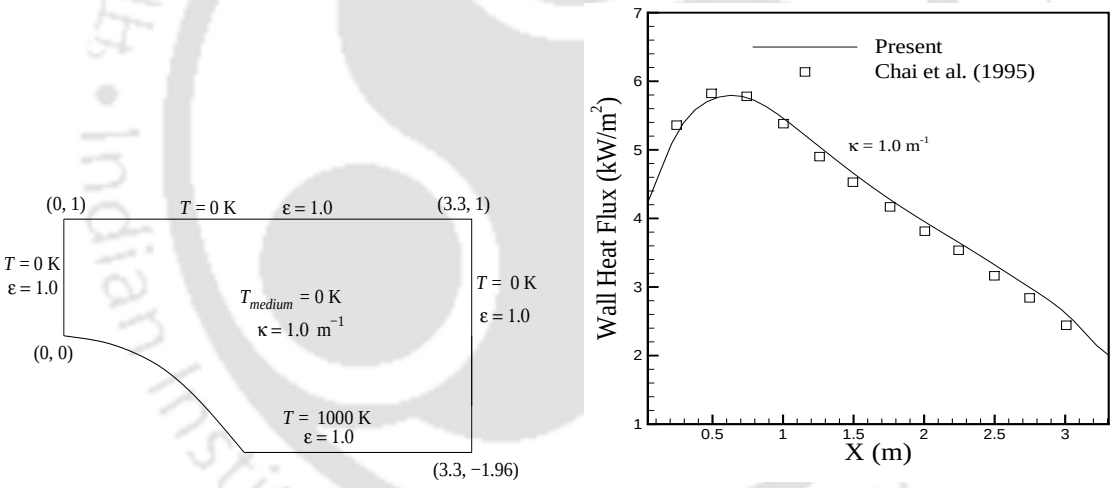

Figure 3.5: (a) Curved geometry, (b) heat flux at the top wall for κ_a=1.0 m^{-1}.

3.2.7 Radiative heat transfer in a rectangular idealized furnace

A three-dimensional radiative heat transfer problem is shown in Fig. 3.6. The problem represents a idealized combustion chamber of size 4 m × 2 m × 2 m proposed by Mengüç and Viskanta [122]. The combustion chamber is filled with a absorbing-emitting and non-scattering medium with κ_a= 0.5 m^{-1}, with a uniform heat generation of 5.0 kW/m^2. The wall boundary conditions are defined as.

X= 0 m ϵ_w= 0.85 T_w= 1200 K

X= 4 m ϵ_w= 0.70 T_w= 400 K

Rest of the walls are at 900 K with an emissivity of 0.7. The spatial domain is discretized into 25×25×25 hexahedral cells with an angular resolution of of 4 × 20 following the work of Chai et al. [5]. This problem requires the energy equation to be solved iteratively due to the presence of internal heat source term. The temperature can be updated using the relation

$$T^4 = \frac{1}{4\sigma}\left(\frac{q_{gen}}{\kappa_a} + G\right) \tag{3.4}$$

where G is the irradiation, defined as $G = \int_{4\pi} I d\Omega$ and σ is the Stefan-Boltzmann constant.

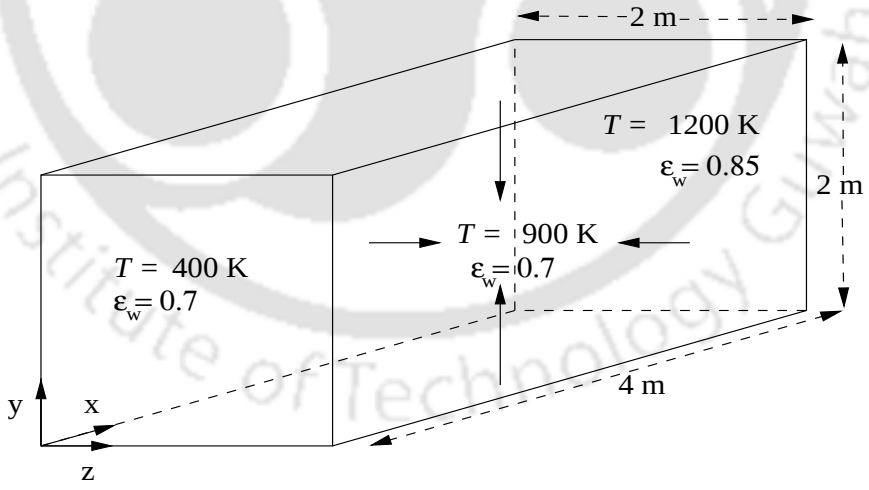

Figure 3.6: Representation of idealized combustion chamber

Figure 3.7(a) shows the temperature variation at three different planes at X= 0.4 m, 2.0 m and 3.6 m along the center line at y = 1.0 which are compared with the

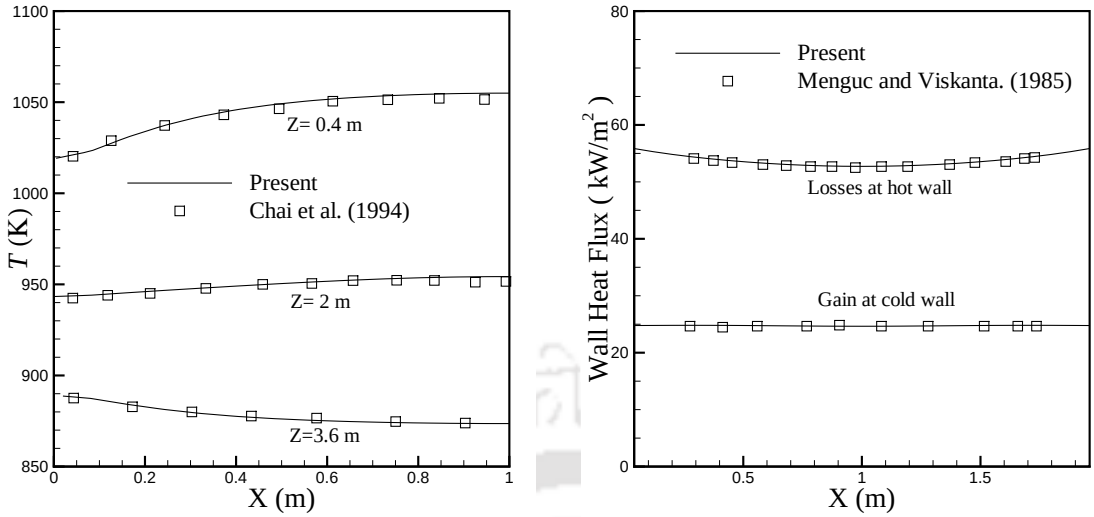

(a) (b)

Figure 3.7: (a) Comparison of temperature variations at planes X=0.4 m, 2.0 m and 3.6 m a y= 1 m, (b) radiative heat flux distribution along the hot and cold walls.

results of Chai et al. [5]. Heat flux distribution along the hot and cold walls is also shown in Fig. 3.7(b), fluxes are compared with the result of Mengüç and Viskanta [122]. Results from the present solver have a good comparison with the results of literatures.

3.2.8 Three-dimensional kidney shaped combustion chamber

A validation of three-dimensional radiative heat transfer in kidney shaped combustion chamber as shown in Fig. 3.8(a) proposed by Beak et al [16]. The dimensions of the combustion chamber are 4 m × 2 m × 2 m in X-, Y-, and Z-direction, respectively. The problem consists of a combustion chamber filled with an absorbing-emitting and non-scattering medium with a uniform heat generation of 5.0 kW/m^2. The wall boundary conditions are defined as.

X=0 m ϵ_w=0.85 T_w = 1200 K

X=4 m ϵ_w=0.70 T_w= 400 K

Rest of the walls are at 900 K with an emissivity of 0.7. The spatial domain is discretized into 20 × 10 × 10 grids in X-, Y- and Z-direction, respectively with

an angular resolution of 8 × 24 following the work of Beak et al. [16]. The energy equation is solved iteratively with radiative transfer equation until a steady state is achieved. The temperature is updated using the relation as given in Eq. (3.4)
The problem is further analyzed for κ_a=0.1, 1.0 and 5.0. The variation of isotherms at the mid-plane ($Z = Z_0/2$) for various absorption coefficient are presented in Figs. 3.8(b, c, d). Further, the radiative heat fluxes along the cold and hot walls are shown in Fig. 3.9

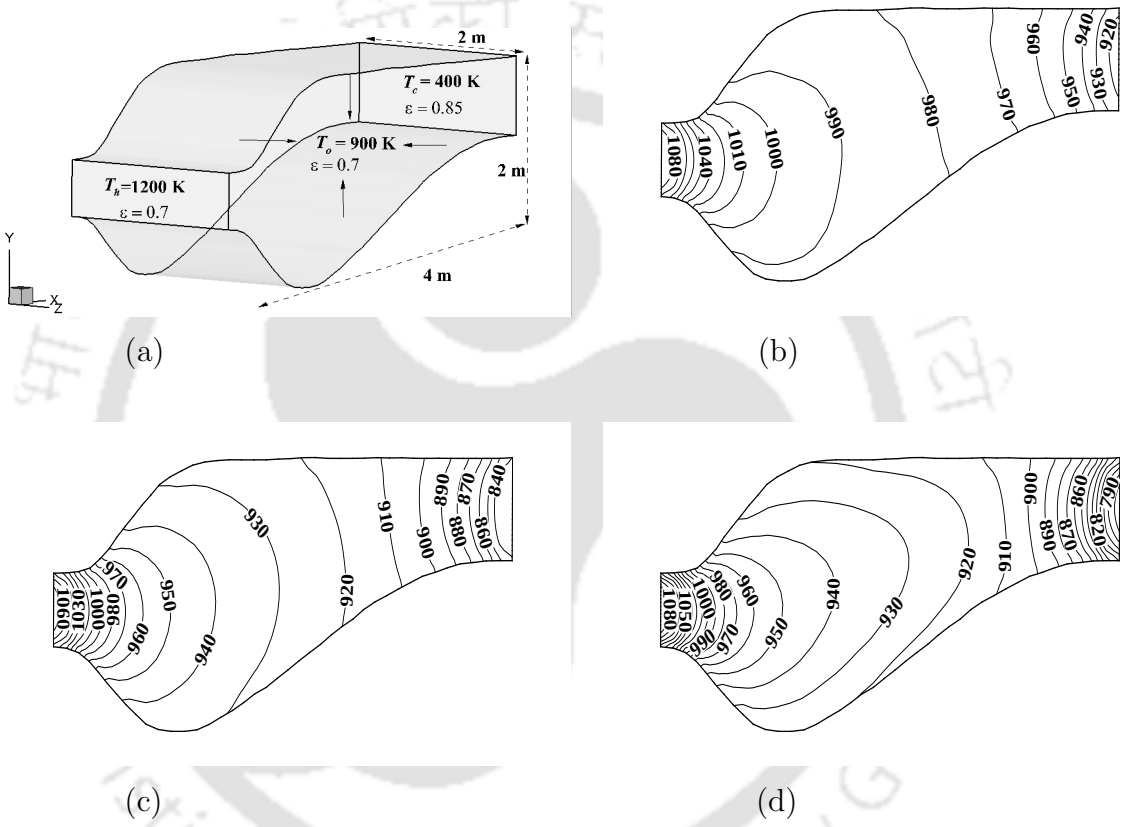

Figure 3.8: Isotherms at the mid plane z=1.0 for (b) κ_a=0.1, (c) κ_a=1.0 and (d) κ_a=5.0

From Fig. 3.9 it is evident that the heat flux decreases as the extinction coefficient increases for both hot and cold walls. The increase in extinction coefficient diminishes the mean free path which leads to an increase in total radiation absorbed by the medium. Further, from the isotherms, it is observed that for a lower extinction coefficient $\beta = 0.1$ m^{-1} the temperature is higher and more uniformly distributed

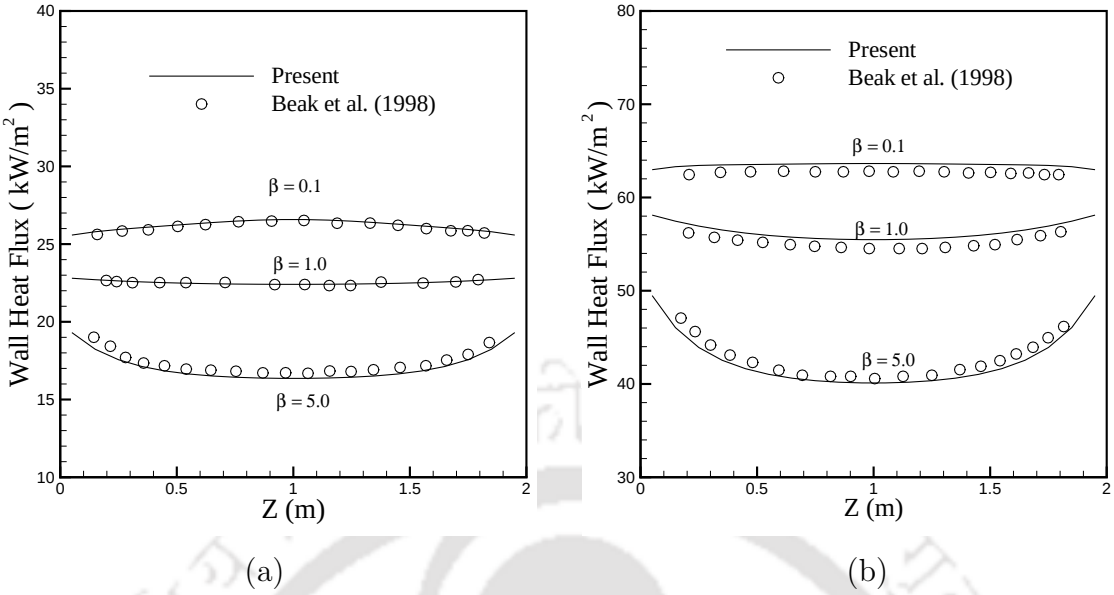

Figure 3.9: Radiative heat flux along (a) the cold wall, (b) the hot wall.

throughout the medium. This is due to the large extent of radiation in equalizing the temperature. As the extinction coefficient increases more and more radiation is absorbed by the medium which leads to a reduction in the temperature gradients near the walls. This results in a decreased heat flux at the hot and cold walls.

3.2.9 Enclosure filled with scattering medium

In this section radiative heat transfer in the pure scattering medium is discussed. The source term in RTE does not have any contribution from absorption and emission. Figure 3.5 (a) shows the geometry of the problem. All the walls are black with the bottom wall at 1000 K, while rest of the walls are at 0 K. The medium is at 0 K with scattering coefficient of 1.0 m^{-1}. The objective is to calculate radiative heat flux at the top wall. The problem is solved numerically by using a spatial resolution of 40 $\times$ 40 grid points while an angular resolution of 4 $\times$ 24 control angles is used in the θ and ϕ directions, respectively following the work of Chai et al.[7]. Figure 3.10 shows the radiative heat flux at the top wall compared with the results of Chai et al.[7]. A similar problem considering absorbing emitting medium was discussed in the previous section, comparing the heat flux from Fig. 3.5 shows that the heat flux is higher in the present case considering only the scattering medium. The increase in

heat flux is due to the far-reaching effect of radiation and negligible self-extinction of the medium.

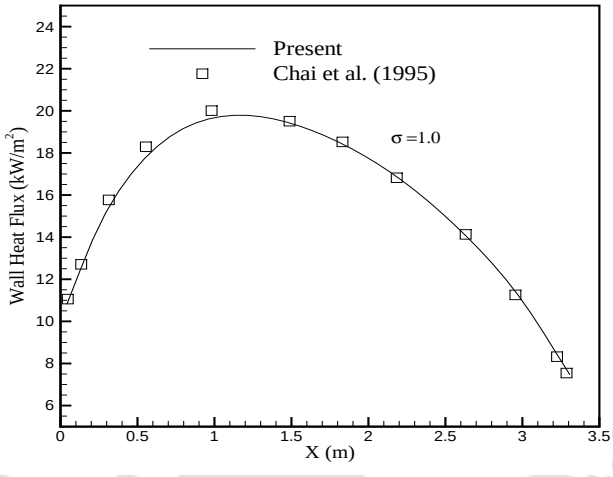

Figure 3.10: Heat flux at top wall

3.2.10 Enclosure filled with absorbing emitting and scattering medium

In this section, the entire RTE considering the absorbing, emitting and scattering medium is discussed. The validation problem discussed here is similar to the problem discussed in section 3.2.7, the problem is now resolved including the scattering effects with the same spatial and angular grids as previously used in section 3.2.7. The medium has a scattering albedo $\omega = 0.7$ and extinction coefficient of $\kappa_a = 0.5$ m^{-1}. Figure 3.11 shows the temperature variation at three different locations at $X = 0.4$ m, 2.0 m and 3.6 m along a line at $Y = 1$ m compared with the results of Truelove [123].

3.3 Variable Density Flows at Large Temperature Difference

In this section validation studies are presented for the developed low-Mach number algorithm for variable density flows at large temperature difference. The developed

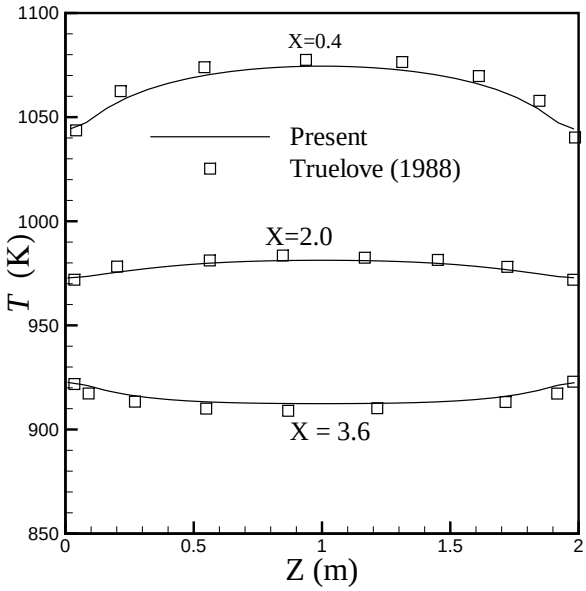

Figure 3.11: Temperature distribution at $Y = 1$ m

low-Mach number solver is validated against a simple differentially heated cavity problem at $Ga = 1.2$, $Ra = 10^6$. Contribution from various researchers was collected and published as a benchmark solution for this problem involving low-Mach number flows. The problem is solved for $Ra = 10^6$ and $Pr = 0.71$. The initial temperature of the cavity is 600 K and for a temperature difference parameter (Boussinesq parameter, $\frac{\Delta T}{2T_o}$=0.6) the hot and cold wall temperatures are obtained as 940 K and 260 K. At this large temperature difference, Boussinesq approximation fails to encounter the density variation arising due to large temperature gradients, hence this problem serves as a perfect validation for the present algorithm. The geometry of the problem is shown in Fig. 3.12 (a). The problem is solved by considering density variation with constant and variable temperature dependent thermo-physical properties. The property variation is considered using Sutherland's law. A uniform grid size of 300×300 is employed in the present study following the work of Darbandi and Hosseinizadeh [124] and a time step size of $\Delta t = 10^{-2}$ is used.

Tables 3.3 and 3.4 represent the average Nusselt number variation at the hot and cold walls compared with the results presented by various researchers Le Quéré et al.[125]. Furthermore, the local Nusselt number variation at the hot and cold walls is compared with the results of Darbandi and Hosseinizadeh [124] as presented in Fig. 3.12 (b). The local and average Nusselt number values are in excellent agreement

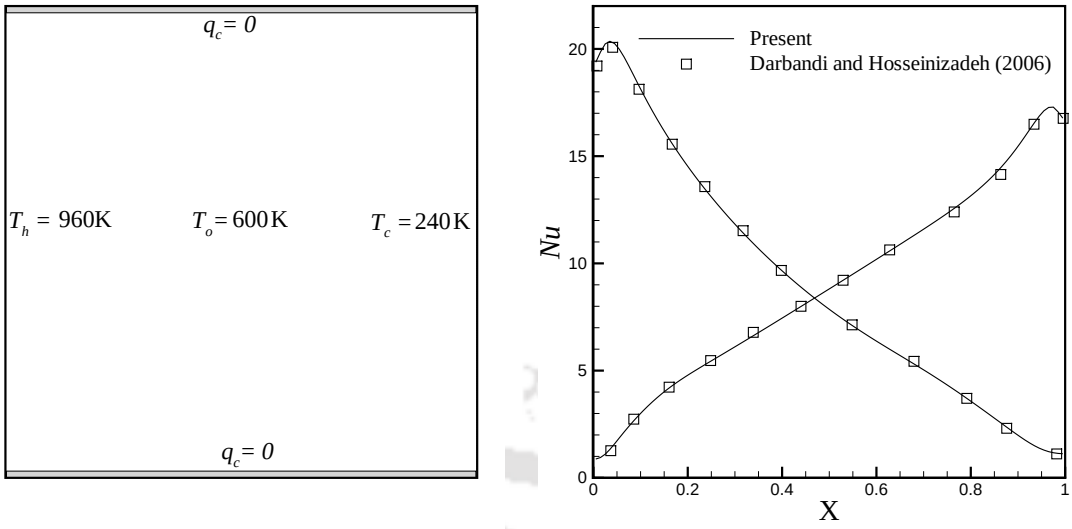

(a) (b)

Figure 3.12: (a) Geometry with boundary condition, (b) Nusselt number variation at hot and cold walls.

Table 3.3: Comparison of average Nusselt number at $Ra = 10^6$, $Ga = 1.2$ and constant thermo-physical properties with Le Quéré et al. (2005).

Parameters	**Vierendeels and Dick**	**Le Quéré**	**Locke**	**Present**
Nu_h	8.85	8.85	8.85	8.86
Nu_c	8.85	8.85	8.85	8.86

with the literature.

3.4 Variable Density Flows at Large Temperature Difference Coupled with Radiation

This section presents validation studies for buoyancy assisted convection with gas radiation in a two-dimensional square enclosure differentially heated at large temperature difference with significant influence of radiative heat transfer. The problem is solved for $Ra = 5 \times 10^6$, $Pr = 0.71$, $Pl = 0.02$ and $Ga = 0.66$. The optical

Table 3.4: Comparison of average Nusselt number at $Ra = 10^6$, $Ga = 1.2$ and temperature dependent thermo-physical properties with Le Quéré et al. (2005).

Parameters	**Vierendeels and Dick**	**Le Quéré**	**Locke**	**Present**
Nu_h	8.68	8.68	8.68	8.68
Nu_c	8.68	8.68	8.68	8.68

thickness value of $\tau = 0.20$ is used in the present simulation with an aim to validate a non-Boussinesq combined radiative-convective heat transfer in an absorbing, emitting medium. The basic geometry of the problem is depicted in Fig. 3.13 (a), the problem is solved with two spatial grids (a) a uniform hexahedral mesh of size 300×300 and (b) a non-uniform tetrahedral mesh with 94696 control volumes. The grid resolution of 300×300 and angular resolution of 1×14 has been chosen following the work of Darbandi and Abrar [33]. The details of the non-uniform mesh has been defined in Fig. 3.13 (b) and a time step size of $\Delta t = 10^{-2}$ is used in the present simulation. Figure 3.14 (a) represents the variation of local values of convection, and total (convection and radiation) Nusselt number along the hot and cold walls. Figure 3.14 (b) represents the centerline velocity variations along the horizontal and vertical mid-plane of the cavity. These results depict very good agreement with the work of Darbandi and Abrar [33]. The average values of Nusselt number (convection, radiation and total) at the hot and cold walls are tabulated in Table 3.5 and the values are compared with the literature. From these results, it is seen that the present model can accurately predict non-Boussinesq natural convection with gas radiation inside enclosures.

Table 3.5: Average convective, radiative and total Nusselt number at the hot and cold wall for $\tau = 0.20$: Comparison with Darbandi and Abrar (2014).

Nusselt number	Nu_c	Nu_c	Nu_r	Nu_r	Nu_t	Nu_t
Wall	Hot	Cold	Hot	Cold	Hot	Cold
Darbandi and Abrar (2014)	8.44	15.29	37.98	30.12	46.43	46.41
Present hexahedral mesh	8.43	15.30	37.95	31.08	46.38	46.38
Present tetrahedral mesh	8.45	15.27	37.96	31.14	46.41	46.41

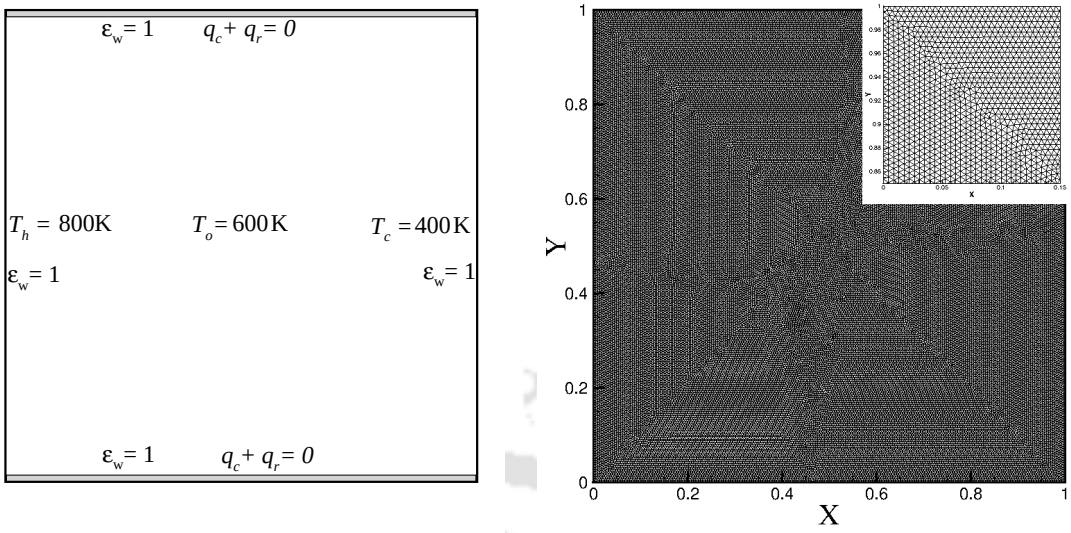

(a) (b)

Figure 3.13: Schematic of the computational domain and mesh used in the study.

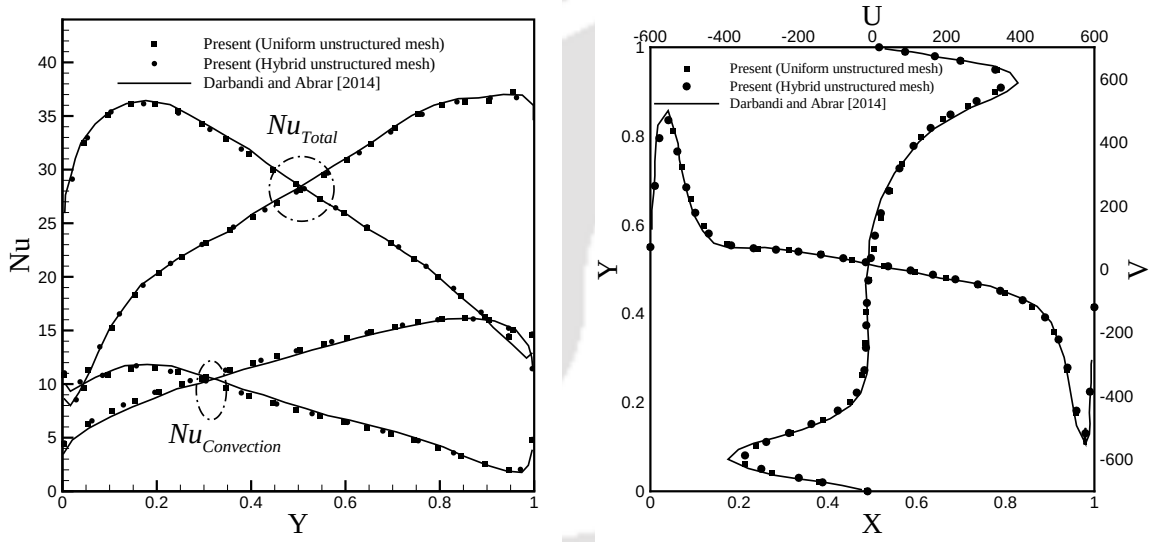

(a) (b)

Figure 3.14: (a) Local Nusselt number variation at hot and cold walls, (b) velocity variation along the horizontal and vertical centerline.

3.5 Turbulent Natural Convection Inside the Enclosure

In this section, studies are performed to validate the present low-Mach number model for simulating turbulent natural convection in a differentially heated cavity

for two different Rayleigh numbers $Ra = 1.58 \times 10^9$ and $Ra = 5 \times 10^{10}$.

Comparison at $Ra = 1.58 \times 10^9$

This study consists of an experimental validation involving turbulent natural convection in a cavity of dimensions 0.75 × 0.75 × 1.5 m performed by Ampofo and Karayiannis [80]. They reported two-dimensional results at a Rayleigh number of $Ra = 1.58 \times 10^9$. The experimental benchmark data provided by Ampofo and Karayiannis [80] has been extensively used by many researchers to validate the numerical models for turbulent natural convection in the enclosure by Sharma et al. [90], Miroshnichenko et al. [97]. The present validation study is carried out by using the experimental and numerical data using the work of Ampofo and Karayiannis [80], Sharma et al. [90] and Miroshnichenko et al. [97].A non-uniform mesh of size 120×120 following the work of Miroshnichenko et al. [97] has been employed and a time step size of $\Delta t = 10^{-3}$ is used to carry out the simulation.

Figure 3.15 (d, e) represents the comparison of centerline temperature and velocity variation at the horizontal mid-plane. Results are also presented by using an incompressible model for solving buoyancy driven turbulent flows by using RANS equation. The results obtained using both incompressible and quasi-incompressible LMN model are seen to be in good agreement with the experimental results presented by Ampofo and Karayiannis [80].

Comparison at $Ra = 5 \times 10^{10}$

This study consists of a numerical validation of turbulent natural convection in a differentially heated cavity performed by Henkes and Hoogendoorn [84]. They presented numerical results at $Ra = 5 \times 10^{10}$, $Pr = 0.71$ using a standard $k - \varepsilon$ model and compared the results provided with ten other researchers. Hence, this test case serves as an ideal problem for validation of the developed solver. A non-uniform mesh of size 160×160 following the work of Henkes and Hoogendoorn [84] has been employed to carry out this study. Furthermore, the grid refinement has been carried out by using a relation for grid distribution as suggested by Henkes and Hoogendoorn [84]. Figure 3.16 (a-c) represents the comparison of temperature, velocity, and the ratio of turbulent to laminar viscosity respectively with the results of Henkes and Hoogendoorn [84]. The variations of temperature, velocity and viscosity ratio are seen to match well with the published literature. This study demonstrates the capability of the developed incompressible and quasi-incompressible low-Mach number solver for simulating laminar and turbulent buoyancy-driven convection coupled with thermal radiative heat transfer in enclosures.

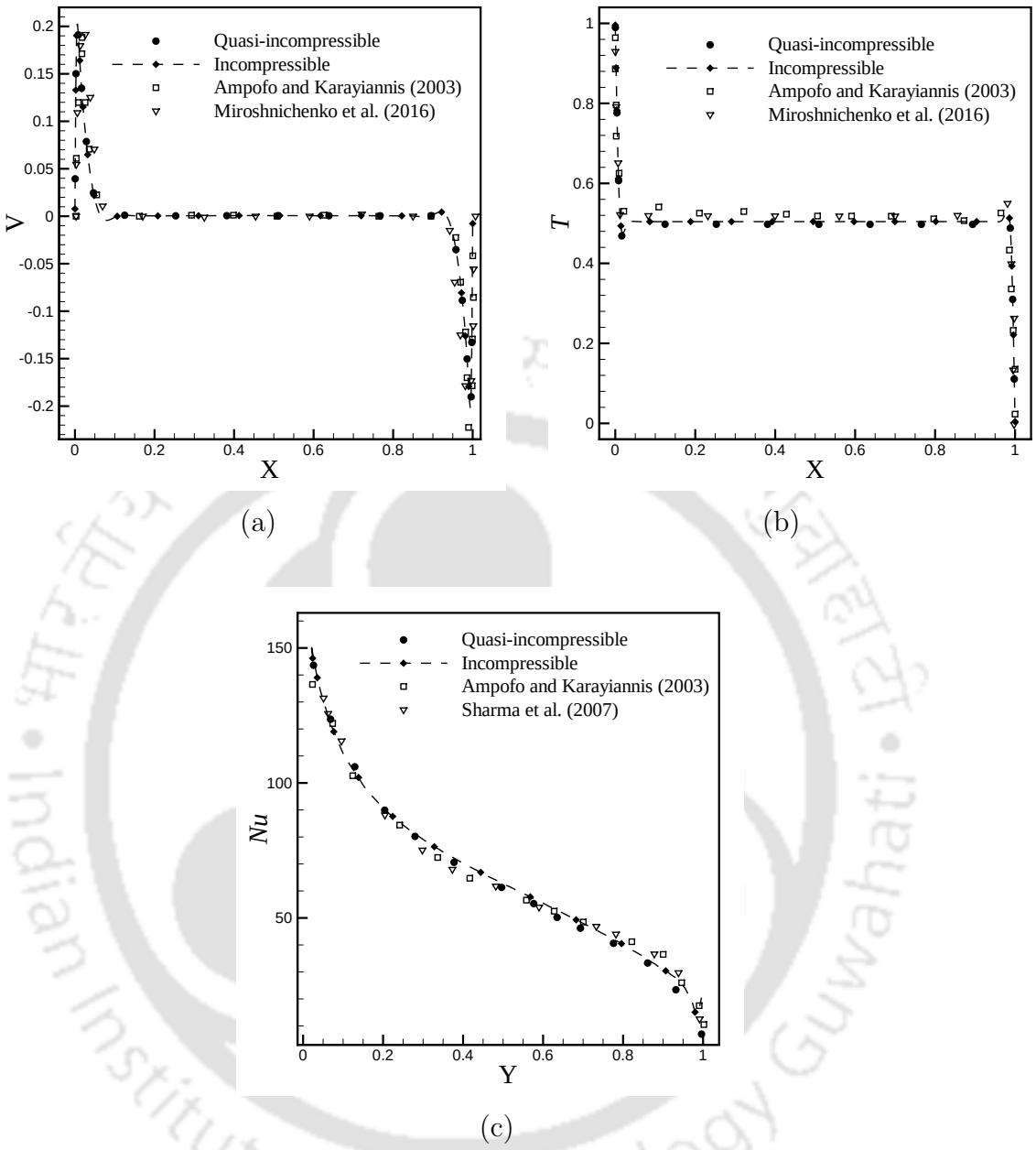

Figure 3.15: Validation of turbulent natural convection with the experimental results of Ampofo and Karayiannis (2003), Sharma et al. (2007), and Miroshnichenko et al. (2016), (a) comparison of velocity variation along the horizontal centerline, (b, e) comparison of temperature variation along the horizontal centerline, (c) comparison of local Nusselt number variation at the hot wall.

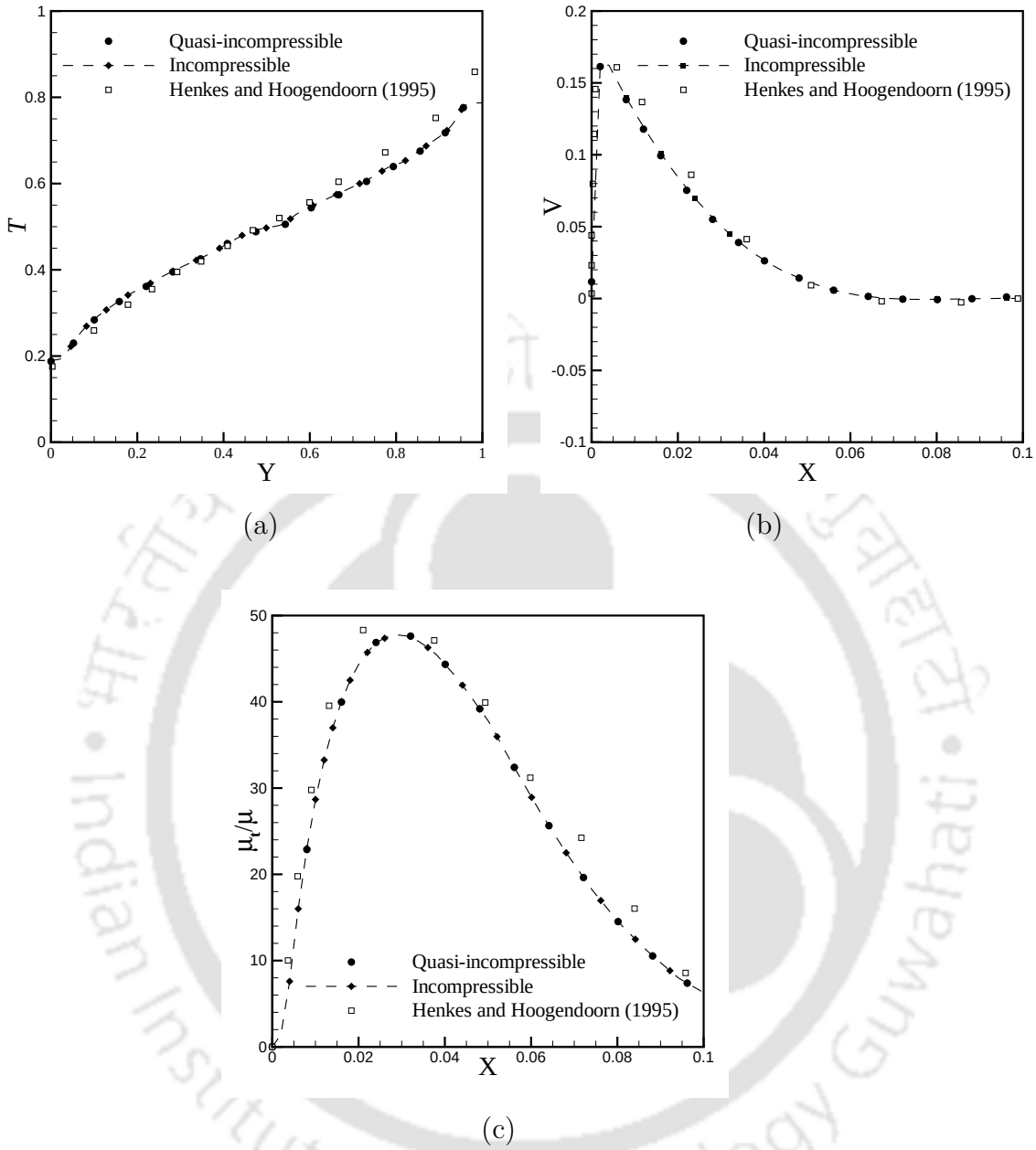

Figure 3.16: Validation of turbulent natural convection in a differentially heated cavity with the numerical results of Henkes and Hoogendoorn (1995), (a) temperature variation along the vertical centerline, (b) velocity variation along the horizontal centerline, (c) ratio of turbulent to laminar viscosity along the horizontal center line.

3.6 Closure

In this chapter, a detailed validation of the developed solver for simulating coupled buoyancy-driven convection (laminar and turbulent) with the radiative transfer is performed. A number of validation studies comprising of pure radiative heat transfer, laminar natural convection flows at large temperature difference with and without the influence of thermal radiation and turbulent natural convection in enclosures is performed. All the test cases presented in the validation study depict an excellent agreement with the published literature.

Chapter 4

Applicability of Boussinesq Approximation to Radiative-Convective Flows

4.1 Introduction

In this chapter, investigations are performed to check the validity of Boussinesq approximation which is typically used in the radiative-convective flows. Incompressible flow solver based on constant density advection, zero velocity divergence and Boussinesq approximation based on a first-order series expansion of density as a function of temperature field in the body force terms is a preferred choice for solving these class of problems. However, in problems involving large temperature difference natural convection and those coupled with radiation, the use of Boussinesq approximation does not remain valid. In this chapter, the investigations are targeted at quantifying the deviations in the results when the Boussinesq approximation is violated. Fur-

The contents of this chapter have been published as Parmananda, M., Dalal, A., and Natarajan, G., 2018, "Critical assessment of numerical algorithms for convective-radiative heat transfer in enclosures with different geometries", International Journal of Heat and Mass Transfer, (available online, DOI: https://doi.org/10.1016/j.ijheatmasstransfer.2016.12.033).

thermore, the results from the present non-Boussinesq low-Mach number solver is verified by performing comparisons against the results obtained using a compressible model of OpenFOAM [121].

4.2 Validity of Incompressible Model for Radiative-Convective Flows

In this section numerical studies have been performed to check the validity of popularly used incompressible model based on the Boussinesq approximation for radiative-convective flow and heat transfer in an enclosure. It is very well known that the incompressible model is based on zero velocity divergence, however, the low-Mach number model presented in this work uses a non-zero velocity divergence condition presented in Eq. (4.1).

$$\frac{\partial u_j}{\partial x_j} = \frac{1}{\overline{P}} \left[\frac{-1}{\gamma} \frac{d\overline{P}}{dt} + \frac{Ga}{\sqrt{Ra\,Pr}} \frac{\partial}{\partial x_j} \left(\frac{\partial T}{\partial x_j} \right) + \frac{1}{Pl\,\sqrt{Ra\,Pr}} \frac{\partial q_{rj}}{\partial x_j} \right] \tag{4.1}$$

From Eq. (4.1) it is evident that at large Ga (large temperature difference) and small Pl (significant radiation) the divergence of velocity has a finite non-zero value that increases with increase in temperature difference and as radiative heat transfer becomes significant. In this context, studies have been performed for combined buoyancy driven convection coupled with thermal radiation in enclosures using an incompressible model based on Boussinesq approximation, a quasi-incompressible model based on low-Mach number formulation (LMN) and compressible model using OpenFOAM [121]. The first case presents radiative-convective flow and heat transfer in an enclosure with a heated cylinder at small temperature difference with the moderate influence of radiation where it is expected that the Boussinesq and non-Boussinesq models would produce same results. Secondly, a similar problem comprising of coupled convection at large temperature difference with a moderate influence of surface and gas radiation is studied. This test case is studied with an aim to check the validity of Boussinesq approximation at large temperature difference in presence of radiation. In the third test case, a similar problem is solved where the temperature difference is small however the mean temperature is high enough so that the radiative heat transfer effects become significant. This test case depicts the

invalidity of Boussinesq approximation for convective radiative flows with significant influence of thermal radiation. The solutions obtained using the compressible model of OpenFOAM are shown to agree well with the quasi-incompressible LMN model and hence this study also presents a verification of the developed LMN model.

4.2.1 Convective-radiative flows at small temperature difference

The test problem consists of a combined convection with surface radiation heat transfer in a square enclosure of dimension H containing a heated cylinder of radius $0.2H$ as depicted in Fig. 4.1 (a). The vertical walls of the enclosure are isothermal cold walls whereas the horizontal top, and bottom walls are adiabatic, and the cylinder is heated at a constant temperature. The values of non-dimensional parameters governing the flow and heat transfer are $Ra = 10^6$, $Pr = 0.71$, $Ga = 0.05$. The problem was originally solved by Mezrhab et al. [71] using an incompressible model based on Boussinesq approximation. The given problem has been numerically simulated by employing a hybrid mesh of 41100 control volumes. The details of the non-uniform unstructured mesh is depicted in Fig. 4.1 (b) and consists of a combination of hexahedral and tetrahedral elements. The spatial grid size of 41100 control volumes has been considered following the work of Mezrhab et al. [71] who have used a mesh size of 200×200. A angular resolution of 4×16 is used in the present study for the computations of radiative heat transfer. A time step size of $\Delta t = 10^{-2}$ is used for arriving at steady state. Figure 4.2 represents the comparison of temperature variation along the horizontal planes at $Y = 0$ and $Y = H$ of the square enclosure with the published work of Mezrhab et al. [71]. Table 4.1 represents the average Nusselt number variation at the heated cylinder for the incompressible, quasi-incompressible (LMN) and compressible model of OpenFOAM compared with the results of Mezrhab et al. [71]. The results are in excellent agreement with the published literature. From these results, it is seen that incompressible model are able to capture the correct flow physics at small temperature difference with the moderate influence of radiation.

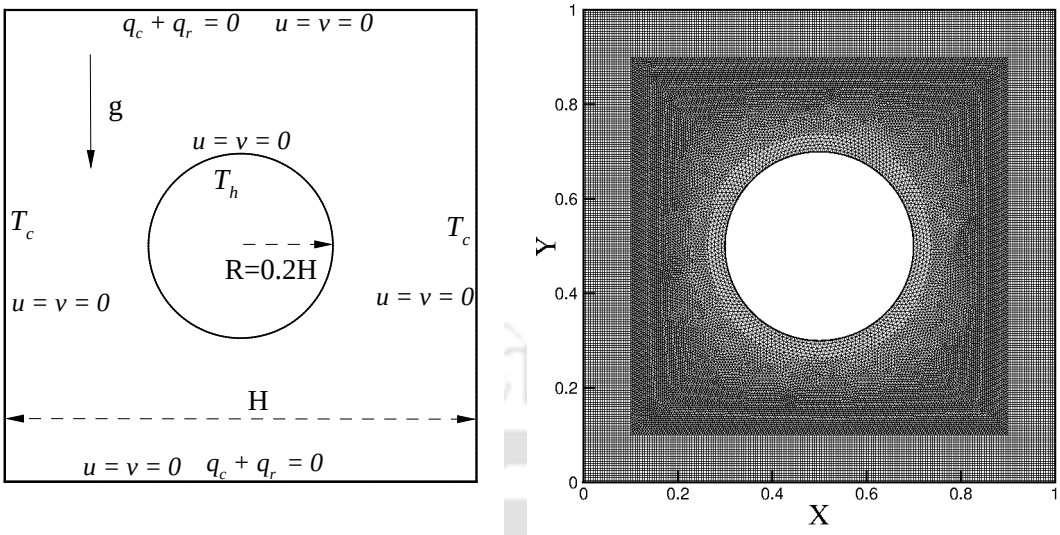

(a) (b)

Figure 4.1: Schematic of the computational domain and mesh used in the present study.

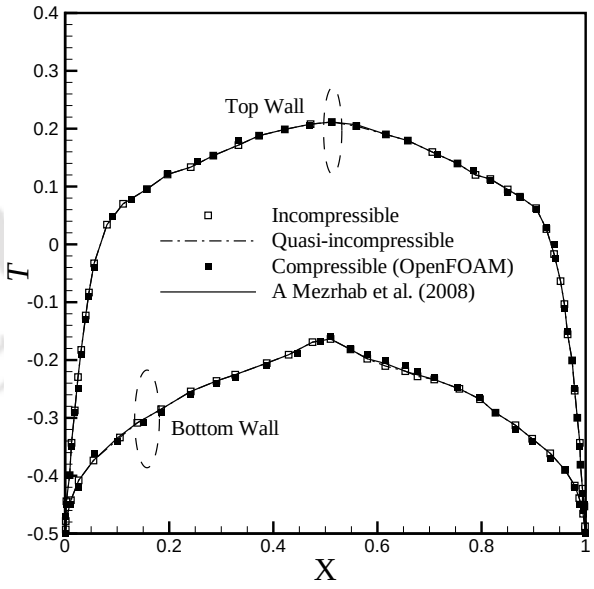

Figure 4.2: Comparison of the temperature variation at the top and bottom walls of the cavity using incompressible, LMN, and compressible models with the published results of Mezrhab et al. (2008).

Table 4.1: Comparison of average values of Nusselt number at the heated cylinder with the work of Mezrhab et al. (2008).

Author	Nu_c	Nu_r	Nu_t
Mezrhab et al. (2008)	14.354	16.654	31.00
Present	14.410	16.626	31.040

4.2.2 Convective-radiative flows at large temperature difference

In the present study, the interest is to numerically investigate a combined radiative-convective heat transfer inside a cavity with a heated cylinder at large temperature difference. The geometry consists of a square cavity of length H enclosing a heated triangular cylinder as shown in Fig. 4.3. The side of the heated cylinder is 0.2 times the length of the square cavity. The cavity is filled with air as the participating medium at an initial temperature of $T_0 = 600$ K, constant air properties are evaluated at the initial medium temperature. The Boussinesq parameter of ($\frac{\Delta T}{2T_o}$=0.5) is used in the present study which leads to the hot cylinder and cold enclosure wall temperatures as $T_h = 900$ K, $T_c = 300$ K, respectively. The non-dimensional hot and cold wall temperatures are obtained as 1 and 0, respectively while the values of other non-dimensional parameters used in the present study are $Ra = 10^6$, $Pr = 0.68$, $Ga = 1$ and $Pl = 0.0135$.

The boundary conditions are given below.

$$\text{Walls of square cavity:} \quad u = v = 0,\ T = 0$$

$$\text{Cylinder wall:} \quad u = v = 0,\ T = 1$$

$$I_w(\mathbf{r}, \mathbf{s}) = \varepsilon_w I_b + \frac{1 - \varepsilon_w}{\pi} \int\limits_{\mathbf{s}\cdot\hat{\mathbf{n}}>0} I(\mathbf{r}, \mathbf{s})\, \mathbf{s} \cdot \hat{\mathbf{n}}\, \mathrm{d}\Omega \tag{4.2}$$

where $\hat{\mathrm{n}}$ is the outward normal vector at the boundary and Nu_c, Nu_r and Nu_t are the local convective, radiative and total Nusselt number at the heated cylinder. These are calculated from the heat flux as follows.

$$Nu_c = \frac{q_c L}{k\Delta T},\ Nu_r = \frac{q_r L}{k\Delta T},\ Nu_t = Nu_c + Nu_r \tag{4.3}$$

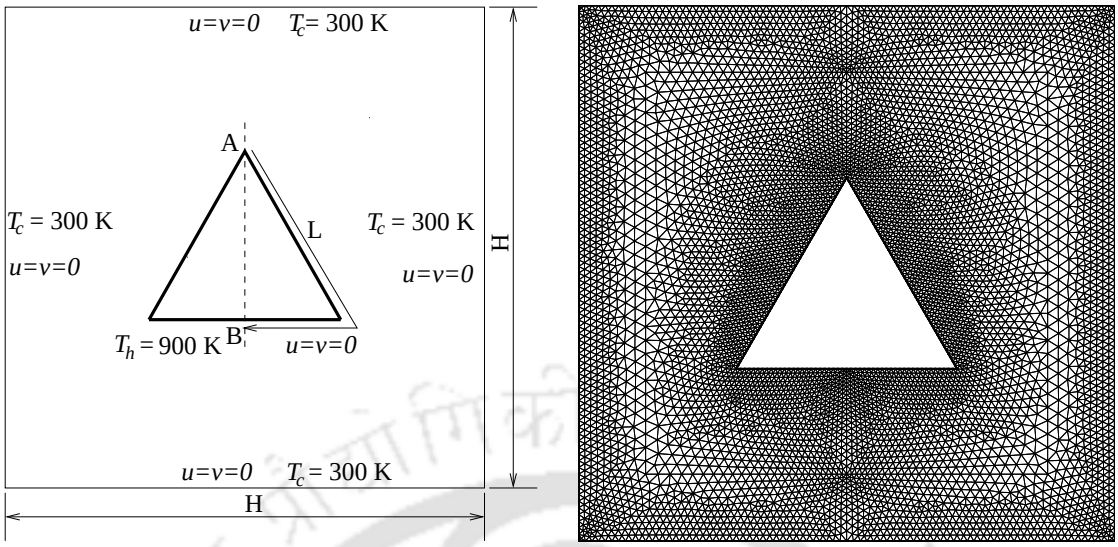

(a) (b)

Figure 4.3: Schematic of the computational domain and mesh used in the present study.

Where q_c and q_r are the convective and radiative fluxes and L is half of the perimeter of the heated cylinder from A to B taken clockwise as shown in Fig. 4.3.

Before solving the present problem, a spatial and angular grid independent tests were performed to obtain an optimal resolution of the spatial and angular domain. The study considered the case of participating medium having an optical thickness of $\tau = 2.0$. Three different spatial grids of size 6961, 15941 and 34105 cells were used with fixed angular size of 2×8. The Nusselt number values of 54.50, 53.83 and 53.80 were obtained at the hot wall between A-B (Fig. 4.3 (a)) using the quasi-incompressible approach as shown in Table 4.2. Any grid size larger than 15941 does not change the value of Nusselt number significantly. Nusselt number values of 53.99, 53.83 and 53.81 are obtained for an angular resolution of 2×8, 4×8 and 4×16 as seen from Table 4.2 with a fixed spatial grid of 15941. Any angular resolution larger than 4×8 does not change the solution significantly. Hence, an angular resolution of 4×8 and a grid size of 15941 are used in all simulation. Notable, this study was performed by using non-uniform tetrahedral elements with grid clustering near the heated cylinder and enclosure walls as depicted in Fig. 4.3 (b) and a time step size of $\Delta t = 5 \times 10^{-3}$.

The average Nusselt number of the heated cylinder is the line-averaged value of

Table 4.2: Average Nusselt number(total) values obtained for various spatial and angular mesh used in the grid independence study for a square cavity containing a heated cylinder.

Angular Grid ($N_\theta \times N_\phi$)	2×8		
Spatial Grid ($N_x \times N_y$)	6961	15941	34105
Nusselt number (Nu_t)	54.50	53.83	53.80
Spatial Grid ($N_x \times N_y$)	15941		
Angular Grid ($N_\theta \times N_\phi$)	2×8	4×8	4×16
Nusselt number (Nu_t)	53.99	53.83	53.81

Nu. The variation of flow and heat transfer in the square enclosure with a triangular shaped heated cylinder is studied using quasi-incompressible LMN model. Further, the effects of non-participating (surface to surface radiation) and the participating gas medium are investigated. Isotherms are shown in Figs. 4.4 (a, b, c) for the surface to surface and gas radiation with optical thickness values of $\tau = 2$ and 5. Isotherms and streamlines for surface radiation in Figs. 4.4 (a, d) depict that a strong buoyancy current causes the fluid above the heated cylinder to rise up till the top wall. The cold top wall cools the impinging hot plume and deviates it towards the side walls. The interaction of the fluid with the side walls causes it to cool, which further descends the fluid to the bottom of the cavity. The cold fluid at the bottom half of the cavity again interacts with the heated cylinder and a flow pattern comprising of two primary vortices rotating in opposite direction symmetrically along the mid vertical plane of the cavity is formed as shown in Fig. 4.4 (d). The formation of flow pattern is assisted by sharp temperature gradients as observed near the heated cylinder and also along the top wall of the cavity. The temperature gradients are homogeneous near the bottom wall. This cause density variation which actuates flow inside the cavity.

However, the inclusion of gas radiation depicts the formation of secondary vortices in addition to two primary vortices, as seen in Figs. 4.4 (e, f) just above the heated cylinder. The secondary vortices deviate the hot plume above the heated

cylinder to rise diagonally, along the vertical axis of the cavity. The formation of secondary vortices causes the temperature just above the heated cylinder to dip and as a result, sharp temperature gradients are observed near the top of the heated cylinder as shown in Figs. 4.4 (b, c). The cores of the primary vortices are located near the top of the heated cylinder for the surface to surface radiation case seen in Fig. 4.4 (d). The location of cores in the primary vortices indicates the presence of strong buoyancy currents in the upper half of the enclosure. With the presence of participating medium, the total radiation absorbed by the medium increases. The increase in absorption of the radiation by the participating medium leads to reduced temperature gradients near the hot and cold walls. With a reduction in the temperature gradients near the hot walls, the density gradients are diminished. This weakens the buoyancy currents in the upper half of the cavity above the heated cylinder. The effect of participating medium as seen from Figs. 4.4 (e, f) is to push the core of the primary vortices to the bottom half of the cavity due to weak buoyancy currents above the heated cylinder. The weakened buoyancy currents above the heated cylinder also cause the formation of secondary vortices just above the heated cylinder for optical thickness τ= 2. Further increase in the optical thickness of the participating medium to τ = 5, adds to the weakening of the buoyancy currents. As a result of this weakening the primary vortices are yet pushed to the bottom of the cavity and strength of secondary vortices are diminished.

The importance of using a non-Boussinesq model for coupled buoyancy driven convection with surface and gas radiation at large temperature difference is realized from the isotherms and streamlines variation depicted in Fig. 4.5 for optical thickness τ=5 case. From Fig. 4.5 it is clearly seen that the results at all optical thickness between the different models are consistent between LMN and fully compressible approaches. This consistency is also reflected in the isotherms and streamlines where excellent agreement is obtained between the results of LMN and compressible model as seen in Fig. 4.5. However, it also shows that results from incompressible formulation are completely different from those obtained with other two models. The secondary vorticec formed just above the heated cylinder are accurately captured by the quasi-incompressible (LMN) and compressible model of OpenFOAM. Whereas, the incompressible model depicts the formation of primary vortex Fig. 4.5 (d) only. The implications of using an incompressible model are briefly described from the temperature, velocity and Nusselt number variation inside the enclosure.

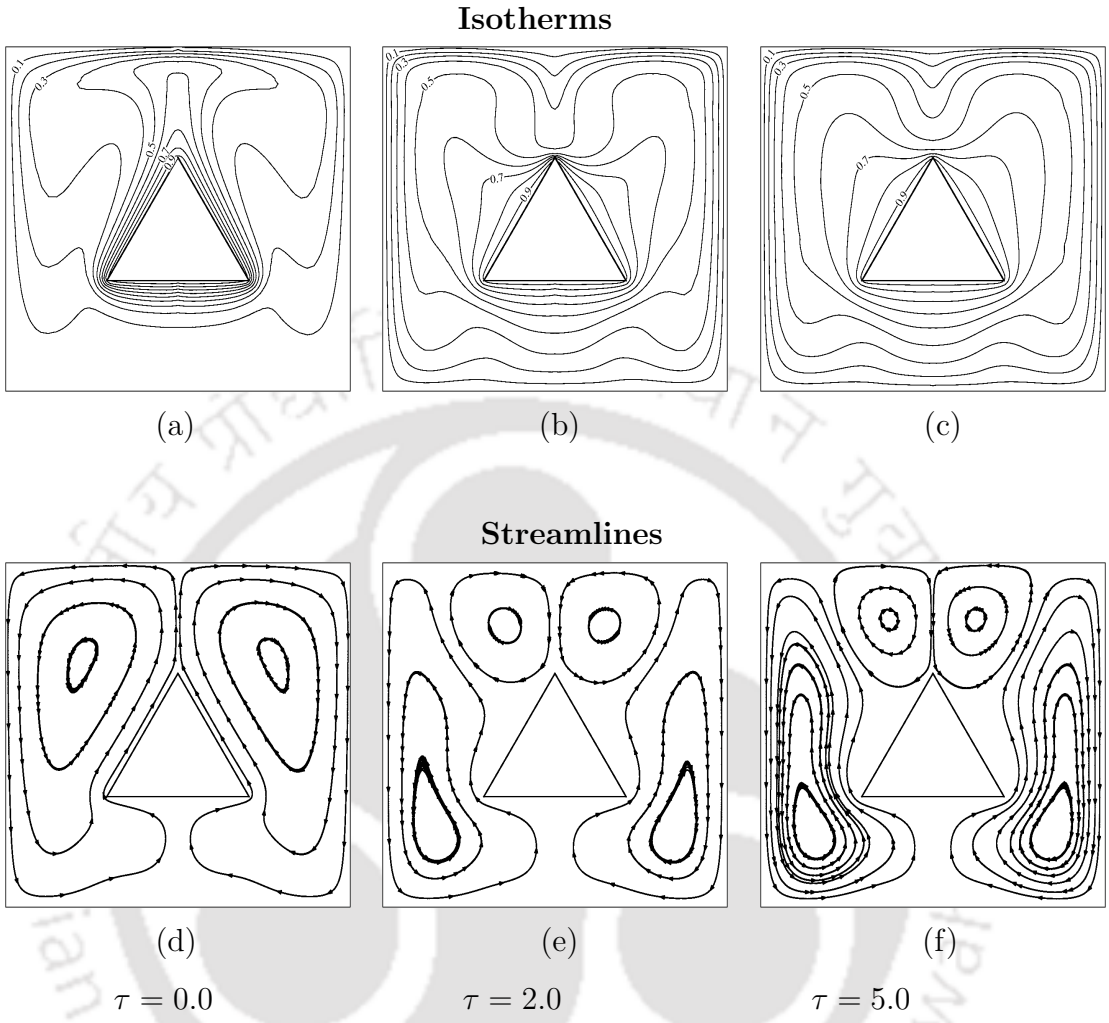

Figure 4.4: Isotherms and streamlines inside square enclosure using quasi-incompressible (LMN) approach for various optical thickness.

Figure 4.6 shows the velocity variation in the medium for different optical thickness. In these figures, horizontal velocity variation is plotted at $X = 0.2$ and the vertical velocity variation is plotted at $Y = 0.8$. In the case of flow visualization using LMN approach, one can identify two different types of streamline plots as seen in Fig. 4.4. In the case of the surface to surface radiation ($\tau = 0$), two primary vortices are formed as shown in Figs. 4.4 (d). The U-velocity attains its peak value in the core region of the primary vortices. In the case of the transparent medium, core of the primary vortex is located in the upper half of the cavity close to the

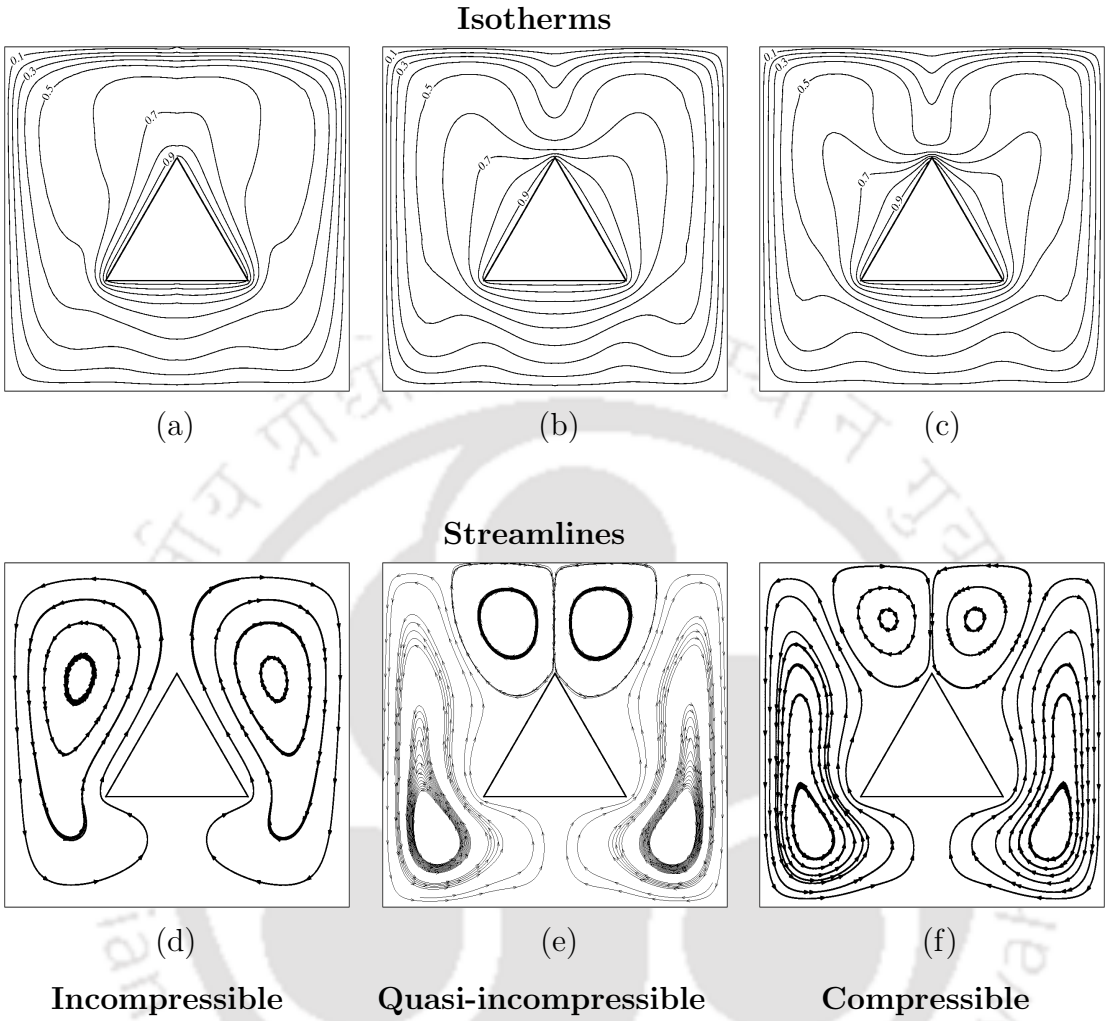

Figure 4.5: Isotherms and streamlines inside square enclosure at optical thickness, $\tau = 5.0$ using different models.

$Y = 0.8$ line as seen from Fig. 4.6(a). With the presence of gas radiation, secondary vortices are also formed just above the heated cylinder in addition to primary vortices. The role of participating medium is to decrease buoyancy currents. This causes the core of the primary vortices to descend to the bottom half of the cavity. This effect is reflected in the U-velocity variation where the peaks of U-velocity are obtained at the bottom of the cavity as seen from Fig. 4.6(c). The shift of the peaks in the velocity variation is consistent with those observed in streamlines. Similar deviations are also observed in the case of V-velocity distribution. The formation of

secondary vortices over the heated cylinder causes a dip in the velocity distribution for optical thickness $\tau = 2$, 5. However, quantitative differences in the magnitudes of velocity and temperature distribution are observed between the Boussinesq and non-Boussinesq models for all cases. The differences are significant in the case of optical thickness $\tau = 5$ as seen in Fig. 4.6(c).

Similarly, center-line temperature variations at two different locations $Y = 0.2$ and $Y = 0.8$ are plotted in Fig. 4.7 in order to understand better the variations in isotherms already presented in Fig. 4.4. From Figs. 4.7 (b, c) it is observed that the medium temperature in the region just above the heated cylinder is reduced. This reduction in temperature is due to the formation of a secondary vortex. However, in cases with absence of secondary vortices, the maximum temperature is attained in the area above the heated cylinder as the hot gasses rise up from the heated cylinder due to buoyancy effects (Fig. 4.7(a)). Medium temperature seems to increase with gas radiation as more and more radiation is absorbed by the participating gases. Radiation effects make the entire enclosure thermally active which is apparent from the temperature plot at $Y = 0.2$ in Fig. 4.7. Despite the differences in mathematical formulation between the LMN and the purely compressible approach of OpenFOAM, their flow contours, and temperature variations are in excellent agreement as seen in Figs. 4.4, 4.5, 4.6 and 4.7. The use of Boussinesq model shows qualitative similarities with the non-Boussinesq models for surface radiation. However, in presence of gas radiation, large discrepancies are observed in the results concerning streamlines, isotherms, temperature and velocity variations.

Studies were also performed to see the differences coming from various models in terms of Nusselt number computations at the heated cylinder and top wall of the enclosure as shown in Fig. 4.8. The variation between incompressible and quasi-incompressible models in the convective Nusselt number is more compared to its radiative counterpart for the heated cylinder. These differences are extensive for τ= 5.0 case where deviations in the streamline profiles cause the discrepancy in both the convective and radiative Nusselt number. The maximum variation in the convective Nusselt number for the two models is around 23.60 %. For surface and gas radiation with optical thickness $\tau = 2.0$ the local radiative Nusselt number distribution between incompressible and quasi-incompressible approach is qualitatively same. For higher optical thickness τ= 5.0, the maximum variation in radiative Nusselt number is around 15.0 %. However, quantitative analysis concerning Nusselt number variations at the top and bottom walls of the cavities shows that even at

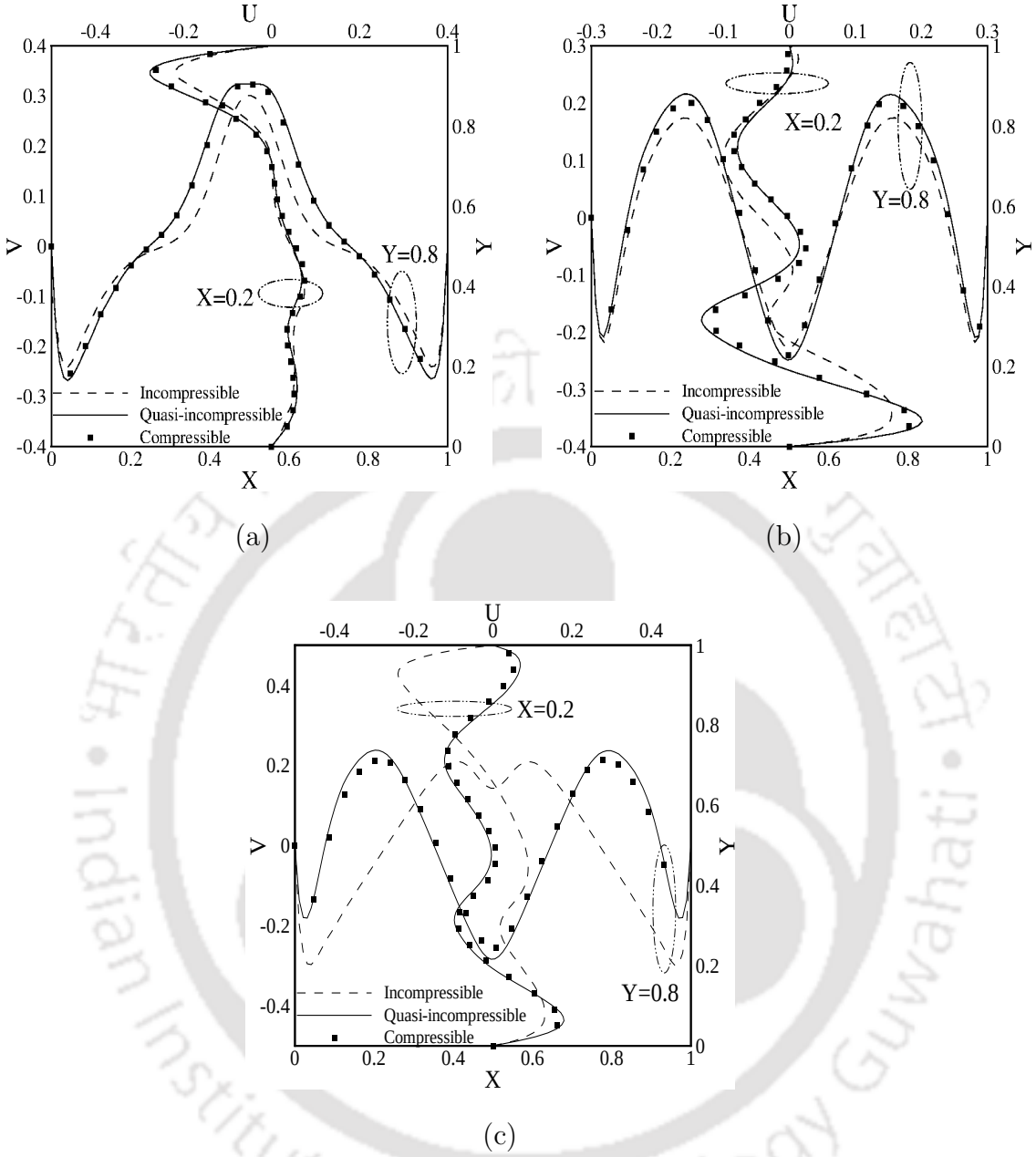

Figure 4.6: Dimensionless horizontal velocity profiles along the Y-axis at $X = 0.2$ and vertical velocity profiles along the X-axis at $Y = 0.8$ for different optical thickness: (a) $\tau = 0.0$, (b) $\tau = 2.0$, (c) $\tau = 5.0$

low optical thickness the Nusselt number variation deviates largely from the non-Boussinesq results as seen from Fig 4.8 (b). These deviations arise at all ranges of optical thickness. For the transparent medium, the maximum variation in the

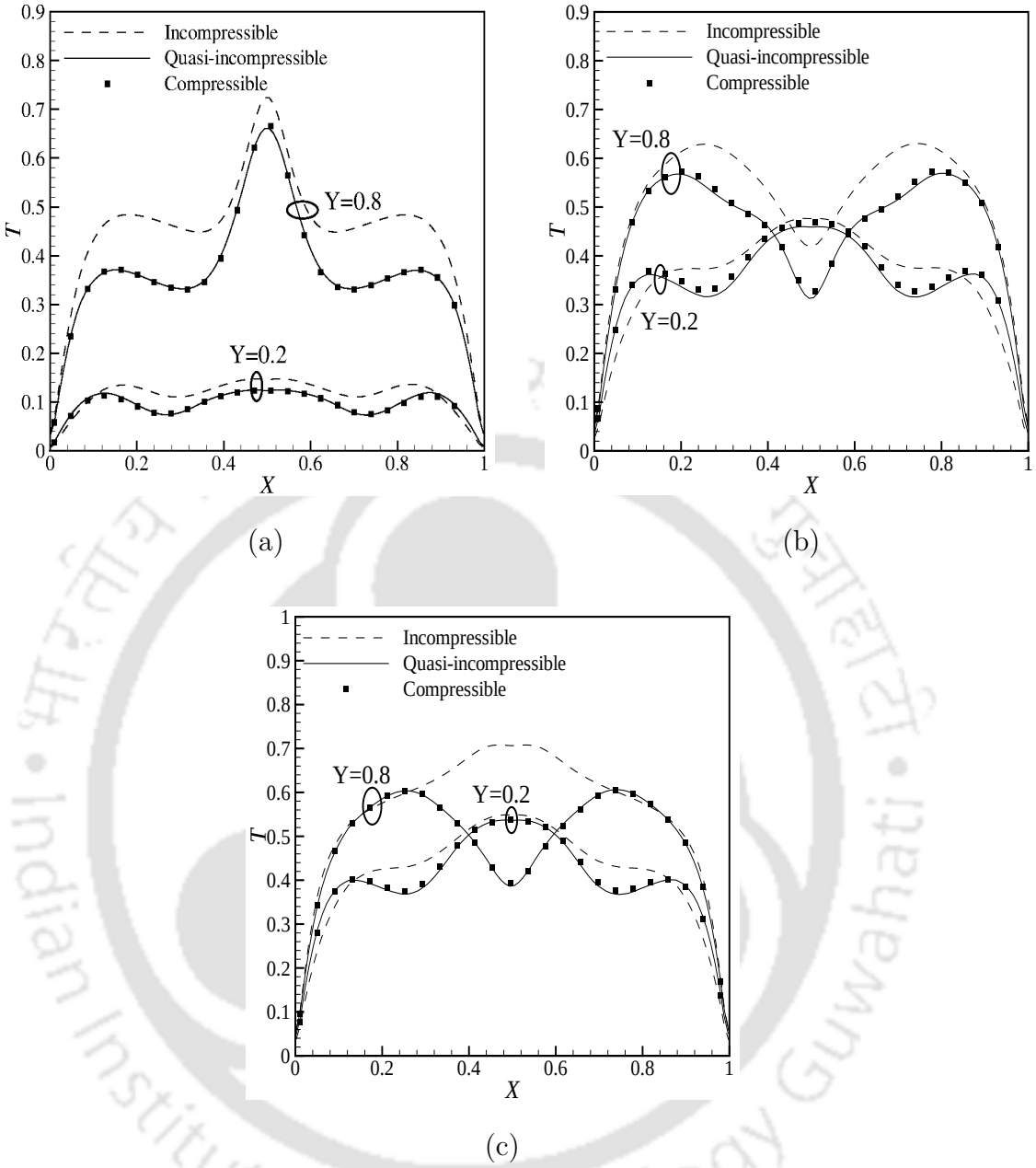

Figure 4.7: Dimensionless temperature profiles along the X-axis at $Y = 0.2$ and $Y = 0.8$ for different optical thickness: (a) $\tau = 0.0$, (b) $\tau = 2.0$, (c) $\tau = 5.0$.

convective Nusselt number is around 25.0 %. From these results, it is apparent that quasi-incompressibility effects are dominant, and LMN model is necessary as Boussinesq approximation completely fails for these class of problems.

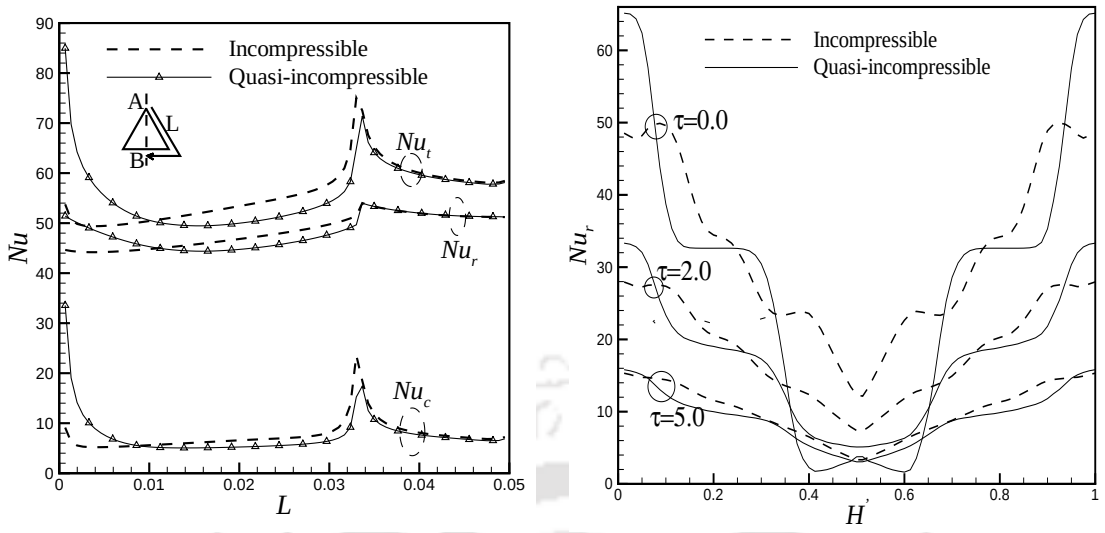

Figure 4.8: Comparison of Nusselt number variation between incompressible and quasi-incompressible LMN models. (a) Convective, radiative and total Nusselt number variation at the heated cylinder for gas radiation with $\tau = 2.0$, (b) radiative Nusselt number variation at the top wall for $\tau = 0.0$, $\tau = 2.0$ and $\tau = 5.0$.

4.2.3 Convective-radiative flows with significant influence of radiation

In this present test case, the validity of Boussinesq approximation is investigated in scenarios where the radiative heat transfer effects are significant at small temperature differences. A buoyancy-induced combined convective-radiative heat transfer is simulated in a square enclosure with a heated triangular cylinder at its center. The basic geometry of the problems is shown in Fig. 4.9 which consists of a heated equilateral triangular cylinder inside a cold square cavity of length H. Sides of the triangle are of length $0.2H$. The non-dimensional parameters are $Ga = 0.1$, $Ra = 5 \times 10^6$, $Pr = 0.71$ and Pl is varied from 0.0002 to 0.2. The present problem is solved considering absorbing-emitting medium with optical thickness 0.1. The temperature differences are kept very small to highlight the influence of radiative heat transfer on quasi-incompressibility effects. Further, spatial and angular grid independence study is performed for $Pl = 0.2$. Hybrid spatial grids (hexahedral and tetrahedral) of size 13938, 21243, 36564 and 50921 cells with a fixed angular size

of 4×16 as observed from Table 4.3 are used. The total Nusselt number values of 6.86, 7.95, 8.21 and 8.25 were obtained at the top wall of the cavity using the quasi-incompressible algorithm. In the same lines, using a fixed spatial grid of 36564 elements gives total Nusselt number values of 7.5, 7.95, 8.21 and 8.23 for an angular resolution of 2×8, 4×8, 4×16 and 4×20 respectively as shown in Table 4.3. This study shows that spatial grids of size 36564, and angular resolution of 4×16 provide mesh independent solutions for the present study under investigation. Furthermore, a time step size of $\Delta t = 5 \times 10^{-3}$ is used to achieve steady state solutions. Notable, this study was performed by using a combination of non-uniform hexahedral and tetrahedral elements with grid clustering near the heated cylinder and enclosure walls as depicted in Fig. 4.9(b).

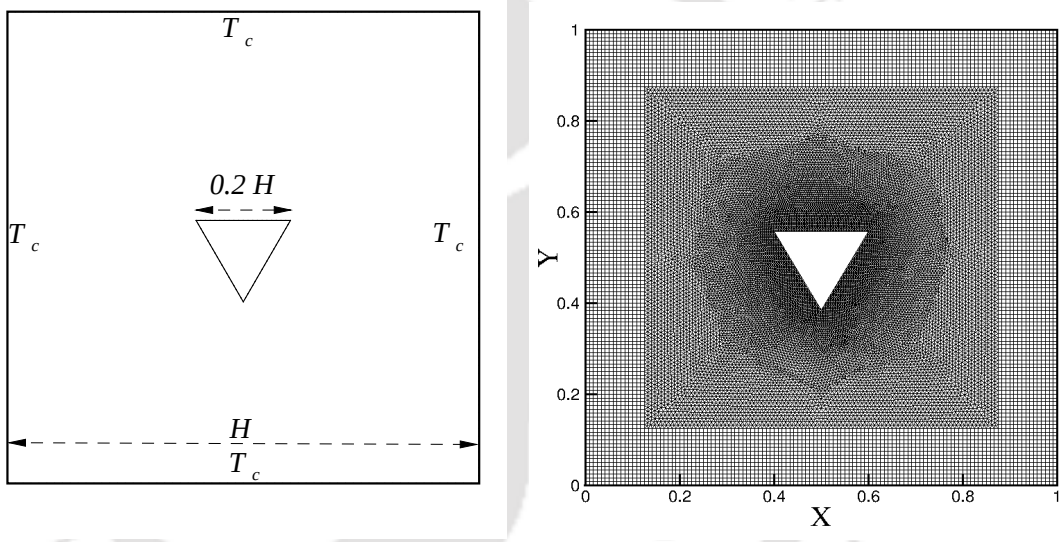

(a) (b)

Figure 4.9: Schematic of the computational domain and mesh used in the present study.

$$\begin{aligned} \text{Walls of square cavity}: \quad & u = v = 0, \; T = 0 \\ \text{cylinder wall}: \quad & u = v = 0, \; T = 1 \\ I_w(\mathbf{r}, \mathbf{s}) = \varepsilon_w I_b + \frac{1 - \varepsilon_w}{\pi} & \int\limits_{\mathbf{s}\cdot\hat{\mathbf{n}}>0} I(\mathbf{r}, \mathbf{s})\, \mathbf{s} \cdot \hat{\mathbf{n}} \, \mathrm{d}\Omega \end{aligned} \tag{4.4}$$

where $\hat{\mathbf{n}}$ is the outward normal vector at the boundary.

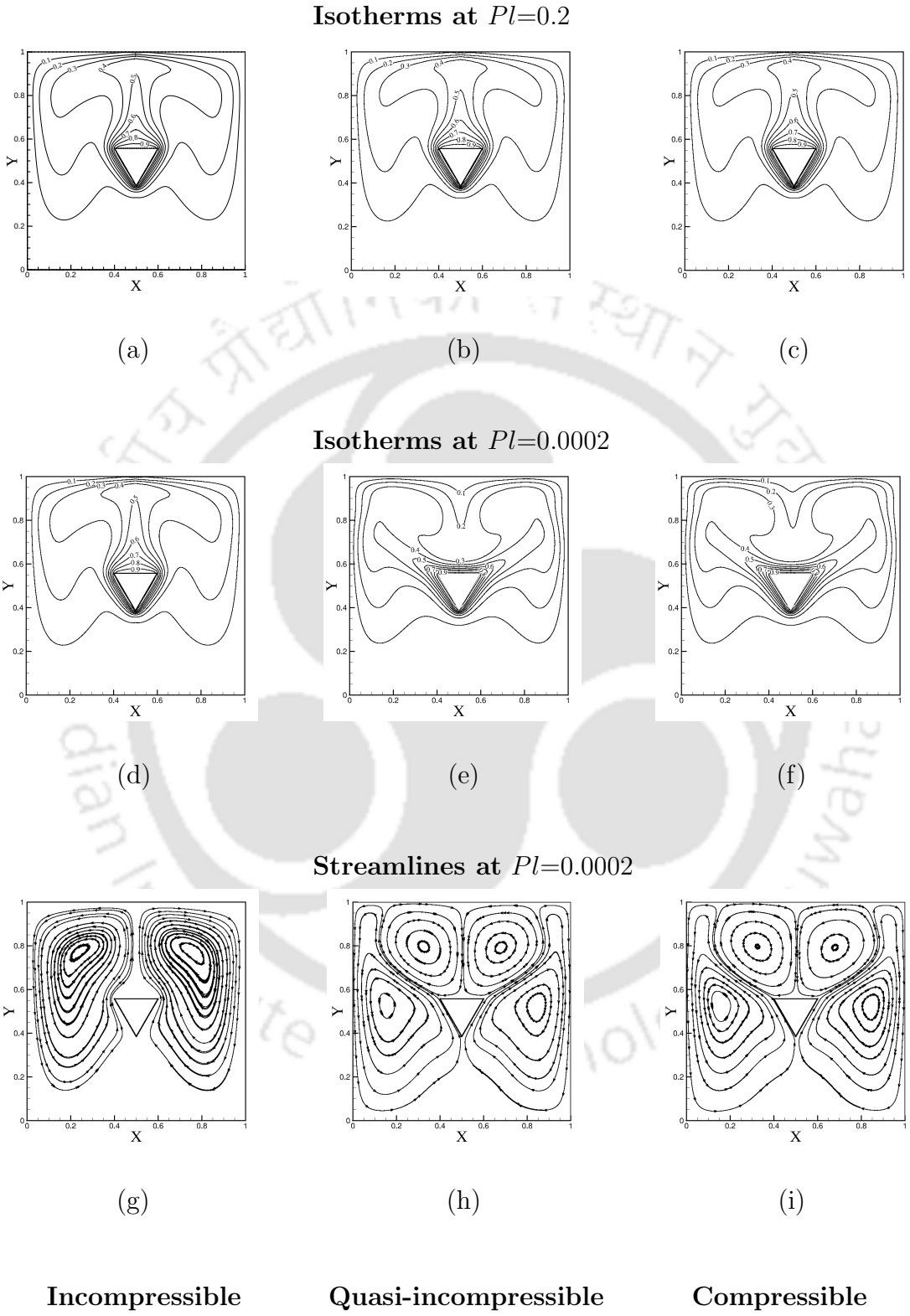

Figure 4.10: (a-c) Isotherms for $Pl = 0.2$, (d-f) isotherms for $Pl = 0.0002$, (g-i) streamlines for $Pl = 0.0002$ using different models.

Table 4.3: Average Nusselt number(total) values obtained for various spatial and angular mesh used in the grid independence study for a square cavity containing a heated cylinder.

Angular Grid ($N_\theta \times N_\phi$)	4×16			
Spatial Grid ($N_x \times N_y$)	13938	21243	36564	50921
Nusselt number (Nu_t)	6.86	7.95	8.21	8.25
Spatial Grid ($N_x \times N_y$)	36564			
Angular Grid ($N_\theta \times N_\phi$)	2×8	4×8	4×16	4×20
Nusselt number (Nu_t)	7.5	7.95	8.21	8.23

Figures 4.10 (a-c) represent the isotherms for $Pl = 0.2$ using incompressible, quasi-incompressible and compressible models, respectively. From the isotherm, it is seen that the buoyancy force causes the fluid above the heated cylinder to rises upwards from the heated cylinder. The rising hot fluid is driven towards the side walls after interacting with the top wall. Heat transfer of the fluid due to interaction with cold walls (top and side) causes the fluid to cool and hence it is compelled to descend down. The heavy cold fluid at the base of the cavity again rises up upon contact with the heated cylinder. This phenomenon leads to the formation of two primary convection currents, which are rotating in contrary directions along the vertical centerline of the cavity. The formation of these vortices is similar to the one described in Fig. 4.10 (g), and no variations in the streamlines are seen between the three models for this high value of Planck number. Isotherms variation depicts sharp temperature gradients in the vicinity of the heated cylinder, near the top and vertical walls of the cavity as seen in Figs. 4.10 (a-c). However, near the bottom wall, the temperature gradients are homogeneous.

Figures 4.11 and 4.12 represent the non-dimensional temperature and velocity distribution along the horizontal and vertical lines. These distributions confirm that at large Planck numbers and small temperature difference all three models predict the same results. This is because the velocity divergence reduce nearly to zero for this particular case and the problem reduces to a simple Boussinesq convection with

low radiative heat transfer. However, minor deviations are observed between the Boussinesq and non-Boussinesq models as the Planck numbers are further reduced up to 0.002 although not shown here. A major contrast between the results obtained using Boussinesq and non-Boussinesq models can be observed as the Planck numbers are further reduced to 0.0002. The presence of strong radiation effects causes a decrement in temperature gradients near the top walls and increase in temperature gradients near the heated cylinder. The decreased temperature gradients inherently reduce the density gradients which leads to weakening of the buoyancy currents. The diminished buoyancy force causes the core of the primary vortex to be pushed to the bottom of the cavity as additional secondary vortices are formed just above the heated cylinder.

From isotherm distribution in Figs. 4.10 (d-f) it is seen that the region just above the cylinder is heated in case of an incompressible model as hot plume rises up. However, the isotherms obtained using non-Boussinesq models depict a sharp dip in temperature in the region just above the heated cylinder due to the formation of secondary vortices as seen from the streamlines variation in Figs. 4.10 (h, i). These secondary vortices are not captured by the incompressible model whereas the non-Boussinesq models capture the secondary vortices precisely Figs. 4.10 (h, i).

The effects of the formation of secondary vortices can be better understood from the temperature and velocity distributions. From Figs. 4.12 (a, b) it is seen that the formation of secondary vortices above the heated cylinder causes an increase in the medium temperatures along the side walls whereas a reduction in the medium temperature in the region just above the heated cylinder. However, in cases with absence of secondary vortices, the maximum temperature is attained in the area above the heated cylinder. Similar deviations can also be observed from velocity variations in Figs. 4.12 (c - d). Qualitative similarities in the temperature and velocity variation can be seen in the region below the heated cylinder. However, large differences can be observed in the region just above the heated cylinder where the effects of buoyancy driven convection and radiation are dominant. The formation of secondary vortices causes a dip in the velocity in the region just above the heated cylinder whereas in the absence of secondary vortices the maximum velocity is obtained in this region. The results obtained using quasi-incompressible and compressible model match qualitatively and quantitatively and are in large contrast with the incompressible model as seen from isotherms, velocity, and temperature distribution. The average Nusselt number at the top wall of the heated cylinder

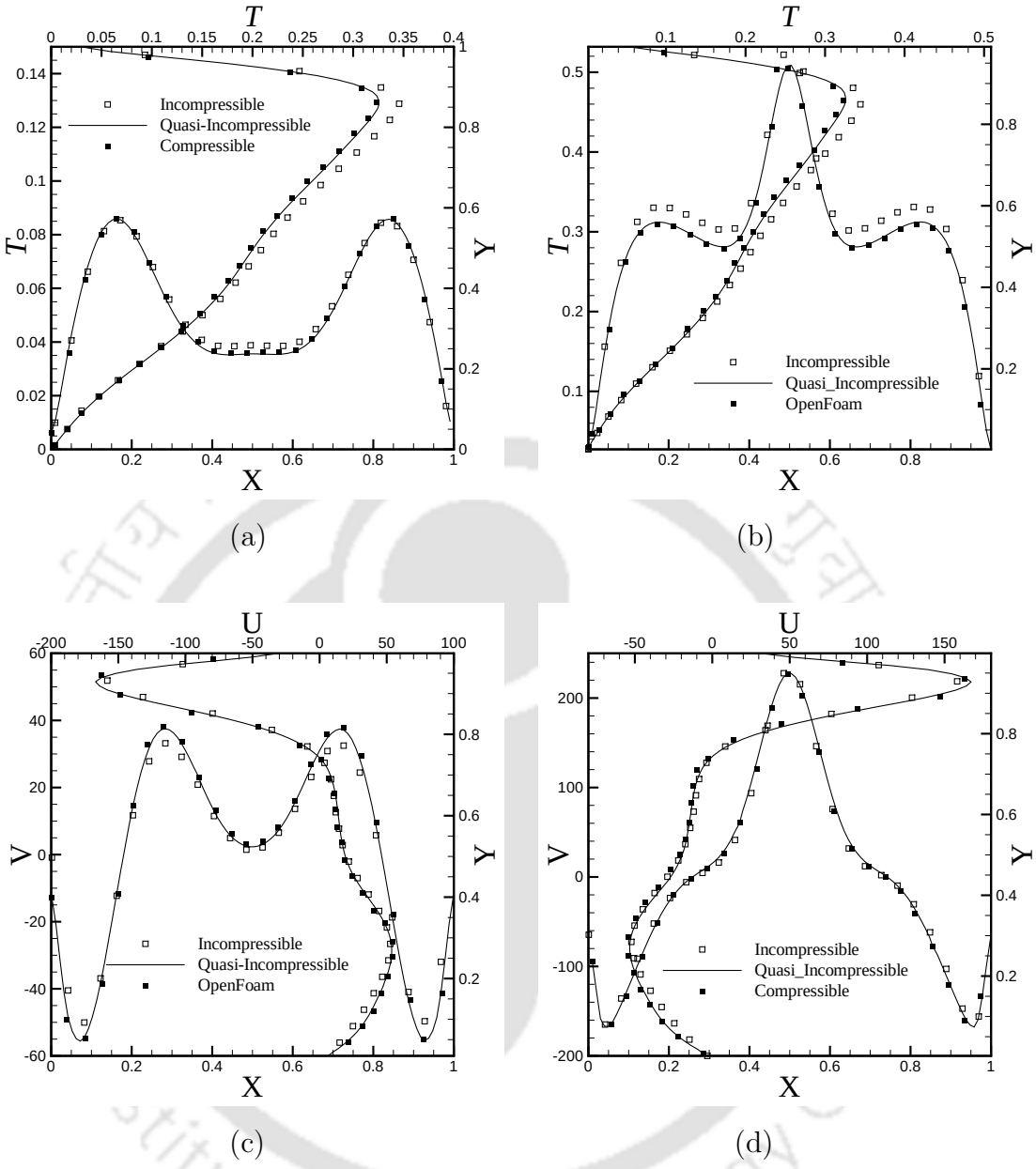

Figure 4.11: Dimensionless temperature variation (a, b) and dimensionless velocity variation (c, d) along the horizontal and vertical axis at (X=0.2, Y=0.2) and (X=0.8, Y=0.8) for Pl=0.2.

is presented in Table 4.4. It is seen that deviation between the Nusselt number obtained using Boussinesq and non-Boussinesq models is significant in the case of

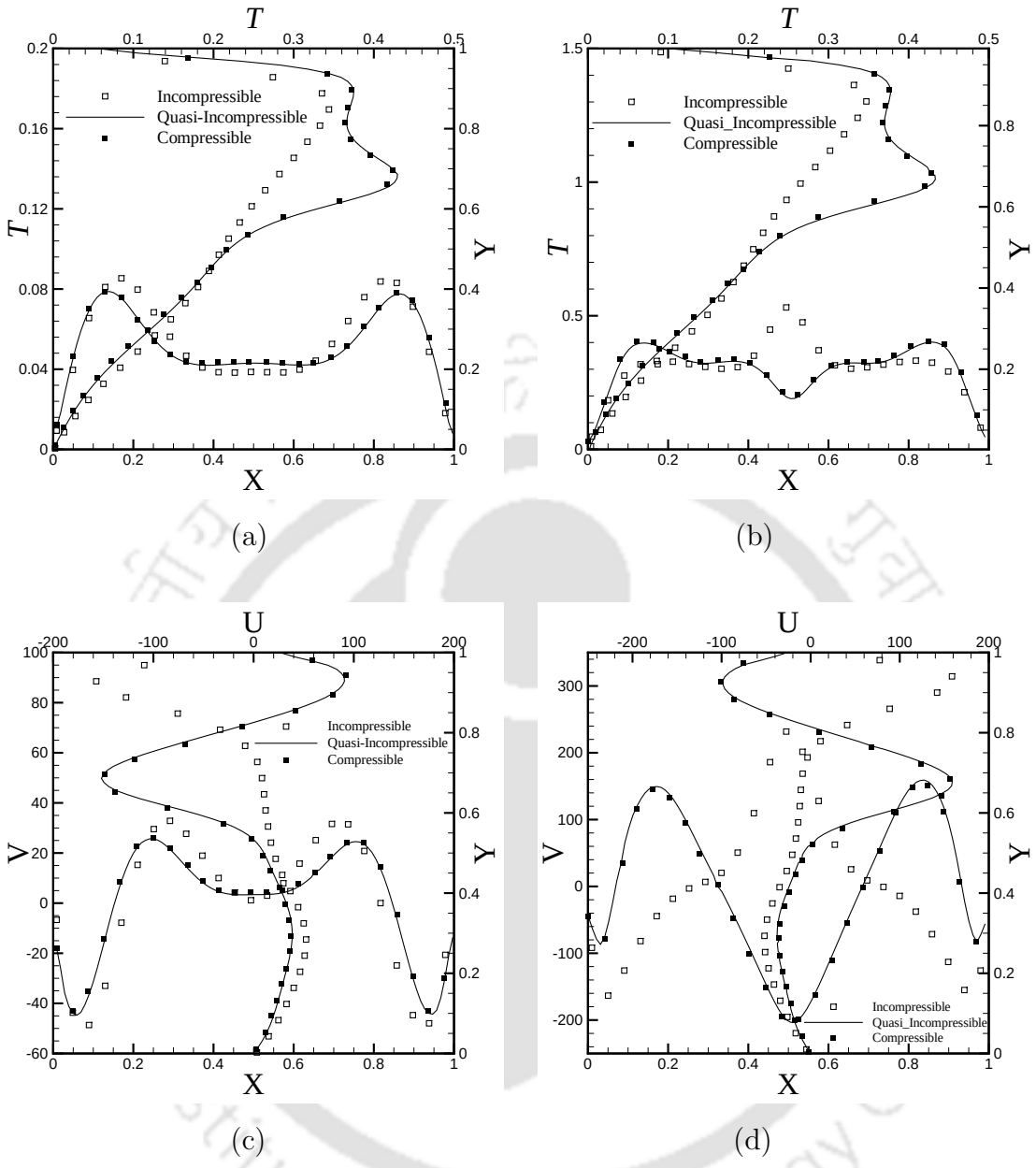

Figure 4.12: Dimensionless temperature variation (a, b) and dimensionless velocity variation (c, d) along the horizontal and vertical axis at (X=0.2, Y=0.2) and (X=0.8, Y=0.8) for Pl = 0.0002.

the convective Nusselt number and radiative Nusselt number. From the above results, it is seen that incompressible assumption gives inaccurate results for combined

convective-radiative heat transfer in enclosures, even at small temperature difference with significant effects of radiative heat transfer.

Table 4.4: Comparison of average Nusselt numbers at top wall of the cavity for Pl = 0.2 and 0.0002

Planck Number	0.2	0.2	0.2	0.0002	0.0002	0.0002
Model	Nu_c	Nu_r	Nu_t	Nu_c	Nu_r	Nu_t
Incompressible	6.898	1.346	8.244	6.898	5499.460	5506.358
Quasi-incompressible	6.896	1.346	8.242	5.691	5210.890	5216.581
Percentage deviation	0.02%	0.0%	0.024%	17.50%	5.24%	5.24%

4.3 Closure

In this chapter, a critical assessment of numerical algorithms and the need for non-Boussinesq low-Mach number approximation in numerical simulation of convective-radiative heat transfer problems is presented. For problems involving small temperature difference with negligible radiation the Boussinesq approximation holds true and the flow can be assumed to be incompressible. However, at large temperature difference ($Ga \rightarrow \infty$) and significant radiation ($Pl \rightarrow 0$) it is seen that a velocity divergence condition gives a non-solenoidal velocity field as a result of which true solution departs from the one predicted using the Boussinesq approximation. Despite the differences in mathematical formulation between the LMN and the purely compressible approach of OpenFOAM, their results are in excellent agreement. However, both the models show considerable deviation with the incompressible approach at large temperature difference and significant radiation. From these results, it is apparent that quasi-incompressibility effects are dominant, and LMN model is necessary as Boussinesq approximation completely fails for these class of problems.

Chapter 5

Comparison of Algorithms for Radiative-Convective Flows

5.1 Introduction

In this chapter, three different algorithms are investigated for the numerical simulation of non-Boussinesq convection with thermal radiative heat transfer based on a low-Mach number formulation. The three algorithms compute the coupled governing equations using a conservative form of momentum equations in conjunction with a variable coefficient pressure Poisson equation. However, the Algorithm A uses conservation of mass and energy equation to compute density and temperature while the Algorithms B and C calculate temperature and density, respectively from the equation of state. Further, Algorithms B and C solves a conservative form of the continuity and energy equation to obtain density and temperature, respectively. The energy and mass conservation errors arising due to the use of Algorithms B and C are derived and the significance of these errors in radiative-convective flows is highlighted by performing investigations over a range of Rayleigh, Prandtl, and Planck numbers. Finally, the role of balancing of the pressure and buoyancy terms is emphasized for robust calculations of large temperature difference thermo-buoyant convection with radiative heat transfer.

5.2 Solution Algorithm

The solution methodology adopts a fractional step approach with a detailed discussion on specific implementation of three different algorithms of interest.

5.2.1 Algorithm A

This algorithm is referred to as the discretely conservative algorithm since it solves all transport equations. The values of density, momentum, and temperature are obtained by solving the following non-dimensional conservation equations.

$$\frac{\partial \rho}{\partial t} + \frac{\partial \left(\rho u_j\right)}{\partial x_j} = 0 \tag{5.1}$$

$$\frac{\partial \left(\rho u_i\right)}{\partial t} + \frac{\partial \left(\rho u_i u_j\right)}{\partial x_j} = -\frac{\partial p}{\partial x_i} + \sqrt{\frac{Pr}{Ra}}\frac{\partial \tau_{ij}}{\partial x_j} + \frac{1}{Ga}\ (1-\rho)\,\hat{\mathbf{e}}_{\mathbf{y}} \tag{5.2}$$

$$\frac{\partial \left(\rho T\right)}{\partial t} + \frac{\partial \left(\rho T\ u_j\right)}{\partial x_j} = \frac{1}{\sqrt{Ra\,Pr}}\frac{\partial}{\partial x_j}\left(\kappa \frac{\partial T}{\partial x_j}\right) + \frac{\gamma - 1}{\gamma\, Ga}\frac{d\overline{P}}{dt} + \frac{1}{Pl\, Ga\sqrt{Ra\,Pr}}\frac{\partial q_r}{\partial x_j} \tag{5.3}$$

Furthermore, the two pressures, i.e., the hydrodynamic (p) and thermodynamic pressure ($\overline{P}$) are obtained using Eqs. (5.4) and (5.5), respectively.

$$\frac{2\Delta t}{3}\sum_f \left(\frac{\nabla p}{\rho}\right)_f \cdot \mathbf{S}_f = \sum_f {F_{0f}}^* + \sum_f \frac{2\Delta t}{3Ga}\left(\frac{1-\rho_f}{\rho_f}\right)\mathbf{S}_f \cdot \hat{\mathbf{e}}_{\mathbf{y}} -$$
$$\frac{1}{\overline{\overline{P}}}\left[\frac{-1}{\gamma}\frac{d\overline{P}}{dt}V_P + \frac{1}{\sqrt{RaPr}}\left\{Ga\sum_f \left(\kappa \nabla T\right)_f \cdot \mathbf{S}_f + \frac{1}{Pl}\nabla \cdot \mathbf{q_r} V_P\right\}\right] \tag{5.4}$$

$$\overline{P}(t) = \frac{m_0}{\int_\Omega \frac{d\Omega}{1+Ga\,T}} \tag{5.5}$$

The time rate of change of thermodynamic pressure $\frac{d\overline{P}}{dt}$ is obtained from the below equation.

$$\frac{d\overline{P}}{dt} = \frac{\gamma}{\Upsilon\sqrt{RaPr}}\left\{Ga\int_\Omega \nabla \cdot \left(\kappa \nabla T\right) d\Omega + \frac{1}{Pl}\int_\Omega \nabla \cdot \mathbf{q_r}\ d\Omega\right\} \tag{5.6}$$

5.2.2 Algorithm B

In this algorithm, all transport equations except the thermal energy conservation equation are solved. The temperature is then obtained from EOS using Eq. (5.7) as,

$$T^n = \frac{\overline{P} - \rho}{\rho Ga} \tag{5.7}$$

Moreover, the thermodynamic pressure follows from an explicit expression as shown in Eq. (5.8) followed by temperature update using $\overline{P}^{n+1}$ as shown in Eq. (5.9).

$$\overline{P}^{n+1} = \frac{4}{3}\overline{P}^{n} - \frac{1}{3}\overline{P}^{n-1} + \frac{2}{3}\Delta t \left[\frac{\gamma}{\Upsilon\sqrt{RaPr}} \left\{ Ga \sum_{bf} (k\nabla T)_f \cdot \mathbf{S}_f + \frac{1}{Pl} \sum_{NC} \nabla \cdot \mathbf{q_r}\, V_P \right\} \right] \tag{5.8}$$

$$T^{n+1} = \frac{\overline{P} - \rho}{\rho Ga} \tag{5.9}$$

5.2.3 Algorithm C

This is similar to Algorithm B, except that the continuity equation is not solved. The density is then obtained from EOS as,

$$\rho^{n+1} = \overline{P}^{n+1} - (\rho T)^{n+1} Ga \tag{5.10}$$

while the thermodynamic pressure ($\overline{P}$) is obtained using the global mass conservation criteria as explained in Eq. (5.5). It may be remarked that the momentum equations are solved conservatively for all three algorithms. The only difference between Algorithm A and those in Algorithms B and C is that the latter two do not satisfy all discrete conservation laws. On the contrary, while Algorithms B and C respect the EOS, there is no attempt to enforce it for Algorithm A discretely. Notably, the primitive variables of interest are $\rho, u, v, w, p, \overline{P}, T$ and there are equations governing these quantities. Besides, $\rho, \overline{P}$ and T are related through EOS. Evidently, there are more equations than variables leading to an over-determined system. The thermodynamic pressure and associated EOS are therefore the reason for a violation in each of the algorithms. While Algorithm A violates the discrete

EOS, Algorithms B and C commit discrete errors in the conservation of temperature and density, respectively. We shall now study the nature of these errors and its impact and implication on numerical simulations in the following sections. For the sake of completeness and clarity, the three algorithms are also presented side by side in Table 5.1.

5.2.4 Discrete mass conservation error

The discrete mass conservation error appears in Algorithm C since it does not explicitly solve the continuity equation for density transport but preferably updates density using the solution for temperature and EOS. Starting from the discrete energy equation described as,

$$V_P \frac{(\rho T)_{\mathrm{P}}^{n+1} - (\rho T)_{\mathrm{P}}^{n}}{\Delta t} + \sum_f (\rho T)_f^{n+1} F_f^n = \frac{1}{\sqrt{RaPr}} \sum_f \frac{\partial T}{\partial n} \mathbf{S}_f + \frac{\gamma - 1}{\gamma} \frac{d\overline{P}}{dT} \frac{V_P}{Ga} + \frac{1}{PlGa\sqrt{RaPr}} \frac{\partial q_r}{\partial x_j} V_P \tag{5.11}$$

Substituting the EOS $\rho T = \frac{\overline{P}-\rho}{Ga}$ in Eq. (5.11) and rearranging we get,

$$V_P \frac{\rho_{\mathrm{P}}^{n+1} - \rho_{\mathrm{P}}^{n}}{\Delta t} + \sum_f \rho_f^{n+1} F_f^n = \frac{\overline{P}^{n+1} - \overline{P}^{n}}{\Delta t} V_P + \sum_f \overline{P}^{n+1} F_f^n + \sum_f \overline{P}^{n+1} F_f^{n+1} - \sum_f \overline{P}^{n+1} F_f^{n+1} - \frac{Ga}{\sqrt{RaPr}} \sum_f \frac{\partial T}{\partial n} \mathbf{S}_f - \frac{\gamma - 1}{\gamma} \frac{d\overline{P}}{dt} V_P - \frac{\partial q_r}{\partial x_j} \frac{V_P}{Pl\sqrt{RaPr}} \tag{5.12}$$

The discrete form of velocity divergence condition in Eq. (2.67) is given by,

$$\sum_f F_f^{n+1} = \frac{1}{\overline{P}} \left[\frac{Ga}{\sqrt{RaPr}} \sum \frac{\partial T}{\partial n} \mathbf{S}_f - \frac{1}{\gamma} \frac{d\overline{P}}{dt} V_P + \frac{1}{Pl\sqrt{Ra\,Pr}} \frac{\partial q_{rj}}{\partial x_j} V_P \right] \tag{5.13}$$

Substituting Eq. (5.13) in the Eq. (5.12) and rearranging gives,

$$V_P \frac{\rho_{\mathrm{P}}^{n+1} - \rho_{\mathrm{P}}^{n}}{\Delta t} + \sum_f \rho_f^{n+1} F_f^n = \frac{\left(\overline{P}^{n+1} - \overline{P}^{n}\right) V_P}{\Delta t} - \sum_f \overline{P}^{n+1} \left(F_f^{n+1} - F_f^n\right) - \frac{d\overline{P}}{dt} V_P \tag{5.14}$$

Table 5.1: Three algorithms for coupling of radiation with flow.

Algorithm A	**Algorithm B**	**Algorithm C**
1. Solve RTE Eq. (2.27) to obtain intensity I.	1. Solve RTE Eq. (2.27) to obtain intensity I.	1. Solve RTE Eq. (2.27) to obtain intensity I.
2. Solve the continuity equation Eq. (5.1) to obtain density ρ^{n+1}.	2. Solve the continuity equation Eq. (5.1) to obtain density ρ^{n+1}.	2. Solve the energy conservation equation Eq. (5.3) to obtain (ρT^{n+1}).
3. Solve the energy equation Eq. (5.3) to obtain temperature ρT^{n+1}.	3. Compute temperature from EOS Eq. (5.7).	3. Update the thermodynamic pressure using Eq. (5.5) and $\frac{d\overline{P}}{dt}$ using Eq. (5.6).
4. Update the thermodynamic pressure using Eq. (5.5) and $\frac{d\overline{P}}{dt}$ using Eq. (5.6).	4. Calculate the thermodynamic pressure using Eq. (5.8), recalculate temperature and $\frac{d\overline{P}}{dt}$ using Eq. (5.9) and Eq. (5.6) respectively.	4. Update density using equation of state as described in Eq. (5.10).
5. Find ρu_i^* by solving the provisional momentum equations Eq. (2.109).	5. Find ρu_i^* by solving the provisional momentum equations Eq. (2.109).	5. Find ρu_i^* by solving the provisional momentum equations Eq. (2.109).
6. Calculate flux F_f^* using u_i^* and evaluate pressure using Poisson equation Eq. (5.4).	6. Calculate flux F_f^* using u_i^* and evaluate pressure using Poisson equation Eq. (5.4).	6. Calculate flux F_f^* using u_i^* and evaluate pressure using Poisson equation Eq. (5.4).
7. Calculate flux using the momentum interpolation formula Eq. (2.114)	7. Calculate flux using the momentum interpolation formula Eq. (2.114)	7. Calculate flux using the momentum interpolation formula Eq. (2.114).
8. Update velocity using Eq. (2.115).	8. Update velocity using Eq. (2.115)	8. Update velocity using Eq. (2.115).

Equation (5.14) represents the discrete form of mass conservation with the non-zero terms in the RHS representing the mass conservation error $E(t)$ in a given cell. Each of the non-zero expressions can be further simplified as follows. Using Taylor series expansion the equations are simplified further,

$$\frac{\left(\overline{P}^{n+1}-\overline{P}^{n}\right)V_P}{\Delta t}=\frac{d\overline{P}}{dt}V_P+\frac{\partial^2\overline{P}}{\partial t^2}V_P\Delta t+O\left(\Delta t^2\right) \tag{5.15}$$

Simplifying the second term using the discrete velocity divergence condition we get,

$$\overline{P}^{n+1}\sum_f\left(F_f^{n+1}-F_f^n\right)=\frac{Ga}{\sqrt{RaPr}}\sum_f\frac{\partial^2 T}{\partial t\partial n}\mathbf{S}_f\Delta t-\frac{1}{\gamma}\frac{\partial^2\overline{P}}{\partial t^2}V_P\Delta t$$
$$+\frac{1}{Pl\sqrt{Ra\,Pr}}\frac{\partial^2 q_{rj}}{\partial t\partial x_j}V_P\Delta t+O\left(\Delta t^2\right) \tag{5.16}$$

After algebraic simplifications we get,

$$V_P\frac{\rho_{\mathrm{P}}^{n+1}-\rho_{\mathrm{P}}^{n}}{\Delta t}+\sum_f\rho_f^{n+1}F_f^n=-\frac{Ga}{\sqrt{RaPr}}\Delta t\sum_f\frac{\partial^2 T}{\partial n\partial t}\mathbf{S}_f$$
$$+\frac{\gamma+1}{\gamma}\frac{\partial^2\overline{P}}{\partial t^2}V_P\Delta t-\frac{\partial^2 q_r}{\partial n\partial t}\frac{V_P\Delta t}{Pl\sqrt{RaPr}}+O\left(\Delta t^2\right) \tag{5.17}$$

The discrete mass conservation error associated with Algorithm C in any cell at time (t) is therefore given by

$$E(t)=\frac{Ga}{\sqrt{RaPr}}\Delta t\,C_1(t)+\Delta t\,C_2(t)+\frac{\Delta t}{Pl\sqrt{RaPr}}C_3(t) \tag{5.18}$$

where $C_1(t), C_2(t)$ and $C_3(t)$ are functions of transients of temperature, thermodynamic pressure and radiative heat transfer, respectively. One can note that for steady state problems the time derivatives of temperature, thermodynamic pressure, and radiative heat transfer approaches zero and hence the discrete mass conservation error vanishes at steady state if the latter is achieved. From Eq. (5.18) it is also clear that the magnitude of these errors is functions of non-dimensional parameters Ga, Pl, Ra and Pr as well as the numerical inputs like time step Δt. It may be remarked that the discrete mass conservation error approaches zero as ($\Delta t \to 0$, $Ga \to 0$, $Pl \to \infty$ and product of $RaPr \to \infty$). The situations corresponding to $Ga \to 0$ and $Pl \to \infty$ represent a small temperature difference buoyancy driven flow with negligible radiative heat transfer effects. Nevertheless, in case of problems involving large temperature difference such as non-Boussinesq natural convection and

particularly with radiation one can expect significant errors and its impact needs to be adjudged for practical applications.

5.2.5 Discrete energy conservation error

The discrete energy conservation error appears in Algorithm B since it does not explicitly solve the energy equation but instead updates temperature using the solution for density and EOS. Starting from the discrete continuity equation described as,

$$V_P \frac{\rho_{\mathrm{P}}^{n+1} - \rho_{\mathrm{P}}^{n}}{\Delta t} + \sum_f \rho_f^{n+1} F_f^n = 0 \tag{5.19}$$

Substituting the equation of state $\rho^{n+1} = \overline{P}^{n+1} - (\rho T)^{n+1} Ga$ in Eq. (5.19) and rearranging results in,

$$V_P \frac{(\rho T)_{\mathrm{P}}^{n+1} - (\rho T)_{\mathrm{P}}^{n}}{\Delta t} + \sum_f (\rho T)_f^{n+1} F_f^n = \frac{1}{Ga}\left[\frac{\overline{P}^{n+1} - \overline{P}^{n}}{\Delta t} V_P + \sum_f \overline{P}^{n+1} F_f^n\right]$$
$$+ \frac{1}{Ga}\left[\sum_f \overline{P}^{n+1} F_f^{n+1} - \sum_f \overline{P}^{n+1} F_f^{n+1}\right] \tag{5.20}$$

The discrete form of velocity divergence condition in Eq. (2.67) is given by,

$$\sum_f F_f^{n+1} = \frac{1}{\overline{P}}\left[\frac{Ga}{\sqrt{RaPr}} \sum \frac{\partial T}{\partial n}\mathbf{S}_f - \frac{1}{\gamma}\frac{d\overline{P}}{dt} V_P + \frac{1}{Pl\sqrt{Ra\,Pr}} \frac{\partial q_{rj}}{\partial x_j} V_P\right] \tag{5.21}$$

Substituting Eq. (5.21) in Eq. (5.20) and rearranging gives,

$$V_P \frac{(\rho T)_{\mathrm{P}}^{n+1} - (\rho T)_{\mathrm{P}}^{n}}{\Delta t} + \sum_f (\rho T)_f^{n+1} F_f^n = \frac{1}{Ga}\left[\frac{\overline{P}^{n+1} - \overline{P}^{n}}{\Delta t} V_P\right]$$
$$+ \frac{1}{Ga}\overline{P}^{n+1} \sum_f (F_f^n - F_f^{n+1}) + \frac{1}{\sqrt{RaPr}} \sum_f \frac{\partial T}{\partial n}\mathbf{S}_f$$
$$- \frac{1}{\gamma Ga}\frac{d\overline{P}}{dt} V_P + \frac{\partial q_r}{\partial x_j} \frac{V_P}{PlGa\sqrt{RaPr}} \tag{5.22}$$

Rearranging further results in Eq. (5.23).

$$V_P \frac{(\rho T)_{\mathrm{P}}^{n+1} - (\rho T)_{\mathrm{P}}^{n}}{\Delta t} + \sum_f (\rho T)_f^{n+1} F_f^n - \frac{1}{\sqrt{RaPr}} \sum_f \frac{\partial T}{\partial n} \mathbf{S}_f + \frac{1}{\gamma Ga} \frac{d\overline{P}}{dt} V_P$$

$$-\frac{\partial q_r}{\partial x_j} \frac{V_P}{PlGa\sqrt{RaPr}} = \frac{1}{Ga} \left[\frac{\overline{P}^{n+1} - \overline{P}^{n}}{\Delta t} V_P \right] + \frac{1}{Ga} \overline{P}^{n+1} \sum_f (F_f^n - F_f^{n+1}) \tag{5.23}$$

Equation (5.23) represents the discrete form of energy conservation equation with the non-zero terms in the RHS representing the energy conservation error $E(t)$ in a given finite cell. Each of the non-zero expressions can be further simplified as follows. Using Taylor series expansion we have,

$$\frac{\left(\overline{P}^{n+1} - \overline{P}^{n}\right) V_P}{\Delta t} = \frac{d\overline{P}}{dt} V_P + \frac{\partial^2 \overline{P}}{\partial t^2} V_P \Delta t + O\left(\Delta t^2\right) \tag{5.24}$$

One can simplify the second term using the discrete velocity divergence condition as,

$$\overline{P}^{n+1} \sum_f \left(F_f^{n+1} - F_f^n\right) = \frac{Ga}{\sqrt{RaPr}} \sum_f \frac{\partial^2 T}{\partial t \partial n} \mathbf{S}_f \Delta t - \frac{1}{\gamma} \frac{\partial^2 \overline{P}}{\partial t^2} V_P \Delta t + \frac{1}{Pl\sqrt{Ra\,Pr}} \frac{\partial^2 q_{rj}}{\partial t \partial x_j} V_P \Delta t + O\left(\Delta t^2\right) \tag{5.25}$$

After algebraic simplifications we get,

$$V_P \frac{(\rho T)_{\mathrm{P}}^{n+1} - (\rho T)_{\mathrm{P}}^{n}}{\Delta t} + \sum_f (\rho T)_f^{n+1} F_f^n - \frac{1}{\sqrt{RaPr}} \sum_f \frac{\partial T}{\partial n} \mathbf{S}_f + \frac{1-\gamma}{\gamma Ga} \frac{d\overline{P}}{dt} V_P - \frac{\partial q_r}{\partial x_j} \frac{V_P}{PlGa\sqrt{RaPr}} = \frac{\Delta t}{\sqrt{RaPr}} \sum_f \frac{\partial^2 T}{\partial n \partial t} \mathbf{S}_f + \frac{\partial^2 \overline{P}}{\partial t^2} \frac{V_P \Delta t}{Ga} + \frac{\partial^2 q_r}{\partial x_j \partial t} \frac{V_P \Delta t}{PlGa\sqrt{RaPr}} + O\left(\Delta t^2\right) \tag{5.26}$$

The discrete energy conservation error associated with Algorithm B in any cell at time t therefore given by

$$E(t) = \frac{\Delta t}{\sqrt{RaPr}} C_1(t) + \frac{\Delta t}{Ga} C_2(t) + \frac{\Delta t}{PlGa\sqrt{RaPr}} C_3(t) + O\left(\Delta t^2\right) \tag{5.27}$$

where $C_1(t), C_2(t)$ and $C_3(t)$ are functions of transients of temperature, thermodynamic pressure and radiative heat transfer, respectively. As already discussed in Section 5.2.4 that the time derivatives of temperature, thermodynamic pressure, and radiative heat transfer approach zero at steady state. Hence, the discrete energy conservation error vanishes at steady state. In the same lines with the discrete mass conservation error the discrete energy conservation error also approaches zero as $\Delta t \rightarrow 0$, $Pl \rightarrow \infty$ and product of $RaPr \rightarrow \infty$. However, unlike the discrete mass conservation error, the energy conservation vanishes as $Ga \rightarrow \infty$. Hence, even in the Boussinesq limit as $Ga \rightarrow 0$ Algorithm B has a finite error. Hence one can expect Algorithm A and C to be superior to Algorithm B in the Boussinesq limit. Aforementioned concludes that the performance of temperature update algorithm requires further investigations for scenarios involving small temperature difference Boussinesq convection with significant influence of radiative heat transfer.

5.2.6 Implications of mass and energy conservation errors in a combined radiative convective heat transfer scenario

This section highlights the implications of the mass and energy conservation errors arising due to the use of temperature update (Algorithm B) and density update (Algorithm C) algorithms in buoyancy assisted flows with thermal radiative heat transfer scenario. As already discussed in Sections 5.2.4 and 5.2.5 that the magnitude of discrete mass and energy conservation error increases as $Pl \rightarrow 0$ and product of $RaPr \rightarrow 0$. However, the dependence on temperature difference parameter Ga varies for the discrete mass and energy conservation errors. The discrete mass conservation error increases as $Ga \rightarrow \infty$ (highly non-Boussinesq) whereas the discrete energy conservation error surprisingly is greater as $Ga \rightarrow 0$ (Boussinesq limit). The magnitude of these errors plays an important role in steady-state convergence while performing simulations with a pseudo-transient approach. We have carried out numerical studies in a 1×1 differentially heated enclosure as shown in Fig. 5.1(a), with 200×200 uniform hexahedral grids with an angular domain of 6×20 rays. The boundary conditions used in this study are explained as,

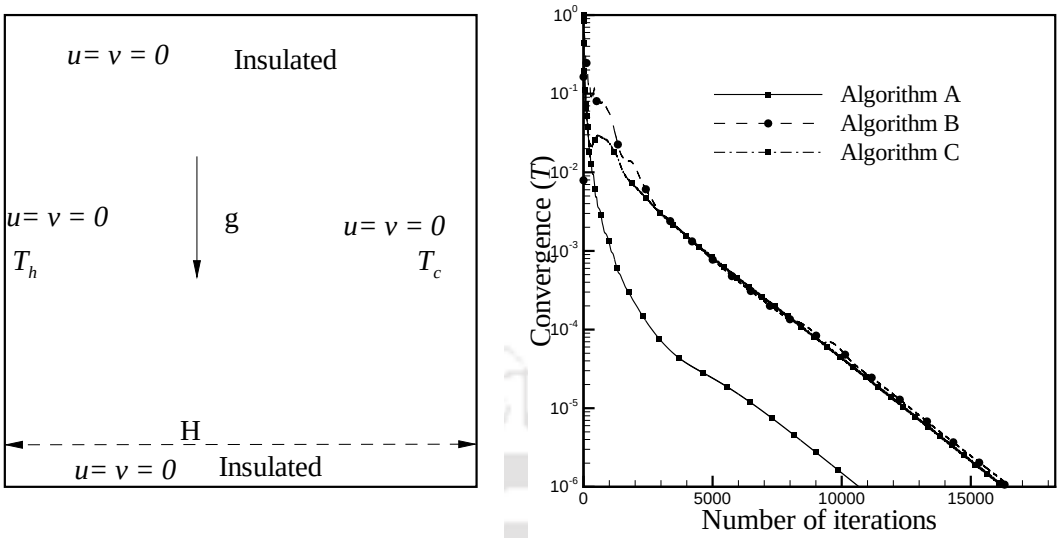

(a) (b)

Figure 5.1: (a) Computational domain consisting of 1×1 differentially heated cavity. (b) convergence rate for the three algorithms under consideration for Case 2.

$$\begin{aligned} &\text{Enclosure walls} : u = v = 0 \\ &\text{Isothermal wall at } X = 0 : T = 1 \\ &\text{Isothermal wall at } X = 1 : T = 0 \\ &\text{Adiabatic walls at } Y = 0, 1 : \frac{\partial T_w}{\partial n} + \frac{1}{GaPl} \int_{4\pi} I \; \hat{\mathbf{s}} \cdot \hat{\mathbf{n}} d\Omega = 0 \end{aligned} \tag{5.28}$$

$$I_w \left(\mathbf{r_w}, \hat{\mathbf{s}} \right) = \varepsilon_w I_b + \frac{1 - \varepsilon_w}{\pi} \int\limits_{\mathbf{s} \cdot \hat{\mathbf{n}} > 0} I \left(\mathbf{r_w}, \hat{\mathbf{s}} \right) \hat{\mathbf{s}} \cdot \hat{\mathbf{n}} d\Omega$$

We choose four different sets of parameters which are pertinent to applications like boiler and furnace design, solidification and melting as shown in Table 5.2 for varying values of Ra, Pr, Pl, and Ga. This study aims to understand the role played by various parameters for flow and heat transfer in the robustness of the algorithms based on the expression of conservation errors derived in this section.

A comparative analysis of the performance of the three algorithms for combined convection with thermal radiation for various values of non-dimensional parameters is summarized in Table 5.2. The following salient conclusions can be made from the Table 5.2.

Table 5.2: Implications of discrete mass and energy conservation errors on stability and convergence to steady state in a two-dimensional buoyancy assisted convection with thermal radiative heat transfer.

Case	Parameters	Algorithm	$\Delta t = 10^0$	10^{-1}	10^{-2}	10^{-3}	10^{-4}
Case 1	$Ra = 10^5$ Pr=0.71 Ga=1.2 Pl =0.02	A	**Stable**	Stable	Stable	Stable	Stable
		B	Unstable	Unstable	Stable	Stable	Stable
		C	Unstable	Unstable	Stable	Stable	Stable
Case 2	$Ra = 10^5$ Pr=0.71 Ga=1.2 Pl =0.0002	A	Unstable	**Stable**	Stable	Stable	Stable
		B	Unstable	Unstable	Unstable	Stable	Stable
		C	Unstable	Unstable	Unstable	Stable	Stable
Case 3	$Ra = 10^3$ $Pr = 10^{-3}$ Ga=1.2 Pl =0.02	A	Unstable	**Stable**	Stable	Stable	Stable
		B	Unstable	Unstable	Unstable	Unstable	Stable
		C	Unstable	Unstable	Unstable	Unstable	Stable
Case 4	$Ra = 10^3$ $Pr = 10^{-3}$ Ga=0.01 Pl =0.02	A	Unstable	**Stable**	Stable	Stable	Stable
		B	Unstable	Unstable	Unstable	Unstable	Stable
		C	Unstable	Unstable	Unstable	Stable	Stable

• It is clear that for simulating non-Boussinesq convection with strong radiative heat transfer effects using a pseudo-transient approach, the Algorithm A is the most robust among three algorithms for scenarios including high temperature difference natural convection with radiation.

• The values of smaller Planck number corresponds to greater radiative heat transfer effect necessitating the use of smaller Δt for all three algorithms. However, the time

step required for Algorithm A is at least two orders greater than Algorithms B and C. It is due to the energy and mass conservation errors associated with Algorithms B and C.

• The same effect can also be seen when the product of Ra, Pr becomes smaller; the algorithms require a further reduction of Δt. Algorithm A remains stable at the same $\Delta t = 10^{-1}$. However, Algorithms B and C would require very low time steps to achieve steady results.

• In the Boussinesq limit, it can also be seen that Algorithm A retains its robust character. In this case it is interesting to note that Algorithm C is stable for $\Delta t = 10^{-3}$ whereas Algorithm B is found to be stable for Δt one order lower than C. In the case of Boussinesq limit for very low Ra, Pr one can see that Algorithm C is superior to B due to the superior conservation errors of C above B as $Ga \to 0$. The lower time step requirement for Algorithm B may also be attributed to the use of explicit relation for calculation of thermodynamic pressure as defined in Eq. (5.8).

Never the less in all the cases Algorithm A performs best because it allows for the largest possible time step and takes least iterations for convergence to steady state among all algorithms as see from the convergence history for Case 2 depicted in Fig. 5.1(b). When converged solutions are obtained, one may note that no significant discrepancies can be observed among the three algorithms as also highlighted in detail in the next section.

5.3 Results and Discussion

In this section, we shall discuss the three algorithms for practical problems involving both two-dimensional and three-dimensional combined natural convection with surface and gas radiation in enclosures. In the first test case, a two-dimensional study is performed considering a differentially heated square cavity with baffles. The temperature difference used in this problem is small enough to be modeled using Boussinesq assumption. This test case highlights the capability of the three algorithms in computing small temperature difference natural convection problem

coupled with surface radiation. The second test case consists of large temperature difference non-Boussinesq convection with gas radiation. The participating medium used in this test case absorbs, emits and scatters radiation. This test case serves as an ideal problem to highlight the capability of the present three algorithms in computing large temperature difference non-Boussinesq convection with significant influence of thermal radiative heat transfer and the role of conservation errors on their robustness. The third test case consists of radiative-convective heat transfer in a square enclosure with a heated cylinder. This simulation is performed to confirm the capability of the three algorithms to perform computations in complex scenarios requiring the use of hybrid unstructured meshes. The results are validated against those in published literature for all test cases.

5.3.1 Small temperature difference natural convection in a partitioned cavity coupled with surface radiation

The first test case consists of an experimental study involving a square enclosure with baffles from the top and bottom walls. The cavity is differentially heated, and the participating medium consists of air and carbon dioxide. Bajorek and Lloyd [65] initially performed this experimental study, furthermore the numerical simulations were carried out by Han and Baek [70] where they only considered the influence of surface radiation in their simulations. The geometry of the problem consists of a partitioned differentially heated square enclosure of height $H = 6.35$ cm with hot and cold wall temperatures (dimensional temperature) as $T_h = 312.1$ K and $T_c = 296.6$ K. The length of baffles are $0.1H$ and height of $0.25H$ as shown in Fig. 5.2 (a). Figure 5.2 (b) represents the comparison of temperature variation along the horizontal center line with the literature. All the algorithms compute the same temperature difference at steady state. However, from the time step required for achieving steady simulations in Table 5.3 it is seen that Algorithm B require using a value of time step two order and Algorithm C requires one order smaller than that required for Algorithm A. The implications of the time-step requirement for convergence to steady state can be realized by analyzing the convergence rate depicted in Fig. 5.3. From the Fig. 5.3 it can be seen that the Algorithm A requires the minimum number of iterations while Algorithm B requires the maximum number of iterations for convergence to steady state.

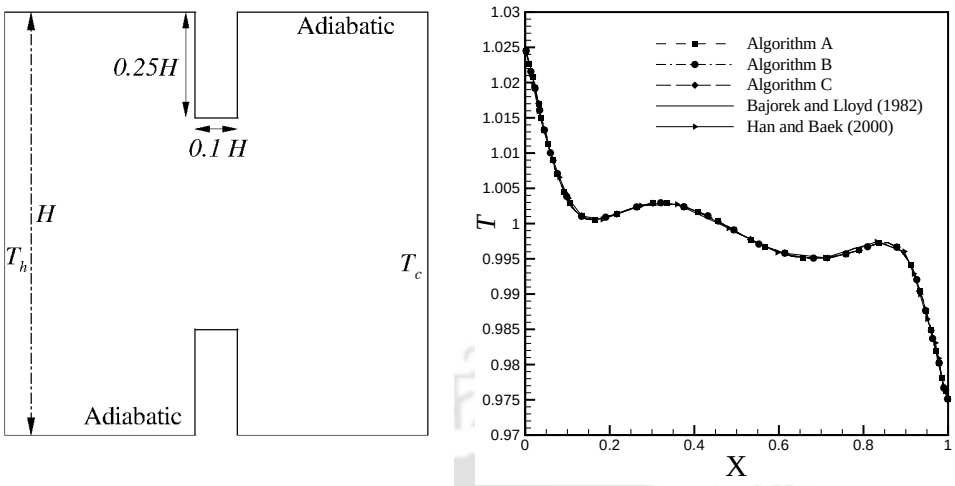

(a) (b)

Figure 5.2: Combined natural convection with surface radiation in a square cavity with baffles, compared with the experimental results of Bajorek and Lloyd (1982), (a) computational geometry, (b) comparison of non-dimensional temperature variation along the horizontal mid-plane.

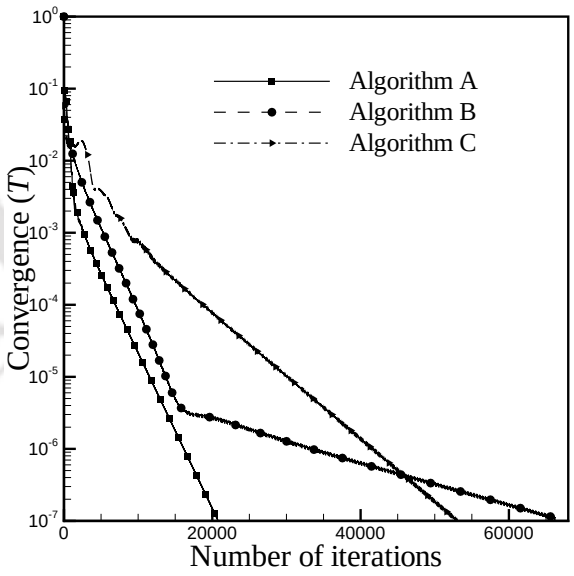

Figure 5.3: Comparison of convergence rate among the three algorithms for coupled convection with surface radiation in two-dimensional enclosure with baffles.

Table 5.3: Time step requirement for achieving steady state results using Algorithms A, B and C.

Time step	$\Delta t = 10^0$	$\Delta t = 10^{-1}$	$\Delta t = 10^{-2}$
Algorithm A	Stable	Stable	Stable
Algorithm B	Unstable	Unstable	Stable
Algorithm C	Unstable	Stable	Stable

5.3.2 Large temperature difference natural convection coupled with gas radiation

This test case consists of buoyancy assisted convection with gas radiation in a two-dimensional square enclosure differentially heated at large temperature difference with significant influence of radiative heat transfer. The problem is solved for $Ra = 5 \times 10^6$, $Pr = 0.71$, $Pl = 0.02$ and $Ga = 0.66$ using all three algorithms. The scattering albedo $\omega = 0.8$ and optical thickness $\tau = 5.0$ are used in the present simulation with an aim to validate a non-Boussinesq combined radiative-convective heat transfer by absorbing, emitting and scattering medium. Figure 5.4 (a) represents the temperature variation inside the square enclosure. Figure (5.4) (b) demonstrates the velocity variation (streamlines) inside the enclosure whereas, Fig. 5.4 (c) depicts the variation of local values of convection, radiation, and total (convection+radiation) Nusselt number along the hot and cold walls. Figure 5.4 (d) represents the centerline velocity variations along the horizontal and vertical mid-plane of the cavity. These results depict excellent agreement with the work of Darbandi and Abrar [33]. The average values of Nusselt number (convection, radiation and total) at the hot and cold walls are tabulated in Table 5.4 and compared with the literature. From these results, it is seen that all the three-algorithms can accurately predict non-Boussinesq natural convection with gas radiation inside enclosures. However, from Table 5.5 it may be observed that both the Algorithms B and C have to use a value of time step Δt which is two orders less than that needed for Algorithm A. On comparing the convergence rate depicted in Fig. 5.5 it is clear that Algorithm A obtains the steady state with minimum iterations.

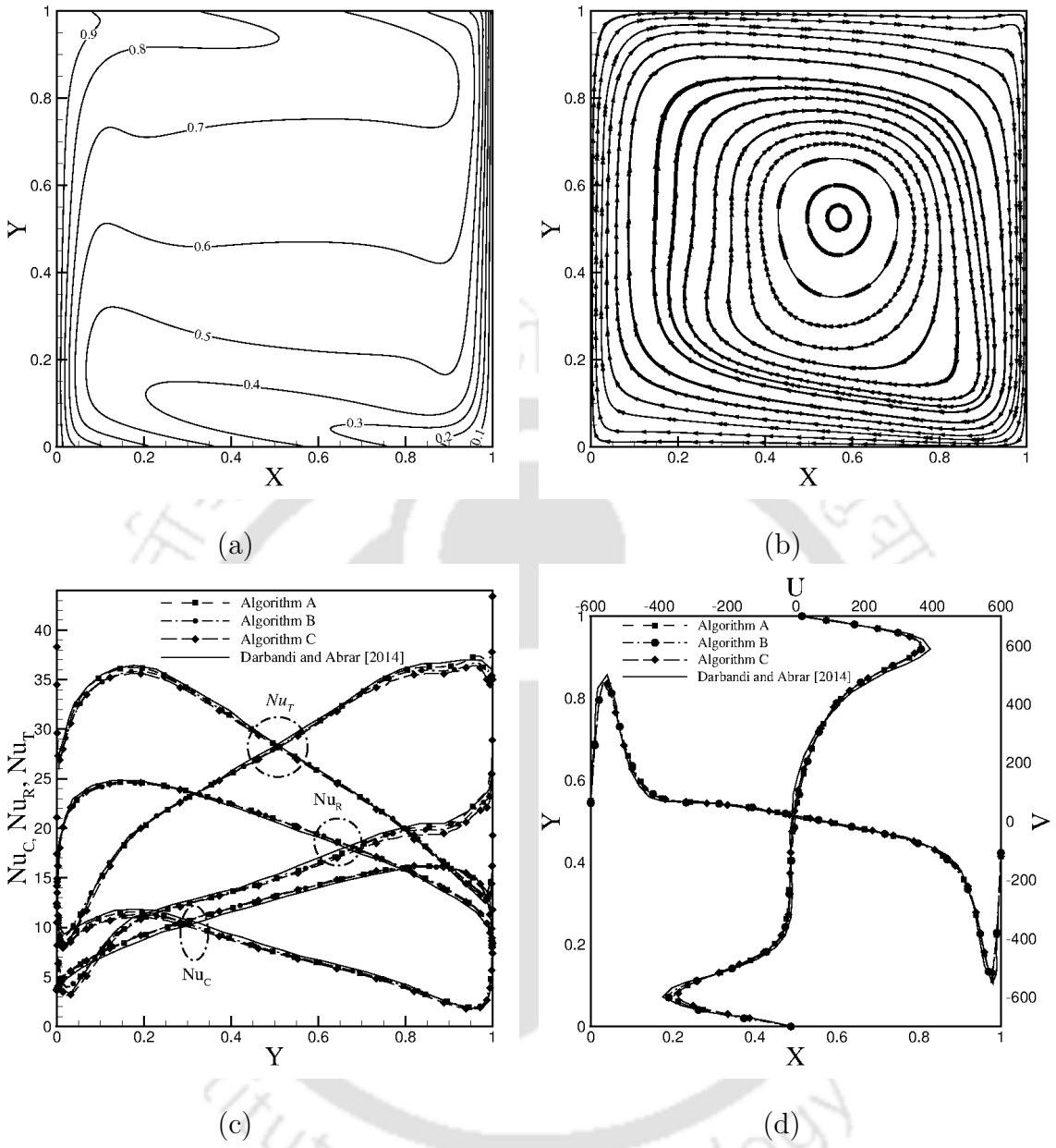

Figure 5.4: Buoyancy assisted convection coupled with gas radiation in a square cavity: validation of the present results using Algorithms A, B and C with the published work of Darbandi and Abrar (2014), (a) isotherms inside the square enclosure, (b) streamlines inside the square enclosure, (c) comparison of local Nusselt number variation along the hot and cold walls, (d) comparison of centerline velocity variations inside the cavity along the horizontal and vertical mid-planes.

Table 5.4: Average values of Nusselt number at the hot and cold walls: Comparison between Darbandi and Abrar (2014), and present Algorithms A, B, and C.

Author	$Nu_{convective}$		$Nu_{radiative}$		Nu_{total}	
Wall	Hot	Cold	Hot	Cold	Hot	Cold
Darbandi and Abrar (2014)	7.717	19.700	27.417	12.093	15.318	27.411
Algorithm A	7.698	19.750	27.448	12.051	15.397	27.448
Algorithm B	7.685	19.690	27.375	11.972	15.403	27.375
Algorithm C	7.697	19.713	27.410	11.978	15.432	27.410

Table 5.5: Time step requirement for achieving steady state results using Algorithms A, B and C.

Time step	$\Delta t = 10^0$	$\Delta t = 10^{-1}$	$\Delta t = 10^{-2}$
Algorithm A	Stable	Stable	Stable
Algorithm B	Unstable	Unstable	Stable
Algorithm C	Unstable	Unstable	Stable

5.3.3 Combined convection with surface radiation in a square cavity enclosing a heated cylinder

The third test case consists of a combined convection with surface radiation heat transfer in a square enclosure of dimension H containing a heated cylinder of radius $0.2H$ as depicted in Fig. 5.6 (a). The vertical walls of the enclosure are isothermal cold walls whereas the horizontal walls are adiabatic, and the cylinder is heated at a constant temperature. The values of non-dimensional parameters governing the flow and heat transfer are $Ra = 10^6$, $Pr = 0.71$, $Ga = 0.05$. This test case is validated to depict the capability of the algorithms in solving complicated geometries. Figure 5.6 (b) represents the comparison of temperature variation along the horizontal planes at $Y = 0$ and $Y = H$ of the square enclosure with the published work of Mezrhab et al. [71]. Figures 5.7 (a) and (b) represent the isotherms and streamlines variation inside the square cavity with the heated cylinder. From the isotherms in Fig. 5.7 (a) one can see the hot fluid rising above the heated cylinder and leads to the formation

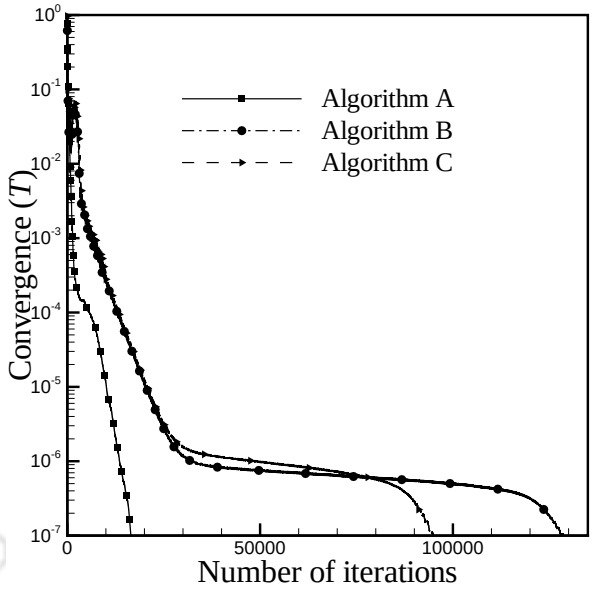

Figure 5.5: Comparison of convergence rate among the three algorithms for coupled convection with gas radiation in a two-dimensional square enclosure.

of two primary vortices which are symmetric about the vertical mid-plane (Fig. 5.7 (b)).

Table 5.6: Comparison of average values of Nusselt number (convection, radiation and total) at the heated cylinder using Algorithms A, B and C with the work of Mezrhab et al. (2008)

Author	Nu_c	Nu_r	Nu_t
Mezrhab et al. (2008)	14.35	16.65	31.00
Algorithm A	14.41	16.62	31.04
Algorithm B	14.32	16.66	30.98
Algorithm C	14.39	16.65	31.05

The isotherms and streamlines depicted in Figs. 5.7 (a) and 5.7 (b) are consistent with the results of Mezrhab et al. [71]. Table 5.6 represents the average Nusselt number variation at the heated cylinder for the three algorithms A, B, and C compared with the results of Mezrhab et al. [71]. The results are in excellent agreement

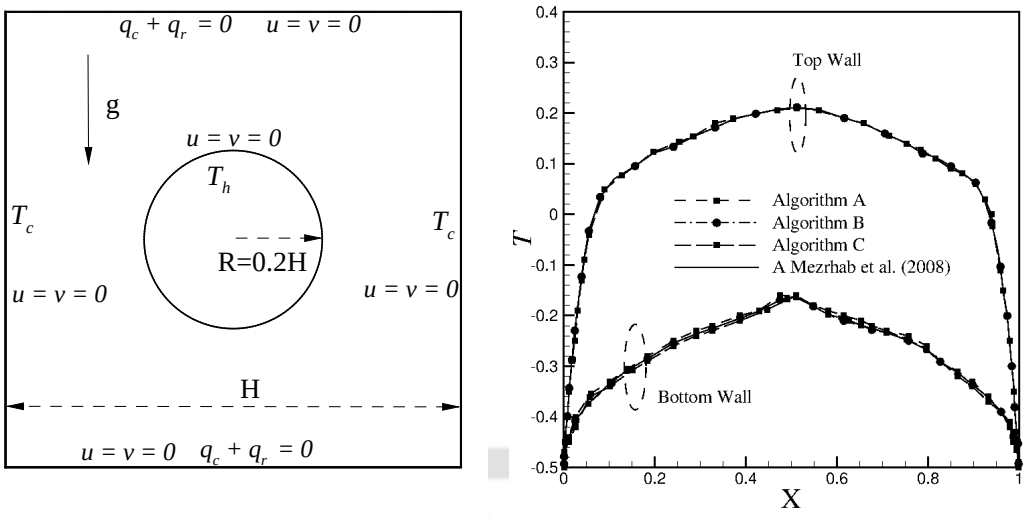

(a) (b)

Figure 5.6: Comparison of the present results using Algorithm A, B and C with the results of Mezrhab et al. (2008). (a) Computational domain, (b) comparison of temperature variation at the top and bottom walls of the cavity.

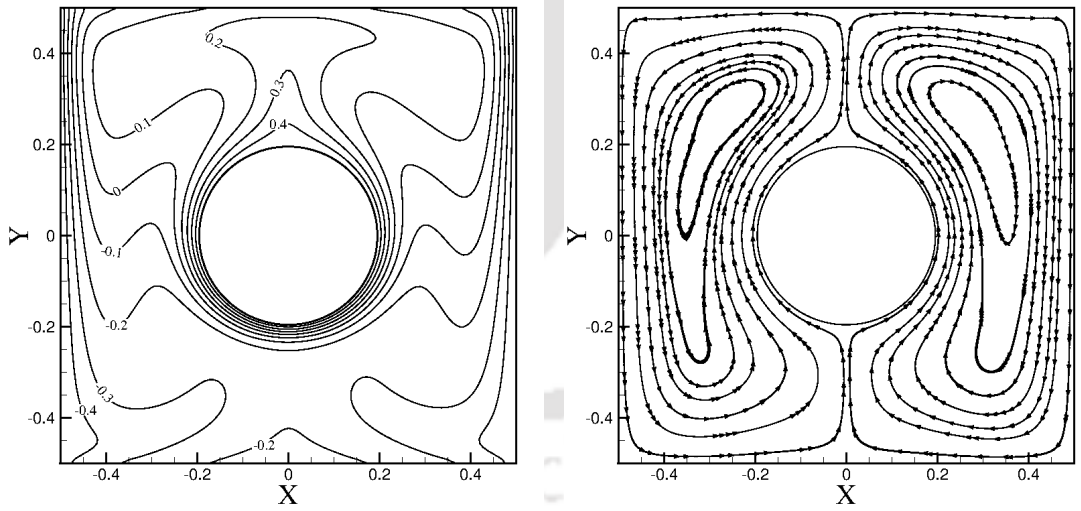

(a) (b)

Figure 5.7: Combined convection with surface radiation in a square cavity enclosing a heated cylinder, (a) isotherms inside the enclosure, (b) streamlines inside the enclosure.

with the published literature. However, the time step required for achieving steady state as shown in Table 5.7 suggests that Algorithm B requires using a value of time step two order and Algorithm C requires one order smaller than that required for Algorithm A similar to the observations in Section 5.3.2. The implications of the time step requirement can be understood from the comparison of convergence rate for the three-algorithms as shown in Fig. 5.8. From Fig. 5.8 it is seen that the performance of Algorithm B is inferior as compared to the other algorithms as it requires maximum number of iterations for convergence to steady state.

Table 5.7: Time step requirement for achieving steady state results using Algorithms A, B and C.

Time step	$\Delta t = 10^0$	$\Delta t = 10^{-1}$	$\Delta t = 10^{-2}$
Algorithm A	Stable	Stable	Stable
Algorithm B	Unstable	Unstable	Stable
Algorithm C	Unstable	Stable	Stable

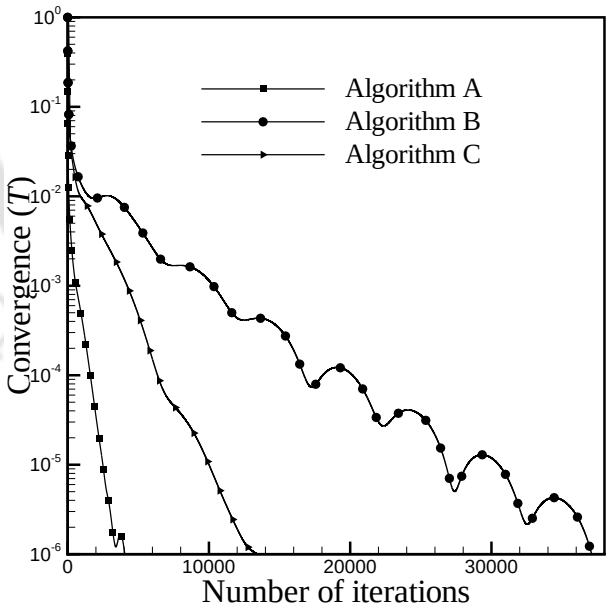

Figure 5.8: Comparison of convergence rate among the three algorithms for coupled convection with surface radiation in a square enclosure containing a heated cylinder.

5.4 The Balanced Force Algorithm

The studies in the previous section have categorically underlined the relation between discrete conservation errors and the time step requirement for pseudo-transient simulations in radiative-convective heat transfer. Discussions on yet another pertinent numerical artifact which could hamper robustness of flow solvers for such applications is presented. For problems involving large temperature difference non-Boussinesq convection, it is imperative to implement the algorithms in a manner that allows for a "balanced force approach". This means that one should consider the gravity and pressure forces in the Poisson equation (Eq. (2.110)) rather than the provisional momentum equations (Eq. (2.109)) while dealing with strong body forces involved in combined radiative-convective heat transfer. Such an approach is very similar to those encountered in multi-phase flow simulations as depicted in the work of Patel and Natarajan [126]. Investigations on the necessity of such implementation for robust simulations of combined radiation with convection heat transfer problems in enclosures is presented. As mentioned earlier, in the case of a balanced algorithm, the "provisional momentum" is computed by dropping both the pressure and buoyancy terms from the momentum equations (as described in Section 2.7) while for an unbalanced algorithm only the pressure term is dropped. Therefore, the "provisional momentum" equations for the balanced and unbalanced algorithms are given by Eqs. (5.29) and (5.30), respectively.

$$\frac{\partial\left(\rho u_i^*\right)}{\partial t}+\frac{\partial\left(\rho u_i^* u_j\right)}{\partial x_j}=\sqrt{\frac{Pr}{Ra}}\frac{\partial \tau_{ij}}{\partial x_j} \tag{5.29}$$

$$\frac{\partial\left(\rho u_i^*\right)}{\partial t}+\frac{\partial\left(\rho u_i^* u_j\right)}{\partial x_j}=\sqrt{\frac{Pr}{Ra}}\frac{\partial \tau_{ij}}{\partial x_j}+\frac{1}{Ga}(1-\rho)\hat{\mathbf{e}}_{\mathbf{y}} \tag{5.30}$$

The dropping of buoyancy term from the "provisional momentum" equation ensures consistent treatment of both the pressure and buoyancy term in the pressure equation defined by Eq. (5.31).

$$\frac{2\Delta t}{3}\sum_f \frac{1}{\rho_f}\left(\nabla p\right)_f \cdot \mathbf{S}_f=\sum_f F_{0f}^*-\sum_f F_f^{n+1}+\frac{2}{3}\sum_f \frac{\Delta t}{Ga}\left(\frac{1-\rho_f}{\rho_f}\right)\hat{\mathbf{e}}_{\mathbf{y}}\cdot\mathbf{S_f} \tag{5.31}$$

This leads to a variable coefficient pressure equation for non-homogeneous Neumann boundary condition. The momentum interpolation for the fluxes at "$n+1$", as well

as the update of velocities, are also suitably modified and represented in Eqs. (2.114) and (2.115) respectively. Furthermore, it is clear that dropping of buoyancy term from the "provisional momentum" equation leads to the appearance of buoyancy term in Poisson equation as well as the momentum interpolation and velocity update equations. We now look at the impact of a balanced force approach described herein for numerical computations of non-Boussinesq flows.

5.4.1 Balanced vs. unbalanced approach: spurious currents arising due to the unbalanced algorithm

To highlight the numerical implications of using a balanced versus unbalanced approach, we consider a square enclosure of size 1×1 as shown in Fig. 5.9 with a fixed linearly varying temperature profile $T(y) = Y$, where Y represents the distance along the height of the enclosure varying from 0 to 1. The density is obtained from the equation of state $\rho = \frac{\overline{P}}{1+GaT}$ and is used as the initial condition. No radiative heat transfer effects are considered to focus purely on the balancing between pressure and buoyancy terms. The test case is solved using Algorithm A by employing both the balanced and unbalanced approach. The non-dimensional parameters used in the present study corresponds to Ra=10^6, $Pr = 0.71$ and $Ga = 0.66$. The boundary conditions used in the present test case are summarized below.

$$\begin{aligned} \text{Enclosure walls} &: u = v = 0 \\ \text{Isothermal bottom wall at Y} = 0 &: T = 0 \\ \text{Isothermal top wall at Y} = 1 &: T = 1 \\ \text{Adiabatic walls at X} = 0,\ 1 &: \frac{\partial T_w}{\partial n} = 0 \end{aligned} \tag{5.32}$$

Notably, by employing a fixed temperature and density profile inside the enclosure, there is only one way coupling between temperature and velocity, i.e., the velocity cannot influence the temperature and hence the density. Ideally, the numerical solution to the above problem must result in a pressure field which should balance the buoyancy term without any generation of flow inside the enclosure. While the balanced approach does lead to machine zero spurious currents, the unbalanced algorithm leads to anomalous velocities of order $O(10^{-2})$ as shown in Figs. 5.10 (a) -

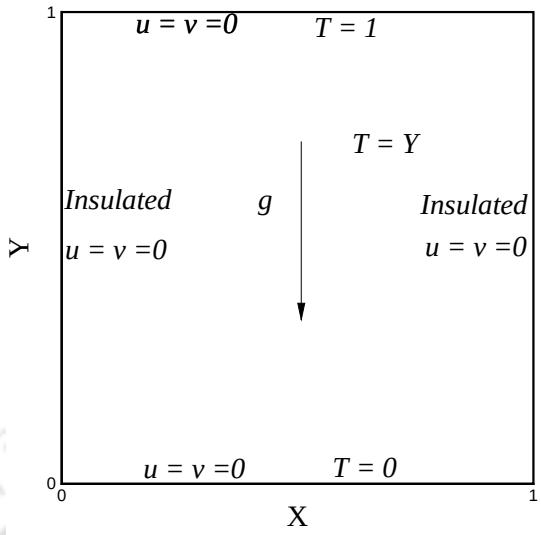

Figure 5.9: Computational domain consisting of 1×1 cavity with linear variation of temperature and density.

(d) even after running the simulation for considerable time steps. Such spurious currents in practice could lead to numerical instability in problems where body forces could be significant, and a discrete balance is not affected. We precisely investigate such a scenario for a three-dimensional test case in the following section. The idea of balanced formulation is inherently linked with the modification to momentum interpolation and therefore also to the means of avoiding the checker boarding issue in incompressible flows. In fact, there have been studies in the past that have considered modifications to the momentum interpolation approach when body forces are involved (See Refs [127–129]). However, these approaches are not generic having been restricted to structured meshes (barring Danner and Wachem [128]) and do not discuss the interplay between pressure and buoyancy forces. In fact, studies in Choi et al. [127] have shown the existence of spurious velocities for natural convection case on uniform grids with a collocated framework that vanish with grid refinement when momentum interpolation is employed. The proposed balanced force formulation may be recognized as a generic modification to Rhie-Chow interpolation [112] that clearly highlights the origin of spurious velocities as the "discrete imbalance" between competing forces i.e pressure and buoyancy in the case of natural convective flows.

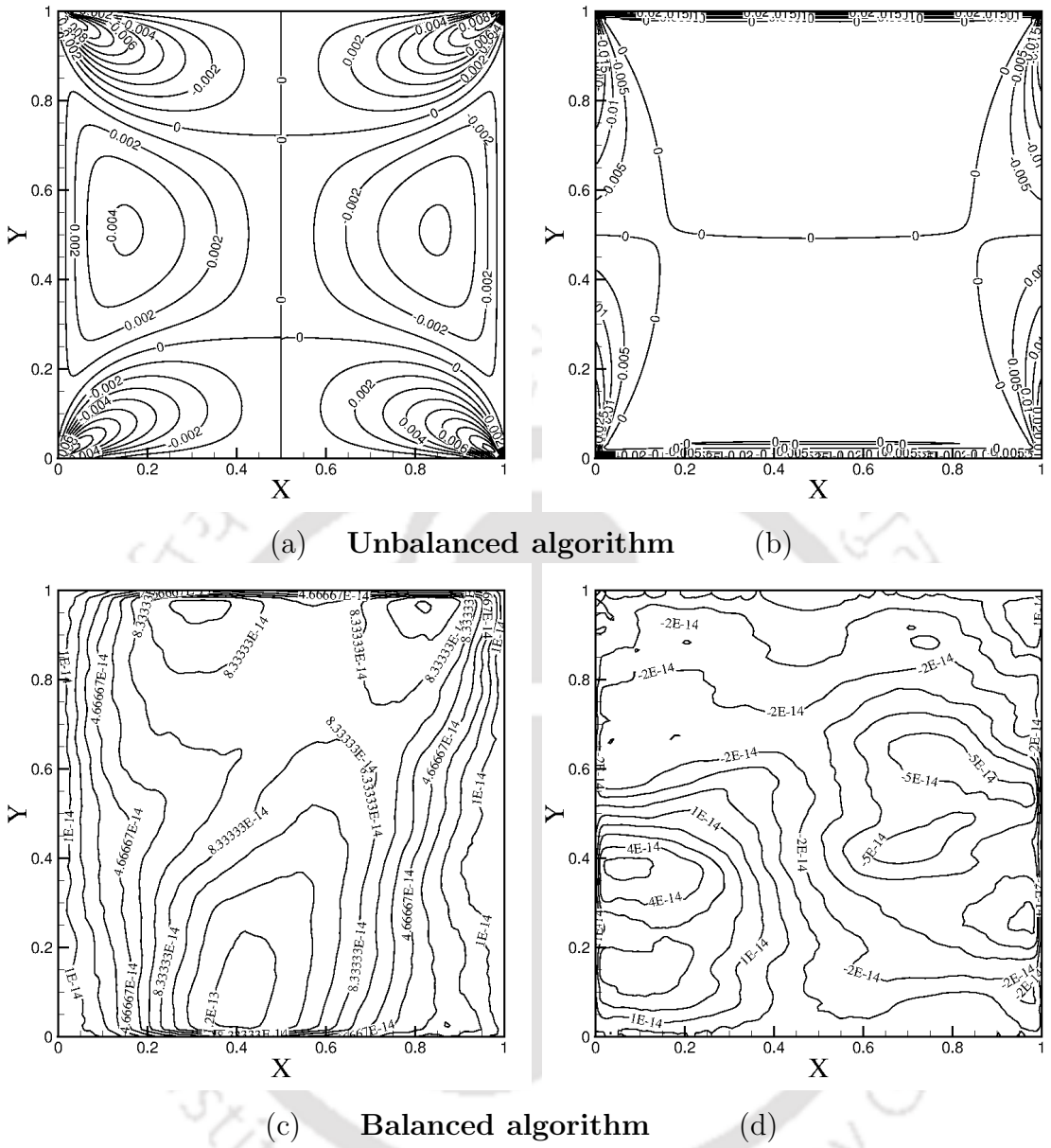

Figure 5.10: Spurious currents generated inside the cavity for the balanced and unbalanced algorithm. Contours of u, v velocity using the (a, b) unbalanced and (c, d) balanced formulation respectively.

5.4.2 Three-dimensional buoyancy driven flow coupled with gas radiation

The problem consists of buoyancy assisted convection with gas radiation inside a cubical enclosure previously studied by Kumar and Eswaran [31]. The geometry of

the problem is described in Fig. 5.11 (a) and consists of a $1 \times 1 \times 1$ differentially heated cubical enclosure with dimensional temperature values of $T_h = 1000$ K and $T_c = 500$ K, the top bottom and front back walls are adiabatic. The dimensionless parameters used in the simulations are $Ra = 5 \times 10^5$, $Pr = 0.71$, and $N = 0.1$, where N is the conduction-radiation parameter. The participating medium consists of an absorbing, emitting gas with optical thickness $\tau = 1.0$. The temperature difference used in this test case is large enough to be treated using a non-Boussinesq formulation. The study is carried out using a grid size of $61 \times 61 \times 61$ and angular discretization of 6×8 as also used in the work of Kumar and Eswaran [31]. Figure 5.11 (b) depicts the local variation of total Nusselt number (convection and radiation) at the hot wall of the cubical enclosure whereas Table 5.8 represents the comparison of average values of the total Nusselt number at the hot wall with the results of Kumar and Eswaran [31]. These results are in excellent agreement with the published results of Kumar and Eswaran [31] and depict the capability of the algorithm to accurately predict combined natural convection with gas radiation in three-dimensional enclosures. Importantly, while we could compute the problem with $\Delta t = 10^{-1}$ using a balanced approach, stable simulations were possible with an unbalanced approach only for $\Delta t = 10^{-3}$ as shown in Table 5.9. Hence, the use of balanced formulation enables one to obtain physically correct results with fewer iterations and at a cheaper computational cost as depicted in Fig. 5.12. Not surprisingly, both the methods found identical numerical solutions on convergence to steady state. It may be embarked that one could adopt such an approach with Algorithms B and C as well. However, since Algorithm A has been shown to be superior in terms of robustness we have limited our study only to Algorithm A. One can, therefore, conclude that use of a discretely conservative algorithm with a balanced force approach contributes to the robust formulation for simulation of convective-radiative heat transfer problems. The numerical studies in the present work provide sufficient evidence to confirm this observation. It is recommended that potential researchers keen on developing solution algorithms account for the role of force balancing and discrete conservation in the design of robust and accurate flow solvers. We believe that the presence of spurious velocities when an unbalanced formulation is employed in a simple canonical problem described in section 5.4.1 could likely trigger instabilities in case of the solution of non-linear Navier-Stokes equations in quasi-incompressible regimes studied here. This is possibly the reason why the balanced formulation allows for larger time steps than the unbalanced counter-

part for buoyancy-driven flows on a given mesh, without compromising on solution accuracy. While further studies are required to establish the grid size dependence, we speculate that for a given time step, the balanced formulation would remain stable for meshes with smaller grid resolution than the unbalanced formulation. The observation that balanced formulation was necessary to compute accurately the turbulent natural convection problems described in Chapter 7 is an indirect evidence of the ability of the force balancing in devising robust and accurate algorithm to solve non-Boussinesq fluid flows.

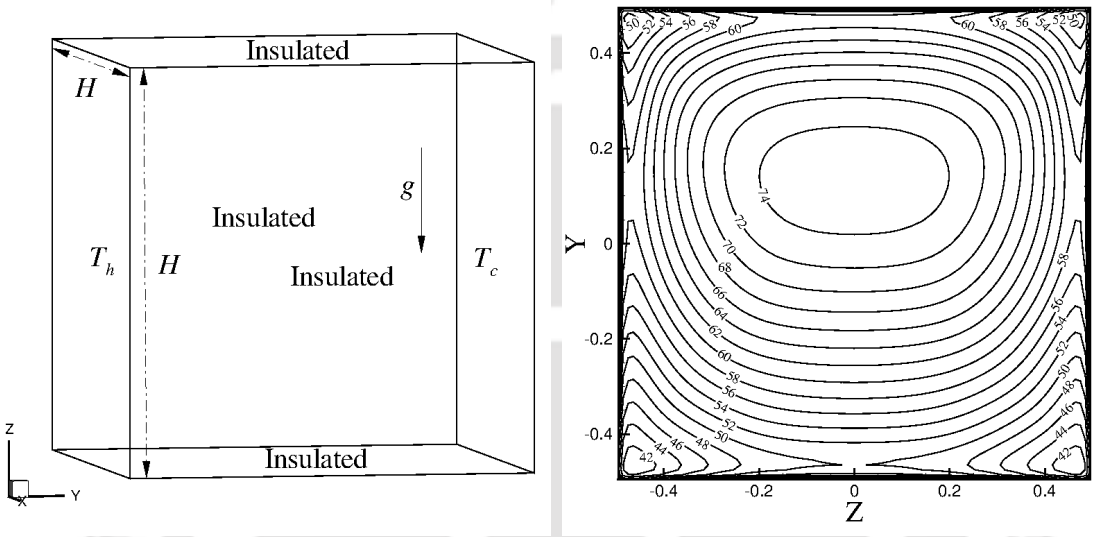

(a) (b)

Figure 5.11: Combined natural convection with gas radiation in a cubical enclosure, (a) the computational domain, (b) total Nusselt number variation at the hot walls.

Table 5.8: Comparison of average total Nusselt number at the hot wall using a fully balanced discretely conservative Algorithm A with Kumar and Eswaran (2010).

Author	Nu_t
Kumar and Eswaran (2010)	62.560
Algorithm A (Balanced)	62.549

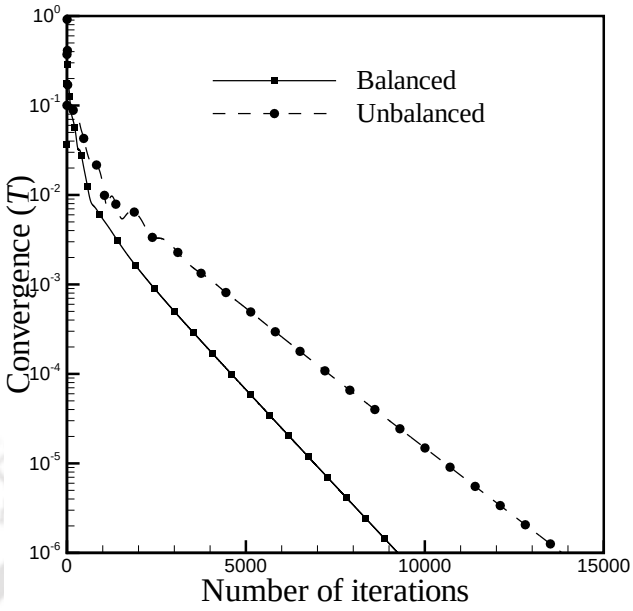

Figure 5.12: Comparison of convergence rate among the balanced and unbalanced algorithms for coupled convection with surface radiation in a three-dimensional cubical cavity.

Table 5.9: Time step requirement for achieving steady state results for balanced and unbalanced Algorithm A

Timestep	$\Delta t = 10^{-1}$	$\Delta t = 10^{-2}$	$\Delta t = 10^{-3}$
Balanced	Stable	Stable	Stable
Unbalanced	Unstable	Unstable	Stable

5.5 Closure

In this chapter, three different algorithms are presented for the numerical simulation of non-Boussinesq convection with thermal radiative heat transfer based on a low-Mach number formulation. The three algorithms differ in the way they use EOS for computing either of temperature, density or thermodynamic pressure. Several numerical studies are performed to depict the capability of the three-algorithms in computing coupled convection with thermal radiation in Boussinesq and non-Boussinesq limits. Further, the energy and mass conservation errors arising due to

the use of update based algorithms (B and C) are derived. The significance of these errors in radiative-convective flows is highlighted by performing investigations over a range of Rayleigh, Prandtl, and Planck numbers. In addition, the balancing of the pressure and buoyancy terms is emphasized for robust calculations of large temperature difference thermo-buoyant convection with radiative heat transfer. Based on the numerical studies performed in this chapter it is reported that the conservative algorithm A with balanced force formulation is best suited for robust computation of convective-radiative flows and heat transfer in enclosures.

Chapter 6

Convective-Radiative Heat Transfer in 3D Partitioned Cavity

6.1 Introduction

In this chapter, the developed numerical framework is applied to investigate the influence of partitions on buoyancy induced convection with thermal radiation in a differentially heated cubical enclosure. Four distinct arrangements of partitions from the top-bottom and front-back walls are examined by adopting a symmetric (inline) and asymmetric (offset) configuration of partitions. Comparative analysis of average and local Nusselt number variation at the isothermal walls and temperature variation inside the enclosure is presented for all configurations of partitions considered. Irreversibilities associated with conduction, convection, and radiation heat transfer with viscous dissipation are studied to examine the role of partitioning walls in overall volumetric entropy production. This study aims at achieving optimum thermal design (higher heat transfer rates with minimum entropy production)

The contents of this chapter have been published as Parmananda, M., Dalal, A., and Natarajan, G., 2018, "The influence of partitions on predicting heat transfer due to the combined effects of convection and thermal radiation in cubical enclosures", International Journal of Heat and Mass Transfer, (available online, DOI: https://doi.org/10.1016/j.ijheatmasstransfer.2018.01.031).

among all partition configurations. Finally, the importance of three-dimensional analysis in convective-radiative flows is highlighted by depicting the significance of non-Boussinesq effects in a three-dimensional scenario in comparison to the two-dimensional assumption of the same problem.

6.2 Problem Description

This study presents numerical investigations on combined convective-radiative heat transfer in a differentially heated cubical enclosure with partitions. Figure 6.1 depicts four distinct configurations of restricting walls where Figs. 6.1 (a) and 6.1 (b) represent top-bottom partitions and Figs. 6.1 (c) and 6.1 (d) represent front-back partitions. Furthermore, two sets of inline and offset configuration of partitions are also studied. The symmetric (inline) configuration is one where the separating walls are at the center of the cavity (X=0.5, 0.5) as seen in Figs. 6.1 (a) and 6.1 (c). An offset configuration is one where the position of the restricting walls is adjacent to the isothermal walls at (X=0.25, 0.75). The computational domain consists of a cubical enclosure of height H, the length of the partitions is $0.25H$ and width is $0.1H$. It is to be noted that X, Y, Z and U, V, W corresponds to the non-dimensional co-ordinates and velocity used in the present study. The left and right walls of the cubical cavity at (X=0, 1) are isothermal whereas, the rest of the walls are adiabatic. The study is performed by considering several non-dimensional parameters such as Rayleigh number $Ra = 10^6$, Prandtl number $Pr = 0.71$, Gay-Lussac number $Ga = 1.2$ and Planck number $Pl = 0.01$. For a given physical domain, computations are performed considering buoyancy-driven convection in the absence of radiation (pure convection), secondly convective-radiative heat transfer with surface radiation and lastly thermal convection in the presence of gas radiation with optical thickness τ=0.2.

6.2.1 Grid independence study

In this section, spatial and angular grid independence tests are carried out. The objective of this study is to achieve a minimum number of spatial and angular grids for obtaining accurate results. The grid independence study (spatial and angular) has been performed for a combined convection with gas radiation inside a cubical en-

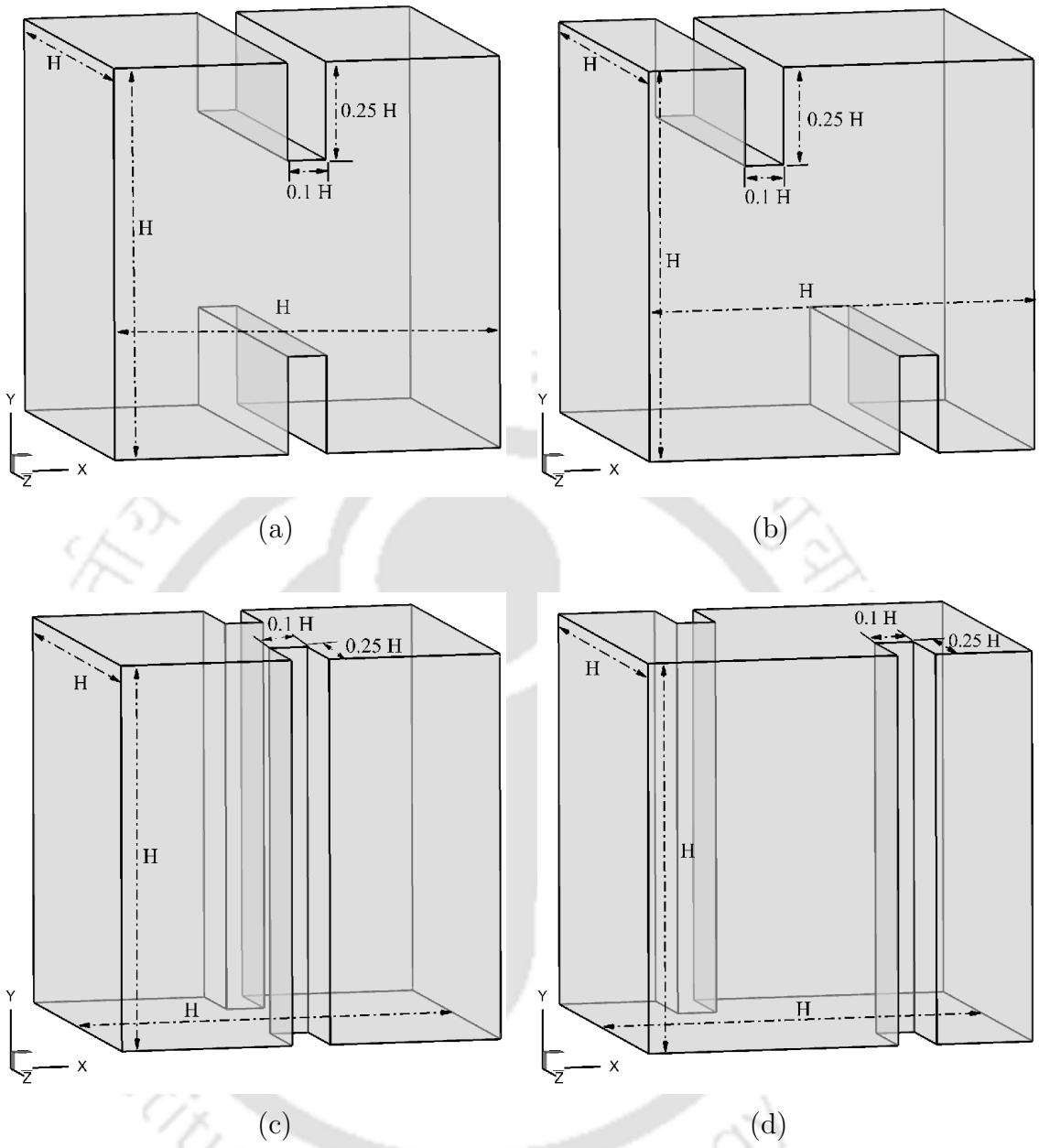

Figure 6.1: Schematic of the partitioned cubical enclosure: (a, b) partitions along the top and bottom walls, (c, d) partitions along the front and back walls.

closure with partitions extruding from the top-bottom walls as shown in Fig. 6.1(a). Four spatial grids of size 41×41×41, 61×61×61, 81×81×81 and 101×101×101 were used with a fixed angular domain of 4×18. A suitable grid refinement was used

near the cavity walls and also near the partitions. The total Nusselt number values (convection, radiation) of 32.25, 34.925, 35.687 and 35.81 were obtained at the hot and cold walls. Furthermore, for a fixed spatial grid of 81×81×81 three angular grids of size 2 × 8, 4 × 16 and 8 × 24 gave total Nusselt number values of 32.45, 35.57 and 35.64. Based on the study a spatial resolution of 81×81×81 and angular resolution 8×24 are used in the present work. The non-uniform mesh is generated using a commercial grid generation software GAMBIT [130]. Figures 6.2 (a) and (b) represent the non-uniform grids on the $X-Y$ and $Y-Z$ planes respectively for the cubical enclosure with symmetric partitions along the top and bottom walls. The point distribution in the grid ensures sufficient clustering near the walls as shown in Fig. 6.2 (a) and (b) to capture the gradients and hence the numerical solution accurately.

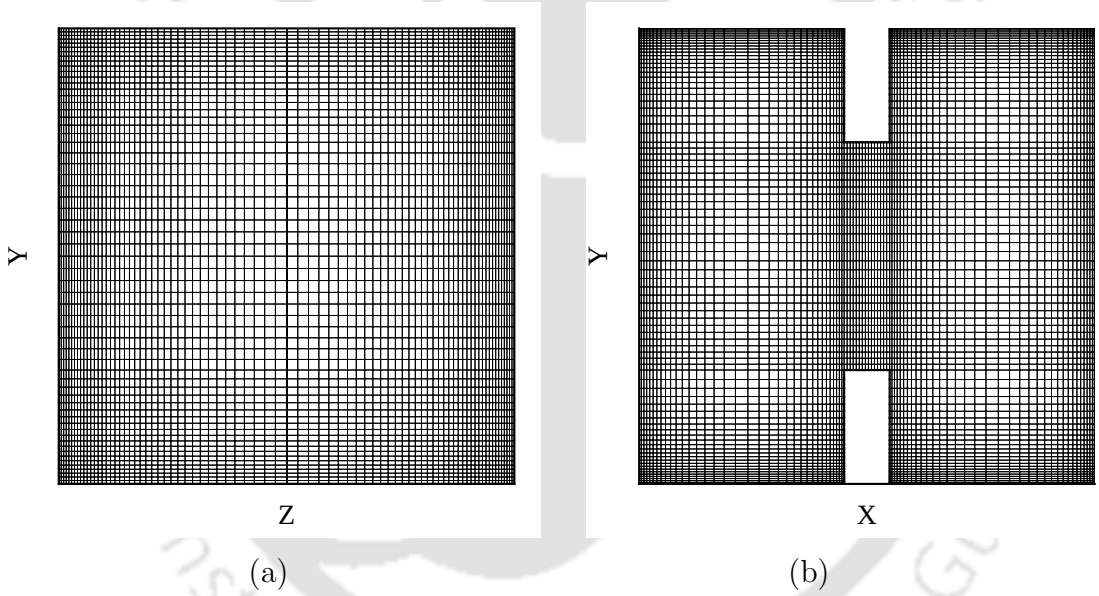

Figure 6.2: Details of the non-uniform grid (a, b) used for symmetric partitions along the top and bottom walls.

6.3 Results and Discussion

In this section, studies on buoyancy induced flow with radiative heat transfer inside the cubical enclosure with partitions are carried out. Numerical simulations considering pure thermal convection (no radiation), thermal convection coupled with

surface radiation and participating medium of optical thickness ($\tau = 0.2$) are carried out to isolate the influence of surface and gas radiation compared to a pure convection case. The problem is solved for the non-dimensional parameters such as $Ra = 10^6$, $Pr = 0.71$, $Ga = 1.2$ and $Pl = 0.01$. The Q-criterion represents the equivalence of shear strain rate and vorticity magnitudes. A positive value of Q signifies dominance of vorticity magnitude over the extent of strain rate and thus indicates generation of the vortex in that region.

$$Q = \frac{1}{2}\left(W_{ij}W_{ij} - S_{ij}S_{ij}\right)$$

$$W_{ij} = \frac{1}{2}\left(\frac{\partial u_i}{\partial x_j} - \frac{\partial u_j}{\partial x_i}\right)$$

$$S_{ij} = \frac{1}{2}\left(\frac{\partial u_i}{\partial x_j} + \frac{\partial u_j}{\partial x_i}\right) \tag{6.1}$$

Where W_{ij} is the vorticity tensor and S_{ij} is the strain rate tensor. Isosurface of temperature and Q values are presented for visualization of temperature distribution and flow inside the enclosures with partitions. Furthermore, the Nusselt number distribution at the isothermal walls signifies the influence of partitions on heat transfer. The values of convection, radiation and total Nusselt number are determined as follows.

$$Nu_c = \frac{q_c H}{k\Delta T},\ Nu_r = \frac{q_r H}{k\Delta T},\ Nu_t = Nu_c + Nu_r \tag{6.2}$$

Where q_c and q_r are the convective and radiative fluxes. The average Nusselt number $\overline{Nu}$ is the area-averaged value of Nu.

6.3.1 Influence of inline and offset configuration of top-bottom partitions

In this section discussions on buoyancy induced flow with radiative heat transfer inside a cubical enclosure with partitions protruding from top-bottom walls are presented. Studies have been performed with two configurations of partitions along the X-axis namely inline partitions at $X = 0.5$, 0.5 and offset partition at $X = 0.25$ and 0.75. The fundamental nature of flow and heat transfer corresponds to a buoyancy driven flow in a differentially heated cubical enclosure. The induction of primary flow inside the cubical enclosure is due to the interaction of the fluid with hot and

cold walls. However, the partitions along the top and bottom walls significantly alter the flow and heat transfer characteristics as described in the present study.

From the isosurface of temperature and Q in Figs. 6.3 (a) and (d) it is seen that in pure convection, apparently two-dimensional nature of temperature variation is perceived. The temperature variation exhibit centro-symmetry along the X-Y plane at Z=0.5 as also seen from the temperature contours along the X-Y plane at Z=0.1, 0.3, 0.6 and 0.9 in Figs. 6.5 (a) and (c). The presence of large density variations arising due to significant temperature difference attributes to the minor deviations from exact symmetry, apparent in the present work. The flow and temperature fields in the pure convection case depict the growth of hydrodynamic and thermal boundary layers near the vertical isothermal walls at (X=0 and 1) with thermal stratification along the horizontal plane in the inner core of the cavity. The three-dimensionalities associated with the flow and temperature fields can only be perceived near the end walls at (Z=0 and 1). The three-dimensional nature of the flow fields is significant in comparison to the temperature, and hence it is further investigated from the isosurface of Q as depicted in Figs. 6.3 (d) and 6.4 (d). The isosurface of Q in Figs. 6.3 (d) and 6.4 (d) represent the formation of two primary vortices near isothermal walls at X=0.25 and 0.75. The two main vortices represent strong convection currents which are develop due to the substantial gradients of temperature near the isothermal walls. These vortices are anti-symmetric concerning the line Y=0.5 and Z =0.5 but exhibit symmetry along the mid-plane at Z=0.5.

With the inclusion of surface and gas radiation the symmetric nature of the flow and temperature distribution as observed in the pure convection is deformed. An apparent three-dimensionality in the flow and temperature variation has been perceived from the isosurface of temperature and Q in Figs. 6.3 (b, c, e, f) and 6.4 (b, c, e, f). The three-dimensional nature of temperature distribution is also demonstrated from the contours of temperatures at various $X-Y$ plane along Z= 0.1, 0.3, 0.6 and 0.9 as shown in Figs. 6.5 (b) and (d). The radiative exchange between the surfaces and gas volume increases the mean temperature as indicated by the clustering of the isosurface of temperature near the cold wall. The increase of average cavity temperature thickens the boundary layers at the isothermal walls as compared to a pure convection case without radiation. The combined convective-radiative effects lead to the inward folding of the isosurface of temperature adjacent to the adiabatic

walls. The curved isothermal surface of opposite curvature near the adiabatic top and bottom wall indicates the dominance of convective heating and cooling at the top and bottom walls, respectively.

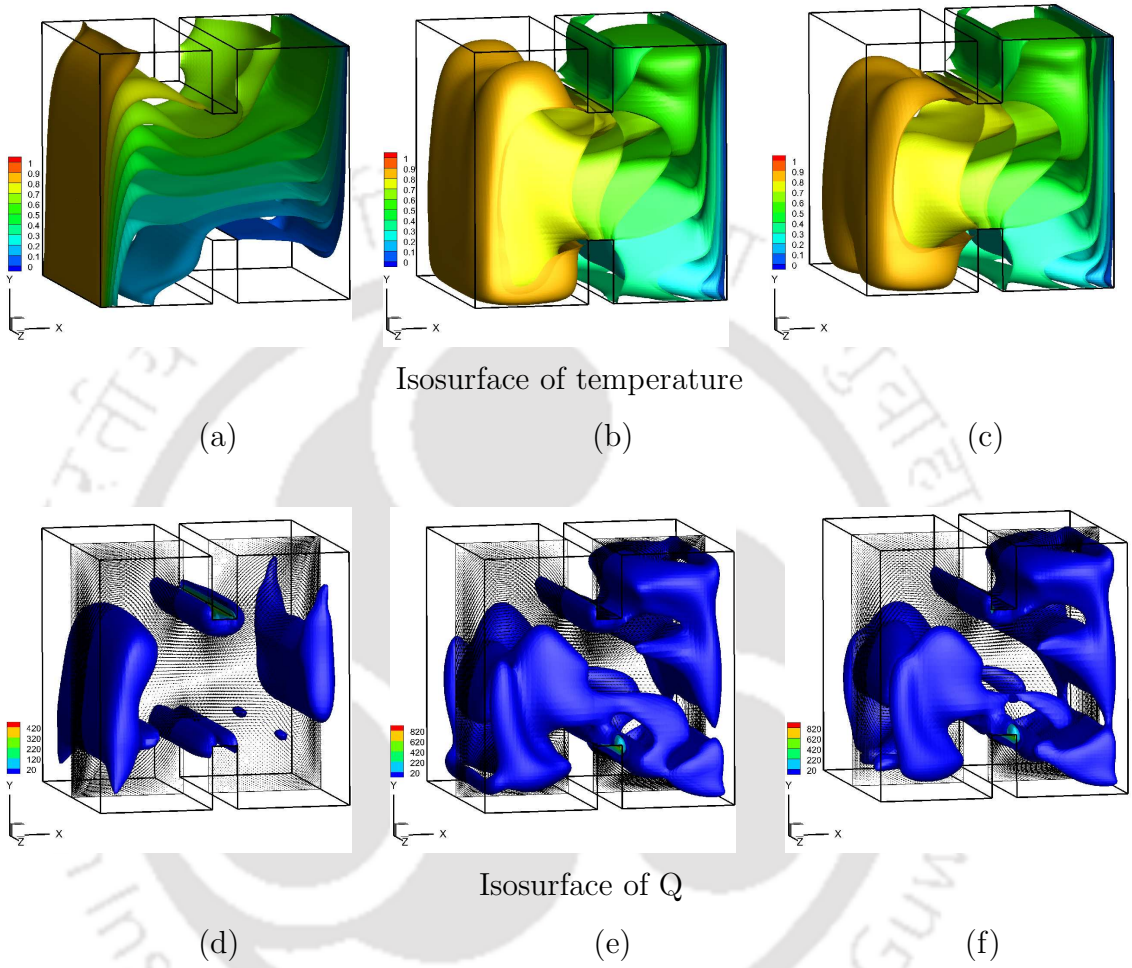

Figure 6.3: Isosurface of temperature and Q for inline configuration of top-bottom partitions: (a, d) pure convection, (b, e) combined convection with surface radiation at optical thickness $\tau = 0.0$, (c, f) combined convection with gas radiation at optical thickness $\tau = 0.20$.

The increased temperature distribution due to radiative exchange also intensifies the flow field evident from the large clustering of the vorticity values near the end walls. The velocity fields generated in case of surface and gas radiation differ im-

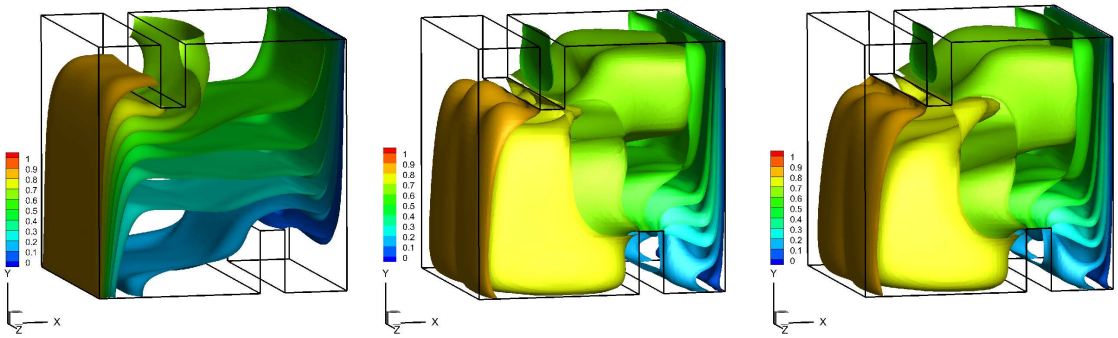

Isosurface of temperature

(a) (b) (c)

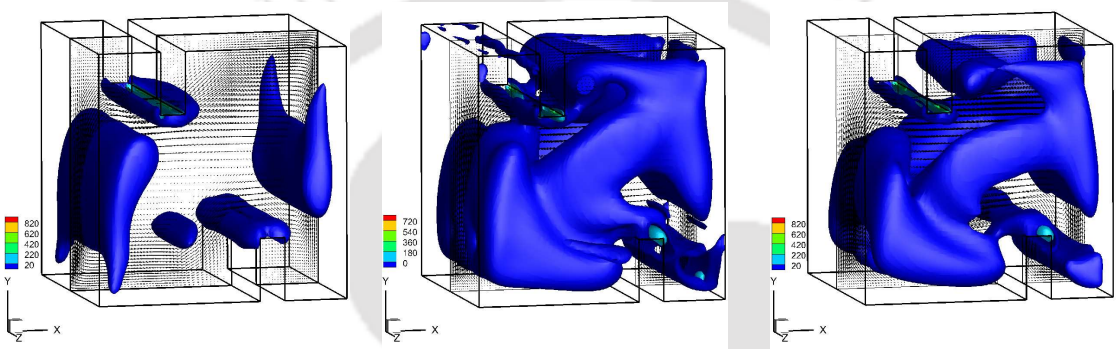

Isosurface of Q

(d) (e) (f)

Figure 6.4: Isosurface of temperature and Q for offset configuration of top-bottom partitions: (a, d) pure convection, (b, e) combined convection with surface radiation at optical thickness $\tau = 0.0$, (c, f) combined convection with gas radiation at optical thickness $\tau = 0.20$.

mensely to a pure convection case. In general, the flow-fields consist of primary vortices, downstream or secondary vortices, and end-wall vortices. In the case of pure convection, the formation of primary vortices has been recognized at X=0.25 and 0.75. For radiation, the primary vortices have dominant strength in addition to the presence of weak secondary vortices near the cold wall. Formation of secondary

vortices along the top-bottom partitions at $X = 0.6$ is observed in Figs. 6.3 (e) and (f) (inline partition case) and X=0.3, X=0.8 as seen in Figs. 6.4 (e) and (f) (offset partition case). The flow physics in the case of combined convection with surface and gas radiation depict multi-layer flow-structures with large vorticity values near the end walls at ($Z = 0$ and 1). The formation of multi-layer flow structure signifies sharp inward bending of the isosurface of temperature near the insulated walls with a thin layer of fluid flowing opposite to the direction of primary flow. It indicates increased three-dimensionality of the flow with a high concentration of the end-wall vortices at Z= 0 and 1, respectively.

The difference in flow and temperature variation between pure convection and convection with gas radiation ($\tau = 0.2$) is explained for inline and offset partitions at various $X - Y$ planes inside the cubical enclosure at Z= 0.1, 0.3, 0.6 and 0.9 in Figs. 6.5 (a - d). The temperature variation for pure convection case represents a quasi-two-dimensional behavior as seen from Fig. 6.5 (a) where the temperature variation at various $X - Y$ planes at Z= 0.1, 0.3, 0.6 and 0.9 does not show any appreciable change. The velocity variation as depicted through streamlines represents the formation of two primary vortices in each half of the cavity. However, a secondary vortex is formed adjacent to the top partition at the center core of the cavity. The strength of the secondary vortex diminishes near the end walls at Z= 0.1 and 0.9 due to end wall effects. The inclusion of gas radiation as shown in Fig. 6.5 (b) elevates the mean temperature distribution with increased three-dimensionality of both temperature and flow as seen in various sections. The presence of gas radiation causes three-dimensional effects not only near the end walls but also in the center core of the cavity. The velocity distribution represents the formation of two supplemental secondary vortices of equal strength in addition to the two primary vortices as also seen for the case of pure convection from Figs. 6.5 (a) and (b).

However, in case of offset partitions, the formation of a single primary vortex is observed at the center core of the cavity with one secondary vortex formed next to the partition protruding from the top wall in case of pure convection as seen from Fig. 6.5 (c). With the inclusion of gas radiation two secondary vortices are formed just adjacent to the top and bottom partition but with different strength as seen from Fig. 6.5 (d). The secondary vortex adjacent to the top partition signifies larger strength in comparison to the one formed next to the bottom partition. The

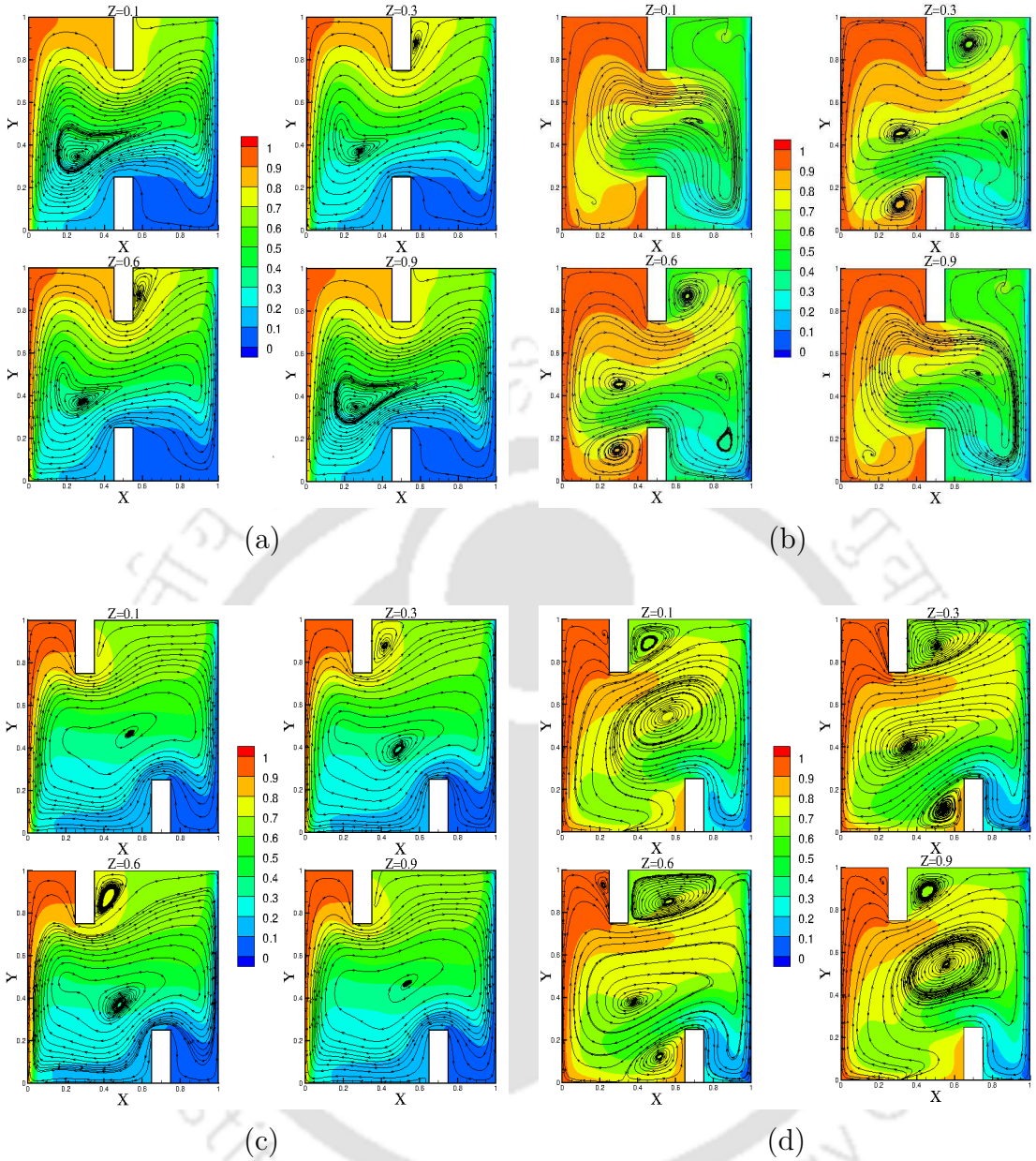

Figure 6.5: Plots of surface contours at various $X-Y$ planes for temperature distribution and streamlines variation at $Z = 0.1, 0.3, 0.6$ and 0.9 respectively in case of partitions protruding from the top and bottom walls: (a) pure convection case for inline partitions, (b) gas radiation case with ($\tau = 0.20$) for inline partitions, (c) pure convection case for offset partitions, (d) gas radiation case with ($\tau = 0.20$) for offset partitions.

implications of the larger secondary vortex in offset partitions can be understood from increased heat transfer (larger Nusselt number distribution as seen from Fig. 6.8) at the base of hot wall and top of the cold wall in comparison to the inline partitions as seen from Fig. 6.7.

The fundamental nature of flow and heat transfer remains similar between inline and offset configuration of partitions protruding from the top-bottom walls. However, noticeable differences can be observed in the overall heat transfer rates as revealed from the local distribution of Nusselt numbers in Figs. 6.7 and 6.8 and from the average Nusselt numbers values shown in Tables 6.1 and 6.2. The offset configuration of partitions in a pure convection case as described in Fig. 6.4 (a) reveals that the hot rising fluid near the isothermal hot wall at $X = 0$ and the cold descending fluid near the cold wall at $X = 1$ are trapped adjacent to the isothermal walls by the partitions. The flow entrapment results in a decrease of temperature gradients near the isothermal hot and cold walls as evident from the temperature variation along the vertical axis at X=0.1 and 0.9 in Figs. 6.6 (a) and (b). The reduced temperature gradients cause a decrease in the convection Nusselt number of offset configuration as shown in Tables 6.1 and 6.2.

Reduction in convection Nusselt number can also be observed for offset configuration in case of surface radiation due to the effect of flow entrapment with the role of radiation to equalize the temperature. However, from the temperature variation in Figs. 6.6 (a) and (b) for surface radiation case it is evident that the role of convection in cooling the bottom wall and heating the top wall is dominant in case of inline partitions than offset separation. It indicates stronger convection currents for inline configuration with the cores of the primary vortices dominant near the bottom and top wall at $X = 0.25$ and $X = 0.75$. The presence of gas radiation is expected to cause a decrement in convection Nusselt number as gas radiation tends to homogenize the temperature and hence the strength of buoyancy-driven convection currents are reduced.

Comparison of average values of the Nusselt number from Tables 6.1 and 6.2 between inline and offset configuration of partitions depicts larger values of radiation Nusselt numbers for offset configuration. It signifies that inline configuration of partitions offers extensive blockage to radiation in comparison to offset. An inline design of

partitioning walls separate regions of hot and cold fluid in two half of the cavity. The temperature variation along the X-axis at (Y= 0.5, Z = 0.5) as shown in Fig. 6.6 (c) signifies the separation of hot and cold zones due to an inline configuration of partitions. Larger mean temperatures in the first half of the cavity till X=0.5 and smaller mean temperatures in the second half are indications of extensive obstruction of flow and heat transfer by the inline configuration. The temperature variation along the Z-axis at (X= 0.5, Y=0.5) in Fig. 6.6 (c) shows thicker thermal boundary layer near the end wall (Z = 0, 1) for inline partitions. It indicates that three-dimensional nature of heat transfer is more prominent in the case of inline partitions. Figures 6.7 and 6.8 represent the local convection and radiation Nusselt number contours at the isothermal walls in inline and offset configuration of top-bottom partitions for gas radiation. Contours of convection Nusselt number as shown in Figs. 6.7 (a) and 6.8 (a) depict an increasing value adjacent to the vertical Y-axis at the cold wall. The convection Nusselt number distribution at the hot walls as shown in Figs. 6.7 (c) and 6.8 (c) signifies higher values at Y=0 with a progressive decrement along the Y-axis. The local variation of convective heat transfer represents significant heat transfer at the top and base of cold and hot walls, respectively. In general, the values of the convection Nusselt number at the cold wall are larger in comparison to the convection Nusselt number values at the hot wall. The large values of convection Nusselt number at the cold wall are an indication of the extent of radiation to equate the temperature. In contrast to the convection Nusselt number, radiation Nusselt numbers values are significant at the hot wall with maximum values obtained at the center of the wall as shown in Figs. 6.7 (d) and 6.8 (d).

Convection Nusselt number distribution shows symmetry about the Y-axis whereas the radiation Nusselt number distribution is asymmetric. The asymmetric nature of radiation Nusselt number distribution differs for offset and inline partitions due to variation in radiation blockage by the partitions. In the case of offset partitions clustering of lower values of radiation Nusselt number can be observed at the bottom of the cold wall as shown in Figs. 6.7 (b) and 6.8 (b) and the top of the hot wall as seen in Figs. 6.7 (d) and 6.8 (d). It is due to the presence of partitions near the top and bottom of hot and cold wall respectively. However, the radiation Nusselt number variation in case of inline partitions is stretched along the Z-axis with minor clustering along the top and bottom wall as shown in Figs. 6.7 (b) and (d). Higher values of the radiation Nusselt number distribution at offset arrangement of restraining walls is due to small blockage of radiation in comparison to inline parti-

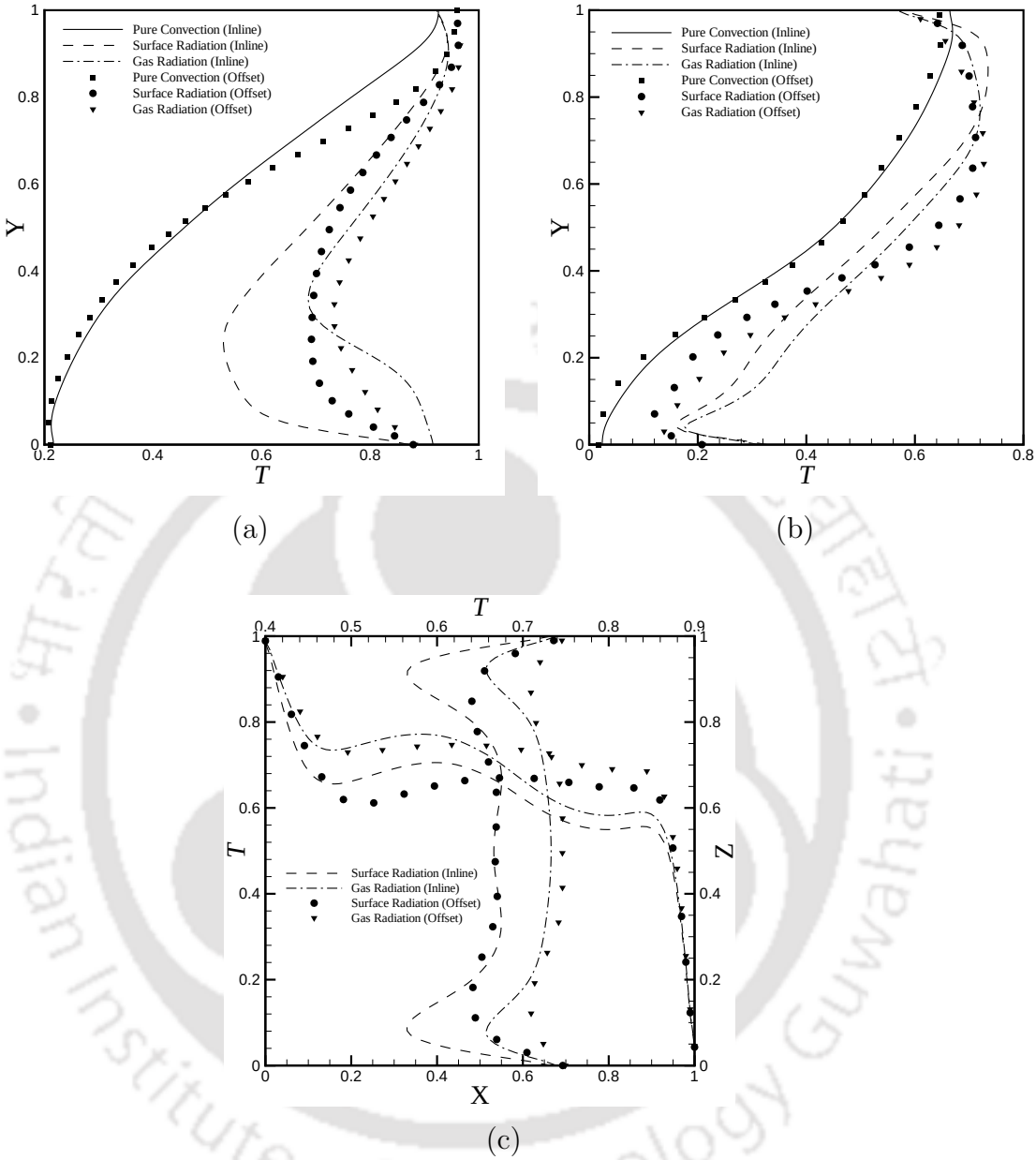

Figure 6.6: Comparison of temperature variation between an inline and offset configuration of top-bottom partitions: (a) temperature variation along the vertical Y-axis at $Z = 0.5$ and $X = 0.1$, (b) temperature variation along the vertical Y-axis at $Z = 0.5$ and $X = 0.9$, (c) temperature variation along the X and Z-axis at the mid-plane $Y = 0.5$, $Z = 0.5$ and $X = 0.5$, $Y = 0.5$.

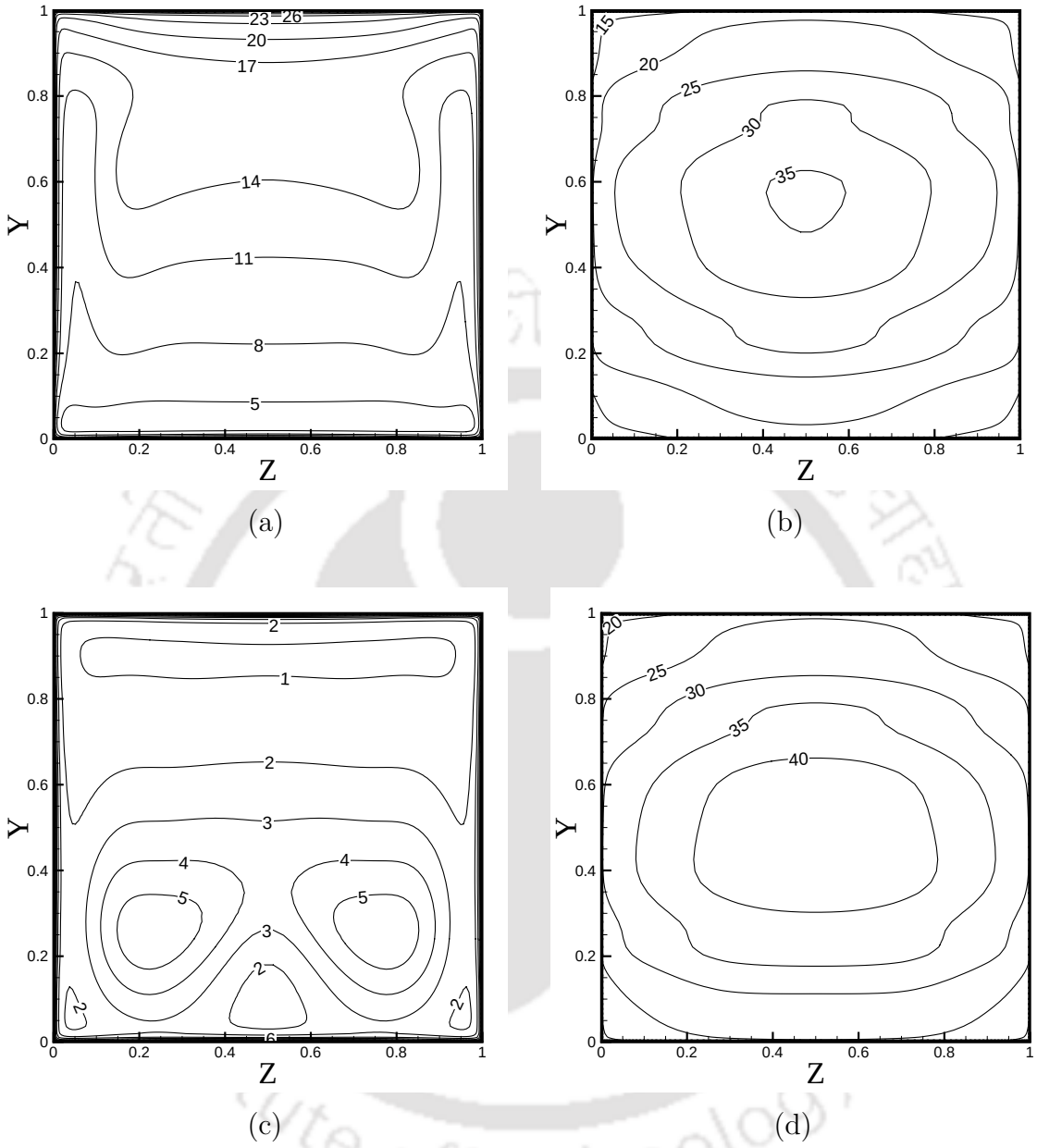

Figure 6.7: Contours of the local Nusselt number variation on the hot and cold walls for inline configuration of top-bottom partitions: (a, c) convective Nusselt number, (b, d) radiative Nusselt number, (a, b) Nusselt number on cold walls, (c, d) Nusselt number on hot walls.

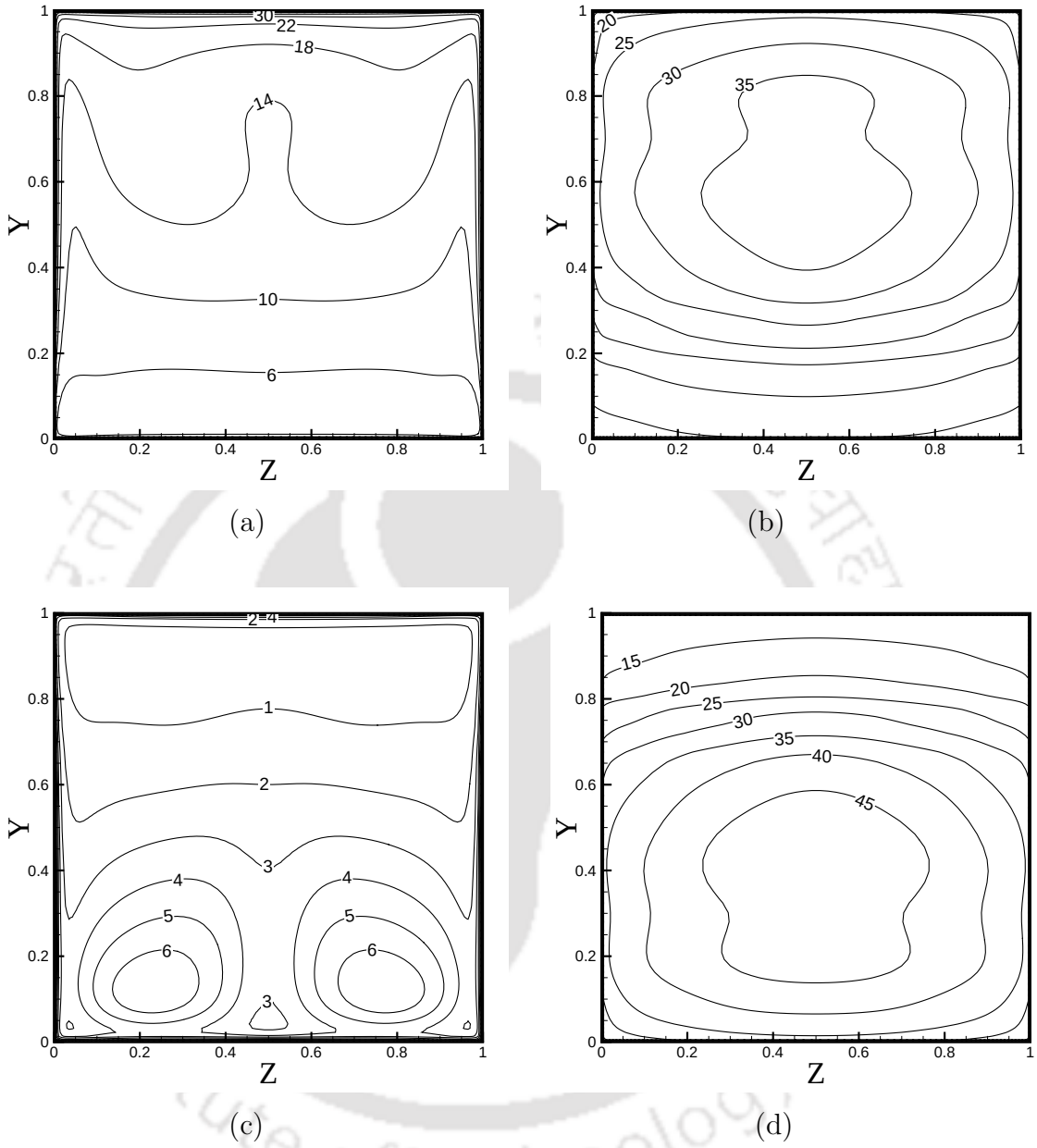

Figure 6.8: Contours of the local Nusselt number variation on the hot and cold walls for offset configuration of top-bottom partitions: (a, c) convective Nusselt number, (b, d) radiative Nusselt number, (a, b) Nusselt number on cold walls, (c, d) Nusselt number on hot walls.

Table 6.1: Average Nusselt number values at the hot and cold walls with an inline configuration of top-bottom partitions.

	HotWall			Cold Wall		
Nusselt number	Nu_c	Nu_r	Nu_t	Nu_c	Nu_r	Nu_t
Pure Convection	8.399	NA	8.399	8.399	NA	8.399
Surface Radiation	3.859	33.275	37.134	11.392	25.735	37.128
Gas Radiation	2.737	32.940	35.678	11.925	23.748	35.674

Table 6.2: Average Nusselt number values at the hot and cold walls with offset configuration of top-bottom partitions.

	HotWall			Cold Wall		
Nusselt number	Nu_c	Nu_r	Nu_t	Nu_c	Nu_r	Nu_t
Pure Convection	8.164	N.A	8.164	8.164	N.A	8.164
Surface Radiation	3.687	34.971	38.658	11.687	26.968	38.655
Gas Radiation	2.872	34.704	37.576	12.374	25.197	37.572

tions. The Nusselt number distribution signifies that radiation is more susceptible to the presence of separating walls than convective heat transfer.

6.3.2 Influence of inline and offset configuration of front-back partitions within the cubical enclosure

In this section discussion on buoyancy-driven flow in the presence of radiative heat transfer inside a cubical enclosure with partitions protruding from front and back walls is presented. Studies have been performed with two configurations of partitions along the X-axis namely inline configuration at $X = 0.5$, 0.5 and offset configuration at $X = 0.25$ and 0.75. From the isosurface of temperature and Q in Figs. 6.9 (a), 6.10 (a) and 6.10 (d) it is seen that for pure convection the two-dimensional nature of the temperature distribution is prominent with high thermal stratification along

the horizontal plane not only in the central core but also along the top and bottom walls. In the case of inline partitions, the temperature and velocity distributions depict symmetric behavior along the X-Y plane at ($Z = 0.5$) as seen in Figs. 6.9 (a) and (d). However, for offset arrangement of partitions, the symmetric nature of flow and temperature distribution is distorted as shown in Figs. 6.10 (a) and (d) due to the asymmetric arrangement of the separating walls. The three-dimensionality of the flow becomes prominent near the end walls (Z= 0, 1) as partitions along the front and back walls contribute to the three-dimensionality of the flow. The fundamental nature of flow in pure convection case as shown in Figs. 6.9 (d) and 6.10 (d) depicts formation of two primary vortices near hot and cold wall at X=0.25, 0.75 with end wall vortices adjacent to the partitions at $Z = 0, 1$. The strength of end wall vortices is prevalent in the case of offset partitions which demonstrate increased three-dimensionality in the overall flow and heat transfer.

The presence of surface/gas radiation adds to the three-dimensionality of the flow and heat transfer as also observed previously in the case of partitions from the top-bottom walls. However, the isosurface of temperature and Q in Figs. 6.9 (b, c, e, f) and 6.10 (b, c, e, f) depict remarkable differences in the overall flow and heat transfer. The change in sign of the curvature of the isosurface of temperature near the top and bottom walls reveals the dominating influence of convective cooling and heating at the bottom and top wall, respectively. The increased concentration of curved isosurface of temperatures at the bottom wall indicates an elevated convective cooling. The enhanced cooling of the base wall due to convection has been substantiated by the large concentration of isosurface of Q near the bottom wall for both inline and offset partitions. Sharp bending of the isosurface of temperature near the adiabatic front and back wall is more prominent in the present case as compared to the case with partitions along the top and bottom wall. Larger curvatures of the iso-temperature surface near the front and back wall are apparent from the end wall vortices observed near the front and back wall in Figs. 6.9 (b, c, e, f) and 6.10 (b, c, e, f).

The influence of partitions along the front-back walls on overall heat transfer is studied by investigating the average Nusselt number on the hot and cold wall as shown in Tables 6.3, 6.4, and also through the local Nusselt number distribution from Fig. 6.13. From the mean values of the Nusselt number in Tables 6.3, 6.4, it

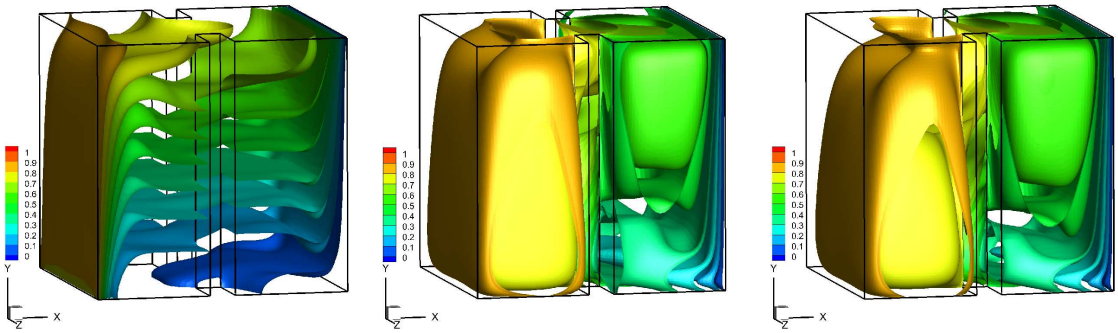

Isosurface of temperature

(a) (b) (c)

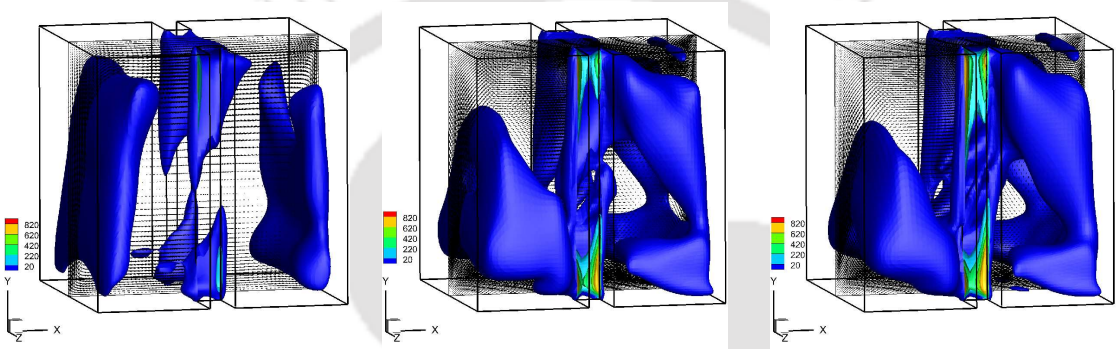

Isosurface of Q

(d) (e) (f)

Figure 6.9: Isosurface of temperature and Q for inline configuration of front-back partitions: (a, d) pure convection, (b, e) combined convection with surface radiation at optical thickness $\tau = 0.0$, (c, f) combined convection with gas radiation at optical thickness $\tau = 0.20$.

is seen that the presence of inline and offset configuration of partitions has minimal influence on the convection Nusselt number in all the three cases (pure convection, surface, gas radiation). The independence of convection Nusselt number on inline and offset arrangement of partitions is established from the temperature variation along the Y-axis near the hot and cold wall at X= 0.1, 0.9 at mid-plane (Y=0.5, Z=0.5) as shown in Figs. 6.12 (a-c). From Figs. 6.12 (a) and (b) it is evident that the temperature variation between the inline and offset partitions is minimal

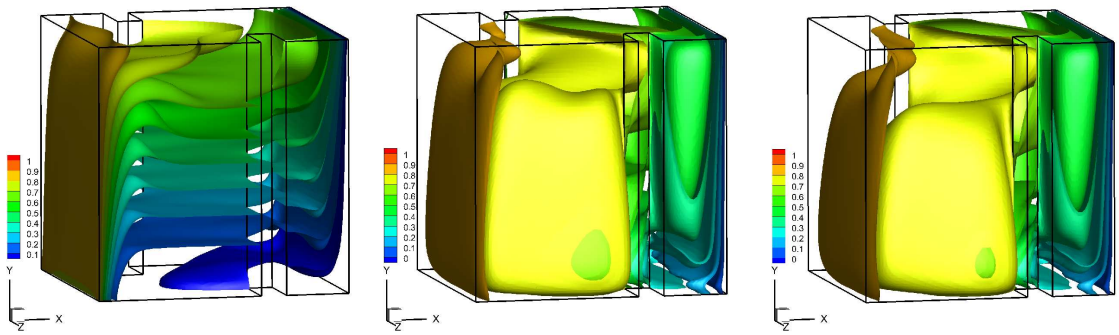

Isosurface of temperature

(a) (b) (c)

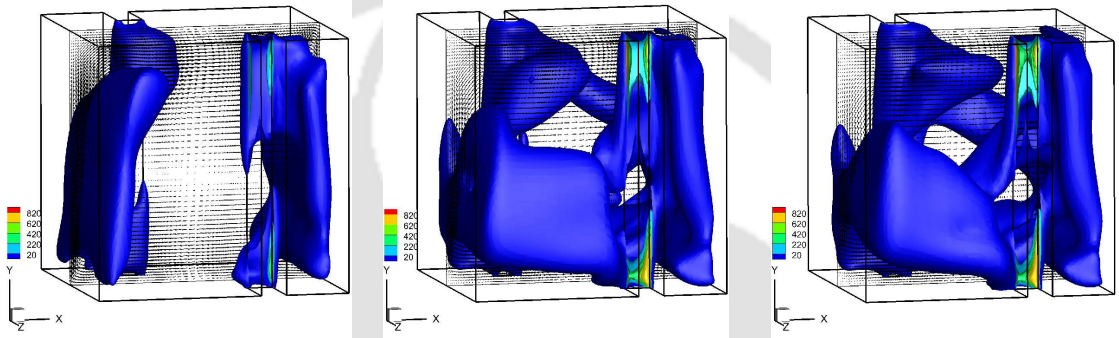

Isosurface of Q

(d) (e) (f)

Figure 6.10: Isosurface of temperature and Q for offset configuration of front-back partitions: (a, d) pure convection, (b, e) combined convection with surface radiation at optical thickness $\tau = 0.0$, (c, f) combined convection with gas radiation at optical thickness $\tau = 0.20$.

near the hot wall. However, the temperature field near the cold wall is marginally higher for offset configuration. Higher temperature near the cold wall for offset configuration is also seen from the temperature variation along the horizontal X-axis at mid-plane (Y=0.5, Z=0.5) in Fig. 6.12(c). The deviations in temperature near the cold walls between offset and inline configuration are imperceptible to influence the average convection Nusselt number. The average radiation Nusselt numbers are higher for offset configuration of restraining walls. The inline partitions offer larger

interference to radiation hence isolate the hot and cold fluid in the two halves of the cavity. These observations are consistent with the radiation Nusselt number variations for partitions along the top and bottom walls.

In general higher values of convective and radiation, Nusselt number are obtained in the present case with front-back partitions in comparison to the top-bottom partitions. The inline configuration of front-back and top-bottom partitions obstructs radiation equally, but the enhanced radiation Nusselt number for the present case is a consequence of increased heat transfer by convection. The temperature variation in Fig. 6.12 (c) shows the symmetric distribution of temperature along the Z-axis for inline partitions whereas the temperature distributions are asymmetric for offset arrangement of obstructing walls. The temperature distributions exhibit enhanced gradients along the Z-axis for offset configuration, signifying increased three-dimensional heat transfer for the offset configuration of separating walls.

The difference in flow and temperature variation between pure convection and gas radiation ($\tau = 0.2$) is briefly explained for inline and offset partitions at various $X - Y$ planes inside the cubical enclosure at Z= 0.1, 0.3, 0.6 and 0.9 in Figs. 6.11 (a-d). The flow and temperature variation inside the enclosure with inline partitions represents centro-symmetry about $X - Y$ plane at Z=0.5 as seen from Figs. 6.11 (a) and (b). The pure natural convection heat transfer as seen from Fig. 6.11 (a) depicts quasi-two-dimensional behavior along the center core of the cavity. However, larger deviations from the exact centro-symmetry is observed near the end walls due to wall and partition effect. The presence of radiation increases the mean temperature inside the enclosure and also the flow along the Z direction. The streamlines pattern in the various $X - Y$ planes as shown in Fig. 6.11 (b) does not form a closed loop rather it signifies spiraling flow along the Z-direction towards the side walls. The symmetric nature of flow and temperature variation is completely lost due to the asymmetric distribution of partitions in case of offset partitions as seen from Figs. 6.11 (c) and (d). As observed previously for inline partitions, the offset partitions also signify inner spiraling flow along the Z-direction. The increased three-dimensional behavior of flow inside the cubical enclosure with partitions along the front and back walls is responsible for increased convective heat transfer as seen from Figs. 6.13 and 6.14 in comparison to partitions along the top and bottom walls as shown in Figs. 6.7 and 6.8.

Figures 6.13 and 6.14 represent the local variation of convective and radiative Nusselt number at the isothermal hot and cold walls of the cubical enclosure for inline and offset arrangement of partitions from the front and back walls. The contours of convective and radiative Nusselt number for inline partitions are symmetric about the vertical centerline as seen from Fig. 6.13 with maximum values of convective Nusselt number distribution at the top (ceiling) of cold wall and bottom (floor) of hot wall. Similar observations can also be made for the variation of the convective and radiative Nusselt number in case of offset partitions as shown in Fig. 6.14 with asymmetric distribution about the vertical centerline. In general, the higher value of convective Nusselt number is obtained at the cold wall in comparison to the hot wall for both inline and offset configuration of partitions due to the influence of radiation to equalize the temperature. In contrast to the convective Nusselt number, the radiative Nusselt number distribution depicts higher magnitudes at the hot wall in comparison to the cold wall. For offset partitions, the radiative Nusselt number distribution depicts clustering near the side walls due to the blockage of radiation by the partitioning walls as shown in Figs. 6.14 (b) and (d).

The local variation of convective and radiation Nusselt number at the isothermal walls for gas radiation in Figs. 6.13 and 6.14 represents a symmetric Nusselt number distribution along the Y-axis in the case of inline partitions as shown in Fig. 6.13. However, the symmetric arrangement of convective and radiation Nusselt number variation has been entirely deformed in the event of offset configuration as seen from Fig. 6.14. The local variation of convection Nusselt number for inline partitions as referred in Figs. 6.13 (a) and 6.14 (c) shows enhanced convective heat transfer near the top and bottom of cold and hot walls, respectively. The radiation Nusselt number variation for inline configuration as shown in Figs. 6.13 (b) and 6.14 (d) exhibits larger radiative heat exchange along the mid-plane with clustering of smaller values of the radiation Nusselt number near the front and back walls at Z= 0, 1.

In the case of offset partitions, the high convective heat transfer near the top of cold wall and bottom of the hot wall is demonstrated in Figs. 6.14 (a) and (c). The contours of convection Nusselt number exhibit asymmetry with reduced convective heat transfer adjacent to the X-Y plane at Z=1 for cold wall and Z=0 for the hot wall. The reduction in convective heat transfer is due to partial entrapment of hot and

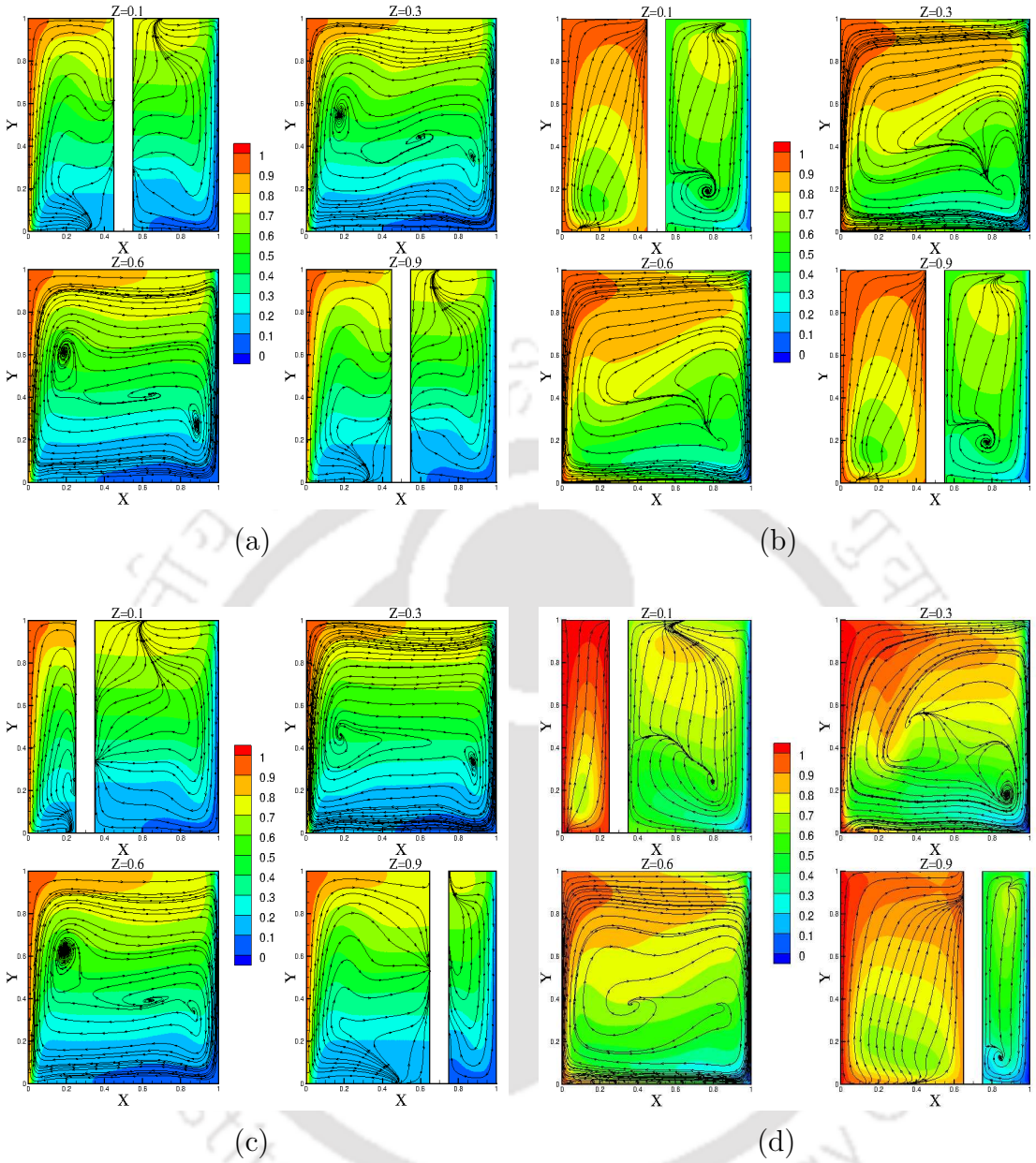

Figure 6.11: Plots of surface contours at various $X-Y$ planes for temperature distribution and streamlines variation at $Z = 0.1, 0.3, 0.6$ and 0.9 respectively in case of partitions protruding from the front and back walls: (a) pure convection case for inline partitions, (b) gas radiation case with ($\tau = 0.20$) for inline partitions, (c) pure convection case for offset partitions, (d) gas radiation case with ($\tau = 0.20$) for offset partitions.

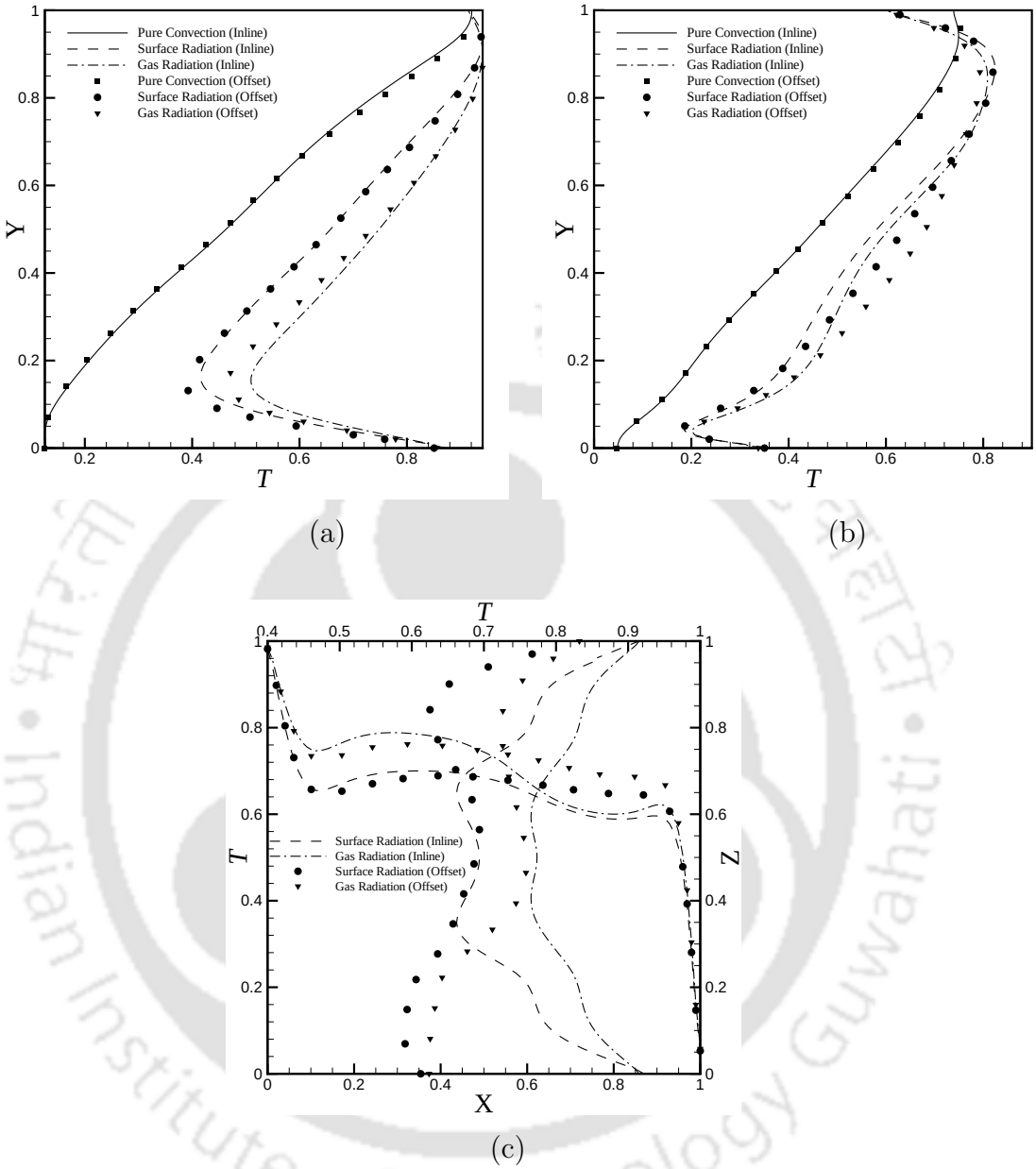

Figure 6.12: Comparison of temperature variation between an inline and offset configuration of front-back partitions : (a) temperature variation along the vertical Y-axis at $Z = 0.5$ and $X = 0.1$, (b) temperature variation along the vertical Y-axis at $Z = 0.5$ and $X = 0.9$, (c) temperature variation along the X- and Z- axis at the mid-plane $Y = 0.5$, $Z = 0.5$ and $X = 0.4$, $Y = 0.5$.

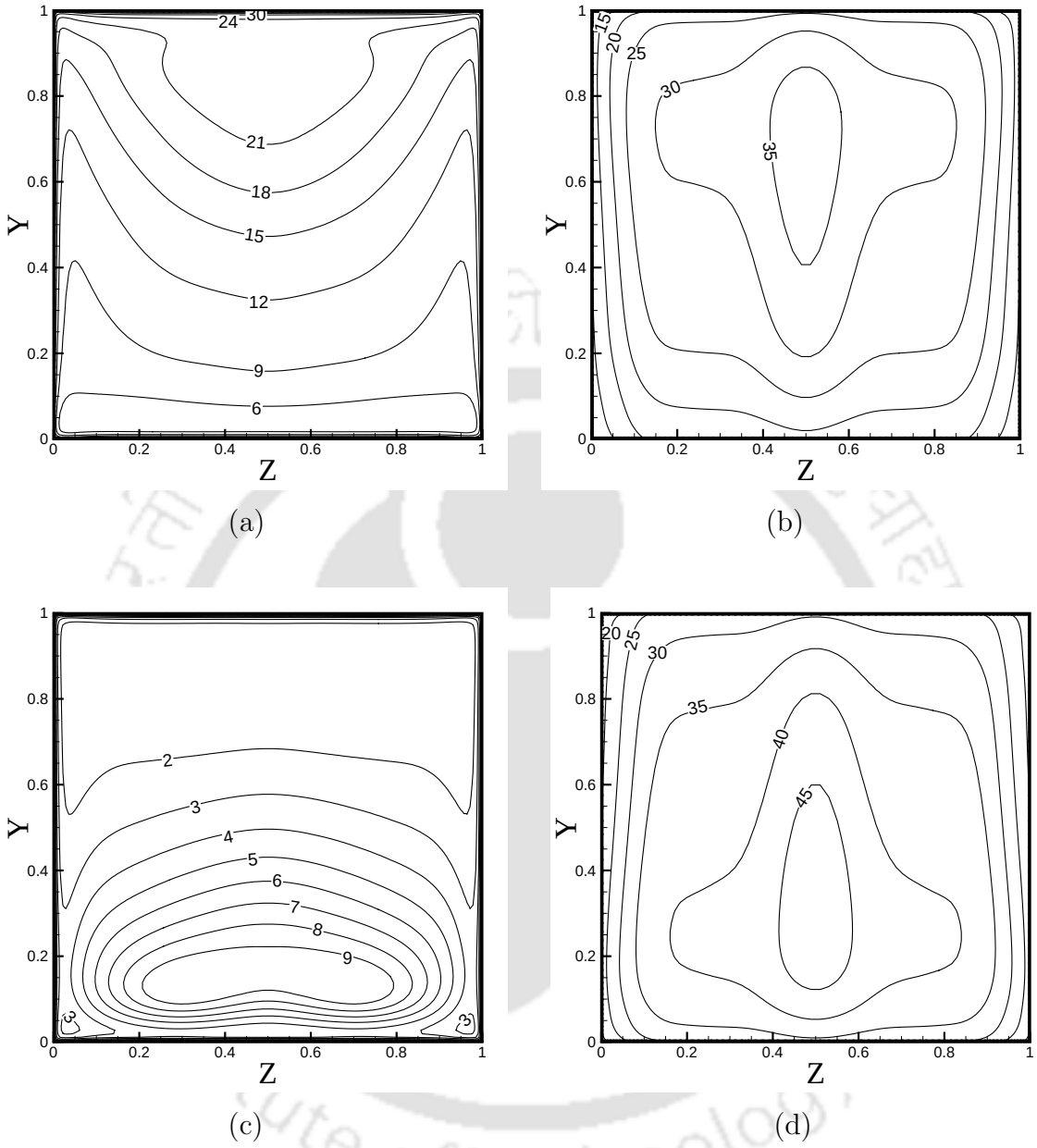

Figure 6.13: Contours of local Nusselt number on the hot and cold walls for inline configuration of front-back partitions: (a, c) convective Nusselt number, (b, d) radiative Nusselt number, (a, b) Nusselt number on cold walls, (c, d) Nusselt number on hot walls.

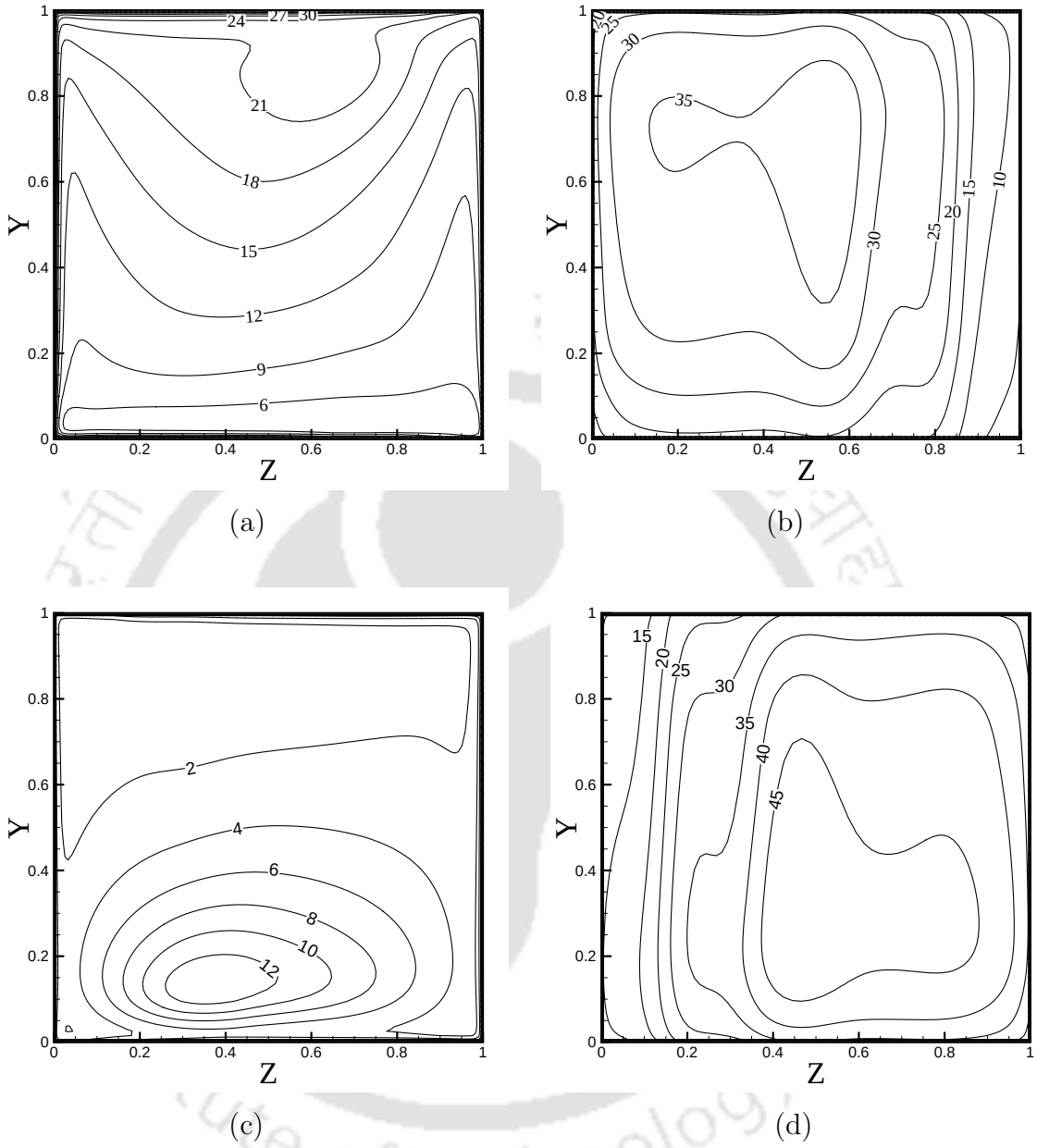

Figure 6.14: Contours of local Nusselt number on the hot and cold walls for offset configuration of front-back partitions: (a, c) convective Nusselt number, (b, d) radiative Nusselt number, (a, b) Nusselt number on cold walls, (c, d) Nusselt number on hot walls.

Table 6.3: Average Nusselt number values at the hot and cold walls with an inline configuration of front-back partitions.

	Hot Wall			Cold Wall		
Nusselt number	Nu_c	Nu_r	Nu_t	Nu_c	Nu_r	Nu_t
Pure Convection	9.392	NA	9.392	9.392	NA	9.392
Surface Radiation	4.867	35.524	40.392	12.877	27.508	40.385
Gas Radiation	3.944	35.897	39.841	13.825	26.008	39.833

Table 6.4: Average Nusselt number values at the hot and cold walls with offset configuration of front-back partitions.

	Hot Wall			Cold Wall		
Nusselt number	Nu_c	Nu_r	Nu_t	Nu_c	Nu_r	Nu_t
Pure Convection	9.363	NA	9.363	9.363	NA	9.363
Surface Radiation	4.972	36.378	41.350	13.062	28.265	41.328
Gas Radiation	4.124	36.168	40.293	13.823	26.463	40.286

cold fluids at the partitions. Similarly, the radiation Nusselt number distribution in Figs. 6.14 (b) and (d) demonstrates clustering of lower values of the radiation Nusselt number near Z=1 for cold wall and Z=0 for the hot wall. The decrease in radiation Nusselt number is a consequence of the presence of partitions acting as partial radiation barriers.

6.4 Entropy Generation

Analysis of thermodynamic irreversibilities associated with loss of heat in a thermodynamic system instigates need for entropy generation. In a buoyancy-induced natural convection coupled with thermal radiation, the local volumetric entropy generation rates are associated with viscous dissipation, conduction, convection,

and radiation. The velocity and temperature gradients are accountable for the entropy production by conduction, convection, and viscous dissipation. On the other hand, the long-range nature of radiation compels the radiative entropy generation rates to be independent of the local temperature gradients. The radiation entropy production rates are dependent on the gross temperature field of the entire system. The entropy production rate for buoyancy-induced convection under the influence of radiative heat transfer is shown in Eq. (6.3), following the work of Slimi [131]

$$S_G = \frac{k}{T_0^2}\left[\left(\frac{\partial T}{\partial x_j}\right)^2\right] + \frac{1}{T_0}\left[\tau_{ij}\frac{\partial u_i}{\partial x_j}\right] + \frac{\kappa}{T_0}\left[4\pi I_b - \int_{4\pi} I d\Omega\right] \tag{6.3}$$

where

$$\tau_{ij} = \mu\left[\frac{\partial u_i}{\partial x_j} + \frac{\partial u_j}{\partial x_i} - \frac{2}{3}\frac{\partial u_i}{\partial x_i}\right] \tag{6.4}$$

The terms on the right hand side of Eq. (6.3) represent the rate of entropy production by convection, fluid friction, and radiative heat transfer. The dimensionless form of Eq. (6.3) is obtained by rescaling using Eq. (2.66) as done previously for obtaining the non-dimensional form of governing equations. The dimensionless form of entropy generation is described in Eq. (6.5) by dropping the superscripts.

$$S_G = \left[\left(\frac{\partial T}{\partial x_j}\right)^2\right] + \phi_0\left[\left(\frac{\partial u_i}{\partial x_j} + \frac{\partial u_j}{\partial x_i} - \frac{2}{3}\frac{\partial u_i}{\partial x_i}\right)\frac{\partial u_i}{\partial x_j}\right] + \phi_1\left[4\pi I_b - \int_{4\pi} I d\Omega\right] \tag{6.5}$$

In the above equation for entropy generation, ϕ represents the irreversibility ratio defined as

$$\phi_0 = \frac{\mu\, T_0\, u_0^2}{k\,(\Delta T)^2},\ \phi_1 = \frac{\tau\, I_0\, H\, T_0}{k\,(\Delta T)^2} \tag{6.6}$$

The values of $\phi_0 \approx 10^{-6}, \phi_1 \approx 2.2$ are obtained based on order of magnitude analysis at initial condition of $T_0 = 600$ K, $\mu = 5.34 \times 10^{-5}, k = 0.07$ with $u_0^2 \approx 1.08$ and $\tau = 0.20$ are used for a $\Delta T = 720$ K. Figure 6.15 represents the isosurface of entropy generation for partitions protruding from the top-bottom walls. Figures 6.15 (a) and (d) correspond to the local heat transfer irreversibility (HTI), Figs. 6.15 (b) and (e) show the fluid friction irreversibility (FFI) and Figs. 6.15 (c) and (f) express the radiative heat transfer irreversibility (RTI). The local variation of entropy generation in Fig. 6.15 reveals that the heat transfer (conduction, radiation)

is the dominant mechanism of irreversibilities. On the other hand, fluid friction irreversibility is insignificant in comparison to heat transfer as the strength of the convection currents are rather weak in a typical natural convection driven flow. The dominance of entropy generation by heat transfer is also recognized from the average and maximum values of entropy production as seen from Tables (6.5, 6.6). From the heat transfer irreversibilities in Figs. 6.15 (a) and (d) it is observed that the maximum entropy production by heat transfer is obtained near the base and head of hot and cold isothermal walls, respectively. On analyzing the average entropy production between the inline and offset configurations from Tables 6.5, 6.6 it is observed that the mean value of entropy generation by inline configuration exceeds that of an offset configuration of partition. The maximum value of heat transfer irreversibilities is higher for offset configuration of top-bottom and front-back partitions. The offset arrangement of separating walls offers lesser obstruction to flow and radiation. The enhanced heat transfer due to secondary obstruction increases the temperature gradients near the isothermal walls. Higher temperature gradients are accountable for preeminent values of irreversibility by heat transfer. The significance of entropy production by fluid friction is realized near the isothermal walls at X=0, 1 and adiabatic front and back walls at Z= 0, 1. However, the contribution of viscous dissipation in the total entropy generation is almost negligible. The isosurface of entropy generation by radiation reveals the appearance of maximum entropy generation near the isothermal hot wall at X=0. Additionally, radiative entropy production also contributes along the top wall, posterior to the partition.

Figure 6.16 depicts the entropy generation for partitions along the front and back walls. The primary distribution of entropy production by convection, fluid friction and radiation remain same as observed previously in the case of partitions along the top and bottom walls. The maximum value of heat transfer irreversibilities is obtained near the cold isothermal wall for both inline and offset configuration. It is important to notice that these values are marginally higher than those obtained for partitions along the top and bottom walls. This study demonstrates that inline configuration depicts higher values of entropy generation as compared to offset configuration for both top-bottom and front-back partitions. Maximum entropy production is obtained for inline configuration of top-bottom partitions.

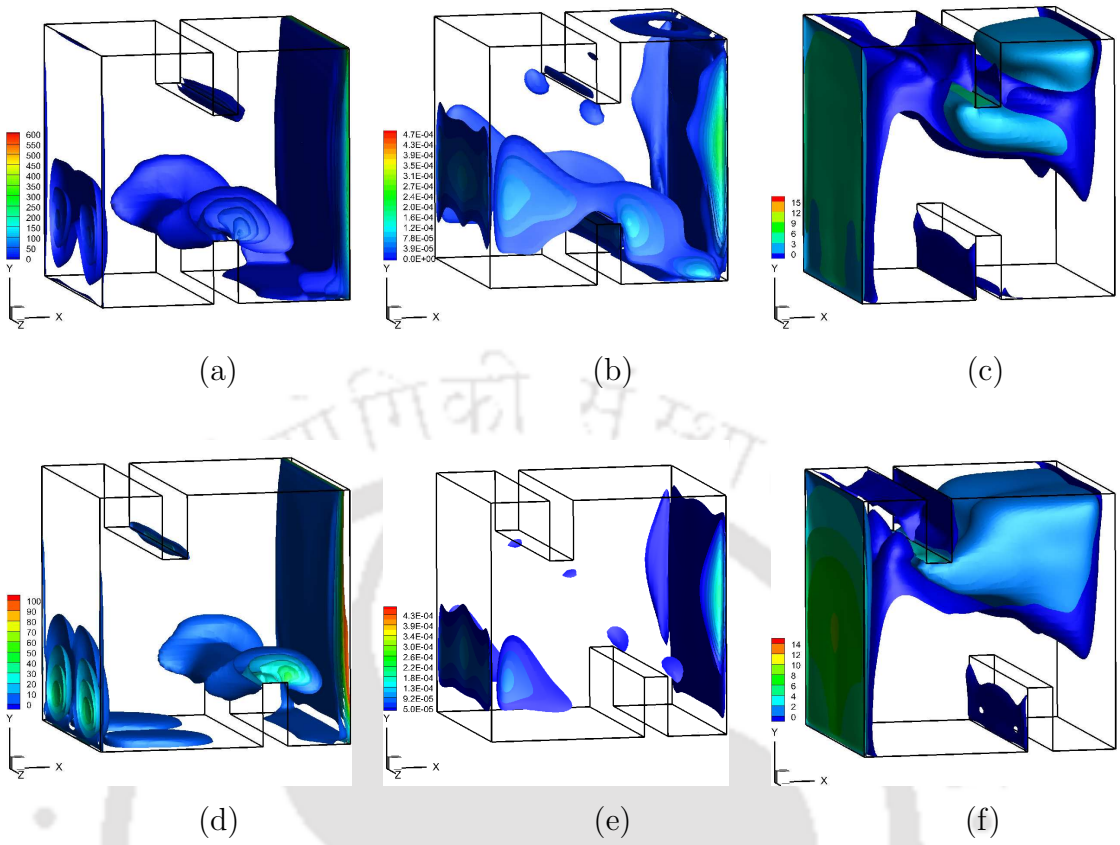

Figure 6.15: Isosurface of local entropy generation in an inline and offset configuration of top-bottom partitions: (a, d) entropy generation due to heat transfer, (b, e) entropy generation due to fluid friction, (c, f) entropy generation due to radiative heat transfer at an optical thickness of $\tau = 0.20$.

Table 6.5: Maximum and average values of entropy generation for inline and offset configuration of top-bottom partitions.

	Average values			Maximum values		
Entropy generation	HTI	FFI	RTI	HTI	FFI	RTI
Inline Configuration	11.91	8.5×10^{-6}	6.15	590	0.0004	13.8
Offset Configuration	7.16	6.0×10^{-6}	3.16	680	0.0004	11.80

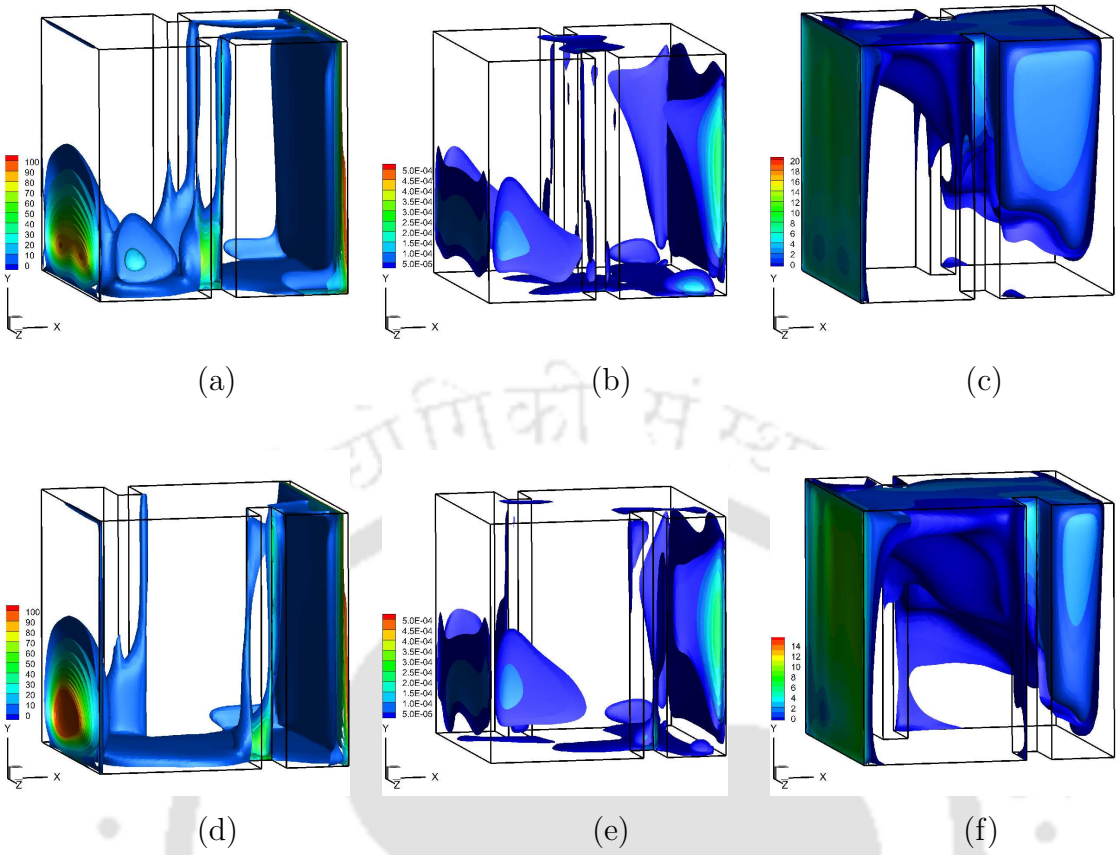

Figure 6.16: Isosurface of local entropy generation in an inline and offset configuration of front-back partitions: (a, d) entropy generation due to heat transfer, (b, e) entropy generation due to fluid friction, (c, f) entropy generation due to radiative heat transfer at an optical thickness of $\tau = 0.20$.

Table 6.6: Maximum and average values of entropy generation for inline and offset configuration of front-back partitions.

	Average values			Maximum values		
Entropy generation	HTI	FFI	RTI	HTI	FFI	RTI
Inline Configuration	8.92	8.5×10^{-6}	3.41	606	0.0005	17.34
Offset Configuration	8.90	8.1×10^{-6}	3.22	695	0.0005	15.93

6.5 The Importance of Three-Dimensional Non-Boussinesq Analysis for Convective Radiative Heat Transfer

In this section, numerical studies are performed to highlight the importance of three-dimensional simulations for combined convective-radiative flow and heat transfer problems. The study is realized by comparing the non-Boussinesq effects for large temperature difference buoyancy driven flow and heat transfer in two-dimensional and three-dimensional enclosure coupled with thermal radiation (surface and gas). The geometry of the problem as described in Fig. 6.17 (a, b) represents a three-dimensional and two-dimensional differentially heated square enclosure of side H respectively. The problem is solved for the non-dimensional parameters such as $Ra = 10^6$, $Pr = 0.71$, $Ga = 1.2$ and $Pl = 0.01$ for scenarios including pure convection, convection with surface and gas radiation of optical thickness $\tau = 0.2$ and 5, respectively. The problem is solved by employing an incompressible model based on Boussinesq approximation with constant thermo-physical properties whereas the quasi-incompressible model used herein considers the density variation based on ideal gas law. Furthermore, the thermo-physical properties are assumed temperature dependent and computed using Sutherland law,

$$\mu = \mu_{ref} \left(\frac{T}{T_{ref}} \right)^{1.5} \left(\frac{T_{ref} + T_s}{T + T_s} \right) \tag{6.7}$$

$$k = \frac{\mu}{c_p Pr} \tag{6.8}$$

where $T_{ref} = 273$ K, $T_s = 110.5$ K and $\mu_{ref} = 1.6 \times 10^{-5}$ $\frac{\text{kg}}{\text{m·s}}$.
The motivation behind the study is to compare the differences in the results for incompressible and quasi-incompressible models between a three-dimensional and two-dimensional convection influenced by thermal radiation. Figures 6.18 (a-d) represent the iso-surface of temperature for pure convection, convection with surface and gas radiation of optical thickness $\tau = 0.2$ and 5, respectively. The fundamental flow and temperature variations inside the cavity are driven by buoyancy due to the interaction of the fluid with hot and cold walls.

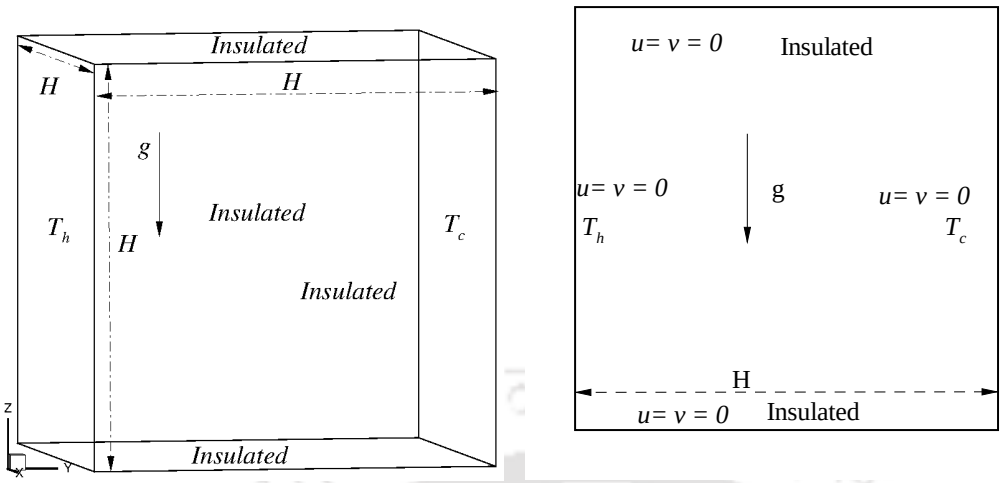

(a) (b)

Figure 6.17: Schematic of the computational domain. (a) Three-dimensional differentially heated cavity. (b) Two-dimensional differentially heated cavity.

The temperature variation for pure convection case as seen from Fig. 6.18 (a) depicts two-dimensional nature with the growth of boundary layers both hydrodynamic and thermal along the vertical isothermal walls with thermal stratification along the horizontal midplane at the center core of the cavity. With the inclusion of thermal radiation, the two-dimensional nature of flow and heat transfer is completely distorted and strong three-dimensionality can easily be perceived from the iso-surface of temperature as seen from Fig. 6.18 (b-d). The inclusion of radiation leads to the increased mean temperature inside the enclosure as evident from the clustering of iso-surface of temperature near the cold vertical wall. The increased temperature levels due to radiation reduce the temperature gradients near the walls and hence decreases the convection currents which leads to the formation of thicker boundary layers as compared to a pure convection case. The influence of gas radiation causes an increased heating of the top wall due to the combined influence of buoyancy and the role of radiation in elevating the mean temperatures. The inclusion of surface and gas radiation causes the entire cavity to be thermally active as regions of cold fluid are limited only to the bottom of the cold wall which influences the flow and heat transfer immensely.

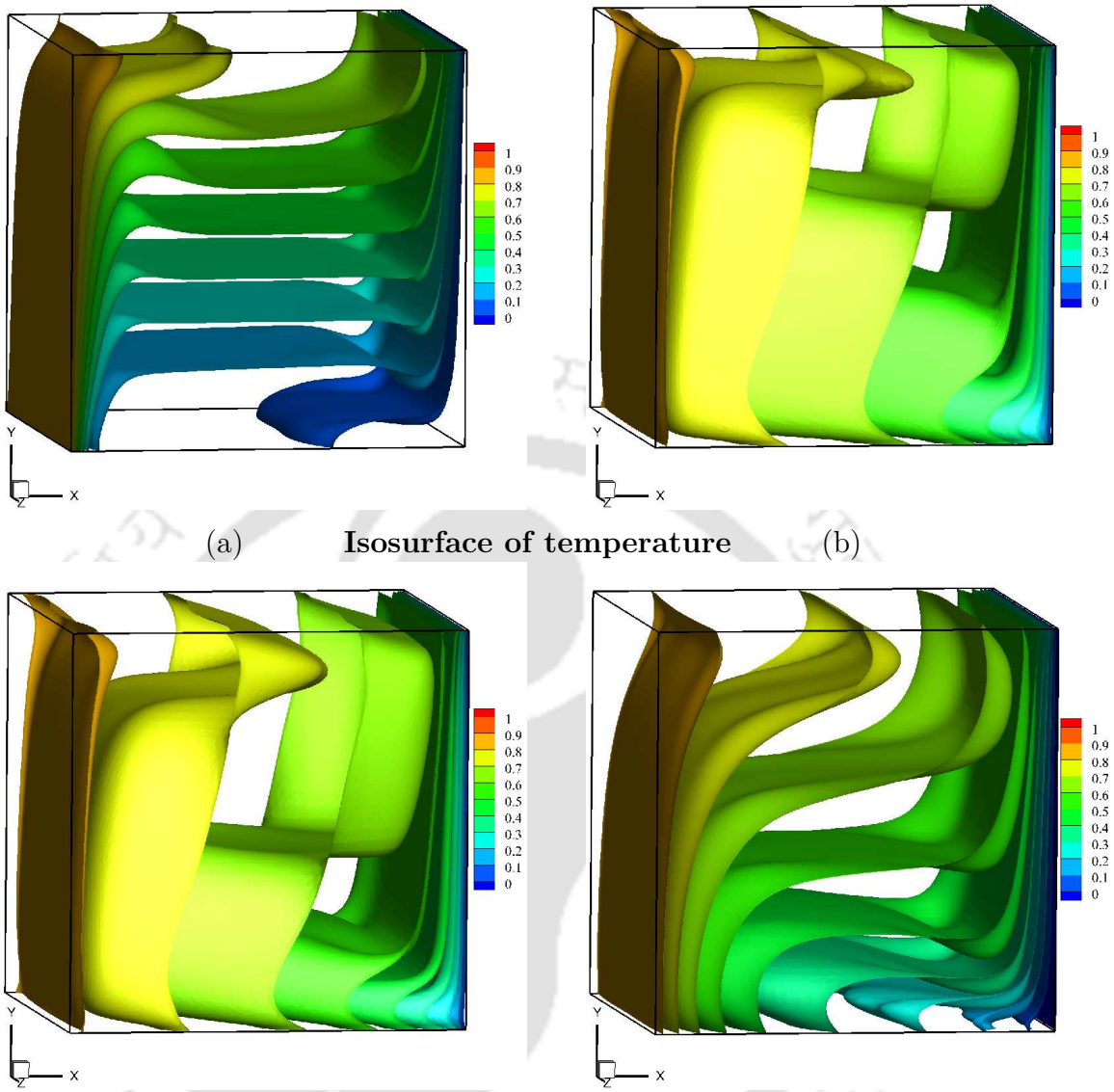

Figure 6.18: Isosurface of temperature for natural convection flow with and without the influence of thermal radiation. (a) pure convection, (b) combined convection with surface radiation, (c) combined convection with gas radiation of optical thickness $\tau = 0.2$, (d) combined convection with gas radiation of optical thickness $\tau = 5.0$.

As the optical thickness of the medium increases, a major part of the radiation is absorbed by the participating medium and as a consequence, the temperature lev-

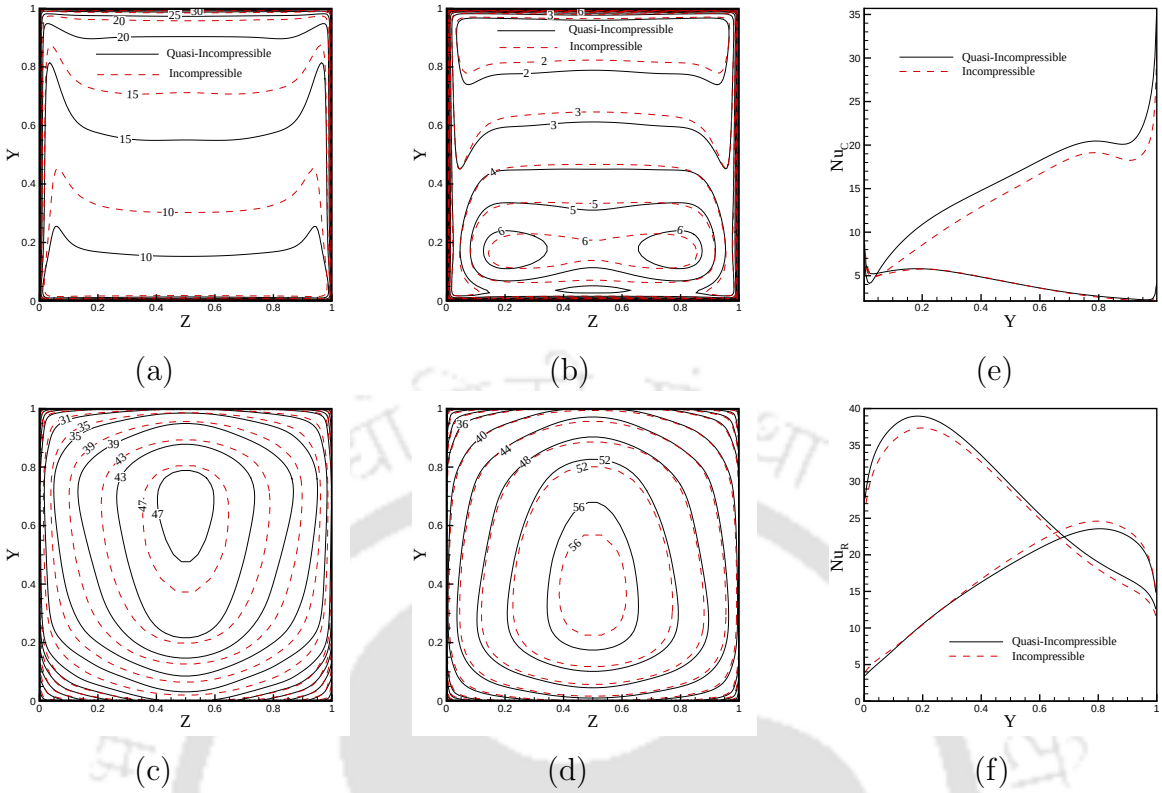

Figure 6.19: Local variation of convective and radiative Nusselt number at the hot and cold wall for three-dimensional (a, b, c, d) and two-dimensional (e, f) combined convection with gas radiation of optical thickness $\tau = 0.2$ using incompressible and quasi-incompressible low-Mach number model respectively: (a) convective Nusselt number variation at the cold wall, (b) convective Nusselt number variation at the hot wall, (c) radiative Nusselt number variation at the cold wall, (d) radiative Nusselt number variation at the hot wall, (e) convective Nusselt number variation at the hot and cold walls, (f) radiative Nusselt number variation at the hot and cold walls.

els are further elevated as seen in Fig. 6.18 (c). The participating gas of optical thickness $\tau = 5$ attenuates most of the radiation as a consequence the flow and temperature distribution depicts strong two-dimensional behavior with very little three-dimensionality observed near the adiabatic walls. The isotherms in case of combined convection with radiation case depict sharp bending near the adiabatic walls. The curved iso-surface of temperature near the adiabatic top and bottom

walls follow opposite curvature due to the combined effect of convection and radiation. The curved iso-surface of opposite curvature depicts enhanced heating and cooling of the top and bottom wall respectively due to convection. The influence of surface and gas radiation on overall heat transfer is realized from the average convective and radiative Nusselt number variation at the isothermal hot and cold walls from Table 6.7. The Nusselt number reveals that the symmetric nature of heat transfer in case of pure convection turns asymmetric with the inclusion of radiation. The asymmetric nature of heat transfer with the inclusion of surface and gas radiation is easily realized from the enhanced convective heat transfer at the cold wall in comparison to the hot wall. Large convective heat transfer at the cold wall is due to the enhanced temperature levels as a consequence of radiation to equalize the temperature. Moreover, the radiative Nusselt number reveal enhanced heat transfer due to radiation at the hot wall. Similar results are also obtained for the local variation of convective and radiative Nusselt number as seen from Fig. 6.19.

Figure. 6.19 (a, b) represents the local variation of the convective Nusselt number at the cold and hot walls respectively. It can be easily seen that large convection heat transfer rates are obtained at the top and base of cold and hot walls due to the interaction of the hot rising and cold descending fluid with the cold and hot walls respectively. Figures 6.19 (c, d) represents the local variation of the radiative Nusselt number at the cold and hot walls respectively, the variations signify larger radiative heat transfer rates at the hot wall in comparison to the cold wall. Enhanced heat transfer at the hot wall due to radiation is due to the attenuation of radiation by the absorbing medium. Similar variations can also be observed from the two-dimensional simulation of the same case as shown in Fig. 6.19 (e, f).

On comparing the average and local Nusselt number variation obtained using the incompressible and quasi-incompressible low-Mach number model in Table 6.7 and Fig. 6.19 it is seen that considerable deviations are obtained. The deviations are remarkably high for convective heat transfer, specifically at the cold wall. The maximum deviation of 18.5% in the convective heat transfer is obtained at the cold wall for a combined convection with gas radiation of optical thickness $\tau = 0.2$ case. The maximum variation in the radiative Nusselt number of 5.29% is obtained at the cold wall for combined convection with gas radiation of optical thickness $\tau = 0.2$ case. Furthermore, Table 6.8 represents the deviation in the results obtained between

Table 6.7: Average convective and radiative Nusselt number at the isothermal hot and cold walls using incompressible and LMN model for pure convection and convection with surface and gas radiation.

Geometry	Hot Wall		Cold Wall	
Model	Nu_C	Nu_R	Nu_C	Nu_R
pure convection				
Incompressible	8.683	NA	8.683	NA
Quasi-Incompressible (LMN)	9.442	NA	9.422	NA
Percentage deviation	8.03%	NA	8.03%	NA
Convection with surface radiation				
Incompressible	4.757	49.218	11.633	42.342
Quasi-Incompressible (LMN)	4.546	50.620	14.096	41.070
Percentage deviation	4.64 %	2.75%	17.4%	3.09%
Convection with gas radiation $\tau = 0.2$				
Incompressible	3.943	47.430	12.353	39.020
Quasi-Incompressible (LMN)	3.798	48.953	15.171	37.580
Percentage deviation	3.81%	3.11%	18.5%	3.83%
Convection with gas radiation $\tau = 5.0$				
Incompressible	4.031	25.568	13.760	15.840
Quasi-Incompressible (LMN)	4.058	26.650	15.662	15.044
Percentage deviation	0.6%	4.06%	12.14%	5.29%

an incompressible and quasi-incompressible model for a combined convection with surface radiation problem using a two-dimensional and three-dimensional analysis. The results from Table 6.8 reveal that the deviation between the incompressible and quasi-incompressible model increases in case of three-dimensional simulation in comparison to the two-dimensional approximation. In case of two-dimensional simulations, it is shown that the quasi-incompressibility effects, influence the con-

Table 6.8: Comparison of percentage deviation between the average convective and radiative Nusselt number at the isothermal hot and cold walls between a two dimensional and three-dimensional analysis obtained using incompressible and LMN model.

Geometry	Hot Wall		Cold Wall	
Model	Nu_C	Nu_R	Nu_C	Nu_R
Convection with surface radiation 2D analysis				
Incompressible	5.702	61.849	11.204	56.346
Quasi-Incompressible (LMN)	5.757	62.449	12.404	55.780
Percentage deviation	0.9 %	0.96%	9.6%	1.01%
Convection with surface radiation 3D analysis				
Incompressible	4.757	49.218	11.633	42.342
Quasi-Incompressible (LMN)	4.546	50.620	14.096	41.070
Percentage deviation	4.64 %	2.75%	17.4%	3.09%

vective heat transfer only as the deviation in the radiative Nusselt number are very small. However, from the three-dimensional simulations, it is apparent that quasi-incompressibility effects influence not only the convective heat transfer but also the radiative heat transfer significantly. The deviations from incompressible results are also shown for the local Nusselt number variation at the hot and cold walls in Fig. 6.19. These results signify that quasi-incompressibility effects are significant in three-dimensional combined convective radiative heat transfer scenario and influence the heat transfer due to convection and radiation both. Hence, a variable density formulation should be a preferred choice of numerical model for accurately simulating accidental fire and flow of air and smoke spread in buildings.

6.6 Closure

In this chapter numerical studies on the influence of partitions on buoyancy induced convection with thermal radiation in cubical enclosures are carried out by employ-

ing four distinct arrangements of partitions. These partitions follow a symmetric (inline) and asymmetric (offset) configuration from the top-bottom and front-back walls. Detailed analysis of flow, heat transfer, Nusselt number and irreversibilities due to conduction, convection, and radiation are performed for all configuration of partitions considered. The simulation results reveal that heat transfer irreversibility is the dominant mechanism of entropy production. Furthermore, the offset configuration with front-back partitions exhibits highest heat transfer rates with minimum total entropy generation. The non-Boussinesq effects are highlighted for a large temperature difference convective-radiative heat transfer problem in a three-dimensional enclosure compared with a two-dimensional approximation of the same problem. It is shown that for two-dimensional simulations, the quasi-incompressibility effects, influence the convective heat transfer only and the deviation in the radiative Nusselt number are very small. However, from the three-dimensional simulations, it is apparent that quasi-incompressibility effects influence not only the convective heat transfer but also the radiative heat transfer significantly.

Chapter 7

Turbulence-Radiation Interaction in Buoyancy Driven Flows

7.1 Introduction

This chapter presents a numerical simulation of buoyancy-driven turbulent natural convection with and without the influence of thermal radiation in a differentially heated square cavity at large temperature difference. The impact of surface and gas radiation on overall flow dynamics and heat transfer is discussed by performing comparisons with a classic natural convection case at $Ra = 10^{10}$. The results from the present study reveal that the inclusion of surface and gas radiation leads to asymmetry in the flow and heat transfer. Furthermore, the convection currents intensify, and the magnitude and extent of the turbulence effects primarily increase with the consideration of thermal radiation in the simulation. This study also quantifies the deviations between the proposed variable density low-Mach number model and popularly used incompressible model based on Reynolds averaged governing equations. Studies on coupled turbulent convection with thermal radiation report that the deviations between the results obtained using a Boussinesq and low-Mach number model grow with the increment in the optical thickness of the medium.

7.2 Problem Description

The present study numerically investigates buoyancy driven turbulent flow with and without the influence of radiative heat transfer (surface and gas radiation) in a differentially heated square cavity at large temperature difference. The geometry of the problem as depicted in Fig. 7.1 consists of a square cavity of unit size. The left and right walls of the enclosure are differentially heated isothermal hot and cold walls respectively, while the top and bottom walls are adiabatic. Simulations are performed considering pure convection and convection with thermal radiation (surface and gas radiation) at large temperature difference using a low-Mach number formulation. Furthermore, investigations are performed for the set of dimensionless parameters where Ra=10^{10}, $Pr = 0.71$, $Pr_t = 0.85$, and $Ga = 1.2$. Here, $Ga = 1.2$ corresponds to a non-Boussinesq convection at large temperature difference. Moreover, simulations involving the influence of thermal radiation are performed considering surface radiation $\tau = 0$, convection with gas radiation of optical thickness $\tau = 0.2$ and 1.0. This study highlights the role of thermal radiation in turbulent buoyancy driven convection at large temperature difference. The deviations in the numerical results between an incompressible and LMN model are presented for large temperature difference turbulent non-Boussinesq convection with and without the influence of thermal radiation.

7.2.1 Mesh independence study

This section describes the minimum spatial and angular meshes required to accurately compute turbulent buoyancy induced natural convection with thermal radiative heat transfer in a square enclosure. Non-uniform hexahedral meshes are used in the present study. Furthermore, a grid distribution suggested by Henkes and Hoogendoorn [84] is employed to place the sufficient number of cells in the viscous sublayer as reported in Table 7.1. This implies that the normalized distance to the wall y^+ is sufficiently low in the near wall region. To carry out the mesh independence study, four non-uniform meshes viz. 50×50, 100×100, 200×200 and 400×400 with an angular resolution of 6×20 are considered in the X and Y direction. A unit cell in the Z direction is employed as the intent is to solve a two-dimensional problem using a three-dimensional code. The details of the non-uniform mesh used

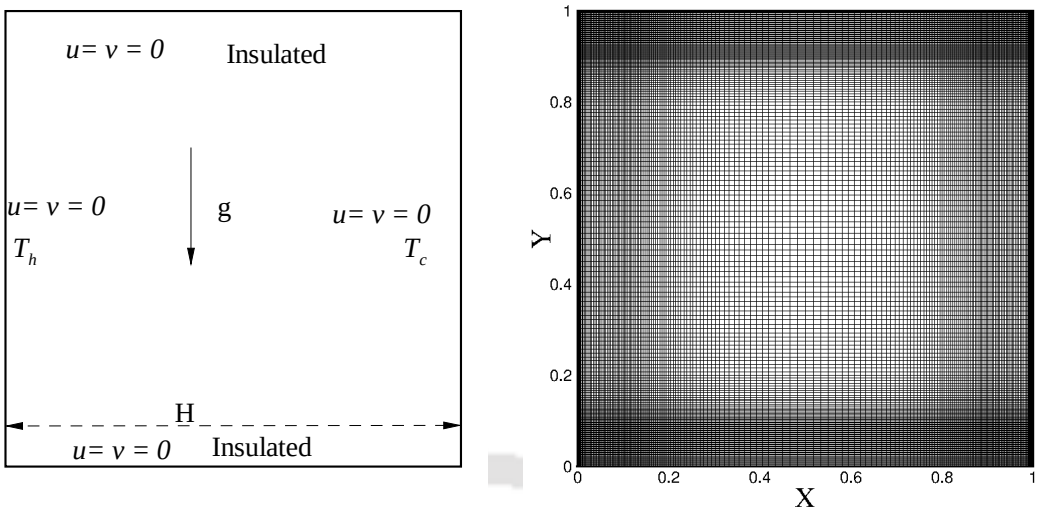

(a) (b)

Figure 7.1: (a) Computational domain with boundary conditions, (b) representation of non-uniform mesh used in the present study.

in the present study are presented in Fig. 7.1 (b) respectively.

The turbulent natural convection case at $Ra = 10^{10}$ with optical thickness $\tau = 1$ is chosen, and the average values of the Nusselt number at the hot and cold walls are presented in Table 7.2. From the Table 7.2 it is evident that the quantitative difference between 200×200 and 400×400 grids are negligibly small. Further computations are carried out using 400×400 spatial grid. In the similar lines three-angular grids of resolution 2×12, 4×18 and 6×24 are used with a spatial mesh of 200×200. Using the three angular meshes total Nusselt number values of 1495.12, 1530.45 and 1532.18 are obtained which concludes that 6×24 is the ray-independent mesh and hence this is used for carrying out the simulations. In the present study, no wall functions are employed. Instead, as previously employed in many investigations [84, 88, 89], sufficiently fine grids are placed in the viscous sublayer to capture the large gradients of mean flow quantities with Dirichlet boundary conditions for k and ε at the walls. Sharma et al. [89] reported that the epsilon value at the walls ε_w should be more than 10^{22} to get the grid independent solution. Hence, We use $k_w = 0$ and $\varepsilon_w = 10^{25}$ at the no-slip walls in the present study.

Table 7.1: Position of first grid point from wall.

Grid size	Non-dimensional distance of first cell center from wall (X_p/H)
50×50	9.256×10^{-4}
100×100	8.036×10^{-5}
200×200	3.881×10^{-5}
400×400	1.907×10^{-5}

Table 7.2: Average Nusselt number at the hot and cold walls for three different grids of size 50×50, 100×100, 200×200 and 400×400 at $Ra = 10^{10}$ and $\tau = 1$.

Grid size	Hot wall		Cold wall	
	Nu_c	Nu_r	Nu_c	Nu_r
50×50	44.888	1504.083	270.056	1279.266
100×100	43.150	1498.275	279.141	1262.206
200×200	40.566	1492.980	275.120	1258.410
400×400	40.233	1491.947	274.899	1257.164

7.3 Results and Discussion

In this section, results on the flow and heat transfer in a buoyancy-driven turbulent non-Boussinesq convection with and without the influence of thermal radiative heat transfer are discussed. Simulations are carried out for various non-dimensional parameters like Ra=10^{10}, $Pr = 0.71$, $Pr_t = 0.85$, $Ga = 1.2$ are used in the present study. $Ga = 1.2$ corresponds to a non-Boussinesq convection at large temperature difference. The influence of surface and gas radiation on buoyancy driven natural convection at large Rayleigh number is demonstrated by comparing with pure convection case. The study is concluded by comparing the results between an incompressible and quasi-incompressible low-Mach number formulation. Furthermore, the deviations between the incompressible and quasi-incompressible models are quantified for the range of parameters used in the present study.

7.3.1 Influence of surface and gas radiation on turbulent non-Boussinesq convection

This study highlights the influence of thermal radiation (surface and gas radiation) in a non-Boussinesq buoyancy driven turbulent flow inside a differentially heated square enclosure at $Ra = 10^{10}$. Figures 7.2 and 7.3 depict the isotherms and streamlines, respectively, inside the square cavity for pure-convection, combined convection with surface and gas radiation of optical thickness $\tau = 0.2$ and 1. The streamlines for the pure convection case depict a clockwise flow inside a primary convection cell with the formation of two secondary cores near the isothermal walls. The flow recirculations are caused due to the combined influence of viscous shear and buoyancy. The isotherms and streamlines for classic convection case as seen from Figs. 7.2 (a) and 7.3 (a) represent a generation of thin boundary layers both thermal and hydrodynamic adjacent to the isothermal walls. These boundary layers grow steadily along the isothermal vertical walls and attenuate near the top and bottom of hot and cold walls, respectively. The boundary layers adjacent to the isothermal walls represent the zone of maximum velocity with stagnant thermal and hydrodynamic stratified region in the center of the cavity. The moving fluid in the boundary layer interacts with the stagnant stratified core; this causes the hot rising and the cold descending fluid near the hot and cold walls to pull the core due to viscous shear. However, the opposed buoyancy force causes a flow reversal of the ascending and descending fluid near the hot and cold isothermal walls to maintain a stable stratified flow in the center core. The stable stratified core is responsible for the reduced convection inside the enclosure. The isotherms as seen from Fig. 7.2 (a) also exhibit a similar variation. Furthermore, the non-dimensional temperature difference along the top and bottom walls is of the order of 0.7 with negligible temperature gradients along the horizontal direction just ahead of the boundary layers.

With the inclusion of surface and gas radiation, the flow and heat transfer characteristics are modified substantially. Interestingly, the inclusion of surface radiation thickens the boundary layers along the vertical and horizontal walls as seen from Figs. 7.2 (b) and 7.3 (b). The influence of surface radiation elevates the temperature

levels inside the enclosure. The combined influence of buoyancy in rising the lighter fluid and that of thermal radiation to increase the mean temperature levels inside the enclosure leads to accumulation of hot fluid in the region above the center of the cavity. The augmentation of hot fluid in the upper half of the enclosure leads to asymmetry in the flow and heat transfer, particularly the flow in the top of the cavity is nearly stagnant. The increased temperature levels in the upper half of the cavity reduces the convection currents in the region and the recirculation zone which was observed at the center core of the enclosure for pure convection (Fig. 7.3 (a)) is pushed to the bottom (Fig. 7.3 (b)).

The recirculating flow at the bottom of the cavity diffuses a relatively hotter fluid (temperature levels higher than average) as most of the cold fluid is restricted to the base of the cold wall. The flow reversal which was observed for both hot and cold walls in pure convection case as shown in (Fig. 7.3 (a)) can be only seen near the hot wall for surface radiation case (see Fig. 7.3 (b)). Furthermore, steeper temperature gradients are observed at the adiabatic top and bottom walls to consider the thermal-radiation effects. The consideration of surface radiation has reduced the non-dimensional temperature difference along the top and bottom walls from 0.7 to 0.3 relative to the pure convection case with reduced temperature stratification at the center of the cavity. Streamlines considering gas radiation of optical thickness τ=0.2 as shown in Fig. 7.3 (c) represent a multi-cellular flow field with three vortices in the cavity. In addition to the primary recirculation zone at the base of the enclosure as already observed for surface radiation case (Fig. 7.3 (b)), a secondary convection roll is also noted in the upper half of the cavity. A small tertiary vortex accompanies the two recirculating zones near the hot wall above the mid-plane of the cavity. The temperature variation as seen from Fig. 7.2 (c) represents a thermally active center region with negligible temperature stratification. The influence of participating medium reduces the extent of radiative heat transfer as much of the radiation is absorbed. However, heat transfer due to convection is significantly increased at the adiabatic walls to compensate the reduction in the radiative heat transfer. The sharp bending of the isotherms at the adiabatic top and bottom walls is an implication of the increased convection inside the enclosure. The fast-moving convection currents at the horizontal and vertical boundary layers interact with the thermally active fluids to form primary and secondary recirculation zones inside the cavity. The primary and secondary vortices recirculate most of the hot fluid inside

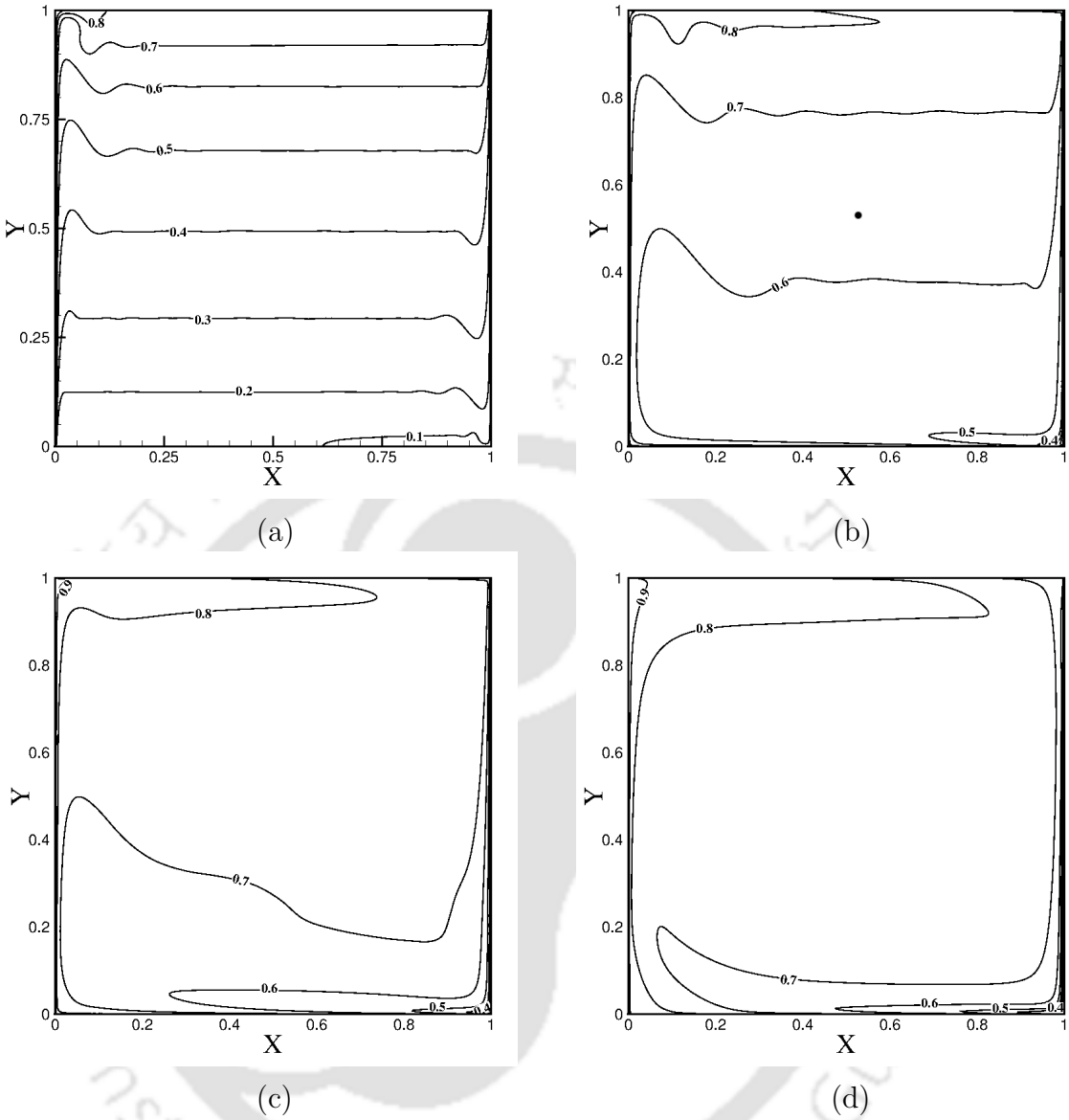

Figure 7.2: Isotherms inside the square cavity at $Ra = 10^{10}$ for (a) non-radiating pure convection, (b) combined convection with surface radiation, (c) convection with gas radiation of optical thickness τ=0.2, (d) convection with gas radiation of optical thickness τ=1.

the enclosure. The tertiary vortex is created as a result of flow reversal along the isothermal hot wall just outside the boundary layer due to the combined influence of viscous drag and opposing buoyancy.

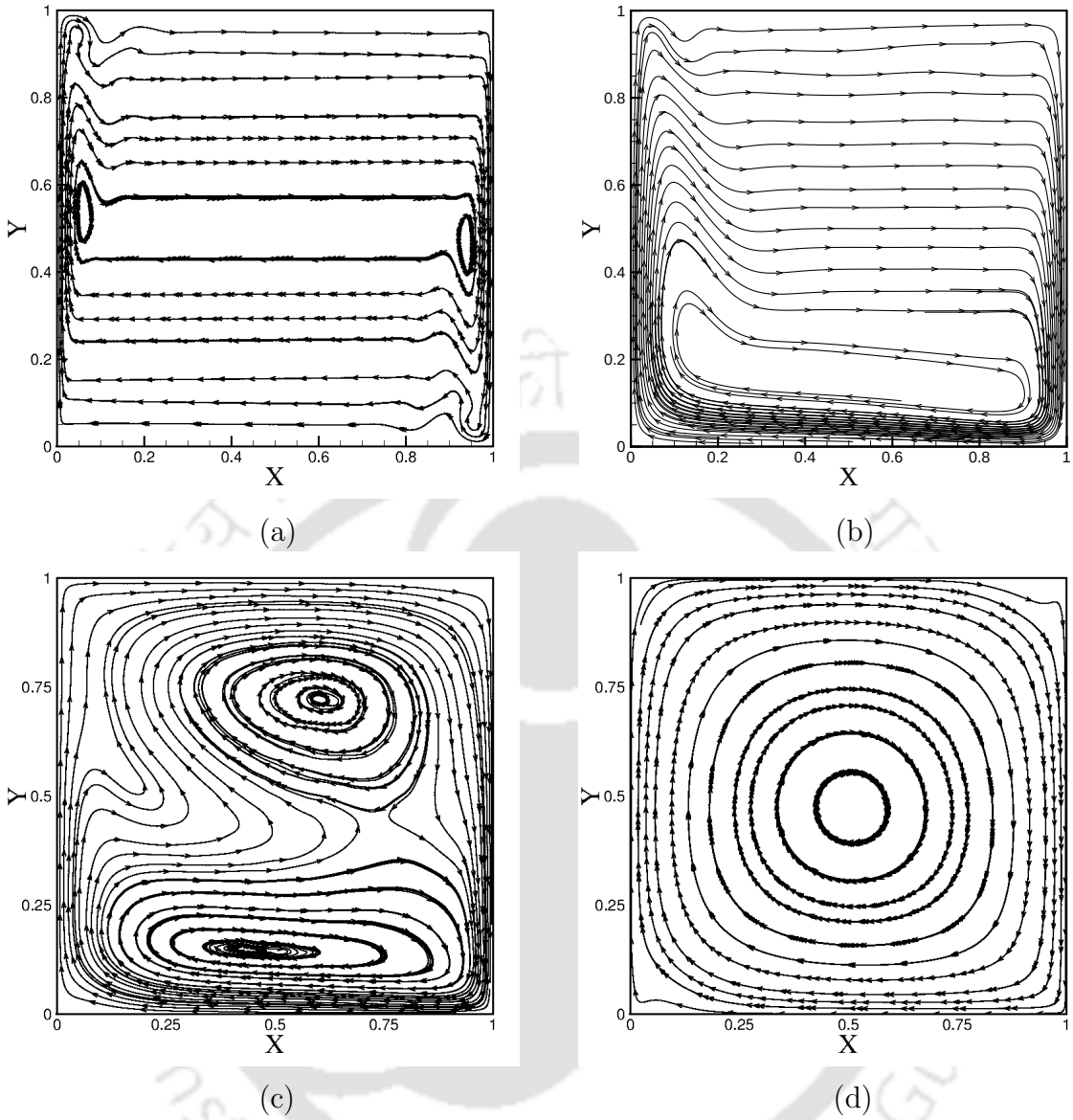

Figure 7.3: Streamlines inside the square cavity at $Ra = 10^{10}$ for (a) non-radiating pure convection, (b) combined convection with surface radiation, (c) convection with gas radiation of optical thickness τ=0.2, (d) convection with gas radiation of optical thickness τ=1.

With the increase in optical thickness of the participating medium from τ=0.2 to 1.0, a unicellular flow field is recognized as depicted in Fig. 7.3 (d). The isotherms

in Fig. 7.2 (d) represent a thermally active center core filled with hot fluid (temperature levels much larger than average temperatures) with negligible temperature gradients along the horizontal and vertical direction. The large absorption of the thermal radiation by the participating medium had lead to a significant increase in the mean temperature inside the enclosure. The thermal stratification previously observed for pure convection case is completely lost. Furthermore, the convection currents have increased drastically with an increase in optical thickness of the participating medium. The increased convective heat transfer can be easily realized from sharp bending of the isotherms with opposite curvature at the adiabatic top and bottom walls. The stronger convection currents interact with the thermally active hot fluid at the center core to form a single recirculation cell. These simulation results reveal that the increment of optical thickness increases the convection currents inside the enclosure.

7.3.2 Influence of surface and gas radiation on temperature and velocity distribution inside the cavity

The influence of thermal radiation on temperature and velocity variation for turbulent buoyancy-driven flow is explained by comparing the centerline profiles. Figure 7.4 represents the temperature and velocity variation along the horizontal and vertical centerline for pure convection and combined convection with surface and gas radiation, respectively. The temperature variation along the horizontal centerline in Fig. 7.4 (a) depicts sharp gradients near the isothermal walls while the temperature gradients are negligible in the region away from boundary layers at the center core. The temperature variation for the pure convection case depicts anti-symmetric distribution along the x-axis while the inclusion of surface and gas radiation breaks the anti-symmetry in the temperature variation. A mean temperature values of 0.4, 0.6, 0.7 and 0.75 are observed just ahead of the boundary layers for pure convection and combined convection with surface and gas radiation of optical thickness 0.2 and 1, respectively. The temperature variation along the vertical centerline in Fig. 7.4 (b) indicates sharp temperature gradients near the bottom walls. However, the temperature gradients at the top wall are minimal in comparison to the bottom wall. The reduced temperature gradients at the top wall are due to the

combined influence of buoyancy and increased temperature levels due to thermal radiation which compels the hotter fluid to accumulate at the top of the cavity. Large temperature gradients at the bottom wall are obtained for surface and gas radiation with optical thickness $\tau = 0.2$ case as the recirculation vortex are forced to the base of the cavity due to the increased temperature levels inside the enclosure.

From the vertical velocity variation along the x-axis in Fig. 7.4 (c) maximum velocity is perceived near the isothermal hot and cold walls. The velocity variation for pure convection and combined convection with gas radiation of optical thickness τ=1 is anti-symmetric while the surface and gas radiation case with optical thickness τ=0.2 depicts asymmetric variation. Large velocity gradients are perceived near the vertical walls while in the central region away from the isothermal walls the velocity variation is almost negligible in the vertical direction. From the horizontal velocity variation along the y-axis at midplane in Fig. 7.4 (d) it is seen that for pure convection case the u-velocity gradients are almost negligible along the vertical axis. However, with the inclusion of surface radiation the velocity variation depicts sharp slopes near the bottom walls whereas in the central and upper half of the cavity the flow is almost stagnant along the horizontal direction. With the consideration of gas radiation with optical thickness τ=0.2 and 1, the horizontal velocity attains its maximum value near the top and bottom walls. The simulation results depict a significant increase in convection currents with the inclusion of thermal radiation. In particular, the horizontal component of velocity achieves its maximum value near the adiabatic walls with the increment in the optical thickness of the participating medium.

7.3.3 Influence of surface and gas radiation on turbulent viscosity variation inside the cavity

Figure 7.5 signifies the influence of surface and gas radiation on the variation of viscosity ratio (turbulent to laminar viscosity). The viscosity ratio contours for classic convection case in Fig. 7.5 (a) depict an anti-symmetric distribution along the vertical mid-plane with maximum values obtained in the boundary layers adjacent to the vertical walls. The viscosity variation for pure convection signifies dominant mixing near the boundary layers at the isothermal walls and the region adjoining

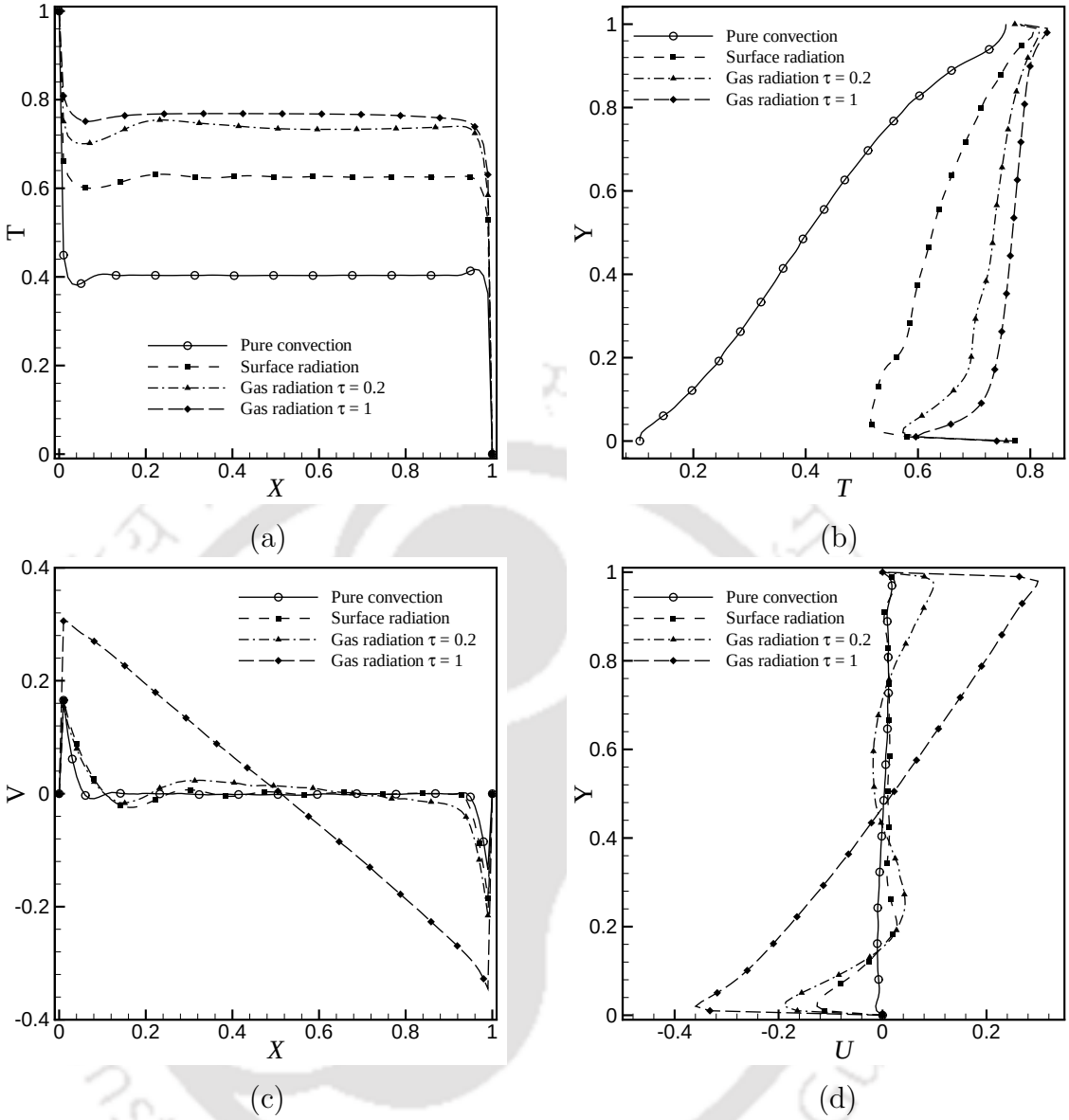

Figure 7.4: Influence of surface and gas radiation on temperature and velocity variation at $Ra = 10^{10}$, (a, b) comparison of temperature variation along the horizontal and vertical mid plane respectively, (c) comparison of vertical velocity variation along the horizontal mid plane, (d) comparison of horizontal velocity variation along the vertical mid plane.

the stratified core and boundary layers. However, the value of turbulent viscosity ratio is almost negligible near the adiabatic walls and also in the center core of

the cavity as the velocity gradients are imperceptible in this region. Notably, the consideration of surface radiation in the simulation increases the magnitude and extent of the turbulent viscosity field. Domains of stronger turbulent viscosity are obtained not only near the vertical boundary layers but also in the vicinity of the bottom wall. The variation of viscosity ratio is asymmetry with a strong inclination to the hot wall. The highest value of the turbulent viscosity is perceived at the base of the isothermal hot wall, and it decreases gradually along the height of the wall. Furthermore, turbulent viscosity field is significant only near the base of the cold wall. The preeminence of turbulent viscosity variation at the bottom wall is because of the increased velocity gradients in the horizontal direction along the bottom wall due to the influence of thermal radiation. As already mentioned that the consideration of gas radiation leads to increased convection currents at the horizontal walls and the suppression of recirculation zones towards the bottom of the cavity. This is the basis of predominant turbulent viscosity fields near the horizontal bottom wall in comparison to the vertical walls for combined convection with gas radiation as seen from Figs. 7.5 (c) and (d).

7.3.4 Influence of surface and gas radiation on Nusselt number variation at the hot and cold walls

The influence of thermal radiation on overall heat transfer is discussed by analyzing the Nusselt number on the hot and cold walls. Figure 7.6 represents the local variation of convective and radiative Nusselt numbers at the hot and cold walls, respectively for pure convection and combined convection with surface and gas radiation. From the convective Nusselt number variation at the heated wall in Fig. 7.6 (a) it is seen that the values of convective Nusselt number decrease with the addition of surface and gas radiation. The highest value of convective Nusselt number for pure convection is perceived at the base of the heated wall, and it further decreases with the wall height. However, at the cold wall, the variation of convective Nusselt number is observed to increase with the inclusion of surface and gas radiation, respectively. The highest value of the convective Nusselt number is remarked at the top of the cold wall, and it decreases gradually with height. The symmetry breaking phenomena observed in the variation of convective Nusselt number for laminar buoyancy driven non-Boussinesq flows at substantial temperature difference can also

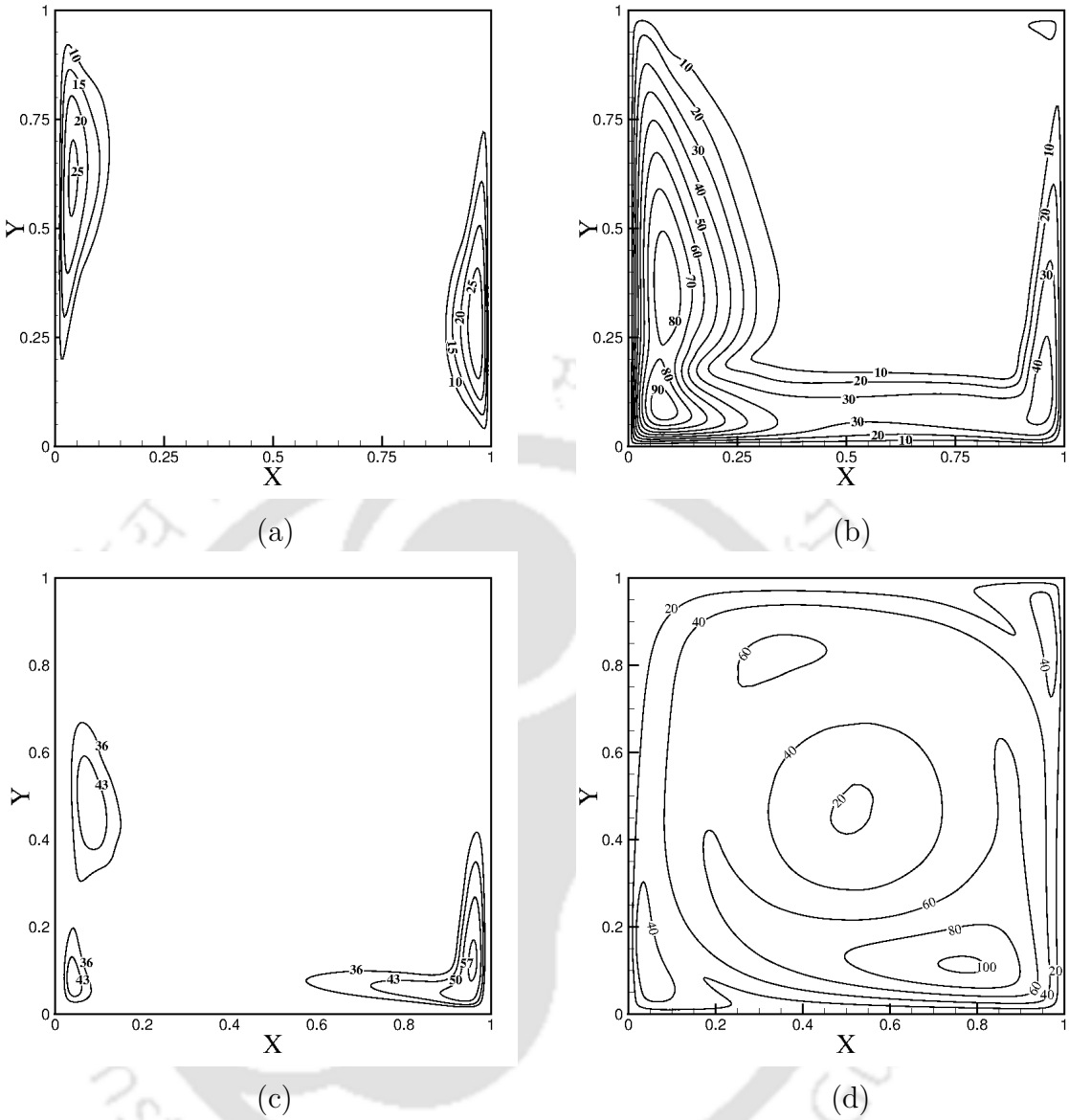

Figure 7.5: Influence of surface and gas radiation on viscosity ratio at $Ra = 10^{10}$. Distribution of viscosity ratio for (a) pure convection, (b) combined convection with surface radiation, (c) convection with gas radiation of optical thickness τ=0.2, (d) convection with gas radiation of optical thickness τ=1.

be seen in turbulent flows.

The attenuation and augmentation of convective Nusselt number with the inclusion

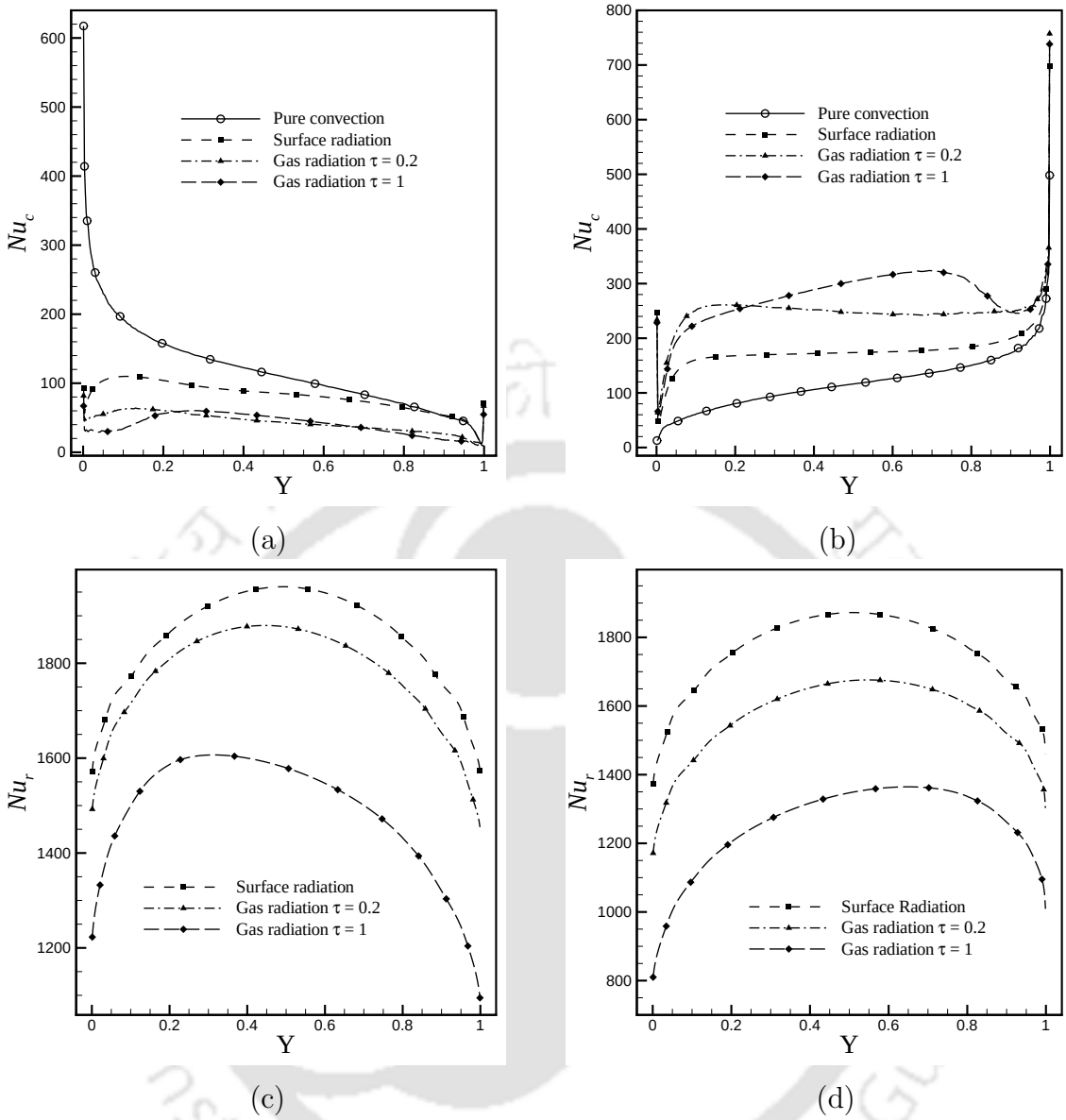

Figure 7.6: Influence of surface and gas radiation on local variation of convective and radiative Nusselt number for turbulent natural convection inside a differentially heated square cavity at $Ra = 10^{10}$. (a) Variation of convective Nusselt number at the hot wall, (b) variation of convective Nusselt number at the cold wall, (c) variation of radiative Nusselt number at the hot wall, (d) variation of radiative Nusselt number at the cold wall.

Table 7.3: Influence of surface and gas radiation on average Nusselt number for Rayleigh number Ra=10^{10}.

Cases considered	Hot wall		Cold wall	
	Nu_c	Nu_r	Nu_c	Nu_r
Pure convection	118.886	NA	118.886	NA
Surface radiation	81.387	1859.243	176.855	1763.775
Gas radiation, $\tau = 0.2$	43.383	1776.308	247.979	1571.495
Gas radiation, $\tau = 1$	40.233	1491.947	274.899	1257.164

of thermal radiation at the hot and cold walls are attributed to the increase in mean temperature levels by thermal radiation. However, higher values of radiative Nusselt number variation can be observed at the hot wall in comparison to the cold wall as seen from Fig. 7.6 (c) and (d). The highest values of radiative Nusselt number variation is observed for the surface radiation case. Furthermore, the values of radiative Nusselt number decrease gradually with increase in optical thickness of the medium. Table 7.3 represents the average values of convection and radiation Nusselt numbers at the isothermal hot and cold walls for pure convection and combined convection with surface and gas radiation. From the average values of the Nusselt number, it is seen that the inclusion of surface and gas radiation induces asymmetry in the heat transfer. The asymmetric heat transfer distribution is evident from the decreased convective Nusselt number at the cold wall. However, at the hot wall the convective Nusselt number values are augmented substantially. The values of radiative Nusselt number decrease with the increment in optical thickness due to the large absorption of thermal radiation by the participating medium.

7.3.5 Influence of variable temperature dependent thermo-physical properties on flow and heat transfer

In this section the significance of non-Boussinesq, variable density formulation is discussed for accurate simulation of turbulent natural convection with thermal radiative heat transfer at large temperature difference. A comparative analysis of

results obtained using an incompressible model based on Reynolds averaging of the governing equations and a variable density low-Mach number model based on Favre-averaging of the governing equations is performed. The differences in the results for temperature, velocity, viscosity ratio and Nusselt number variations are presented for a turbulent natural convection flow coupled with gas radiation. The problem is solved at $Ra = 10^{10}$, $Pr = 0.71$, $Pr_t = 0.85$, $Ga = 1.2$ and $\tau = 1.0$ using incompressible and quasi-incompressible models. Figure 7.7 represents the variation of turbulent viscosity, temperature and velocity variation along the horizontal and vertical centerline respectively. From the results, it is evident that the incompressible assumption over-predicts the temperature, velocity and turbulent viscosity variation in the center core of the cavity. It is interesting to note that the incompressible model over-predicts the temperature gradients near the isothermal hot walls whereas they are under-predicted near the cold walls which influences the Nusselt number variation immensely. Figure 7.8 represents the comparison of local variation of convection and radiation Nusselt number at the isothermal hot and cold walls. From Fig 7.8 it is seen that the incompressible model does not accurately predict the Nusselt number values. From the comparison of average Nusselt number variation in Table 7.4 it is emphasized that the maximum deviation in the convective Nusselt number between the incompressible and quasi-incompressible model is 30.83%, whereas the radiative Nusselt number has a maximum deviation of 3.67%. Furthermore, the differences in the Nusselt number values grow with the increase in optical thickness of the participating gas. The comparison of the quasi-incompressible and low-Mach number models demonstrate the inaccuracy of incompressible models for simulating large temperature difference buoyancy driven turbulent natural convection with thermal radiative heat transfer.

7.4 Closure

In this chapter, numerical simulations of turbulent natural convection with and without the influence of thermal radiation in a differentially heated square cavity are presented at large temperature difference for $Ra = 10^{10}$. It is shown that the inclusion of surface and gas radiation leads to asymmetry in the flow and heat transfer. Also, the convection currents intensify, and the magnitude and extent of the

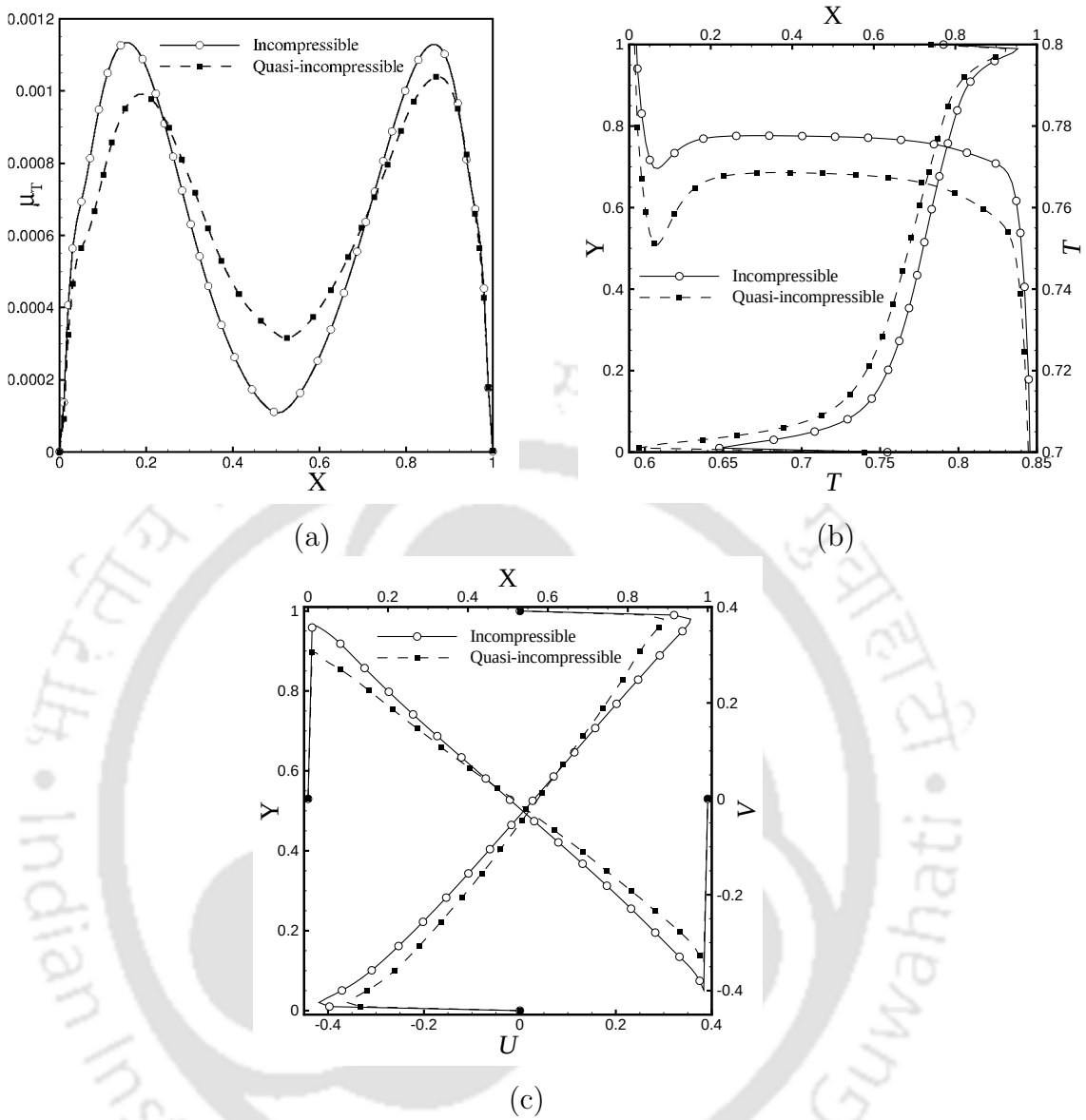

Figure 7.7: Comparison of results between incompressible and variable density low-Mach number model for turbulent natural convection flow coupled with gas radiation at $Ra = 10^{10}$ and $\tau = 1.0$. (a) Comparison of variation of turbulent viscosity along the horizontal mid plane. (b) comparison of centerline temperature variation along the horizontal and vertical mid plane. (c) comparison of center line velocity variation along the horizontal and vertical mid plane.

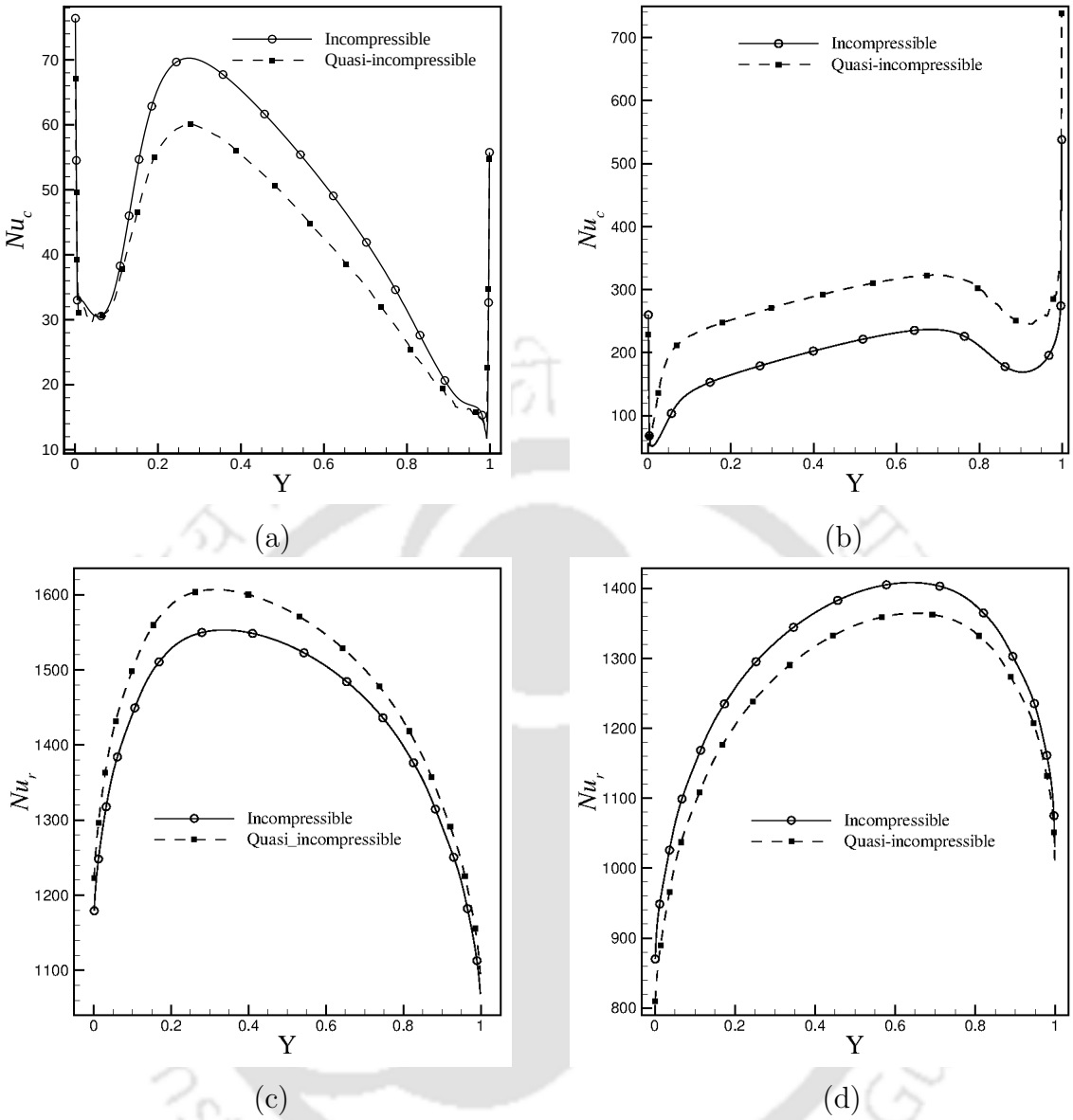

Figure 7.8: Comparison of local Nusselt number variation between incompressible and variable density low-Mach number model for turbulent natural convection flow coupled with gas radiation at $Ra = 10^{10}$ and $\tau = 1.0$. (a) Variation of convective Nusselt number at the hot wall, (b) variation of convective Nusselt number at the cold wall, (c) variation of radiative Nusselt number at the hot wall, (d) variation of radiative Nusselt number at the cold wall.

Table 7.4: Comparison of average Nusselt number variation between incompressible and variable density low-Mach number model at Rayleigh number $Ra = 10^{10}$.

Testcase	Formulation	Hot wall		Cold wall	
		Nu_c	Nu_r	Nu_c	Nu_r
Pure convection	Incompressible	117.360	NA	117.160	NA
	LMN	118.880	NA	118.770	NA
	% deviation	1.27 %	-	1.35 %	-
$\tau = 0$	Incompressible	76.860	1845.280	145.610	1775.690
	LMN	81.380	1859.240	176.850	1760.380
	% deviation	5.56 %	0.75 %	17.66 %	0.86 %
$\tau = 0.2$	Incompressible	43.920	1740.320	174.530	1609.490
	LMN	43.380	1776.300	247.970	1571.490
	% deviation	1.25 %	0.20 %	29.61 %	2.41 %
$\tau = 1$	Incompressible	46.600	1447.010	190.140	1303.320
	LMN	40.230	1491.940	274.890	1257.160
	% deviation	15.83 %	3.01 %	30.83 %	3.67 %

turbulence effects primarily increase with the consideration of thermal radiation in the simulation. The deviations between the proposed variable density low-Mach number model and popularly used incompressible model based on Reynolds averaged governing equations are quantified. Finally, it is reported that the deviations between the Boussinesq and low-Mach number model grow with the increment in the optical thickness of the medium.

Chapter 8

Conclusions and Scope for Future Work

8.1 Conclusions

This thesis presents a unified framework for simulation of buoyancy driven flows (laminar and turbulent) coupled with thermal radiative heat transfer in enclosures. In this context, a detailed mathematical formulation based on FVM is presented for the numerical computation of radiative heat transfer in conjunction with a low-Mach number formulation for laminar and turbulent natural convection flows. Furthermore, a detailed discretization of the governing equations is presented on three-dimensional unstructured polyhedral meshes. A validation study comprising of pure radiative heat transfer, natural convection at large temperature difference, coupled natural convection with surface and gas radiation and turbulent natural convection is performed. The results from the present numerical model are shown to be in excellent agreement with that of the reported literatures. Further, it is shown that a conservative algorithm with balancing of the pressure and buoyancy terms is best suited for robust calculations of large temperature difference thermo-buoyant convection with radiative heat transfer among the three low-Mach number algorithms presented in this thesis. The developed mathematical model is used to study the influence of partitions on buoyancy induced convection with thermal radiation in

a differentially heated cubical enclosure and turbulence radiation interaction in a buoyancy driven flow. A brief summary of the conclusions arrived from investigations carried out in each individual chapters is discussed as follows.

In chapter 4, the invalidity of the incompressible model and the need for a non-Boussinesq model for convective-radiative flows is explored. This is achieved by performing studies for combined buoyancy- driven convection coupled with thermal radiation in enclosures with a heated cylinder. Studies are performed considering large temperature difference convective-radiative flows. Coupled natural convection with thermal radiation at small temperature difference but the mean temperatures are high enough so that the radiative heat transfer effects become significant. Simulations are carried out by using an incompressible model based on Boussinesq approximation, a quasi-incompressible model based on low-Mach number formulation and compressible model using OpenFOAM. The compressible model of OpenFOAM is used with an intent to verify the results of the present low-Mach number model. The main findings are as follows.

• The low-Mach number algorithm is found to be robust and stable for the range of Rayleigh, Gay-Lussac and Planck number studied. The algorithm is able to provide satisfactory results over the range of parameters, agreeing well with the results obtained from a compressible model simulated using OpenFOAM.

• Comparison of results between a Boussinesq and non-Boussinesq models show qualitative similarities for the case of surface radiation. However, these similarities tend to vanish in the presence of gas radiation, with a significant qualitative contrast. Quantitative differences between the two models concerning local Nusselt number variation at the top and bottom walls of the enclosure can be observed.

• The use of incompressible assumption at a high optical thickness ($\tau = 5.0$) results in errors up to 27 % in the convective Nusselt number and 15 % in the radiative Nusselt number at the heated cylinder. The maximum error of 45% in the local convective Nusselt number is encountered at the top wall.

• Significant influence of radiative heat transfer even for small temperature differences can cause the Boussinesq approximation to fail with substantial influence on flow and Nusselt number variation.

In chapter 5, numerical studies are performed to examine the performance of three-different low-Mach number algorithms for simulating coupled convection with ra-

diation. Three different algorithms based on a low-Mach number formulation are presented for tackling the non-Boussinesq effects arising due to substantial temperature difference and radiative heat transfer. These algorithms are categorized as discretely conservative and update based algorithms. The discrete mass and energy conservation errors arising where density and temperature are obtained through the EOS have been derived, and its implications on solving buoyancy driven flows with radiation are discussed in details. Furthermore, the importance of balancing the pressure and buoyancy term for robust simulations of large temperature difference non-Boussinesq convection is presented. The important findings from this study are discussed as follows.

• Solution to buoyancy-driven Boussinesq or non-Boussinesq convection with radiative heat transfer in enclosures can be carried out using a low-Mach formulation where one can solve all the conservation laws or choose to have density or temperature being computed from the equation of state.

• The use of approaches where the density and temperature are computed from the EOS leads to the generation of discrete mass and energy conservation errors in the system. These errors are functions of dimensionless quantities governing the flow and heat transfer $(Ga, Ra, Pr, Pl, \Delta t)$ and approach zero as $\Delta t \to 0$. For a finite Δt the magnitude of these errors plays a vital role in smooth convergence and solution to steady state using a pseudo-transient approach.

• The influence of large temperature difference $(Ga \to \infty)$ and dominance of radiative heat transfer $(Pl \to 0)$ have a considerable impact on the stability of such algorithms where density or temperature is computed from EOS. However, the density update algorithm is shown to be marginally superior to the one where the temperature is computed from the EOS for problems involving small temperature difference $(Ga \to 0)$ and dominance of radiative heat transfer $(Pl \to 0)$.

• In case of large temperature difference non-Boussinesq convection, the balancing of pressure and buoyancy term is found to increase the robustness of the algorithm. In particular, the unbalanced algorithm requires at least two orders lower time step Δt for solution convergence as compared to its balanced counterpart. This is because of the spurious currents that may be generated because of a discrete imbalance between the various terms that could affect the robustness of the solution.

• This study shows that a fully balanced and discretely conservative algorithm is best suited for robust simulation of combined natural convection with thermal radiative heat transfer in enclosures.

In chapter 6, numerical investigations are performed on the influence of partitions for buoyancy-induced convection with thermal radiation in a cubical enclosure at substantial temperature differences. Studies on four distinct configurations of top-bottom and front-back partitions have been performed at $Ra = 10^6$, $Pr = 0.71$, $Ga = 1.2$ and $Pl = 0.01$. The significance of position and orientation of partitioning walls on flow physics, heat transfer characteristics and entropy generation inside the enclosure is considered by applying a symmetric (inline) and asymmetric (offset) arrangement of the partitions. Numerical experiments are carried out for different class of problems considering pure convection as well as buoyancy-induced convection with surface and gas radiation. The intent is to substantiate the impact of partitioning walls on convection and radiation heat transfer. The following are the major conclusions derived from this study.

• The offset configuration of top-bottom partitions depicts lower values of the convection Nusselt number in comparison with the inline configuration. This decrease in the convection Nusselt number is a consequence of entrapment of hot and cold fluid near the isothermal walls. One can observe a maximum reduction of 4.5 % in the convection Nusselt number for the surface radiation case.

• Contrary to the convective heat transfer the offset configuration of top-bottom partitions signifies higher radiation Nusselt number values with reference to the inline configuration. The inline partitions offer substantial blockage to radiation, and hence the radiation Nusselt number diminishes. One can observe a maximum reduction of 5.78 % in the radiation Nusselt number for the gas radiation case.

• Both the offset and inline configuration for front-back partitions have negligible influence on the convection Nusselt number. It signifies that these partitions do not alter the primary convection currents but merely contribute to the three-dimensionality of the flow. Higher values of radiation Nusselt numbers are obtained for the offset configuration as has also been observed similar to the top-bottom partitions.

• Partitions along the front and back walls represent higher values of convective and radiative Nusselt numbers when compared with the top-bottom partitions. This is true for both inline and offset configurations. Despite having the same blockage ratio, the radiative Nusselt number for inline configuration is more significant for front-back partitions in comparison to the top-bottom partitions owing to the enhanced heat transfer due to convection.

• Irreversibilities associated with heat transfer is the predominant mode of entropy production and those by fluid friction are mostly insignificant in the overall entropy production.
• Higher values of total entropy production are obtained for partitions along the top-bottom walls as compared to those along the front-back walls. The inline configuration with top-bottom partitions demonstrates highest values of total entropy generation.
• The offset configuration with front-back partitions exhibits highest heat transfer rates as observed from the values of average Nusselt number with minimum total entropy generation. This result may be of practical value since offset design of partitions could be a preferred choice for a building design and heat transfer point of view.
• Considerable deviations are obtained in the results from an incompressible and quasi-incompressible low-Mach number model for a three-dimensional natural convection influenced by thermal radiation. The deviations are remarkably high for convective heat transfer, specifically at the cold wall.
• The deviation between the incompressible and quasi-incompressible model increases in case of three-dimensional simulation in comparison to the two-dimensional approximation of the same problem. In case of two-dimensional simulations, it is seen that the quasi-incompressibility effects, influence the convective heat transfer only and the deviation in the radiative Nusselt number are very small. However, from the three-dimensional simulations, it is apparent that quasi-incompressibility effects influence not only the convective heat transfer but also the radiative heat transfer significantly.

In chapter 7, the details of a computational model for obtaining numerical solutions of turbulent buoyancy driven non-Boussinesq convection coupled with thermal radiative heat transfer in enclosures are presented. The simulations are carried out using a variable density model based on low-Mach number formulation of the Favre-averaged governing equations, while the turbulence is modeled using a two-equation $(k-\varepsilon)$ method. The developed model is used to highlight the significance of thermal radiation (surface and gas radiation) for buoyancy driven turbulent flows and heat transfer in a differentially heated square cavity at large temperature difference. The deviations in the results arising due to the use of an incompressible model are quantified for the range of parameters studied. The following are the major findings

of this study.

• The non-radiating pure convection case depicts anti-symmetric temperature and velocity distribution along the vertical mid-plane with steep temperature and velocity gradients near the isothermal walls. Regions of thin boundary layers are observed near the vertical walls with relatively stagnant and stratified temperature and velocity distributions at the center core.

• The inclusion of thermal radiation increases the mean temperature levels inside the enclosure. The combined influence of buoyancy and thermal radiation leads to accumulation of hot fluid in the upper half of the cavity which is accountable for the asymmetry in the flow and heat transfer.

• The increased temperature levels inside the cavity due to thermal radiation lead to thickening of the boundary layers. The thickening phenomena are predominant at the heated wall in comparison to the cold wall.

• To accommodate the influence of thermal radiation steeper temperature gradients are obtained at the adiabatic walls compared to the non-radiating pure convection case. The increase in optical thickness of the participating medium attenuates much of the radiation, as a consequence convective heat transfer is enhanced at the adiabatic walls to compensate the reduced radiative heat transfer. Thus the increase in optical thickness of the participating medium augments the intensity of convection inside the enclosure.

• Dominant effects of turbulence are limited to the region near the isothermal walls for the pure convection case. The coupled convection with thermal radiation case signifies increased magnitude and extent of the turbulence. The enhanced turbulence effects are realized at all four walls and also in the interior of the cavity.

• The presence of thermal radiation increases the heat transfer due to convection at the cold wall whereas higher radiative heat transfer rates are observed at the hot wall.

• Considerable deviations are obtained in the variation of temperature, velocity, turbulent viscosity and the local Nusselt number between the incompressible and variable density low-Mach number models. Subsequently, the deviations are found to increase with the increase in optical thickness of the medium. The maximum deviation in the average convective Nusselt number between the incompressible and quasi-incompressible model is 30.83%, whereas the radiative Nusselt number has a maximum deviation of 3.67%.

In a nutshell, the salient contributions of the thesis may be summarized as the development of a low-Mach number flow solver on unstructured meshes and its application for convective-radiative heat transfer. Salient contributions made in this thesis are summarized below. 1. This thesis presents extensive discussions on the circumstances in which variable-density flows can no longer be treated using an incompressible assumption (Boussinesq approximation). This includes problems involving large temperature difference natural convection and those coupled with radiative heat transfer.

2. It is very well known that the Boussinesq approximation does not hold good at large temperature difference. However, studies in the present thesis show that even for small temperature difference, a low enough Planck number (significant influence of radiative heat transfer) may cause the Boussinesq approximation to fail.

3. The importance of discrete conservation of mass and energy in obtaining robust solutions of non-Boussinesq flows has been discussed in detail. Importantly, the use of an algorithm that discretely conserves both mass and energy as opposed to calculating either one using the EOS allows the use of a larger time step on a given mesh without compromising on the solution accuracy. On similar lines, one may be able to use a finer mesh for a given time step in obtaining stable and accurate solutions for such problems.

4. A balanced force algorithm for buoyancy driven flows at large temperature difference is presented and its importance is highlighted for practical problems including turbulent flows. It is shown that at large temperature difference buoyancy driven flows the discrete balance between pressure and buoyancy forces allows for larger allowable time step and therefore more cost-effective solutions for such flows. Furthermore, it is seen that the balanced formulation was necessary to compute accurately the turbulent natural convection problems in an acceptable turn around times. The investigations highlight the need and ability of the force balancing in devising a robust and accurate algorithm to solve non-Boussinesq fluid flows.

5. Applications of the flow solver for practical problems in enclosures in both laminar and turbulent regimes have been carried out. In particular, studies have been carried out for non-Oberbeck-Boussinesq buoyancy-driven turbulent flows in the presence of radiation. The results from the present work may serve as an ideal test case for benchmarking.

8.2 Scope for Future Work

The mathematical model presented in this thesis can further be modified with an aim to enhance the understanding of the coupled flow with radiative heat transfer in various engineering scenario.

• Firstly, a spectral model can be easily incorporated to consider the non-grey nature of gases. This will help in better understanding of the behavior of gases encountered in practical scenarios like combustion, fire and smoke spread in buildings etc.

• While performing studies on turbulence-radiation interaction, the RTE Favre-averaging is approximated by neglecting the instantaneous temperature fluctuations. This approximation was considered by following the work of Mazumder and Modest [116] who have previously shown that the temperature fluctuations are not much significant for non-reacting flows. However, it will be interesting to explore the contribution of these fluctuating terms in non-Boussinesq flows at large temperature difference. The use of other turbulence models in predicting turbulence radiation interaction can be suitably incorporated into the proposed numerical framework. Comparison of solutions obtained with different turbulence models can be studied.

• A deeper investigation into the true connection between momentum interpolation and force balancing with particular emphasis on natural convection problems (both in laminar and turbulent regimes as also those with large temperature differences) can be undertaken in the future.

• It is seen from laminar buoyancy driven flows that the inclusion of thermal radiation increases the three-dimensionality of the flow. Hence, the future studies on turbulence-radiation interaction can be carried out considering the three-dimensional effects.

• The computational expense associated with a full three-dimensional turbulence radiation interaction study will be very high and hence a computational framework for parallel simulations can be implemented.

• The present model can be easily coupled with a reaction model for understanding the role of thermal radiation in reacting flows.

References

[1] Incropera F.P., Dewitt D.P., Bergman T.L., and Lavine A.S. (2013), 'Principles of heat and mass transfer', .

[2] Modest M.F., *Radiative heat transfer* (Academic press, 2013).

[3] Raithby G. and Chui E. (1990) 'A finite-volume method for predicting a radiant heat transfer in enclosures with participating media', *Journal of Heat Transfer*, vol. 112(2), pp. 415–423.

[4] Chui E. and Raithby G. (1992) 'Implicit solution scheme to improve convergence rate in radiative transfer problems', *Numerical Heat Transfer, Part B: Fundamentals*, vol. 22(3), pp. 251–272.

[5] Chai J.C., Lee H.S., and Patankar S.V. (1994) 'Finite volume method for radiation heat transfer', *Journal of Thermophysics and Heat Transfer*, vol. 8(3), pp. 419–425.

[6] Chai J.C., Lee H.S., and Patankar S.V. (1994) 'Treatment of irregular geometries using a Cartesian coordinates finite-volume radiation heat transfer procedure', *Numerical Heat Transfer, Part B: Fundamentals*, vol. 26(2), pp. 225–235.

[7] Chai J.C., Parthasarathy G., Lee H.S., and Patankar S.V. (1995) 'Finite volume radiative heat transfer procedure for irregular geometries', *Journal of Thermophysics and Heat Transfer*, vol. 9(3), pp. 410–415.

[8] Chai J.C. and Moder J.P. (1997) 'Spatial-multiblock procedure for radiation heat transfer', *Numerical Heat Transfer Part B: Fundamentals*, vol. 31(3), pp. 277–293.

[9] Talukdar P., Steven M., Issendorff F.V., and Trimis D. (2005) 'Finite volume method in 3-D curvilinear coordinates with multiblocking procedure for radiative transport problems', *International Journal of Heat and Mass Transfer*, vol. 48(21-22), pp. 4657–4666.

[10] Raithby G. (1999) 'Evaluation of discretization errors in finite-volume radiant heat transfer predictions', *Numerical Heat Transfer: Part B: Fundamentals*, vol. 36(3), pp. 241–264.

[11] Chai J.C. and Patankar S.V. (2000) 'Finite-volume method for radiation heat transfer', *Advances in Numerical Heat Transfer*, vol. 2, pp. 109–141.

[12] Byun D.Y., Baek S.W., and Kim M.Y. (2003) 'Investigation of radiative heat transfer in complex geometries using blocked-off, multiblock, and embedded boundary treatments', *Numerical Heat Transfer: Part A: Applications*, vol. 43(8), pp. 807–825.

[13] Tan H.P., Zhang H.C., and Zhen B. (2004) 'Estimation of ray effect and false scattering in approximate solution method for thermal radiative transfer equation', *Numerical Heat Transfer, Part A: Applications*, vol. 46(8), pp. 807–829.

[14] Hunter B. and Guo Z. (2016) 'Improved treatment of anisotropic scattering in radiation transfer analysis using the finite volume method', *Heat Transfer Engineering*, vol. 37(3-4), pp. 341–350.

[15] Chui E. and Raithby G. (1993) 'Computation of radiant heat transfer on a nonorthogonal mesh using the finite-volume method', *Numerical Heat Transfer*, vol. 23(3), pp. 269–288.

[16] Baek S.W., Kim M.Y., and Kim J.S. (1998) 'Nonorthogonal finite-volume solutions of radiative heat transfer in a three-dimensional enclosure', *Numerical Heat Transfer, Part B*, vol. 34(4), pp. 419–437.

[17] Murthy J.Y. and Mathur S.R. (1998) 'Finite volume method for radiative heat transfer using unstructured meshes', *Journal of Thermophysics and Heat Transfer*, vol. 12(3), pp. 313–321.

[18] Murthy J. and Mathur S. (2000) 'A finite-volume scheme for radiative heat transfer in semitransparent media', *Numerical Heat Transfer: Part B: Fundamentals*, vol. 37(1), pp. 25–43.

[19] Raithby G. (1999) 'Discussion of the finite-volume method for radiation, and its application using 3D unstructured meshes', *Numerical Heat Transfer: Part B: Fundamentals*, vol. 35(4), pp. 389–405.

[20] Asllanaj F., Feldheim V., and Lybaert P. (2007) 'Solution of radiative heat transfer in 2-D geometries by a modified finite-volume method based on a cell vertex scheme using unstructured triangular meshes', *Numerical Heat Transfer, Part B: Fundamentals*, vol. 51(2), pp. 97–119.

[21] Gazdallah M., Feldheim V., Claramunt K., and Hirsch C. (2012) 'Finite volume method for radiative heat transfer in an unstructured flow solver for emitting, absorbing and scattering media', *Journal of Physics: Conference Series*, vol. 369(1), p. 012020.

[22] Kim M.Y., Baek S.W., and Park J.H. (2001) 'Unstructured finite-volume method for radiative heat transfer in a complex two-dimensional geometry with obstacles', *Numerical Heat Transfer: Part B: Fundamentals*, vol. 39(6), pp. 617–635.

[23] Kim M.Y., Baek S.W., and Park S. (2008) 'Evaluation of the finite-volume solutions of radiative heat transfer in a complex two-dimensional enclosure with unstructured polygonal meshes', *Numerical Heat Transfer, Part B: Fundamentals*, vol. 54(2), pp. 116–137.

[24] Capdevila R., Pérez-Segarra C.D., and Oliva A. (2010) 'Development and comparison of different spatial numerical schemes for the radiative transfer equation resolution using three-dimensional unstructured meshes', *Journal of Quantitative Spectroscopy and Radiative Transfer*, vol. 111(2), pp. 264–273.

[25] Lygidakis G. and Nikolos I., 'Improving the accuracy of a finite-volume method for computing radiative heat transfer in three-dimensional unstructured meshes', in 'Proc. ECCOMAS and IACM Special Interest Conference-SEECCM 2013: 3rd South-East European Conference on Computational Mechanics', (2013), pp. 599–620.

[26] Yücel A., Acharya S., and Williams M. (1989) 'Natural convection and radiation in a square enclosure', *Numerical Heat Transfer, Part A: Application*, vol. 15(2), pp. 261–278.

[27] Lari K., Baneshi M., Nassab S.G., Komiya A., and Maruyama S. (2011) 'Combined heat transfer of radiation and natural convection in a square cavity containing participating gases', *International Journal of Heat and Mass Transfer*, vol. 54(23-24), pp. 5087–5099.

[28] Colomer G., Costa M., Consul R., and Oliva A. (2004) 'Three-dimensional numerical simulation of convection and radiation in a differentially heated cavity using the discrete ordinates method', *International Journal of Heat and Mass Transfer*, vol. 47(2), pp. 257–269.

[29] Farouk B., '3-D natural convectionradiation interactions in a cube filled with gassoot mixtures', in 'Fire Safety Science: Proceedings of the Third International Symposium', vol. 10 (Taylor & Francis, 1991), p. 365.

[30] Borjini M.N., Aissia H.B., Halouani K., and Zeghmati B. (2008) 'Effect of radiative heat transfer on the three-dimensional boyancy flow in cubic enclosure heated from the side', *International Journal of Heat and Fluid Flow*, vol. 29(1), pp. 107–118.

[31] Kumar P. and Eswaran V. (2010) 'A numerical simulation of combined radiation and natural convection in a differential heated cubic cavity', *Journal of Heat Transfer*, vol. 132(2), p. 023501.

[32] Ming P. and Zhang W. (2012) 'Numerical simulation of natural convection and radiation heat transfer in two-dimensional enclosure on hybrid grids', *Numerical Heat Transfer, Part B: Fundamentals*, vol. 61(6), pp. 505–520.

[33] Darbandi M. and Abrar B. (2014) 'A compressible approach to solve combined natural convection-radiation heat transfer in participating media', *Numerical Heat Transfer, Part B: Fundamentals*, vol. 66(5), pp. 446–469.

[34] Mezrhab A., Bouali H., Amaoui H., and Bouzidi M. (2006) 'Computation of combined natural-convection and radiation heat-transfer in a cavity having a square body at its center', *Applied Energy*, vol. 83(9), pp. 1004–1023.

[35] Mezrhab A., Jami M., Bouzidi M., and Lallemand P. (2007) 'Analysis of radiation-natural convection in a divided enclosure using the lattice Boltzmann method', *Computers and Fluids*, vol. 36(2), pp. 423–434.

[36] Moufekkir F., Moussaoui M.A., Mezrhab A., Bouzidi M., and Lemonnier D. (2012) 'Combined double-diffusive convection and radiation in a square enclosure filled with semitransparent fluid', *Computers and Fluids*, vol. 69, pp. 172–178.

[37] Mondal B. and Mishra S.C. (2008) 'Simulation of natural convection in the presence of volumetric radiation using the lattice Boltzmann method', *Numerical Heat Transfer, Part A: Applications*, vol. 55(1), pp. 18–41.

[38] Tighchi H.A. and Esfahani J.A. (2017) 'Combined radiation/natural convection in a participating medium using novel lattice Boltzmann method', *Journal of Thermophysics and Heat Transfer*, vol. 31(3), pp. 563–574.

[39] Paulucci S., 'On the filtering of sound from the Navier-Stokes equations', in 'Technical Report', (Sandia National Laboratories, 1982).

[40] Baum H. (1978) 'The equations of motion for thermally driven, buoyant flows', *Journal of Research of the NBS*, vol. 83, pp. 297–308.

[41] Turkel E. (1987) 'Preconditioned methods for solving the incompressible and low speed compressible equations', *Journal of Computational Physics*, vol. 72(2), pp. 277–298.

[42] Paillere H., Viozat C., Kumbaro A., and Toumi I. (2000) 'Comparison of low Mach number models for natural convection problems', *Heat and Mass Transfer*, vol. 36(6), pp. 567–573.

[43] Nerinckx K., Vierendeels J., and Dick E. (2005) 'Mach-uniformity through the coupled pressure and temperature correction algorithm', *Journal of Computational Physics*, vol. 206(2), pp. 597–623.

[44] Najm H.N., Wyckoff P.S., and Knio O.M. (1998) 'A semi-implicit numerical scheme for reacting flow: I. stiff chemistry', *Journal of Computational Physics*, vol. 143(2), pp. 381–402.

[45] Wall C., Pierce C.D., and Moin P. (2002) 'A semi-implicit method for resolution of acoustic waves in low Mach number flows', *Journal of Computational Physics*, vol. 181(2), pp. 545–563.

[46] Nicoud F. (2000) 'Conservative high-order finite-difference schemes for low-Mach number flows', *Journal of Computational Physics*, vol. 158(1), pp. 71–97.

[47] Sewall E.A. and Tafti D.K. (2008) 'A time-accurate variable property algorithm for calculating flows with large temperature variations', *Computers and Fluids*, vol. 37(1), pp. 51–63.

[48] Mary I., Sagaut P., and Deville M. (2000) 'An algorithm for low Mach number unsteady flows', *Computers and Fluids*, vol. 29(2), pp. 119–147.

[49] Bouloumou O., Serre E., Bontoux P., and Fröhlich J. (2012) 'A 3D pseudo-spectral low Mach-number solver for buoyancy driven flows with large temperature differences', *Computers and Fluids*, vol. 66, pp. 107–120.

[50] Kumar M. and Natarajan G. (2017) 'On the role of discrete mass conservation for non-Boussinesq flow simulations in enclosures', *International Journal of Heat and Mass Transfer*, vol. 104, pp. 1283–1299.

[51] Teleaga I., Seaïd M., Gasser I., Klar A., and Struckmeier J. (2006) 'Radiation models for thermal flows at low Mach number', *Journal of Computational Physics*, vol. 215(2), pp. 506–525.

[52] Dubroca B., Seaïd M., and Teleaga I. (2007) 'A consistent approach for the coupling of radiation and hydrodynamics at low Mach number', *Journal of Computational Physics*, vol. 225(1), pp. 1039–1065.

[53] Bouafia M., Hamimid S., and Guellal M. (2015) 'Non-Boussinesq convection in a square cavity with surface thermal radiation', *International Journal of Thermal Sciences*, vol. 96, pp. 236–247.

[54] Yan W.M. and Li H.Y. (1999) 'Radiation effects on laminar mixed convection in an inclined square duct', *Journal of Heat Transfer*, vol. 121(1), pp. 194–200.

[55] Mahapatra S., Nanda P., and Sarkar A. (2006) 'Interaction of mixed convection in two-sided lid driven differentially heated square enclosure with radiation in presence of participating medium', *Heat and Mass Transfer*, vol. 42(8), pp. 739–757.

[56] Guedri K., Ammar Abbassi M., Naceur Borjini M., Halouani K., and Saïd R. (2009) 'Application of the finite-volume method to study the effects of baffles on radiative heat transfer in complex enclosures', *Numerical Heat Transfer, Part A: Applications*, vol. 55(8), pp. 780–806.

[57] Hostikka S. and McGrattan K. (2006) 'Numerical modeling of radiative heat transfer in water sprays', *Fire Safety Journal*, vol. 41(1), pp. 76–86.

[58] Minseok K. and Anand N.K. (2008) 'Three-dimensional combined convective-radiative heat transfer over a horizontal backward-facing step - a finite-volume method', *Numerical Heat Transfer, Part A: Applications*, vol. 54(2), pp. 109–129.

[59] Abbassi M.A., Guedri K., Borjini M.N., Halouani K., and Zeghmati B. (2014) 'Modeling of radiative heat transfer in 2D complex heat recuperator of biomass pyrolysis furnace: A study of baffles shadow and soot volume fraction effects', *World Academy of Science, Engineering and Technology, International Journal of Mathematical, Computational, Physical, Electrical and Computer Engineering*, vol. 8(2), pp. 450–460.

[60] Adams V., Joshi Y., and Blackburn D.L. (1999) 'Three-dimensional study of combined conduction, radiation, and natural convection from discrete heat sources in a horizontal narrow-aspect-ratio enclosure', *Journal of Heat Transfer*, vol. 121(4), pp. 992–1001.

[61] Menchaca-Brandan M.A., Espinosa F.A.D., and Glicksman L.R. (2017) 'The influence of radiation heat transfer on the prediction of air flows in rooms under natural ventilation', *Energy and Buildings*, vol. 138, pp. 530–538.

[62] Martyushev S.G. and Sheremet M.A. (2014) 'Conjugate natural convection combined with surface thermal radiation in a three-dimensional enclosure with a heat source', *International Journal of Heat and Mass Transfer*, vol. 73, pp. 340–353.

[63] Kolsi L., Abidi A., Maatki C., Borjini N.M., and Aissia B.H. (2011) 'Combined radiation-natural convection in three-dimensional verticals cavities', *Thermal Science*, vol. 15(suppl. 2), pp. 383–390.

[64] Lei C. and Patterson J.C. (2003) 'A direct stability analysis of a radiation-induced natural convection boundary layer in a shallow wedge', *Journal of Fluid Mechanics*, vol. 480, pp. 161–184.

[65] Bajorek S. and Lloyd J. (1982) 'Experimental investigation of natural convection in partitioned enclosures', *Journal of Heat Transfer*, vol. 104(3), pp. 527–532.

[66] Chang L., Yang K., and Lloyd J. (1983) 'Radiation-natural convection interactions in two-dimensional complex enclosures', *Journal of Heat Transfer*, vol. 105(1), pp. 89–95.

[67] Nakamura H., Asako Y., and Hirata H. (1984) 'Combined free convection and radiation heat transfer in rectangular cavities with a parting wall.', *Transactions of the Japan Society of Mechanical Engineers*, vol. 50(459), pp. 2647–2654.

[68] Tan Z. and Howell J.R. (1991) 'Combined radiation and natural convection in a two-dimensional participating square medium', *International Journal of Heat and Mass Transfer*, vol. 34(3), pp. 785–793.

[69] Mezrhab A. and Bchir L. (1999) 'Radiation-natural convection interactions in partitioned cavities', *International Journal of Numerical Methods for Heat and Fluid Flow*, vol. 9(2), pp. 186–203.

[70] Han C.Y. and Baek S.W. (2000) 'The effects of radiation on natural convection in a rectangular enclosure divided by two partitions', *Numerical Heat Transfer, Part A: Applications*, vol. 37(3), pp. 249–270.

[71] Mezrhab A., Moussaoui M., and Naji H. (2008) 'Lattice Boltzmann simulation of surface radiation and natural convection in a square cavity with an inner cylinder', *Journal of Physics D: Applied Physics*, vol. 41(11), p. 115502.

[72] Hsu T.H., Hsu P.T., and How S.P. (1997) 'Mixed convection in a partially divided rectangular enclosure', *Numerical Heat Transfer, Part A: Applications*, vol. 31(6), pp. 655–683.

[73] Patil S., Sharma A.K., and Velusamy K. (2016) 'Conjugate laminar natural convection and surface radiation in enclosures: Effects of protrusion shape and

position', *International Communications in Heat and Mass Transfer*, vol. 76, pp. 139–146.

[74] Ren X.H., Hu J.T., Liu D., Liu C.W., Zhao F.Y., and Wang H.Q. (2017) 'Heterogeneous convective thermal and airborne pollutant removals from a partial building enclosure with a conducting baffle: Parametric investigations and steady transition flow solutions', *Energy and Buildings*, vol. 138, pp. 280–300.

[75] Rahimi M. and Sabernaeemi A. (2010) 'Experimental study of radiation and free convection in an enclosure with a radiant ceiling heating system', *Energy and Buildings*, vol. 42(11), pp. 2077–2082.

[76] Cheesewright R. (1986) 'Experimental data for validation of computer codes for the prediction of two-dimensional buoyant cavity flows', *ASME Winter Annual Meeting, 1986*, pp. 75–81.

[77] Betts P. and Bokhari I. (2000) 'Experiments on turbulent natural convection in an enclosed tall cavity', *International Journal of Heat and Fluid Flow*, vol. 21(6), pp. 675–683.

[78] Tian Y.S. and Karayiannis T.G. (2000) 'Low turbulence natural convection in an air filled square cavity: Part I: the thermal and fluid flow fields', *International Journal of Heat and Mass Transfer*, vol. 43(6), pp. 849–866.

[79] Tian Y.S. and Karayiannis T.G. (2000) 'Low turbulence natural convection in an air filled square cavity Part II: the turbulence quantities', *International Journal of Heat and Mass Transfer*, vol. 43, pp. 867–884.

[80] Ampofo F. and Karayiannis T. (2003) 'Experimental benchmark data for turbulent natural convection in an air filled square cavity', *International Journal of Heat and Mass Transfer*, vol. 46(19), pp. 3551–3572.

[81] Paolucci S. (1990) 'Direct numerical simulation of two-dimensional turbulent natural convection in an enclosed cavity', *Journal of Fluid Mechanics*, vol. 215, pp. 229–262.

[82] Le Quéré P. (1994) 'An improved chebyshev collocation algorithm for direct simulation of 2D turbulent convection in differentially heated cavities', *Finite Elements in Analysis and Design*, vol. 16(3-4), pp. 271–283.

[83] Markatos N.C. and Pericleous K.A. (1984) 'Laminar and turbulent natural convection in an enclosed cavity', *International Journal of Heat and Mass Transfer*, vol. 27, pp. 755–772.

[84] Henkes R. and Hoogendoorn C. (1995) 'Comparison exercise for computations of turbulent natural convection in enclosures', *Numerical Heat Transfer, Part B: Fundamentals*, vol. 28(1), pp. 59–78.

[85] Soria M., Trias F.X., Pérez-Segarra C.D., and Oliva A. (2004) 'Direct numerical simulation of a three-dimensional natural-convection flow in a differentially heated cavity of aspect ratio 4', *Numerical Heat Transfer, Part A: Applications*, vol. 45(7), pp. 649–673.

[86] Trias F.X., Soria M., Oliva A., and Pérez-Segarra C.D. (2007) 'Direct numerical simulations of two- and three-dimensional turbulent natural convection flows in a differentially heated cavity of aspect ratio 4', *Journal of Fluid Mechanics*, vol. 586, p. 259293.

[87] Mesyngier C. and Farouk B. (1996) 'Turbulent natural convection-nongray gas radiation analysis in a square enclosure', *Numerical Heat Transfer; Part A: Applications*, vol. 29(7), pp. 671–687.

[88] Velusamy K., Sundararajan T., and Seetharamu K.N. (2001) 'Interaction effects between surface radiation and turbulent natural convection in square and rectangular enclosures', *Journal of Heat Transfer*, vol. 123(6), pp. 1062–1070.

[89] Sharma A.K., Velusamy K., and Balaji C. (2007) 'Turbulent natural convection in an enclosure with localized heating from below', *International Journal of Thermal Sciences*, vol. 46(12), pp. 1232–1241.

[90] Sharma A.K., Velusamy K., Balaji C., and Venkateshan S. (2007) 'Conjugate turbulent natural convection with surface radiation in air filled rectangular enclosures', *International Journal of Heat and Mass Transfer*, vol. 50(3-4), pp. 625–639.

[91] Sharma A.K., Velusamy K., and Balaji C. (2008) 'Interaction of turbulent natural convection and surface thermal radiation in inclined square enclosures', *Heat and Mass Transfer*, vol. 44(10), pp. 1153–1170.

[92] Xamán J., Arce J., Álvarez G., and Chávez Y. (2008) 'Laminar and turbulent natural convection combined with surface thermal radiation in a square cavity with a glass wall', *International Journal of Thermal Sciences*, vol. 47(12), pp. 1630–1638.

[93] Xamán J.P., Hinojosa J.F., Flores J.J., and Cabanillas R.E. (2008) 'Effect of the surface thermal radiation on turbulent natural convection in tall cavities of facade elements', *Heat and Mass Transfer*, vol. 45(2), pp. 177–185.

[94] Wang Y.C., Yang J., Pan Y., Zhang X.J., and Yu Y.F. (2016) 'Turbulent natural convection heat transfer with thermal radiation in a rectangular enclosure partially filled with porous medium', *Numerical Heat Transfer, Part A: Applications*, vol. 70(6), pp. 639–649.

[95] El Moutaouakil L., Zrikem Z., and Abdelbaki A. (2015) 'Interaction of surface radiation with laminar and turbulent natural convection in tall vertical cavities: analysis and heat transfer correlations', *Heat Transfer Engineering*, vol. 36(17), pp. 1472–1484.

[96] Miroshnichenko I.V. and Sheremet M.A. (2015) 'Numerical simulation of turbulent natural convection combined with surface thermal radiation in a square cavity', *International Journal of Numerical Methods for Heat and Fluid Flow*, vol. 25(7), pp. 1600–1618.

[97] Miroshnichenko I.V., Sheremet M.A., and Mohamad A.A. (2016) 'Numerical simulation of a conjugate turbulent natural convection combined with surface thermal radiation in an enclosure with a heat source', *International Journal of Thermal Sciences*, vol. 109, pp. 172–181.

[98] Miroshnichenko I.V. and Sheremet M.A. (2017) 'Turbulent natural convection and surface radiation in a closed air cavity with a local energy source', *Journal of Engineering Physics and Thermophysics*, vol. 90(3), pp. 557–563.

[99] Miroshnichenko I.V. and Sheremet M.A. (2018) 'Turbulent natural convection combined with thermal surface radiation inside an inclined cavity having local heater', *International Journal of Thermal Sciences*, vol. 124, pp. 122–130.

[100] Shati A.K.A., Blakey S.G., and Beck S.B.M. (2013) 'An empirical solution to turbulent natural convection and radiation heat transfer in square and rectangular enclosures', *Applied Thermal Engineering*, vol. 51(1), pp. 364–370.

[101] Zhang Y., Vicquelin R., Gicquel O., and Taine J. (2013) 'A wall model for LES accounting for radiation effects', *International Journal of Heat and Mass Transfer*, vol. 67, pp. 712–723.

[102] Wang P., Fröhlich J., Michelassi V., and Rodi W. (2008) 'Large-eddy simulation of variable-density turbulent axisymmetric jets', *International Journal of Heat and Fluid Flow*, vol. 29(3), pp. 654–664.

[103] Ibrahim A., Saury D., and Lemonnier D. (2013) 'Coupling of turbulent natural convection with radiation in an air-filled differentially-heated cavity at Ra=1.5 $\times$ 10^{9}', *Computers and Fluids*, vol. 88, pp. 115–125.

[104] Xin S., Salat J., Joubert P., Sergent A., Penot F., and Le Quéré P. (2013) 'Resolving the stratification discrepancy of turbulent natural convection in differentially heated air-filled cavities. part iii: A full convection–conduction–surface radiation coupling', *International Journal of Heat and Fluid Flow*, vol. 42, pp. 33–48.

[105] Soucasse L., Rivière P., and Soufiani A. (2014) 'Subgrid-scale model for radiative transfer in turbulent participating media', *Journal of Computational Physics*, vol. 257, pp. 442–459.

[106] Soucasse L., Rivière P., Soufiani A., Xin S., and Le Quéré P. (2014) 'Transitional regimes of natural convection in a differentially heated cubical cavity under the effects of wall and molecular gas radiation', *Physics of Fluids*, vol. 26(2), p. 024105.

[107] Soucasse L., Rivière P., and Soufiani A. (2016) 'Natural convection in a differentially heated cubical cavity under the effects of wall and molecular gas radiation at Rayleigh numbers up to 3 $\times$ 10^{9}', *International Journal of Heat and Fluid Flow*, vol. 61, pp. 510–530.

[108] Zamora B. and Kaiser A.S. (2012) 'Influence of the variable thermophysical properties on the turbulent buoyancy-driven airflow inside open square cavities', *Heat and Mass Transfer*, vol. 48(1), pp. 35–53.

[109] Zamora B. and Kaiser A.S. (2016) 'Radiative effects on turbulent buoyancy-driven airflow in open square cavities', *International Journal of Thermal Sciences*, vol. 100, pp. 267–283.

[110] Zamora B. and Kaiser A.S. (2017) 'Radiative and variable thermophysical properties effects on turbulent convective flows in cavities with thermal passive configuration', *International Journal of Heat and Mass Transfer*, vol. 109, pp. 981–996.

[111] Elkaroui A., Gazzah M.H., Saïd N.M., Bournot P., and Le Palec G. (2017) 'Entropy generation concept for a turbulent plane jet with variable density', *Computers and Fluids*, vol. Article in Press, pp. 1–14.

[112] Rhie C. and Chow W. (1983) 'A numerical study of the turbulent flow past an isolated airfoil with trailing edge seperation', *AIAA Journal*, vol. 21, pp. 1525–1532.

[113] Dalal A., Eswaran V., and Biswas G. (2008) 'A finite volume method for Navier-Stokes equation on unstructured meshes', *Numerical Heat Transfer, Part B: Fundamentals*, vol. 54(2), pp. 238–259.

[114] Murthy J.Y. and Mathur S.R. (1998) 'Finite volume method for radiative heat transfer using unstructured meshes', *Journal of Thermophysics and Heat Transfer*, vol. 12(3), pp. 313–321.

[115] Wilcox D.C. et al., *Turbulence modeling for CFD*, vol. 2 (DCW industries La Canada, CA, 1993).

[116] Mazumder S. and Modest M.F. (1999) 'Turbulence-radiation interactions in nonreactive flow of combustion gases', *ASME Journal of Heat Transfer*, vol. 121, pp. 726–728.

[117] Alves M.A. and Oliveira P.J. (2003) 'A convergent and universally bounded interpolation scheme for the treatment of advection', *International Journal for Numerical Methods in Fluids*, vol. 41(7), pp. 47–75.

[118] Perot B. (2000) 'Conservation properties of unstructured staggered mesh', *Journal of Computational Physics*, vol. 159, pp. 58–89.

[119] LIS (2005) 'Library of iterative solvers for linear systems, lis user guide', *www.ssisc.org/lis*.

[120] Ilis G.G., Mobedi M., and Sunden B. (2008) 'Effect of aspect ratio on entropy generation in a rectangular cavity with differentially heated vertical walls', *International Communications in Heat and Mass Transfer*, vol. 35, pp. 696–703.

[121] 'OpenCFD, OpenFOAM–the open source CFD Toolbox–user's guide, 1st Edition, OpenCFD Ltd.', *United Kingdom, 2010*.

[122] Mengüç M. and Viskanta R. (1985) 'Radiative transfer in three-dimensional rectangular enclosures containing inhomogeneous, anisotropically scattering media', *Journal of Quantitative Spectroscopy and Radiative Transfer*, vol. 33(6), pp. 533–549.

[123] Truelove J.S. (1988) 'Three-dimensional radiation in absorbing-emitting-scattering media using the discrete-ordinates approximation.', *Journal of Quantitative Spectroscopy and Radiative Transfer*, vol. 39(1), pp. 1048–1051.

[124] Darbandi M. and Hosseinizadeh S.F. (2006) 'Numerical simulation of thermobuoyant flow with large temperature variation', *Journal of Thermophysics and Heat Transfer*, vol. 20(2), pp. 285–296.

[125] Le Quéré P., Weisman C., Paillère H., Vierendeels J., Dick E., Becker R., Braack M., and Locke J. (2005) 'Modelling of natural convection flows with large temperature differences: a benchmark problem for low Mach number solvers. part 1. reference solutions', *ESAIM: Mathematical Modelling and Numerical Analysis*, vol. 39(3), pp. 609–616.

[126] Patel J.K. and Natarajan G. (2017) 'A novel consistent and well balanced algorithm for simulations of multiphase flows on unstructured grids.', *Journal of Computational Physics*, vol. 350, pp. 207–236.

[127] Choi S.K., Kim S.O., Lee C.H., and Choi H.K. (2003) 'Use of the momentum interpolation method for flows with a large body force', *Numerical Heat Transfer: Part B: Fundamentals*, vol. 43(3), pp. 267–287.

[128] Denner F. and van Wachem B.G. (2014) 'Fully-coupled balanced-force vof framework for arbitrary meshes with least-squares curvature evaluation from volume fractions', *Numerical Heat Transfer, Part B: Fundamentals*, vol. 65(3), pp. 218–255.

[129] Mencinger J., 'An alternative finite volume discretization of body force field on collocated grid', in 'Finite Volume Method-Powerful Means of Engineering Design', (InTech, 2012).

[130] GAMBIT (2004) 'Gambit 2.2 user's guide', *Fluent Inc., Lebanon, NH,*.

[131] Slimi K. (2006) 'Entropy generation for unsteady natural convection and radiation within a tilted saturated porous channel', *International Journal of Exergy*, vol. 3(2), pp. 174–190.

LIST OF PUBLICATIONS

International Journal

- **Parmananda, M.**, Thirumalaisamy R., Dalal, A., and Natarajan, G., "Numerical simulation of non-Boussinesq turbulent natural convection coupled with thermal radiation in enclosures. International Journal of Thermal Sciences, Volume 134, 2018, pp 298-316.

- **Parmananda, M.**, Dalal, A., and Natarajan, G., "A unified frame-work for combined convective radiative heat transfer problems on hybrid unstructured meshes, International Journal of Heat and Mass Transfer, Volume 126, Part B, 2018, pp. 908-925

- **Parmananda, M.**, Dalal, A., and Natarajan, G., 2018, "The influence of partitions on predicting heat transfer due to the combined effects of convection and thermal radiation in cubical enclosures", International Journal of Heat and Mass Transfer, Volume 121, 2018, pp. 1179-1200.

- **Parmananda, M.**, Dalal, A., and Natarajan, G., 2018, "Critical assessment of numerical algorithms for convective-radiative heat transfer in enclosures with different geometries", International Journal of Heat and Mass Transfer, Volume 108, Part A, 2017, pp. 627-644.

- **Parmananda, M.**, Dalal, A., and Natarajan, G., "Numerical appraisal of three low Mach number algorithms for radiative-convective flows in enclosures, Computer Methods in Applied Mechanics and Engineering (Under Review).

International Conference

- Thirumalaisamy, R., **Parmananda, M.**, Dalal, A., and Natarajan, G., 2017, Development of a Low Mach Number Solver to Study Combined Turbulent Convective-Radiative Heat Transfer, Paper No: ASCHT-17-26, 6th Asian

Symposium on Computation Heat Transfer and Fluid Flow, IIT Madras, India.

- Manik, J., **Parmananda, M.**, Kotoky, S., Borgohain, P., Dalal, A. and Natarajan, G.,2017, Lessons from Anupravaha: Towards a General Purpose Computational Framework on Hybrid Unstructured Meshes for Multi-Physics Applications, Paper No. CHT-17-209, ICHMT International Symposium on Advances in Computational Heat Transfer, Napoli, Italy.

- **Parmananda, M.**, Dalal, A., and Natarajan, G., 2016, A Consistent Approach for Simulating Natural Convection with Radiative Heat Transfer in Participating Media, Paper No: RAD-16-05, Proceedings of the 8th International Symposium on Radiative Transfer, Cappadocia, Turkey.

- **Parmananda, M.**, Khan, S. and Dalal, A., 2016, Numerical Simulation of Natural Convection With Radiative Heat Transfer in a Cavity, 6th International Congress on Computational Mechanics and Simulation, IIT Bombay, India.

- Bajpai, A., Manik, J., **Parmananda, M.**, Dalal, A., and Natarajan, G., 2014, Computation of Variable Density Flows on Hybrid Unstructured Grids, Paper No: 515, 5th International and 41st National Conference on Fluid Mechanics and Fluid Power, IIT Kanpur, India.

- Manik, J., **Parmananda, M.**, Dalal, A., and Natarajan, G., 2013, Development of 3-D Navier-Stokes Solver Over a Hybrid Unstructured Grid, Paper No: HMTC1300353, 22nd National and 11th International ISHMT-ASME Heat and Mass Transfer Conference, IIT Kharagpur, India.